University of Huddersfield Repository

Williamson, James

Dispersed reference interferometry for on-machine metrology

Original Citation

Williamson, James (2016) Dispersed reference interferometry for on-machine metrology. Doctoral thesis, University of Huddersfield.

This version is available at http://eprints.hud.ac.uk/31554/

http://eprints.hud.ac.uk/

Dispersed Reference Interferometry for On-Machine Metrology

James Francis Williamson

A thesis submitted to the University of Huddersfield in partial fulfilment of the requirements for the degree of Doctor of Philosophy

The University of Huddersfield

April 2016

Copyright statement

i. The author of this thesis (including any appendices and/or schedules to this thesis) owns any copyright in it (the "Copyright") and he has given The University of Huddersfield the right to use such Copyright for any administrative, promotional, educational and/or teaching purposes.

ii. Copies of this thesis, either in full or in extracts, may be made only in accordance with the regulations of the University Library. Details of these regulations may be obtained from the Librarian. This page must form part of any such copies made.

iii. The ownership of any patents, designs, trademarks and any and all other intellectual property rights except for the Copyright (the "Intellectual Property Rights") and any reproductions of copyright works, for example graphs and tables ("Reproductions"), which may be described in this thesis, may not be owned by the author and may be owned by third parties. Such Intellectual Property Rights and Reproductions cannot and must not be made available for use without the prior written permission of the owner(s) of the relevant Intellectual Property Rights and/or Reproductions

Abstract

The reliance of emerging engineering and scientific applications on nanometre scale surfaces has led to the requirement for embedded metrology instrumentation for on-machine measurement in precision and ultra-precision manufacturing processes. In-situ measurement provides reduction in waste, cost and production cycle time of manufactured components however the presence of environmental noise and difficulties of integration make embedded metrology challenging.

In this thesis a review of on-machine methods of optical metrology is provided and commercially available instruments are summarised. The requirement for highly miniaturised methods of distance and surface topography measurement for operation within volume limited manufacturing environments is presented and the necessity for smaller, faster probes with increased range, resolution and robustness outlined. The potential for dispersed reference interferometry (DRI) to exceed the capability of existing single-point remote fibre probing instruments is then introduced.

DRI as a technique for single-point distance and surface topography measurement is first evaluated in a bulk optics configuration using a short coherence light source and chromatic dispersion within the reference arm. The resulting spectral interferograms have symmetry positions which are directly related to absolute surface position to yield measurement with a 279 nm axial resolution over a 285 μm axial range.

Improvement of this resolution results from introduction of template matching, a signal processing technique which correlates a measured interferogram with a set of pre-calculated template interferograms resulting in a relative method of measurement with an axial resolution of 0.6 nm across the 285 μm axial range. Combination of this high resolution, relative measurement method with low resolution but absolute position data is then explored to improve the robustness of DRI to discontinuous and structured surfaces. Determination of high resolution wraparound order using low resolution absolute data is demonstrated over a 30 μm range, with extension to the full range of DRI expected as future improvements increase the measurement rate.

Next a DRI topology is introduced which makes use of miniature common-path probes linked by fibre to a remote interrogation interferometer allowing reduction in size of the on-machine metrology apparatus. Modifications to the DRI are described to enable this common-path remote fibre probing, along with changes to the light source, spectrometer and dispersive element which allow extension of the range of DRI to 800 μm while maintaining nanometre axial resolution.

Finally, a further work section offers insights into methods to improve miniaturisation of DRI probes as well as providing discussion of methods of hardware and signal processing optimisation to augment the instrument measurement rate.

Acknowledgements

The last four years of my PhD have been some of the most rewarding of my life. The people I've met, the knowledge I've gained, the encouragement I've received and the faith in me I've experienced are something I shall always remember.

My sincere thanks and respect go to my supervisors Jane Jiang and Haydn Martin. Jane for her inspiration, encouragement and vast knowledge of the subject area. Haydn for his invaluable experience, patience, skill with words and friendship. The trust and encouragement they have given me have been above and beyond.

My parents, John and Jennie undoubtedly deserve my thanks. Their support and encouragement through my undergraduate studies, and their faith in me to return to academia as well as their ever positive advice have been essential to everything I feel I have achieved.

Thanks also to my partner Michelle. Her patience, love and kindness throughout my research and her confidence in me as both my best friend and as a colleague have proved invaluable to me.

Thank you to all of my colleagues at the Centre for Precision Technologies. The opportunity to work with such a diverse but skilled and knowledgeable group of people has been a joy.

Table of Contents

List of Figures

List of Tables

List of Acronyms

AFM	Atomic Force Microscopy
AR	Anti-reflective
BSI	Balanced Spectral Interferometry
CE	Characteristic Equation
CAD	Computer Aided Design
CCM	Confocal Chromatic Microscopy
CCS	Confocal Chromatic Sensing
CCSI	Chromatic Confocal Spectral Interferometry
CMM	Coordinate Measurement Machine
COTS	Commercial Off The Shelf
CSV	Comma Separated Values
CT	Computed Tomography
DLP	Digital Laser Projector
DOF	Depth of Focus
DRI	Dispersed Reference Interferometry
DSP	Digital Signal Processing
EDM	Electro-discharge Machining
FDOCT	Fourier Domain Optical Coherence Tomography
FFT	Fast Fourier Transform
FOV	Field Of View
FPM	Fringe Projection Microscopy
FWHM	Full Width Half Maximum
GPGPU	General Purpose Graphics Processing Unit
HeNe	Helium Neon
HPI	Hyperspectral Interferometry
IFFT	Inverse Fast Fourier Transform
LCI	Low Coherence Interferometry
ISG	Imaging Solutions Group
LCSI	Laterally chromatically dispersed, spectrally encoded interferometer
LVDT	Linear Variable Differential Transformer
MEMS	Micro Electro Mechanical Systems
MWFT	Multi-scale Windowed Fourier Transform
NEMS	Nano Electro Mechanical Systems
NIR	Near Infra-Red

OCT	Optical Coherence Tomography
OPD	Optical Path Difference
PI	Physik Instrumente. Manufacturer of precision motion and positioning systems.
PMD	Phase Measuring Deflectometry
PPM	Parts Per Million
PSI	Phase Shift Interferometry
PV	Photovoltaic
PZT	Lead Zirconate Titanate (piezo-electric actuator)
R2R	Roll-to-roll
PMD	Phase Measuring Deflectometry
PSU	Power Supply Unit
RIFT	Rotation-invariant Feature Transform
SAWLI	Spectral Analysis of White Light Interferograms
SDOCT	Spectral Domain Optical Coherence Tomography
SDPM	Spectral Domain Phase Microscopy
SDSCI	Spatially Dispersed Short Coherence Interferometry
SIFT	Scale-invariant Feature Transform
SMF	Single Mode Fibre
SMPS	Switched Mode Power Supply
SPDT	Single Point Diamond Turning
SRWLI	Spectrally Resolved White Light Interferometry
TCM	Tool Condition Monitoring
TRL	Technology Readiness Level
USI	Unbalanced Spectral Interferometry
VI	Virtual Instrument. A Labview file format.
WFT	Windowed Fourier Transform
WLI	White Light Interferometry
WSI	Wavelength Scanning Interferometry
WT	Wavelet Transform

1 Thesis overview

1.1 Introduction

The reliance of emerging technology on micro and nano-scale surface finishes, structures and features as well as the functional relationship between surface topography and design intentions introduce the necessity for measurement technology to keep abreast of these on-going developments and ensure engineered surfaces are manufactured as intended [1].

The increasing surface form and finish tolerances required for precision and ultra-precision applications necessitate metrology instrumentation embedded within the manufacturing process. Where historically non-contact nanometre resolution measurement has been performed post-process within temperature, humidity and vibration controlled environments, methods robust to these effects have emerged within the last decade allowing embedded measurement, leading to a reduction in measurement cycle time and cost while also allowing measurement without removal of non-conformant parts from the machine.

Development of embedded metrology instrumentation is driven by the requirement to increase axial resolution, range, working distance, measurement rate, environmental robustness, field of view and lateral resolution while reducing measurement cycle time, cost and device size. Improvements to these parameters allows a wider range of applications and improves the value that metrology provides to manufacturing.

The ability of single-point methods to physically separate imaging optics from the interrogation apparatus allows single-point methods to achieve further miniaturisation of the on-machine component of the measurement apparatus at the compromise several measurement parameters. The small form factor allows integration of single-point distance and surface topography measurement instruments within manufacturing processes whose limited work volume previously excluded the use of on-machine measurement.

Existing single-point instruments for embedded metrology achieve limited combinations of range, resolution, measurement rate, cost reduction and miniaturisation. For instruments whose axial resolution to range ratio (dynamic range) is limited, high resolution, high range measurement is not possible. For others a reduction in cost is limited by the requirement for multiple expensive light sources. Within this thesis the implementation of dispersed reference interferometry (DRI) is explored as a method to enable an improved dynamic range solution with a higher degree of probe miniaturisation and a potentially lower cost.

1.2 Aim

This research aims to extend the suitability of DRI as a single point embedded metrology tool for the measurement of distance and surface topography in ultra-precision manufacturing environments. The ability to interrogate remote fibre probes with high potential for miniaturisation while improving upon the state-of-the-art in terms of measurement speed, dynamic range and instrument cost is critical to improve the value provided by single-point embedded metrology.

1.3 Objectives

- Explore the possibility of nanometre axial resolution measurement using DRI.
- Investigate improvement of the axial range of DRI to several millimetres.
- Demonstrate measurement rates in excess of 10 kHz.
- Development of a common-path remote fibre probe topology with considerations for miniaturisation for on-machine operation.
- Design of a prototype DRI apparatus for interrogation of remote fibre probes in a manufacturing environment.

1.4 Thesis structure

Chapter 1: Introduction. This chapter introduces the necessity for a single-point method of embedded metrology making use of remote fibre probes to achieve a high level of miniaturisation at a reduced cost. After introducing these requirements the aim, objectives and structure of this thesis are outlined.

Chapter 2: Metrology instrumentation for on-machine surface topography measurement. The industrial requirement for on-machine surface topography measurement is introduced and a case is made for the requirements of emerging on-machine metrology instrumentation. An overview of currently available embedded metrology tools is provided and the operational principles, strengths and weaknesses of each are presented. This is concluded by a comparison of the methods and analysis of the current capability shortfalls.

Chapter 3: Introduction to DRI – Absolute position encoding by wavelength. A bulk optics implementation of dispersed reference interferometry (DRI) is described and the operational principles outlined. Calculation of interferogram symmetry point using autoconvolution for both simulated and real interferograms are compared and step height measurements are performed. The resolution, range and linearity of this method are assessed.

Chapter 4: High resolution DRI – A signal processing scheme for extracting relative position encoding by phase. A signal processing method is introduced to calculate high resolution measurement data to be obtained without modification of the bulk optics interferometer. The similarities between the application

of template matching to image processing and DRI are put forth before range, resolution, linearity and stability of template matching method for spectral interferograms are evaluated.

Chapter 5: High dynamic range DRI – Combining absolute and relative position encoding. The importance of high resolution, high range and absolute measurement methods is introduced. An attempt at combination of high resolution relative data with high range absolute data is made before the strength and weakness of the signal processing method are discussed.

Chapter 6: Prototype DRI – Development of remote fibre-linked probing. Small, light, cheap and robust fibre probes, remotely located from the interrogation optics are presented as an essential component of successful integration of a surface topography instrument capable of on-machine measurement. In this section the design of such probes and the changes required to a bulk optics DRI are outlined before initial validation of such a method performed. A prototype interferometer is then introduced, having reduced path length, cost and flexibility.

Chapter 7: Conclusions. This chapter relates the outcomes of chapters 2-5 to the requirements for on-machine surface metrology set forth in chapter 2. The progress of DRI towards these requirements is provided and discussion of difficulties is given.

Chapter 8: Further work. Improvements to the DRI apparatus and probe assemblies are discussed to allow DRI to better meet the requirements for on-machine metrology. Improved methods of signal processing for higher measurement rates are proposed which make use reduction of overheads as well as parallel and concurrent signal processing methodologies. Lastly, designs for miniaturised fibre-linked probes are introduced to allow measurement of high aspect ratio features and difficult geometries.

1.5   Contributions to knowledge

The novel work contained within this thesis may be summarised as follows:

- Investigation of a method of signal processing with the ability to extract high resolution relative position data from DRI spectral interferograms. Template matching determines the degree of correlation between interferograms measured by the DRI apparatus and a set of interferograms with known parameters in order to achieve a nanometre resolution.
- Demonstration of DRI as an absolute method of distance and topography measurement with an axial range of 800 μm.
- Development of a method of high resolution, absolute measurement using autoconvolution to determine the phase order of high resolution, relative (phase ambiguous) position data.

- Establishment of a prototype DRI instrument with a common-path fibre-linked probe. Probes with the potential for a high degree of miniaturisation and robustness to environmental noise are demonstrated.

2   Metrology instrumentation for on-machine surface topography measurement

2.1   Introduction

The reliance of emerging technology on micro and nano-scale surface finishes, structures and features as well as the functional relationship between surface topography and design intentions introduce the necessity for measurement technology to keep abreast of these on-going developments and ensure engineered surfaces are as manufactured as intended [1].

The availability of a range of measurement instruments whose capabilities vary so widely mean that surface characterization for a wide range surface topography measurement applications is feasible. However, the historical requirement of these instruments for minimal mechanical noise and contaminants reduces the measurement throughput of such devices while their sensitivity to environmental disturbances such as temperature, humidity, pressure and vibration limit their uptake due to the costs associated with their preference for environmentally controlled measurement labs and the resultant post-process measurement. Despite their initial and on-going expense as well as their sensitivity to environmental disturbances these instruments are capable of varying combinations of range, vertical resolution, lateral resolution, measurement area and measurement rate. However, a typical instrument excels at a selection of the above key measurement parameters with no instrument affording the user the state of the art in all five.

The uptake of metrology instrumentation in the emerging micro and nano-manufacturing sector is a crucial step in improving product/component yield and functionality while reducing wastage and cost [2]. Described below are some of the factors deemed to be limiting the uptake of metrology for emerging micro and nano-manufacturing applications.

Commercially available offline measurement systems are typically designed for mounting of samples within the field of view of the instrument, relying on the rigidity of the instrument and external reduction in environmental noise to achieve acceptable measurement. The trend towards manufacturing of larger components while maintaining nanometre scale surface features introduces several problems for post-process metrology. First, mounting of the sample on a fixed measurement platform becomes impossible as sample sizes exceed tens of centimetres while retaining the requirement for nanometre form tolerance. Second, movement of components from the manufacturing environment to measurement instruments increases production cycle times, reduces throughput and increases the component cost. Lastly, measurements using offline means of metrology are not easily automated, with skilled, time consuming labour required for optical alignment.

Another case where application of metrology for process and quality control is problematic is the measurement of continuous production processes such as the manufacture of flexible photovoltaics (PV), printable electronics, structured films and other roll-to-roll (R2R) manufacturing processes. The stringent functional tolerances required for layer thicknesses of barrier films, the meticulous cleaning requirements to assure minimal water vapour transmission and the vacuum conditions present for printing of electronics mean that on-line measurement of defects, contaminating particles and web properties is highly desirable. The continuous nature of the production make offline measurement of samples impossible and the high throughput of the manufacturing processes combined with the latency of offline measurement mean that detection of defects post-manufacture would result in the wastage of a large quantity of product. Existing machine-vision inspection solutions, incapable of providing height data have proved insufficient for quantifying all defects [3] and so development of on-machine topographic measurement solutions were critical to development of flexible photovoltaics [4]. Experience gained from such applications is likely transferable to other R2R and continuous production processes.

Removal of the workpiece is also problematic for precision manufacturing techniques such as single point diamond turning (SPDT), precision polishing, micro-grinding and micro-electro-discharge machining (μEDM). These are used for the manufacture of plano, spherical or freeform lenses and metallic mirrors as well as high tolerance structured surfaces for injection molding, optics and micro-fluidics among many other applications. Precision spindles and translation kinematics allow the turning of specular optics with a roughness of several nanometres and form accuracy of tens of nanometres [5] with the requirements for such high tolerances problematic for metrology [6]. They necessitate measurement during or after manufacture to ensure a component meets the specifications and achieves required functionality. With current offline measurement methods this requires removal of the work-piece from the manufacturing platform, however with the ratio of mounting tolerance to form tolerance this makes re-machining after removal impossible, resulting in a higher than necessary scrap rate compared to if verification by on-machine measurement were possible. The possibility of using the same flexible on-machine metrology apparatus for tool condition monitoring (TCM), analysis of tool tip/surface wear, is also attractive as a process control method to both reduce machining errors and premature tooling replacement costs. The reduction in production costs afforded by successful unmanned machining has been identified as being strongly reliant on successful identification of tool wear [7].

Finally, a considerable limiting factor to the use of current offline metrology instrumentation is the sensitivity of these instruments to environmental disturbances. Their preference for vibration isolation and environmental control result in low throughput and high latency for measurement of components due to the necessity for transfer to offline metrology. This increased measurement time and cost are barriers for the introduction of components such as precision moulded freeform lenses as well as their

associated mounting structures where not just lens form is important but flatness and roundness of mating surfaces to meet necessary mechanical tolerances.

From these examples it can be seen that in order to increase the availability of metrology for new applications in manufacturing there needs to be a shift in the approach of metrology from offline, lab based solutions towards use of metrology upon the manufacturing platform. This will enact reductions in cost, waste and measurement cycle time as well as introducing metrology to processes where measurement was not previously possible on-machine.

2.2 Definition of on-machine metrology

The transition away from off-line measurement and the advancement of embedded metrology is a crucial step to increase commercial uptake of metrology, enabling measurement of high value parts before removal from the manufacturing environment. It is important to highlight the differences in nomenclature for metrology where within the industry and literature many terms are used.

In-process or in-line metrology can be defined as any measurement method which occurs while the manufacturing process continues. This may include use of the metrology as part of a control system, in the presence of the manufacturing process or later in the manufacturing chain for continuous processes. Challenges for in-process metrology are a) the necessity for instantaneous measurement to allow robustness to the motion of the measurand, b) the requirement for robustness to the increased vibration inherent in the measurement of moving parts and c) robustness to or protection from manufacturing contaminants such as swarf, dust and cooling fluids. Examples of in-process metrology include measurement of moving webs in the roll-to-roll manufacturing sector as well as the measurement of conveyed products.

On-machine, in-situ, on-line or embedded metrology is the process of measuring surfaces without removal of the work piece from the manufacturing platform. Measurement is not limited to simply the workpiece but may extend to the machine tool cutting/grinding/polishing/molding/forming surfaces. All in-process methods of metrology are also on-machine, but the terminology above does not require that manufacturing continues, simply that the measurement of the part occurs within the manufacturing environment. Challenges faced are those such as environmental disturbances and process contaminants. Some examples of on-machine metrology include grinding tool wear measurement, tip geometry characterization of milling cutters, measurement of both the molds and components in precision injection molding industries and, measurement of surface roughness and form deviation of freeform specular surfaces produced by single point diamond turning.

Post-process or offline metrology describes the use of measurement instruments located remotely from the manufacturing process. The measurement latency between production and measurement, the cost of upkeep of a separate facility as well as the operator costs of non-automated metrology are significant drawbacks to the use of offline metrology. The maturity of the technology and the ability to perform measurement of thermally unstable components at a constant temperature is however advantageous.

2.3 Advantages of embedded metrology

The following benefits over off-line surface measurement are offered:

1. Reduced costs.

    1.1. While not true for every available system, the costs associated with off-line metrology include the setup and maintenance of a dedicated metrology lab. This is especially true for nanometer precision measurements for which the requirement for a clean, temperature and humidity controlled environment with minimal vibration make nanometer precision metrology prohibitively expensive for many engineering applications.

    1.2. As development of metrology tools increases their tolerance to the factory environment, on-machine measurement of components will reduce measurement times and in turn reduce the costs associated with labour, production latency and maintenance costs.

2. Component re-indexing. For precision parts there are cases where it is difficult or impossible to re-index a part on a machine tool once removed. For this reason, on-machine metrology will enable re-machining for non-conformant components, reducing waste and cost while improving quality.

3. Reduced training requirements. The automated nature of on-machine metrology means that less operator experience is necessary in the setup, alignment and operation of metrology instrumentation. Alignment of components with optical instruments requires intimate knowledge of their advantages and limitations, meaning operator skill is crucial to successful mounting, alignment and measurement of a sample.

4. Improved measurement cycle time. The necessity to increase measurement speed to improve tolerance to noise mean that the time to acquire a complete measurement will decrease. This will in turn reduce measurement cost per item and increase throughput.

Furthermore, the feasibility of in-process metrology depends greatly upon the method chosen with the following considerations proving difficult to measurement for some applications and methods.

1. Motion. Methods requiring multiple image captures to obtain measurement data benefit from a static measurand. The requirement for the workpiece to be stationary for measurement is a difficulty for on-line metrology. This can be overcome to a certain extent by increasing measurement rate but

single shot optical methods may be more appropriate where measurement of moving components is required.

2. Manufacturing process contaminants. Swarf, lubricant and coolant may all have adverse effects on measurement, with surfaces requiring either pneumatic or mechanical cleaning prior to measurement to ensure that the correct surface is measured.

3. Process speed. Even single shot methods may be unsuitable for in-process metrology if the signal processing required to achieve the desired measurement rate isn't sufficient.

2.4 Requirements for embedded metrology

For the above reasons, the following are key requirements for any embedded metrology tool. In order to match and exceed the performance of offline metrology tools, new instruments must meet as many of the following requirements as achievable:

- **Robust to environment.** The effects of temperature, humidity, vibration, atmospheric pressure and the presence of lubricants/contaminants must not adversely affect the quality of measurement.

- **Compact.** Reduction in size of instruments for integration with machine tools and manufacturing environments is critical where reduction in manufacturing work volume is unacceptable. Reducing measurement instrument size also minimizes costs of integration as well as challenges where retrofitting to existing manufacturing platforms.

- **Measurement rate**. Increasing measurement rate will reduce the effects of environmental noise on the measurement and reduce the time for a complete measurement.

- **Measurement precision** must equal or exceed existing offline methods due to the ever decreasing feature sizes of engineered surfaces.

- **Range.** The ability of an instrument to maintain measurement over range increases the usefulness for components with large surface features.

- **Dynamic range**. The ratio of axial range to resolution is important to a) increase the instrument versatility in measurement and b) reduce the cost associated with the requirement for many probes/objectives to cover a range of measurement regimes.

- **Low cost**. The ability of measurement instruments to provide value to the manufacturing process will increase their uptake.

2.5 Review of optical distance and surface topography measurement techniques

What follows is an overview of the currently available optical methods of on-machine metrology capable of distance and surface topography measurement. The underlying operational principles of each method are introduced followed by details of the specific implementations required for use as an embedded not

offline method of metrology. The inherent strengths and weaknesses of each are reviewed and compared, and where applicable commercial products are presented along with examples of industry uptake and usage.

A review of solely optical methods is undertaken due to the inherent unsuitability of contact methods for on-machine measurement. The superior measurement rate of optical methods reduces measurement time and cost while their non-contact nature prevents damage to delicate measurands or to the measurement instrument itself.

For the most part the methods described in this section are evolutions of historically off-line measurement techniques and so it is useful to describe the operation of each of the original methods before description of modifications to allow for improved robustness for on-machine measurement. In this way it is possible to understand that the changes often require a compromise to the measurement rate, cost or complexity of the method in some way, with the emerging instruments each catering to specific but somewhat overlapping measurement applications.

The following reviews begin with areal methods of metrology which allow full field measurement of surface height data. Their varying ability with respect to range, resolution, measurement rate and ability to measure discontinuous surfaces are discussed. The major shortcoming of each of these methods is the possibility for further miniaturisation of the on-machine measurement hardware and so following their description, single-point methods are introduced. While requiring mechanical or optical scanning to obtain profile and areal measurement data is a considerable drawback of such methods, the ability to separate their interrogation apparatus from the light gathering objective allow significant miniaturisation of the on-machine component of the device, something that is highly attractive for work volume limited manufacturing processes.

2.5.1   Focus Variation

Focus variation employs the mechanical translation of an objective lens or the measured sample followed by analysis of the changing image sharpness across the depth of field to calculate 3d topographical data [8, 9]. The pixel by pixel calculation of image focus and hence surface height is achieved through calculation of the standard deviation of the grey values for an area of pixels surrounding the pixel of interest. Fitting of a curve to the changing standard deviation values for each pixel can allow lateral resolution less than that of the CCD pixel size [10]. Commercially this has resulted in the InfiniteFocus range of offline measurement instruments by Alicona Imaging GmbH.

The absolute nature of the focus variation method allows measurement of discontinuous surfaces containing steep, broken or rough regions and the spatially separated regions may still have their surface heights resolved in relation to one another. The scanning nature of the measurement objective means

that the method has excellent range (up to 25 mm) and while the 10 nm achievable axial resolution does not compete with other methods the high range makes the dynamic range of this method comparable with many others. Additional benefits of the scanning of the lens is the consistent lateral resolution across the range while the use of scattered light allows high acceptance angles, with surfaces slopes of up 80° reported as measurable [11]. Finally, proponents of the method argue that the non-interferometric nature of this method means that it is less susceptible to short term variations in ambient light, temperature, humidity and pressure.

Compared to other methods, the requirement for mechanical scanning of the objective make focus variation a slow method, with measurement rates of less than 1 Hz making it sensitive to vibration and inappropriate for in-line measurement of continuous production processes. Another negative aspect is the necessity for nanoscale surface roughness to back scatter sufficient light for sharpness detection. While this requirement does allow measurement of steep slopes, it makes measurement of low roughness and specular surfaces problematic [12].

Despite these limitations Alicona offer the IF-SensorR25, IF-Portable and IF-Robot for metrology in production environments. IF-SensorR25, a miniaturized version (126 x 153 x 202 mm) for integration with machine tools, has been reported as beneficial for measurement in electro-discharge machining (EDM) centres, allowing a fourfold increase in machining accuracy [13]. IF-Portable and IF-Robot are offered as roughness, waviness and form measurement tools for use in production environments with a focus on the ability to measure on and around traditionally difficult to measure larger components and assemblies. Advertised as providing measurements with high traceability and repeatability irrespective of production conditions, the literature provides a compelling case for use of focus variation over interferometric methods, though it is not clear from the available literature how the effect of mechanical vibration interacts with the many camera frames required during a measurement cycle.

2.5.2   Phase Measuring Deflectometry

Phase measuring deflectometry (PMD) detects the distortions of a sinusoidal fringe pattern reflected by a specular surface to determine surface topography. The fringes are projected by a high resolution diffuse source such as a computer monitor and the distortions are then observed by one or more areal detectors.

As a method of on-machine metrology, deflectometry is one of the most mature methods with measurement of form defects with deflectometry considered an established method for car body panel and windshield measurement in the automotive industry [14]. Companies such as Micro-Epsilon offer inspection systems for form and point accuracy measurement of large engineering surfaces. While capable of on-machine measurement of such surfaces, the large volume and low resolution of these measurements mean that they are out of the scope of this study.

Despite the increased range, field of view and dynamic range of deflectometry compared to other methods of metrology, it is not until recently, that it has matched interferometry for traceability, repeatability and vertical resolution; with measurement of surface topography instead of form demonstrated. Advances in the setup, processing and calibration of deflectometry methods as described by Lehmann et al., show the introduction of measurement regimes capable of approaching surface topography, measuring large areas at resolutions sufficient for roughness measurement [15].

Previously deflectometry was considered qualitative and semi-qualitative [15] with work by Olesch et al. showing the possibility of quantitative PMD measurement repeatable to 100 nm [16]. The measurement of diamond turned samples on-machine in a SPDT machining centre have also been demonstrated along with self-calibration and a novel "virtual camera" system to reduce the required number of image sensors, obtaining full field measurements in under 10 seconds [17]. This includes the time for self-calibration for each measurement, since the large size of the light source means it must be automatically removed from the machining environment after each measurement. One major drawback to deflectometry is that it is limited to smoothly changing non-structured surfaces due to the requirement for neighbouring pixels in the calculation of local surface slope.

2.5.3 Fringe Projection

Fringe projection, a variation of structured light, is used for the measurement of diffuse surfaces by projection of a pattern of light upon the surface. Historically this is using an etched grating, but with recent technological advances it is now more often with a digital laser projector (DLP), allowing variation in the spatial frequency and wavelength of the fringe structure. Imaging of the surface scattered light is followed by analysis to determine the distortions in the projected pattern and produce a wrapped phase map. Lastly, calibration allows conversion from image coordinates to real world coordinates which provides a height map in place of the unwrapped phase map [18].

Similar to PMD, methods of fringe projection are commercially available, with the high measurement rate and large measurement volume making it ideal for measurement of large components and assemblies in a manufacturing environment. Fringe projection instruments from companies such as Isra Vision and PhaseVision are offered for measurement of non-specular components with resolution better than 100 μm over ranges of several metres.

Hand-held variants are offered by companies such as Artec and Shining 3D and make use of photogrammetry for automatic stitching of structured light measurements to achieve measurement of artifacts, environments and people larger than a single measurement volume. Though robust to movements and environmental effects, these are not yet capable of better than 100 μm resolution.

In contrast to the above low resolution, large range fringe projection implementations, higher resolution (10 µm) fringe projection with measurement field sizes in the region of 1 mm2 to 1 cm2 have been reported through use of telecentric imaging systems [19]. These are described as maintaining depth of field over that available by microscope based methods, though don't approach the nanometer axial resolutions demonstrated in literature on fringe projection microscopy (FPM) [20].A limitation to all methods of fringe projection is their requirement for a sufficiently scattering measurand surface, limiting the method to measurement of non-specular surfaces. This excludes use of fringe projection for measurement of ultra-precision turned, polished and moulded surfaces as well as many transparent surfaces such as lenses and, structured and multi-layer films.

2.5.4   Temporal phase shifting interferometry

Interferometric methods of measurement split a beam of coherent light which when recombined results in constructive and destructive interference depending upon the difference in distance travelled. Keeping the path length of one of these beams static (reference arm) while the other arm travels a varying distance (measurement arm) allows properties of the measurement arm and the surface it interacts with to be inferred so long as the path length difference is less than the coherence length of the light source. Due to the short wavelength of visible or near infra-red light, small changes in the path length result in changes in the phase difference between beams and hence easily detectable changing intensity of the interfering beams.

Phase shifting interferometry (PSI), also known as temporal phase measurement [21] is an interferometric method of metrology making use of the changes occurring in an interferogram during a controlled phase shift [22]. These phase changes may be induced mechanically by rotating polarizers, moving diffraction gratings, translation of mirrors or tilting of glass slides [23]. Alternatively electro-optic, acousto-optic and photoelastic devices allow temporal phase modulation at higher rates without mechanical movement [24]. Use of 3-point, 4-point and 5-point phase change algorithms for calculation of phase are common and afford increasing robustness respectively. Higher frame number algorithms have been exhibited to afford even higher resistance to errors at the expense of measurement rate [25]. Other algorithms, such as the Carré algorithm, allow calculation of interferogram phase without application of a known phase shift, assuming that the applied phase shifts are equal each time.

PSI is renowned as having sub-nanometre resolution, with an achievable repeatability of less than 1 nm independent of field size [26]. This advantage is however offset by the measurement rate of PSI which is fundamentally limited by the requirement for capture of multiple camera frames, reducing the measurement rate to a fraction of the camera capture rate, proportional to the number of frames required for the chosen PSI algorithm. This makes PSI particularly susceptible to environmental effects such as vibration, where changes in surface position between frames result in measurement errors.

This measurement rate limitation is compounded by the requirement to induce phase shifts in the interferograms, with the mechanical nature of these shifts with traditional PSI requiring time for translation and mechanical settling prior to frame capture. Also potentially problematic is the requirement to translate a heavy optic thousands of times throughout the life cycle of such an instrument, with the fatigue and ultimate failure associated with these cycles highlighted as a potential limitation of PSI [27]. This requirement for relatively slow mechanical translation can however be overcome to a certain extent by the introduction of non-mechanical methods of temporal phase shifting, with use of electro-optic Pockels cells being one such method to be employed [28]. This allows increased measurement rates without mechanical translation due to the ability to change phase at kilohertz rates.

The final, and perhaps most significant shortcoming of traditional offline phase shifting methods, is the relative nature of PSI. This results in the phenomenon that the measured surface height wraps around every time the surface height deviates by half the illuminating wavelength or more. For continuously varying surfaces this is not a problem, with phase unwrapping algorithms able to track and unwrap this wraparound as it occurs. For surfaces with discontinuities, steps or steep angles where the surfaces are separated by more than half the wavelength however, phase ambiguity occurs and phase unwrapping errors manifest. This means that its use is limited to continuous surfaces having no step heights with measurement of discontinuities with PSI introducing phase order errors leading to unknown surface height determination [21]. Meanwhile, technological advances allowing increase in detector frame rate and signal processing speed means that methods have emerged where the high measurement rate is expected to allow filtering of erroneous data caused by mechanical vibration.

The first method of note is model based method of phase shift interferometry (MPSI, also known as QPSI in some literature). MPSI is an iterative mathematical approach to reducing and correcting the effect of error sources in interferometers. It uses a mathematical model along with a priori knowledge of the interferometer path error sources and their relationships to each other along with a model of the measurand to eliminate phase errors between subsequent interferograms. MPSI is described as being beneficial to all interferometric methods, but has been demonstrated to be of particular importance to the stability of temporal PSI methods, with Deck's 2014 paper demonstrating the ability of MPSI to significantly reduce phase errors between temporal phase shifting interferograms [29].

While error source elimination in traditional PSI instruments has been demonstrated with MPSI, its use has also been adopted as part the software used with Zygo's Verifire and DynaFiz interferometer systems, and in the case of Verifire, it is used to improve interferogram stability on a non-dynamic method of surface metrology.

Another temporal phase shifting method aimed at on-machine measurement makes use of a diffraction grating and focusing optics to spatially disperse the wavelengths of a wide bandwidth source upon the measurand so that the axial surface height across the measurement profile is encoded spectrally. This probe configuration has been exhibited with a variety of wavelength sources and spectral resolving options. A fibre-linked SLED and spectrometer variant named laterally chromatically dispersed, spectrally encoded interferometry (LCSI) demonstrated by Gronle et al. produces a reference beam using a beam splitter within the probe and a reflective grating/achromatic lens pair to form the measurement arm [30]. Meanwhile Hassan et al. have shown a bulk optics interferometer with similar light source and spectrometer while improving on the optical efficiency and potential probe size by use of the zeroth diffracted order as the reference arm instead of a beam splitter and mirror [31]. The possibility of small remote probes and the low computational requirements of the signal processing give this method potential for on-machine implementation with both fast measurement rates and probes capable of fitting within small machining envelopes. Both methods have been shown to operate with phase shifting using movement of the reference mirror as well as spatial methods of frequency analysis such as FFT.

Work by Kumar et al. follows a similar method to LCSI and SDSCI, focusing on the miniaturization of interferometric instrumentation hardware for ease of integration on-machine [32]. In this method a hybrid optical chip interferometer is realized, measuring only 100 x 50 x 20 mm. This is used to interrogate a spatially dispersed fibre linked probe with the wavelength scanned over time acting as a single-point flying spot upon the measurand surface where the surface height of each lateral position is encoded by wavelength. The silica-on-silicon optical chip system offers a high speed, highly miniaturized measurement platform with the use of such embedded photonics technology offering a highly attractive price when manufactured in bulk. Disadvantages of this method, as for all temporal PSI methods, are the requirement for multiple image captures for calculation of surface height, as well as the relative nature of the method.

2.5.5 Spatial phase shift interferometery

Spatial phase shifting interferometry, also known as instantaneous interferometry [33], is an implementation of phase shifting where the required phase shifts do not occur sequentially in time, but instantaneously. Spatial separation of interferograms and their capture all at once avoids the difficulties associated with temporal PSI such as vibration and sample movement while still achieving nanometer resolution. The instantaneous nature inherently increases the measurement rate by elimination of the requirement for multiple camera frames per measurement .

Methods of spatial phase shifting interferometry have introduced these phase shifts by various means including polarization of measurement and reference beams as well as use of multiple detectors [34].

Drawbacks of this method are reported by the authors to include the difficulties in calibrating multiple image sensors as well as the errors introduced by the non-common path nature of spatial PSI. By splitting the light into four separate channels, each channel should be identical with the exception of a change in the phase of each. However, the amplitude of each channel may vary depending upon the precision of the beam splitting. These problems have been solved in part by careful selection of the polarization beamsplitting cubes to within a level which can be corrected electronically with the detector. While this is not ideal, the authors state that by giving each channel its own video gain and offset, the optical difference in each channel can be eliminated.

Dynamic interferometry, a variation of PSI, is a single shot spatial phase shifting method which produces four phase shifted interferograms through use of a quarter wave plate and a pixelated birefringent mask in front of a single detector [35]. It circumvents the problems suffered by previous methods of spatial PSI by removing the necessity for four separate but spatially calibrated detectors. By obtaining the measurement data in a single shot and maintaining a short enough exposure time, the effect of vibration can be eliminated and measurement rates of 6 kHz are achievable on glass with 4% reflection [21] with maximum measurement rates above 30 kHz possible [36]. This method of interferometry was mentioned by Wyant as being one of the three methods showing potential for increasing the number of opportunities in which interferometric metrology can be applied in industrial and research settings [37], namely a single-shot phase-shifting interferometer.

Dynamic interferometry has been commericalised by 4d Technology, with the introduction of their FizCam product line for roughness and form of general optics, large optics and optical flats and their PhaseCam line allowing measurement of large optics and remote on-machine measurement in quality control and clean room applications. The fast, single-shot nature of these implementations of dynamic interferometry allow areal on-machine measurement of surfaces without sensitivity to vibration or air flow through interferometer paths. The small instrument size (in some cases 180 x 160 x 90 mm) [38] allow on-machine integration of interferometers with precision polishing and grinding machines, with Zeeko offering 4d Technology's metrology instruments as part of their on-machine stitching interferometer (OMSI) module for 7 axis precision polishing [39].

A further on-machine development of 4d Technology's dynamic interferometry technology is the reduction in size, cost, flexibility, range and complexity described by a 2015 paper titled "In-line roll-to-roll metrology for flexible electronics." [3]. This paper details simplification, miniaturisation and reduction in cost of their NanoCam dynamic interferometer, with multiple measurement instruments grouped on a gantry above a moving film, with all signal processing performed on-board with small dedicated signal processing hardware. This is of particular interest as contrary to many emerging instrument manufacturers 4d Technology have, with knowledge of a specific target measurement application,

drastically reduced instrument performance to allow vastly improved value metrology when compared to a full capability 4d PhaseCam. The much reduced 30 μm range is within the vertical variation of the bearings guiding the moving substrate while the reduced field of view along the web is acceptable due to the measurement speed of 30 Hz, allowing (with multiple small, cheaper interferometers) full measurement coverage of a 1 m wide web moving at 1 metre per minute.

Despite these benefits, dynamic interferometry is limited to near-perpendicular measurement of surfaces and suffers from the phase ambiguity problems common to all phase shifting techniques. This limits its operation to smooth, continuous surfaces. Lastly, this method has been reported to be not truly common path like traditional Fizeau phase shifting interferometers with the birefringent method of phase shifting allowing introduction of very small non-common path phase errors [40].

2.5.6   Spatial carrier fringe phase shifting

The spatial carrier fringe phase shifting method is put forth in a 1982 seminal paper by Takeda et al. [41]. It operates by introducing carrier fringes to interferograms through tilting of the interferometer reference mirror. Separation of the phase from the local intensity variations can then be achieved through use of the fast Fourier transform (FFT), low-pass filtering, then calculating the inverse FFT (IFFT). This result is then unwrapped using a suitable phase unwrapping algorithm.

The single shot nature of this method means it has been recognised for its strong potential for interferometry in noisy environments when compared to temporal phase shifting interferometery. A 2010 paper by Sykora and de Groot outlines the errors introduced by non-common path interferometers and the limitations of birefringent coatings and materials for spatial phase shifting interferometry [33]. Their preferred solution, the spatial carrier fringe method, utilizes the principles introduced by Takeda et al. coupled with careful consideration and design of a stabilized HeNe laser light source as well as efficient use of light power to achieve acceptable SNR in production environments [42].

This research has been commercialized by their work at Zygo, resulting in the Dynafiz range of interferometers suitable for environmental noise resistant measurement of small and large mirrors, lenses and other specular surfaces. Dynafiz laser interferometers are capable of sub-nanometre resolution surface topography measurement at a rate of 50 Hz; or 82 Hz by sacrificing lateral resolution in favour of measurement rate [43]. These measurement rates allow the Dynafiz to freeze vibration as well as present live measurement data to operators. This is said to effectively reduce the required operator skill by allowing live visual indicators of component mounting stresses and mounting accuracy.

The spatial carrier fringe method outlined has been criticized as having low spatial resolution and limited ability to measure slopes, resulting in the ability to measure only smooth surfaces [44]. This said, efforts

have been made to reduce this limitation through careful optical design and sacrificing resolution for increased slope acceptance angles and higher spatial resolution [45].

Another example of the spatial carrier fringe phase shifting method is an alternative signal processing implementation of the previously mentioned SDSCI by Hassan et al. This profilometer uses a reflective grating to angularly separate the broadband light source by wavelength across the measurand surface. Adjustment of the interferometer reference mirror to introduce tilt fringes allows calculation of wavelength encoded surface height across the lateral range of the interferometer without the previously required temporal phase shifts [46]. This now instantaneous method avoids the problems associated with vibration between PSI frame captures, with the expected small probe size and much improved measurement rate making this method potentially advantageous for on-machine measurement of moving films, webs and other continuous production processes.

2.5.7   Coherence scanning interferometry

Coherence scanning interferometry (CSI) (also known as white light interferometery (WLI) and over 10 other acronyms [47]) uses the short coherence length of a wide bandwidth source, typically several hundred nanometers bandwidth, along with the fact that the interference fringes have highest contrast when the path lengths of the interferometer arms are matched. By mechanically varying the length of one arm of the interferometer the intensity of the interferogram at each pixel is modulated. The pixel-wise intensity pattern generated as mechanical scanning progresses shows a sinusoid whose amplitude peaks at the contrast maximum. Detection of the low resolution but absolute position of the surface is then possible by calculating the peak position of the upper intensity envelope formed by the sinusoidal coherence modulations.

The absolute (as opposed to relative) nature of coherence scanning methods means that they allow determination of surface position even if a surface step or discontinuity of more than half the illumination wavelength is measured [48]. This ability to measure non-continuous surfaces without phase ambiguity is one of the major advantages this method has over the much faster nature of phase shifting interferometry.

Disadvantages of CSI are similar to those of PSI. Mechanical movement of components requires expensive and slow scanning stages. Additionally, the large quantity of camera frames required to calculate the coherence profile make this method highly computationally intensive when compared to phase shifting methods. Signal processing, even with GPU parallelization methodologies, is a large limiting factor to the measurement rates of such instruments.

Commercially, Zygo offer the ZeGage interferometer. This interferometer is advertised as offering nanometer resolution measurement with measurement times of only a few seconds. While not advertised for on-machine use, its robustness to vibration is praised as allowing operation on the factory floor without need for vibration isolation tables or temperature control. Also available is the Zygo APM650 coherence scanning interferometer, an areal measurement instrument offered for automated measurement of vias, holes, tracks and high aspect ratio features during the PCB production and verification process. Both of these instruments are advertised as highly resistant to environmental effects due to their in-built vibration isolation as well as Zygo's proprietry SureScan technology for vibration tolerance in CSI. While the technology behind SureScan is not explicitly explained, Zygo have previously patented methods of CSI vibration stabilization which use high measurement rate phase shift interferometry multiplexed with a coherence scanning interferometer to correct for measurement path changes caused by vibration [49].

One method of eliminating the disadvantages of mechanical scanning and requirement for multiple frames is to compromise the areal nature of the previously described methods of CSI for a single-point implementation, named confocal chromatic sensing. This is demonstrated by a method of white light interferometry in which a reference plate is securely fixed to the measurand [50]. A broadband light source ($\Delta\lambda = 600\,\mathrm{nm}$) is focused upon this measurand and reference pair, with the reference beam of this Fizeau interferometer generated from the reflection from the reference plate and the measurement beam the returned light from the sample surface. These beams are then spectrally analysed using a method of signal processing described by the authors as spectroscopic analysis of white light interferograms (SAWLI), with the interference fringes generated resulting from the differing delay experienced by the broad bandwidth light as it passes through the reference plate to the measurand affecting the phase of the spectral interferogram. Measurement is achieved by calculation of phase by a 7-point algorithm followed by unwrapping, with the slope of the unwrapped phase indicative of separation between the reference plate and sample.

The long coherence length (150 µm) of the source light coupled with the short separation between measurand and reference surface (10 µm) mean that no compensation of the shorter reference path length is required. Profile measurement of surface topography is achieved as the measurement lens is mechanically translated above the reference/measurand pair, with vibration tolerant measurement possible due to the fixed nature of the pair with any vibrations experienced by both.

Commercially, this technology is offered by STIL, with their STIL-DUO instrument offering confocal chromatic and confocal spectral interferometry in one package. The interferometric variant, requiring a fixed reference plate, is capable of sub-nanometre resolution over a range up to the coherence length of the light source, 150 µm. It should be emphasized that while the names and acronyms are similar, this has

an entirely different operating principal, advantages and disadvantages when compared to the similarly named chromatic confocal spectral interferometry (CCSI). Despite being described as an environmentally robust optical method for on-machine measurement, the requirement for a reference plate in physical contact with the measurand means that CCSI could be considered to possess the same unsuitability for on-machine metrology as contact methods of measurement.

2.5.8 Wavelength scanning interferometry

Wavelength scanning interferometry is a technique similar to CSI, where instead of mechanical scanning of interferometer components, a wavelength shift in the incident light is provided [51]. As the wavelength varies, the phase difference between the measurement arm and reference arm changes, resulting in sinusoidal intensity variations of individual pixels. Use of Fourier methods for frequency analysis of these intensity variations allows determination of absolute surface position.

WSI has emerged primarily as a solution to the disadvantages of CSI, predominantly the requirement for mechanical scanning, whose slow nature allows introduction of error from vibration and drift. The improved wavelength rate change over mechanical scan rate mean that the factors limiting measurement rate become the camera exposure time as well as the overhead to process the large amounts of resulting data. Similar to CSI, when compared with the algorithms used for PSI and deflectometry, these are highly computationally intensive.

An early example of WSI is a paper from 2001, in which Yamamoto et al. describe use of a pulsed laser with an output wavelength which can be tuned electronically from between 680 and 1056 nm [52]. Through peak fitting to the Fourier result of the interference signals of each pixel they achieved absolute areal surface measurement with sub-micron vertical resolution. This they extoll along with a measurement time of 9.5 seconds, attributing their success to a greater available wavelength scanning range and use of a camera having improved digital signal processing (DSP) capabilities over those previously available.

The requirement for multiple image frames makes this implementation of WSI unsuitable for use in manufacturing environments due to its sensitivity to noise. A 2010 paper by Jiang et al. addresses this vibration sensitivity by use of a second interferometer multiplexed into the measurement paths of the Linnik wavelength scanning interferometer [53]. This second interferometer operates at a measurement rate above the frequency of the mechanical vibration. Use of the second interferometer for closed-loop control of a PZT allows translation of the WSI reference mirror to compensate for the vibration of the measurand and stabilize the WSI. This improvement was demonstrated to eliminate vibrations at 40 Hz by 12.2 dB while achieving nanometer resolution measurements. This method of increasing interferometer environmental robustness was highlighted by Wyant in 2003 as one of the methods of vibration reduction

in interferometry to allow application of interferometry to industrial settings without reducing the inherent sensitivity [37]. Wyant describes the downside of this method of vibration cancellation as it being limited to vibration cancellation in one axis where vibration caused by tilt as well as higher order vibrations requires additional closed-loop feedback and correction systems.

Despite the advances in detector and processor technology since the WSI implementation by Yamamoto, the increase in computational complexity to achieve the improved vertical and lateral resolution of work by Jiang et al. meant that the measurement time remained near 9 seconds. For this reason, further work included development of algorithms for parallelization of WSI signal processing and comparison of these new algorithms with those for multiple core CPUs [54] enabling measurement rates of WSI to exceed 1 Hz for the first time. The increased measurement rate and vibration tolerance has allowed a comparative study of off-line and on-machine inspection of PV barrier film coating for quality assurance [4].

2.5.9 Hyperspectral Interferometry

Hyperspectral interferometry (HSI) [55] or spectrally resolved white light interfermetry (SRWLI) [56] combines white light interferometry with methods of hyperspectral imaging allowing single-shot absolute measurement of discontinuous regions. The above two implementations of HSI use a broadband light source and a Fabry-Perot etalon to produce a frequency comb which each group of authors use with their chosen interferometric setup. After recombination of the measurement and reference arms, spectral decomposition of the light using a grating and lens results in capture of a set of interferograms as sub-images on an areal detector. Each sub-image contains the interferogram for one wavenumber "bin" produced by the etalon. The phase for a given pixel changes from sub-image to sub-image as the illuminating wavenumber of the measurand changes between sub-images due to the peaks of the etalon's spectral transmission comb. Signal processing of this sinusoidally varying signal provides the absolute measurement position of the measurand surface for each pixel.

The instantaneous capture of areal interferometric data is a large advantage compared to methods such as WLI, WSI and focus variation which all require temporal scanning to obtain full 3D measurement data. The lack of either mechanical or electronic scanning reduces cost, while the instantaneous nature means expensive or complicated methods of image stabilization are not required. HSI is also reported to be more tolerant of optically rough surfaces than other interferometric techniques since it is unaffected by random phase fluctuations due to speckle. This is due to the fact that HSI uses the frequency of the phase change in a single pixel rather than neighbouring pixels.

An axial resolution of 80 nm over a range of 350 µm has been demonstrated. While this dynamic range of 4,375 is low compared to other areal methods, the authors stipulate that axial resolution scales with

source bandwidth, and upgrading from a 30 nm bandwidth source to a 300 nm bandwidth source should yield a ten-fold improvement in measurement resolution.

However, lateral resolution of HSI is limited due to the requirement for many sub-images upon the areal detector. In the case of a 2012 paper by Widjanarko, Huntley and Ruiz, each sub-image has a size of 19x19 pixels, corresponding to a field of view of 81.7 x 81.7 μm^2 [57]. Further work reported by Widjanarko aims to improve the optical system to deliver sub-images across the whole image sensor instead of only a strip across the centre. This improvement in efficiency of sensor use will allow more and larger sub-images to be captured from a single image sensor. Along with higher resolution image sensors this would enact a significant improvement to the lateral resolution or field of view of the HSI instrument [58].

2.5.10 Confocal Chromatic Sensing

Confocal chromatic sensing (CCS), also known as confocal chromatic microscopy (CCM), confocal chromatic spectrometry (CCS) and Chromatic Confocal Sensing (CCS), takes advantage of the chromatic aberration introduced by a lens and the range of focal lengths that it produces for a broadband light source. Through careful design of multiple lenses, this usually unwanted chromatic aberration can be increased so that short wavelengths focus nearer the lens and long wavelengths focus further away [59]. The light gathering ability of lenses mean that wavelengths incident upon the surface but out of focus, do not couple back into the lens as well as the wavelength of light in best focus. By careful spatial filtering (pinhole) of the returned light, one can ensure that only the focused wavelength arrives at a spectrometer, allowing determination of the wavelength of light with best focus. With calibration of the instrument, the distance from longest focus to shortest focus can be determined and so distances in between can be related to one another.

This non-interferometric method of single-point surface topography measurement requires raster scanning of the sample under the measurement head, or scanning of the measurement probe over a measurand but no scanning along the vertical axis. Translation in one axis results in a profilometer arrangement, with a strength over areal methods being, like a mechanical stylus instrument, that the length of the translation can be specified without the need for complicated and time consuming measurement data stitching algorithms. Extension of the translation into a second axis results in areal measurement data, with selected measurement area not dependent on the magnification of the lens but the travel of the translation stages. A drawback of these large measurement areas is the increased time required for full measurements, though it does allow for circular and spiral profiling of turned components. Additional problems introduced by the requirement for physical scanning of the measurement instrument include that the stitching requirements for areal methods are replaced with complicated and time consuming stage calibration operations.

The focus of specific wavelengths across the range of the method mean that the lateral spot size of CCS instruments remains more consistent across the range of the instrument than competing methods and so effectively extends the depth of field (DOF). An upside of the requirement for a pinhole to spatially filter the beam incoming to the spectrometer is that it makes the arrangement easily separable into a probe, light source and interrogation unit. Firstly this allows separation of high power light sources requiring mechanical cooling from vibration sensitive optics. Secondly it allows mounting of smaller on-machine probes, with fibre linked probes for CCS surface topography measurement available from companies such as Micro-Epsilon Precitec, Polytec, Nanovea and Stilsa. These are interrogated by a remote, fibre linked interrogation unit and light source. For low range, high resolution applications these probes remain comparatively small, with 8 x 66 mm (D x L) probes available to cover ranges of 100 μm [60]. As the specified range increases, the number of lenses necessary to achieve the required chromatic aberration increase the cost, size and weight of such a probe. For a range of 25 mm and working distance of 75 mm Precitec offer a 76 x 243 mm (D x L) probe weighing 1637 g [60]. While much smaller and with better range than many areal methods of on-machine metrology the increasing size and mass for higher range probes introduces the need for more robust translation stages, again increasing the cost and size of on-machine implementations. It is difficult to make direct comparisons to the size of probes for other single-point methods in this instance owing to CCS being unique in offering a probe with this working range.

Another problem with CCM is the occurrence of self-imaging [61] also described as ghost foci [59]. When measuring surfaces with curved profiles (lens arrays, curved trenches, grooves with radii) the local radius of the surface refocuses wavelengths of the source light that should be out of focus at the measurand surface. This couples wavelengths of light back into the measurement apparatus which give a false reading of the surface height.

Finally is the topic of measurement rates, with some manufacturers of CCM instruments offering rates of up to 66 kHz [62]. It is important to note that these quoted measurement speeds are for ideal measurement cases; those of specular surfaces at low slope angles using high NA probes. Increasing focal length to improve measurement range as well as measurement of sloped and rough surfaces will result in a reduction in the returned light, requiring increasing of the spectrometer integration time for successful measurement. While these measurement rate compromises are common to most measurement techniques, one problem that is specific to CCM is the requirement for averaging of sequential samples to enhance the axial resolution through improvement of the signal-to-noise ratio, in turn reducing the detection rate [63].

2.5.11 Confocal Chromatic Spectral Interferometry

Confocal chromatic spectral interferometry (CCSI) is an absolute, single point method of metrology borrowing techniques from both CCM and WLI where the areal nature of WLI is sacrificed for a fast, absolute, instantaneous and single-point method.

In CCSI a broadband light source is focused onto the measurand, with a diffractive or refractive lens focusing each wavelength of light at a different axial height. Once returned through the interferometer and combined with a reference beam, the sinusoidally changing coherence envelope overlaying the CCM intensity envelope is analysed to determine the surface height [64].

The introduction of interferometric data provides sub-nanometre resolution in contrast to the 5-10 nm resolution achievable by a high NA CCM probe. An added bonus is the robustness against ghost foci, although the method has a shorter measurement range than possible with CCM [61]. Similar to CCM, CCSI maintains a small focal point over a longer range than other interferometric sensing methods due to the intentionally chromatically aberrated lens, meaning lateral resolution is more consistent over a longer axial range when compared to other non-chromatically dispersed methods.

Demonstration of a Mirau configuration interferometric probe for CCSI has meant that remote probing is possible using identical light source and interrogation unit as commercially available CCM instruments [61]. The interoperability of CCM and CCSI probes adds a level of flexibility which may add value to on-machine measurement processes. An added benefit of the Mirau over the Linnik configuration is the common path travelled by the reference and measurement beams, eliminating different environmental effects experienced by the beams in the fibre when compared with a fibre linked Linnik interferometer.

Despite the methods of fibre probing described above, no commercially available version of CCSI is apparent at the time of writing. The papers presented by Osten, Körner and Papastathopoulos, accompanied by several CCSI-based patents do not yet appear to have a TRL sufficient for commercialisation. Disadvantages of CCSI when compared to MWLI and LCI are the low range of the method as well as the expensive, complex and bulky nature of the chromatically aberrated fibre-linked probes.

2.5.12 Low coherence interferometry

Following on from the principles of white light interferometry, low coherence interferometry (LCI) sacrifices the areal nature of WLI for a method which is single-point but instantaneous, with spatial or spectral decomposition of the white light interferograms providing absolute depth information. This results in methods which require lateral scanning in X and Y to obtain topographic data in lieu of the axial scanning through the Z direction utilised by WLI. An advantage of this approach is that it allows for the

introduction of fibre-linked probes, with the separation of interrogation optics from sensor head having great potential for miniaturisation [65].

Use of a low coherence light source, typically a superluminescent diode (SLED), with a fibre-based Michelson interferometer followed by spectral decomposition of the resulting interferograms is common in medical applications in which this is most often named spectral domain optical coherence tomography (SDOCT), spectral radar or Fourier domain optical coherence tomography (FDOCT) [66]. SDOCT provides instantaneous subsurface imaging for a single point through Fourier analysis of interference between the returned measurement and reference arms. This depth encoded data is commonly called an 'A-scan'. Lateral scanning using galvanometers [67] or MEMS mirrors [68] is then performed to capcture multiple A-scan samples to achieve 2d or 3d measurement.

SDOCT is used extensively in medical research for multilayer thickness measurement of live tissue samples while SDOCT usage for engineering surfaces includes measurement of contact lens thickness profiles [69] as well as online measurement of roll-to-roll printed electronics [70]. Such techniques are capable of measuring multilayer transparent surfaces with axial resolutions in the range of 1-10 µm over ranges of several millimetres.

Building upon SDOCT, spectral domain phase microscopy (SDPM) produces not only depth resolved intensity profiles but also phase profiles allowing subnanometre optical path length sensitivity. By using a common-mode reference and measurement arm topology, it has an improved immunity to environmental disturbances compared to SDOCT [71]. The 2π phase ambiguity problem of such methods has been overcome by Yan et al. in which the phase in the spectral domain is combined with the position in the depth domain, extending the dynamic range of SDPM in biological sample measurement [72].

Methods of LCI have also been demonstrated which take advantage of spatial instead of spectral decomposition of interferograms. Use of a tilted, stepped reference mirror has been demonstrated to achieve 2 nm resolution over a range of 170 µm including use of miniature fibre probes [65]. In this implementation a pair of low coherence SLED light sources with spectrally separated centre wavelengths are coupled into a single mode fibre (SMF). A Fizeau configuration interferometric fibre probe constructed with a GRIN lens at the output of the fibre generates a retro-reflected reference beam from the fibre-GRIN interface with the remaining light incident upon the measurand forming the measurement arm. The two beams coupled back into the fibre are interrogated by an offset Michelson configuration interferometer with a reference arm length modified to compensate for the difference in path length travelled by the two beams within the Fizeau configuration probe. Having been brought back into coherence by the path offset, the pair of beams are made incident upon a detector where the beat frequency occurring between the two SLED spectrums allows higher resolution phase information to be

isolated unlike the purely coherence envelope methods of position detection employed by optical coherence tomography (OCT). Subsequent work by authors in the field have achieved cladded probe diameters of sub-250 µm allowing measurement of micro-bored holes [73].

LCI benefits from the possibility of a high degree of probe miniaturisation making it attractive for on-machine implementation where constricted space makes other methods with more complicated probe configurations problematic. This is well demonstrated by Fionec GMBH whose LCI-based instruments are available in two modes. SMF-1 provides measurement precision of 3 nm (standard deviation) and a range of 80 µm while the SMF-2 achieves a precision of 60 nm and a range of 1 mm (DR = 16,666). This provides a dynamic range (DR) of each respectively of 26,666 and 16,666, where dynamic range is the ratio of range to resolution. Achievement of higher values of dynamic range would allow measurement of a wider range of measurands without the need to buy or maintain separate probes.

2.5.13 Multiwavelength interferometry

Multiwavelength interferometry (MWLI) makes use of multiple multiplexed fibre interferometers to achieve single point measurement of specular and rough surfaces in an absolute manner. An interferometer sourced by a single wavelength is able to use the phenomenon of interference to accurately track the position of a surface to nanometre resolution. The relative nature of such an interferometer however means that surface steps and features of more than half the illumination wavelength cause height ambiguity. By multiplexing two interferometers with different source wavelengths together so that they share a common path a beat frequency is formed, providing an interferometer with a much longer synthetic wavelength which allows determination of the phase order of the higher resolution but relative interferometers. In this way, the unambiguousness of the interferometer can be increased by a thousand-fold [74] allowing measurement tolerant of interruptions and step height measurements up to 1 mm.

Conversion of these multiplexed Michelson interferometers to fibre variants allows use of miniature remote probes for surface measurement, with the required reference beam produced internally. The long coherence length of the narrow bandwidth light sources mean that unlike other methods of fibre probing, no offset is required to bring the two measurement paths back in to coherence before the detector, further miniaturising the system.

A common problem with interferometric methods is the inability to measure optically rough surfaces due to the coherence of the light source. MWLI avoids this problem by introduction of two additional light sources and hence multiplexed interferometers, allowing analysis of the changing speckle patterns when measuring rough surfaces to determine the measurand surface height [75].

The fibre linked nature of this measurement method lends itself to convenient splitting of the light sources to allow interrogation of multiple probes simultaneously. After splitting of the source light into the 2, 4 or 8 paths, a fibre circulator allows continuation of the light to the probes. The returned reference and measurement beam are redirected by the circulator for spectral splitting and phase detection.

The ability to interrogate multiple probes instantaneously leads to an interesting environmentally robust implementation of MWLI, commercialised by Luphos Gmbh. One of the main arguments against single point methods of metrology are their reliance on the accuracy and calibration of translation stages. Four MWLI probes within a reference frame allows spatial relation of one probe to the location of the frame using the remaining three probes. This allows automatic calibration of stage errors as well as tracking of the measurement probe position as it scans radially as a measurand with rotational symmetry is rotated beneath it. This results in a spiral measurement path for an instrument capable of tracking changing surface heights and slopes for optimum measurement of lenses and mirrors in a production environment [76].

A considerable downside of MWLI is the expensive requirement for four precision laser sources with the temporal wavelength stability crucial to precision operation of the instrument. One redeeming feature of which helps counter this high cost is the ability to measure surface position using up to 8 probes simultaneously provides better value metrology than instruments capable of only one measurement.

2.5.14 Dispersed reference interferometry

Dispersed reference interferometry (DRI) is a single point variant of white light interferometry. It makes use of a dispersive element within the reference arm of the interferometer to separate the source light angularly by wavelength. The path length travelled within the reference arm therefore depends upon the wavelength of light, with the short coherence nature of the light source meaning that the length of the measurement arm may be determined by the most strongly interfering wavelength of light. Hlubina et al demonstrated this in 2002 with use of a 700 nm bandwidth source and dispersion introduced by use of a glass slide of known thickness and refractive index [77]. They described how absolute position of the measurement mirror could be determined by calculation of the point of symmetry of the resulting spectral interferogram, achieving a resolution of better than 1 μm over a 130 μm range. Work by Pavlicek and Hausler in 2005 demonstrated higher resolution measurement with a dispersive reference fibre interferometer in a Linnik configuration [78]. Dispersion was provided by using single mode fibre for each arm of the interferometer, with the reference arm using a dispersive fibre to increase the optical path length travelled for longer wavelengths. The advantage of fibre probes over a bulk optics interferometer offered a high level of miniaturisation for on-machine use. A major difficulty with the fibre implementation implemented by Pavlicek and Hausler is the non-common mode nature of the arms of

their fibre interferometer. Instabilities in phase and coherence envelope arise as the fibre reference and measurement arms experience differing environmental effects leading to instabilities in measurement.

Similar implementations of dispersed reference interferometry have also been used for characterization of short lengths of dispersive fibre [79-81], transparent sample thickness measurement [82], thin film thickness measurement [83], chirped mirror characterization [84] and dispersion measurement of transparent samples [85].

No commercialisation of dispersed reference interferometry for distance and surface topography measurement currently exists. Current academic implementations possess axial resolutions suitable for distance measurement but do not yet approach the nanometre resolution requirements for surface topography measurement. The simplicity of the centre wavelength calculation method demonstrated by Hlubina for transparent sample thickness measurement with spectral interferograms [82] mean that a high measurement rate required for single point methods such as this is likely achievable. Meanwhile the possibility for further miniaturisation of probes is attractive, as demonstrated by the use of miniature Fizeau probes by the Fionec SMF-1 and SMF-2 low coherence interferometers [73].

2.6 Summary of methods of non-contact embedded metrology

This chapter has presented a summary of the currently available on-machine metrology methods and an explanation of each of their operational methods as well as their strengths, weaknesses and capabilities. What follows is a short summary of these methods, allowing a general comparison ending in a summary confirming the current needs in the on-machine metrology market as they relate to the requirements outlined in section 2.4.

2.6.1 Areal methods

Areal methods of metrology can be split into two groups; those capable of absolute measurement and those providing relative measurements. The high measurement rate afforded by the relative methods means their on-machine integration is simpler, with the effects of vibration minimised by the high measurement rates. The slower, absolute methods excel for measurements having large step heights or surface features which introduce phase ambiguity in relative methods. The low measurement rate of absolute methods has led to the requirement for closed loop stabilisation of such methods to account for mechanical translation of the measurand during measurement.

For many measurement applications, the capabilities of the available areal measurement methods entirely suffice. With the underlying methods and principles for on-machine areal measurement in place, future developments are likely to incrementally improve range, axial resolution, lateral resolution and most importantly for the absolute methods, the measurement rate. With knowledge of specific measurement applications, the physical size of these methods may continue to reduce with compromise

of other parameters, as demonstrated by FlexCam by 4D Technologies. This reduction in size however is fundamentally limited by the inability of areal methods of metrology to use fibre-linked objectives and so in applications where measurement volume is limited, further development of single-point methods is attractive.

2.6.2 Single-point methods

The potential for operation of single point methods within limited machine tool work volumes is much improved over areal methods due to the ability of miniature fibre probes to relay distance and surface topography information to remote interrogation apparatus. This feature is important for their integration into machine tools such as ultra-precision milling, grinding, electro-discharge machining (EDM), turning and polishing machines as well as having potential in R-2-R manufacturing environments.

Table 2.1 attempts to summarise the capability of existing commercially available single-point measurement methods for probes capable of nanometre resolution. Doing so is difficult due to the focus of each manufacturer on different markets and applications, though the generalised performance of the underlying methods can be compared. Expanding upon the drawbacks of each of these methods provides a compelling case for the further development of a new method of single-point measurement.

Method	CCS	MWLI	LCI
Range	100 μm	1 mm	170 μm
Resolution	< 1 nm	< 1 nm	2 nm
Dynamic Range	100,000	1,000,000	85,000
Typical Sampling Rate	66 kHz	2 kHz [86]	5 kHz
Interrogation unit cost	Low	High	High
Probe cost	High	Low	Low
Probe size	8 x 66 mm (D x L)	18 x 42 mm (D x L)	80 μm (D)
Advantages	Consistent lateral resolution	Multiple simultaneous probes	Smallest probe size

Table 2.1: Table comparing currently available single-point methods of metrology for highest resolution probes.

Summarising the environmental immunity of the above methods concisely is difficult in a table. Fibre probes provide separation of interrogation optics from measurement probes which allows vibration isolation of the interrogation optics while retaining a small on-machine component. CCS does not require a reference surface but both LCI and MWLI incorporate reference surfaces within the probes to ensure the two interferometer arms remain common-path through the fibres, negating environmental effects on the fibres. Additionally, a key aspect of all three highlighted technologies is the ability for single-shot, absolute measurement, allowing rejection of errors possible in methods using multiple frames per data point. The MWLI technology by Luphos has an advantage in that it is sold as a complete measurement

system which uses multiple probes within a metrology frame to measure and cancel out vibration in the measurand.

The miniaturisation of probes by Fionec Gmbh for its LCI based instruments has great potential for measurement of high aspect ratio surface features as well as improving the accessibility of measurement metrology for on-machine use where the work volume is limited. The low complexity, size and price of these probes is offset by the low dynamic range of the method as well as the requirement for multiple expensive SLED light sources.

Conversely, CCS benefits from the simplest and hence lowest cost interrogation unit consisting of simply a single light source and spectrometer, but the requirement for chromatically aberrated probes results in the largest and most expensive probes. While CCS does offer ranges of several millimetres the limited dynamic range of the spectrometer results in much reduced range to achieve a nanometre resolution comparable with MWLI and LCI.

MWLI benefits from the greatest dynamic range of these three methods as well as the possibility of simultaneous interrogation of up to 8 probes without reduction in measurement rate. The requirement for four stabilised laser sources along with supporting fibre circulators and detectors also make the MWLI interrogation apparatus the most expensive.

To increase the value of single-point metrology and its strengths for on-machine metrology, this thesis documents development of a method which attempts to eliminate these deficiencies. Among the outlined methods of single-point metrology, dispersed reference interferometry is one such underdeveloped method which has yet to reach its full potential. Its use for absolute position measurement has been demonstrated for both fibre-linked and bulk optics configurations [77, 78]. While the spectral interferograms produced by DRI have yet to be used for surface topography measurement, a limited dynamic range has been demonstrated and with modifications to the dispersion parameters and spectrometer this can be greatly improved. Meanwhile no implementation has made use of the interferometric nature of spectral interferograms, where successful detection of the wavelength varying phase of the interferogram will provide nanometre resolution measurement information.

Fibre probe variants of DRI have been demonstrated previously but lack environmental robustness due to the non-common path layout shown by Pavlícek et al [78]. Realisation of a DRI fibre probe whose reference and measurement arms share a common path as exhibited by LCI and MWLI will provide a vibration and temperature tolerant design whose use on-machine will be made possible due to the ability to miniaturise such probes beyond that possible by CCS.

The following chapters introduce DRI as a method of distance and surface topography measurement. The operational principles of DRI are examined and methods of nanometre resolution measurement investigated before extension of range described. Following this a common-path remote fibre probe topology is introduced, fibre probe configurations outlined and a prototype interrogation interferometer discussed. These investigations are undertaken with an aim to develop a single-point method of surface topography measurement capable of nanometre resolution over a range of several millimetres. The resulting high dynamic range will allow flexibility of use for a large variety of applications and a wide range of probe topologies. This measurement technique will make use of common-path remote fibre probes for miniaturised on-machine surface topography measurement with a target measurement rate exceeding 10 kHz.

3 Introduction to DRI – Absolute position encoding by wavelength

3.1 Introduction

In this chapter the schematic of a white light Michelson interferometer with a dispersed reference arm is introduced followed by presentation of the relevant characteristic equations to describe the resulting interferogram. Inclusion of dispersive elements in the reference arm of this interferometer results in a chirped spectral interferogram whose balance wavenumber is indicative of surface height, unlike a non-dispersive white light interferometer in which the optical path difference is simply determined from the period of the spectral modulation [78]. This dispersive technique is reported to be capable of an improved ratio of range to resolution, less limited by the bandwidth of the source and resolution of the spectrometer [77].

Next, a discrete implementation of the mathematics is provided for simulation of DRI interferograms using Matlab. Simulation allows direct comparison of theoretical and real behaviour of the subsequently demonstrated dispersed reference interferometer. Using such a bulk optics implementation of the interferometer, evaluation of range, resolution, linearity and repeatability is presented.

These investigations are used to bring the author up to speed on previous implementations of dispersed reference interferometry for distance and surface topography measurement. Finally, use of regularisation and windowing is described to resolve previously unreported monotonicity problems when using autoconvolution for determination of the balance wavenumber of spectral interferograms.

3.2 DRI Schematic

Dispersed reference interferometry makes use of a Michelson interferometer with a dispersive element introduced into the reference arm. In the schematic shown in figure 3.1 the near infra-red short coherence light source, S, is split by a beamsplitter, BS, forming the two arms of the interferometer. In its simplest format the measurement arm of the interferometer contains simply a mirror, M1, returning the measurement arm beam to the beamsplitter.
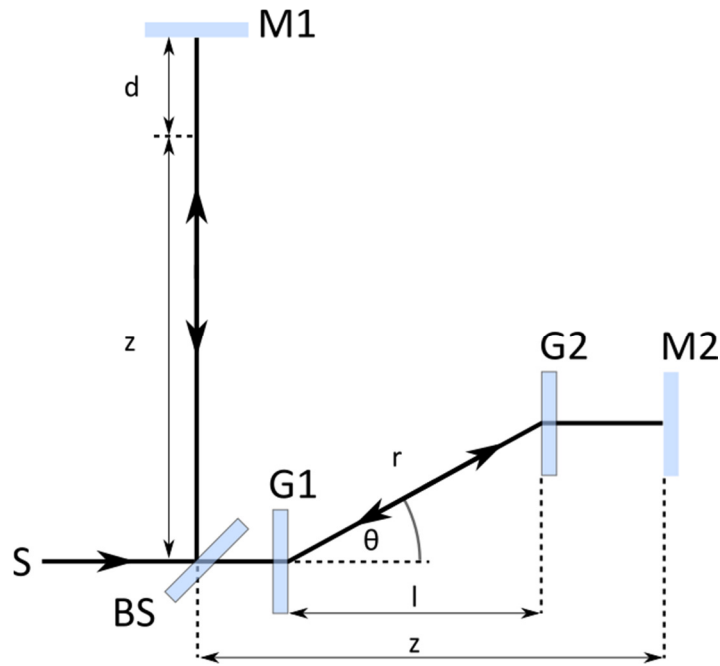
Figure 3.1: Schematic diagram of a dispersed reference interferometer.

In the reference arm light passes through a diffraction grating, G1, with the first negative diffracted order passing through a second diffraction grating, G2, while all other orders are discarded. Passage of the reference beam through this pair of matched diffraction gratings results in a collimated beam incident upon the reference mirror, M2, where the path length travelled by the source light is a function of wavelength with longer wavelengths of light travelling further. M2 returns the reference beam through both gratings, effectively doubling the introduced chromatic dispersion. The reference beam is recombined with the measurement beam at the beam splitter, BS, before a spectrometer (not shown) spectrally decomposes the recombined beams and passes the resultant spectral interferograms to a computer for analysis.

The resulting DRI interferograms appear as a quadratic cosine shape. The measurement arm length is adjusted until the point of symmetry of the interferogram is located at the centre of the detector. When the measurand is at this position, C, the interferometer is said to be balanced. With positive or negative displacements of the measurement mirror by a distance, d, the central point of symmetry of the interferogram shifts left and right respectively.

3.3   Experimental Apparatus

The experimental apparatus is a bulk optics setup comprising a Michelson interferometer with a chromatically dispersed reference arm, a schematic of which is shown in figure 3.2. The optical components for the initial bulk optics layout were chosen for availability and ease of alignment. Alternative component configurations are considered in appendix 11.1 along with discussion of component advantages and disadvantages.

Optical components are mounted in Thor Labs kinematic stages providing tip and tilt adjustment of ±4°. These in turn are mounted on magnetic bases on a Newport optics table allowing flexibility of alignment and improved isolation from building vibration.
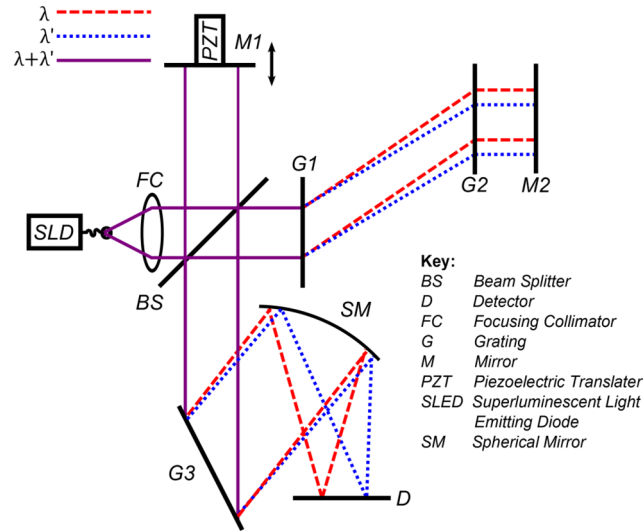
Figure 3.2: Schematic of the experimental bulk optics dispersed reference interferometer.

The light source, S, is a fibre linked superluminescent light emitting diode (SLED) with a centre wavelength of 820 nm and a full width half maximum (FWHM) bandwidth of 25 nm (Exalos EXS210036-01). Collimation of the source as it exits the fibre is performed by a fibre collimator, FC, resulting in a beam waist diameter of 8 mm. The resulting free space beam is split by a cube beam splitter, BS, to form the two arms of the interferometer. In the measurement arm a mirror, M1, reflects the measurement beam back to the beamsplitter. For experimental purposes this mirror is mounted upon a precision piezo-electric translator (PZT) which allows precise control of measurement arm length. This PZT (Physik Instrumente (PI) E-661) is not a requirement of the method but is a convenient tool to assess the range, resolution and linearity of DRI without the complications of scanning across a measurement sample. It has a range of 100 μm, a closed-loop resolution of 0.7 nm and a full range linearity of 0.03 % or ±30 nm [87].

In the reference arm, a pair of matched transmission gratings (G1, G2) introduces chromatic dispersion to the source light. The first grating (G1) acts to separate the source wavelengths angularly while the second grating (G2) re-collimates the beam. The reference mirror (M2) reflects the beam back through both gratings, effectively doubling the dispersion. The effect of using these gratings is that the longer source wavelengths are dispersed by a higher angle, θ, and so travel further than the shorter wavelengths.

The measurement arm simply consists of a mirror (M1). When the position of M1 is such that the path from BS to M1, z, is the same as the perpendicular distance from the beam splitter to the reference mirror (M2) plus the balancing term, d_0, then the interferometer is said to be balanced. At this point, (C),

the resulting interferogram is centred on the spectrometer detector. As the distance of the measurement mirror moves from the balance point, C, a different wavelength comes into balance and so the point of symmetry of the interferogram moves across the detector. Signal processing of the interferogram allows this centre of symmetry to be calculated and thus the measurement mirror position inferred.

An absolute method of surface displacement measurement is achieved by calculation of the interferogram point of symmetry. As the OPD changes the interferogram centre shifts left or right on the detector and tracking of this position results in a measurement method which, being absolute, suffers from no phase ambiguity and so can measure large step heights as well as have samples replaced without a zone of confusion.
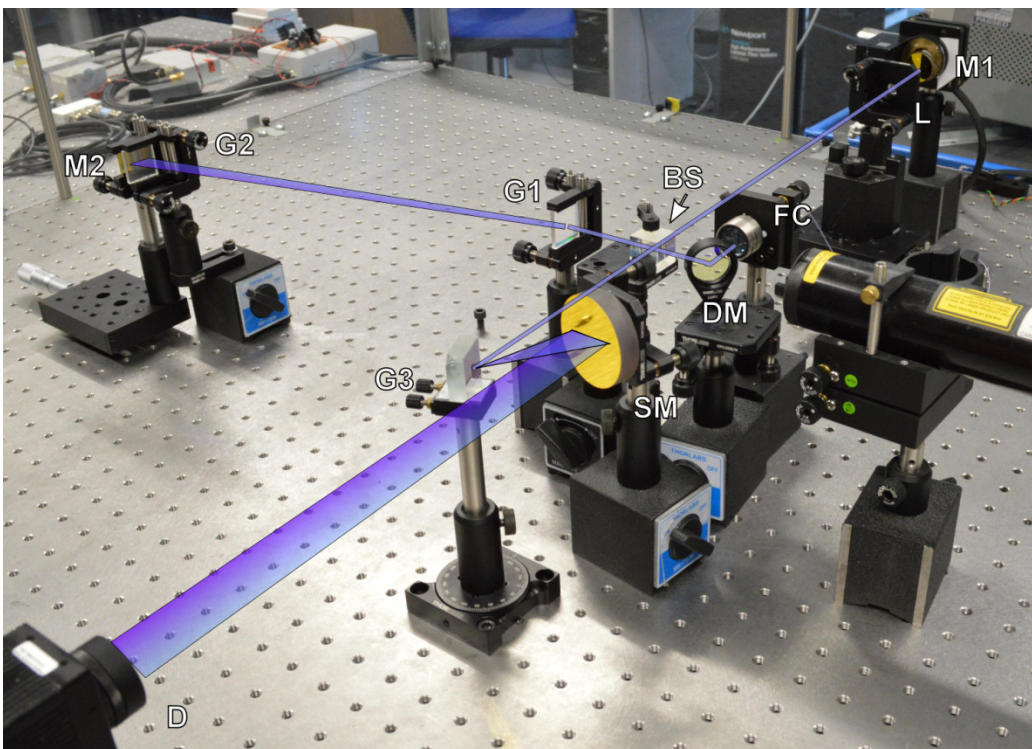
Figure 3.3: DRI bulk optics setup including He-Ne laser placed co-linear to the SLED beam. This was used for alignment purposes.

The table in appendix contains a full parts list of optical devices used within the setup. It does not include components used for alignment such as kinematic mounts, optics pillars, magnetic bases, pin holes or translation stages.

3.4 Characteristic Equations

DRI interferograms can be described fully by equations in this section. Key to the operation of DRI is the introduction of dispersion in the reference arm. Angular dispersion is calculated using the grating equation described in equation 3.1. This is modified to provide the angle of dispersion for angular wavenumber, k, in equation 3.2:

$$\theta_\lambda = \arcsin\left(\frac{\psi\lambda}{D} - \sin\theta_i\right)$$

<div align="right">3.1</div>

$$\theta_k = \arcsin\left(\frac{2\pi}{kD}\right)$$

<div align="right">3.2</div>

Where ψ is the diffracted order, 1, and D is the grating period. For the interferometer illustrated in figure 3.2 the first transmission grating, G1, is placed perpendicular to the reference beam resulting in a zero value for the incident angle, θ_i, and so the sine term present in equation 3.1 also tends to zero. To calculate the wavenumber dependent distance between gratings G1 and G2, the following trigonometric relation is used, with the wavenumber dependent path, $r(k)$, forming the hypotenuse of the triangle formed by the gratings G1 and G2 and the perpendicular distance between them, l.

$$r(k) = \frac{l}{\cos\theta_k}$$

<div align="right">3.3</div>

Substituting equation 3.2 into 3.3 yields a form which can be further simplified using trigonometric relationships while removing the sine and cosine terms.

$$r(k) = \frac{l}{\cos\left[\arcsin\left(\frac{2\pi}{kD}\right)\right]} = \frac{l}{\sqrt{1 - \left(\frac{2\pi}{kD}\right)^2}}$$

<div align="right">3.4</div>

Next, let us consider the measurement and reference arm path lengths, L_M and L_R respectively, for the interferometer shown in figure 3.1. The measurement mirror, M1, is placed at a distance, d, from a reference point, C, where the distance z from the beam splitter to C is equal to the perpendicular distance from the BS to the reference mirror, M2. Taking into account the wavenumber dependent optical path in the reference arm, the measurement and reference arm lengths can be calculated as follows.

$$L_r = 2\left[z - l + r(k)\right]$$

<div align="right">3.5</div>

$$L_m = 2(z + d)$$

<div align="right">3.6</div>

The difference in path length between the two arms of the interferometer is known as the optical path difference (OPD). As d changes with measurand position, the OPD between the measurement arm and reference arm also changes and is described as follows:

$$OPD = L_r - L_m$$
$$= 2\left[z - l + r(k) - z - d\right]$$
$$= 2\left[r(k) - l - d\right]$$

3.7

If the grating parameters, D and θ_i, are chosen carefully for the source wavenumber range, the rate of change of wavenumber dependent dispersion will remain constant across the operating range of the interferometer. In this case, the wavenumber dependent dispersion, $r(k)$, can be replaced with a linear approximation using the wavenumber, k, and the centre wavenumber, k_c, as shown in equation 3.8.

$$r(k) \simeq r(k_c) + r'(k_c)(k - k_c)$$
$$\simeq r(k_c) + \alpha(k - k_c)$$

3.8

In equation 3.9 the first derivative $r'(k)$ is renamed as α for simplicity of further calculations.

$$\alpha = r'(k) = \frac{4\pi^2 l}{d^2 k_c^3 \left[1 - \left(\frac{2\pi}{k_c D}\right)^2\right]^{3/2}}$$

3.9

Next the phase of the interferometer can be calculated using the wavenumber and the OPD, with the result illustrated by figure 3.4. The wavenumber at which the vertex of this quadratic phase function occurs is termed k_v.

$$\phi(k) = 2k\left[r(k_c) + \alpha(k - k_c) - l - d\right]$$

3.10
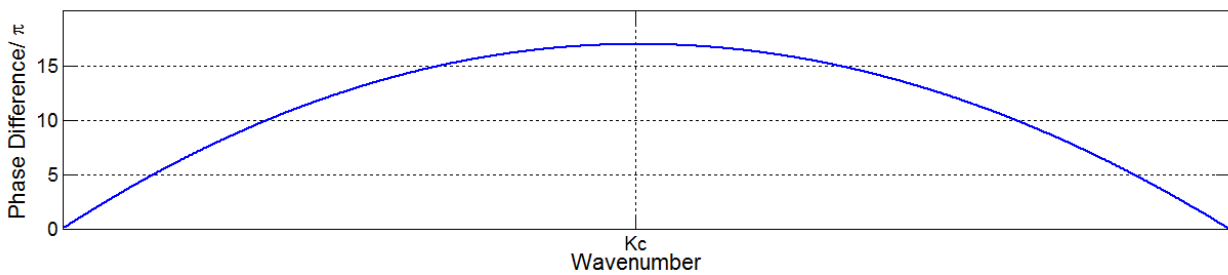
Figure 3.4: Typical quadratic phase function for DRI

To achieve a balanced spectral interferogram where the point of symmetry of the interferogram exists at the centre of the spectrometer a balancing term, d_0, must be subtracted from the measurement path length. Solving equation 3.10 for the phase vertex wavenumber, k_v, and rearranging in terms of the measurement mirror displacement, d, provides the following equation:

$$d = r(k_c) + \alpha(2k_v - k_c) - l \qquad\qquad 3.11$$

For a case where the phase vertex exists at the central wavenumber then $k_v = k_c$ and so d_0 can be expressed with the following simplified equation:

$$\begin{aligned}d_0 &= r(k_c) + \alpha(2k_c - k_c) - l \\ &= r(k_c) + \alpha k_c - l\end{aligned} \qquad\qquad 3.12$$

Rewriting the phase equation to account for the balancing term results in the following equation:

$$\phi(k) = 2k\left[r(k_c) + \alpha(k - k_c) - l - d - d_0 \right] \qquad\qquad 3.13$$

Use of the interferometer equation (eq. 11.2) along with the phase, $\phi(k)$, the spectrum of the source, $I_0(k)$, and the visibility of the interferometer, V, completes generation of an interferogram. For simulated interferograms, this can be reduced to the form seen in equation 3.15 due to constant source intensity and an ideal visibility, resulting in an interferogram for $d = 0$ such as that seen in figure 3.5.

$$I(k) = \frac{I_0(k)}{2}\left\{ 1 + V\cos\left[\phi(k)\right] \right\} \qquad\qquad 3.14$$

$$I(k) = 0.5\left\{ 1 + \cos\left[\phi(k)\right] \right\} \qquad\qquad 3.15$$
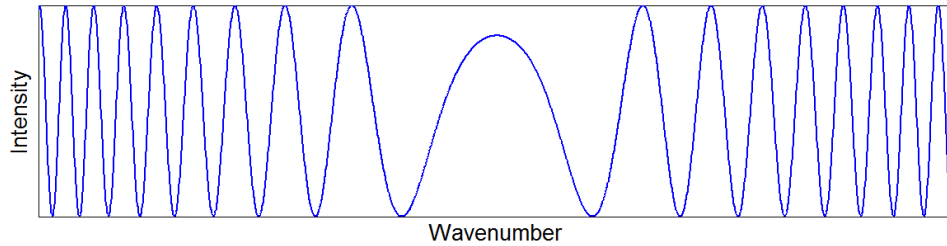
Figure 3.5: Balanced spectral interferogram for $d = 0$.

3.5   Simulation of DRI spectral interferograms using Matlab

With knowledge of the formulae to describe the operation of DRI from section 3.4, it is possible to convert the previous continuous case into a discretised version of equations 3.2 to 3.15. When used with Matlab this enables simulation of interferograms and evaluation of signal processing methods for characterisation of DRI performance with OPD change. Characteristics such as interferogram shape with OPD change can be used to estimate range, resolution and linearity for given physical attributes of the bulk optics interferometer. These attributes include the perpendicular grating separation, l, light source bandwidth, $\Delta\lambda$, as well as the grating period, D. Once signal processing methods have been developed,

these values can be altered in simulation to achieve a desired range and resolution while ensuring that the signal processing methods remain valid.

The discretised versions of equations 3.2 to 3.15 go as follows, with the wavenumber range Δk sampled at m equally spaced points into the vector $\mathbf{k}$:

$$\mathbf{k} = \left(k_1, \cdots, k_i, \cdots, k_m \right)^T \quad \text{where } k_i = \left(k_L + \frac{\Delta k}{m} \right)$$

3.16

and index, $i \in \{1, 2, \cdots, m\}$

Where m is the detector pixel count. A vector, $\mathbf{r}$, containing the wavenumber dependent optical path is next calculated as follows:

$$\mathbf{r} = \left(r_1, \cdots, r_i, \cdots, r_m \right)^T \quad \text{where } r_i = \frac{1}{\sqrt{1 - \left(\frac{2\pi}{k_i D} \right)^2}}$$

3.17

Where the constant, D ¸ is the grating period. Phase values for each wavenumber are calculated using the wavelength dependent optical path, r_i , and l , the distance of the interferogram from the balance wavenumber, k_c. Also required are the previously calculated values α and d_0 .

$$\mathbf{p} = \left(p_1, \cdots, p_i, \cdots, p_m \right)^T \quad \text{where } p_i = 2k_i \left(r_i - \alpha \left(k_i - k_c \right) - l - d - d_0 \right)$$

3.18

Finally, the intensity at each pixel is calculated, resulting in an interferogram contained within vector $\mathbf{h}$.

$$\mathbf{h} = \left(h_1, \cdots, h_i, \cdots, h_m \right)^T \quad \text{where } h_{i,j} = 0.5 \left[1 + \cos \left(p_i \right) \right]$$

3.19

For a displacement, d , of 0 µm an interferogram is generated using 3.16 to 3.19 resulting in a simulated interferogram with the point of symmetry centred on the detector. Increasing or decreasing the imbalance by varying d results in the interferogram point of symmetry shifting left and right on the detector respectively. Figure 3.6 (a) to (c) illustrate this shifting of interferogram symmetry position with changes in d .
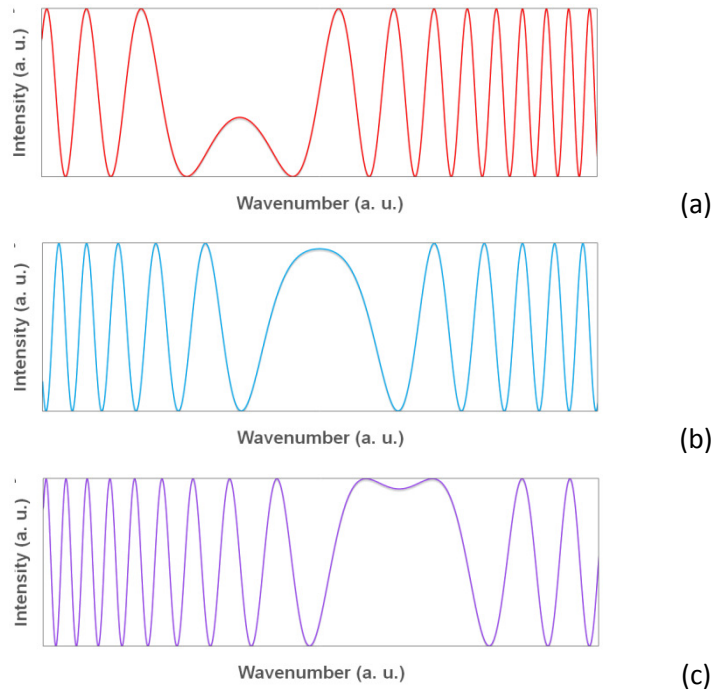
Figure 3.6: Spectral interferograms generated by Matlab simulation. These have an OPD offset from the zero OPD of the central wavenumber by -150 μm (a), 0 μm (b) and +150 μm (c).

The Matlab function contained within Appendix 11.4.2 follows equations 3.16 to 3.19 and can be used to generate a spectral interferogram where $k_v = k_c$ and hence has a point of symmetry upon the centre of the simulated detector.

3.5.1 Interferogram symmetry detection for balanced spectral interferograms

Having described generation of a simulated interferogram in the previous section and demonstrated that the point of interferogram symmetry occurs at the same position as the phase vertex, it is obvious to see how calculation of the position of this symmetry point will yield the surface height for an experimental interferometer generating a real spectral interferogram. This section reviews spectral interferogram literature containing solutions for symmetry detection for balanced spectral interferograms. This includes discussion of autoconvolution and peak averaging for balanced spectral interferograms (BSI) as well as discussion of why frequency domain and wavelet analysis used for unbalanced spectral interferograms (USI) is unsuitable for a BSI such as produced by DRI.

Spectral interferograms, both balanced and unbalanced have been used for measurement of displacement [77, 78], optical fibre length, fibre dispersion , transparent sample thickness [82], thin film thickness [83], chirped mirror characterisation [84] and dispersion of transparent samples [85]. Due to the wide application area of spectral interferograms, a review of methods used for their analysis is useful towards the end goal of DRI interferogram analysis for OPD retrieval.

Autoconvolution: One popular method for analysis of spectral interferogram balance point is convolution, where convolution of a signal with itself is commonly known as autoconvolution. When a signal of length m is convolved with itself it results in a signal of length $2m-1$. The maximally valued peak of this signal is proportional to the index of the point of symmetry in the original signal. Autoconvolution has seen use for absolute distance measurement using a fibre-based dispersed reference interferometer [78], absolute thickness measurement of optical samples of a known refractive index [88] and measurement of dispersion and refractive index. Examples of the decimated-by-2 autoconvolution of three interferograms are shown in Figure 3.7 in green.

(a)

(b)

(c)
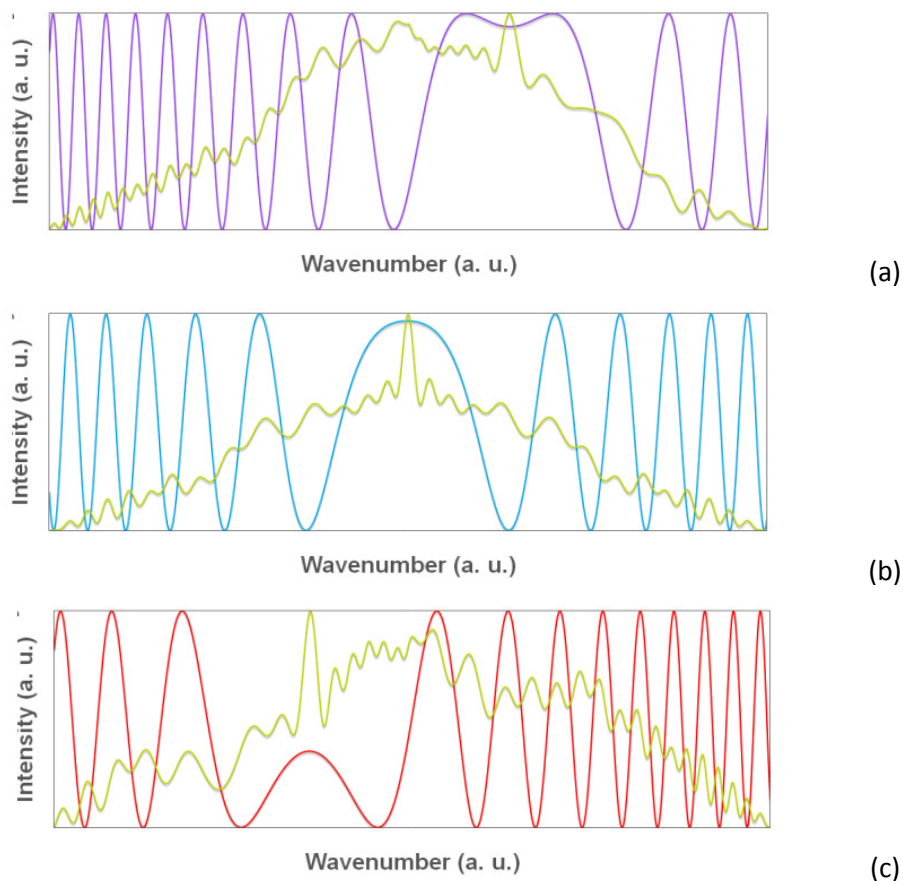
Figure 3.7: Spectral interferogram simulations having phase vertexes at varying points. The decimated by two autoconvolution of each spectral interferogram is shown in green and demonstrates how the peak of the autoconvolution matches the position of the interferogram vertex.

This convolution method differs from cross-correlation in that upon convolving a signal with itself, one of the input signals is reversed. It can be seen in figure 3.7 that this results in an autoconvolution peak (green) which tracks the position of the interferogram symmetry. A cross-correlation of a spectral interferogram with itself results in a similar looking signal whose highest peak remains at the centre of the detector irrespective of the position of the spectral interferogram stationary phase point.

Autoconvolution is reported as having an excellent immunity to noise [89] for real interferogram signals. In addition to this the speed of calculation is favourable when compared to alternative methods and use

of a frequency domain method of autoconvolution for larger data sets allows further signal processing rate improvements [90]. A limitation of autoconvolution over methods used for USIs is its limited range since as the interferogram symmetry point approaches the edge of the detector, the peak of the autoconvolution result deteriorates until the interferogram symmetry can no longer be resolved.

Peak averaging: Similar to autoconvolution, peak averaging methods aim to resolve the phase vertex of a spectral interferogram. By detecting the peaks and valleys of the interferogram then determining the positive and negative matching pairs, spurious results in proximity to the phase vertex may be eliminated and then the position determined by calculating the average of all of the peak/valley positions. The labelling of such peak and valley pairs can be described by Figure 3.8.
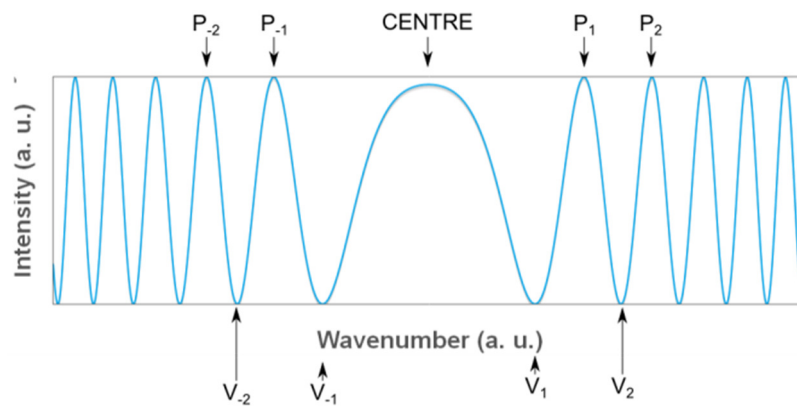
Figure 3.8: Interferogram peak/valley position labelling scheme

Peak averaging has previously been used for phase vertex position calculation in spectral interferometry allowing characterisation of dispersion in short fibres [79]. Similar to autoconvolution, the operational range of peak averaging is limited by the requirement to detect surrounding peaks. As the symmetry position approaches the edge of the detector fewer peaks/valleys are available for fitting on one side of the centre. The range of peak averaging may be extended through use of peak spacing fitting [91], though not indefinitely.

Since peak averaging depends upon the accurate detection of each peak and valley, errors may manifest due to optical and electrical random noise, and wavefront distortion [92]. Furthermore, many peak fitting algorithms require a priori knowledge of the signal amplitude and peak/valley frequency in order to calculate an appropriate value for slope threshold, amplitude threshold and the smoothing required to correctly calculate the peak positions. For methods such as DRI where the visibility, contrast, noise and low-frequency envelopes of interferograms will vary as surface roughness and reflectivity changes, the accurate determination of peak position could be problematic. Furthermore, the necessity to fit to peaks and valleys limits the cases where spectral interferograms can be used since as the frequency increases, more peaks must be detected and the resolution of their position decreases.

Frequency domain methods: Of the frequency domain methods the simplest appears to be extraction of the first harmonic of the FFT, resulting in a wrapped phase. Upon unwrapping, the vertex of this phase indicates the position of the spectral interferogram centre. Used for non-stationary interferograms (those like spectral interferograms, whose frequency changes across the signal) this method is reported as having low spatial resolution [93]. The same paper offers a comparison of windowed Fourier transform (WFT), multi-scale windowed Fourier transform (MWFT) and wavelet transform (WT), with more information on the latter available in papers by Deng et al. [84] and Liebling et al. [94]. These are used for calculation of phase for deflectometry where the sinusoidal patterns have stationary phase points, but no discussion of their usefulness for spectral interferograms is given.

3.5.2 Autoconvolution implementation

For an interferogram containing vector, $\mathbf{h}$, of length m autoconvolution is used to find the interferogram centre as follows. First, convolution of the interferogram with a left-right flip of itself results in a vector, $\mathbf{c}$, of length $2m-1$.

$$\mathbf{c} = \left(c_1, \cdots, c_i, \cdots, c_{2m-1}\right)^T \text{ where } c_{q,j} = \sum_{i=1}^{m} h_{i,j} \cdot h_{(q-i),j} \text{ and index, } q \in \left[1, \cdots, 2m-1\right]$$

3.20

The index of the maximally valued element of this vector indicates the position of the interferogram centre. Figure 3.9 shows a typical simulated interferogram (blue) and autoconvolution result (red). For this graph the autoconvolved interferogram has been decimated by a factor of two and normalised from zero to one (see appendix 11.4.3 for Matlab function) to scale it to allow for comparison to the original interferogram, $\mathbf{h}$.
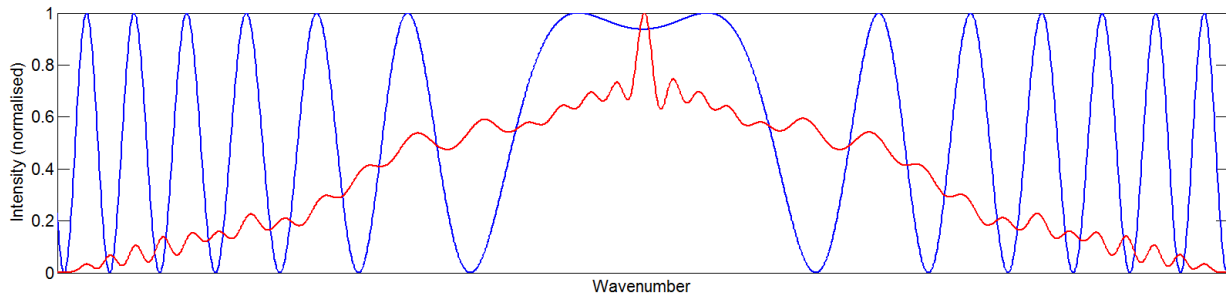
Figure 3.9: Simulated interferogram (blue) and the decimated and normalised autoconvolution of the interferogram (red).

Next the interferogram centre, a, is calculated by finding the index of the maximally valued element of the autoconvolution result holding vector $\mathbf{c}$. This is achieved using a simple max() function. Pixel resolution of the peak may be achieved if using the decimated by two autoconvolution result. Alternatively, the peak of the autoconvolution may be calculated, with division by two relating the autoconvolution result to the shorter original interferogram result. This second method provides a 0.5 pixel resolution. Furthermore, sub-pixel resolution may be realised by using least squares peak fitting algorithms to determine the precise position of the autoconvolution peak. Appendix 11.4.5 shows the peak fitting algorithm Matlab code.

The signal processing limit to DRI range is the shape of the autoconvolution result as the point of symmetry approaches the edge of the detector. As the interferogram centre moves outwards, at some point the peak of the autoconvolution deteriorates until it is not detectable. Figure 3.10 shows the interferogram centre near the edge of the usable autoconvolution range while figure 3.11 shows the shape of the autoconvolution result when the interferogram centre has passed where the autoconvolution peak is the highest. At this point the use of a max() function to detect interferogram centre ceases to be a valid method.
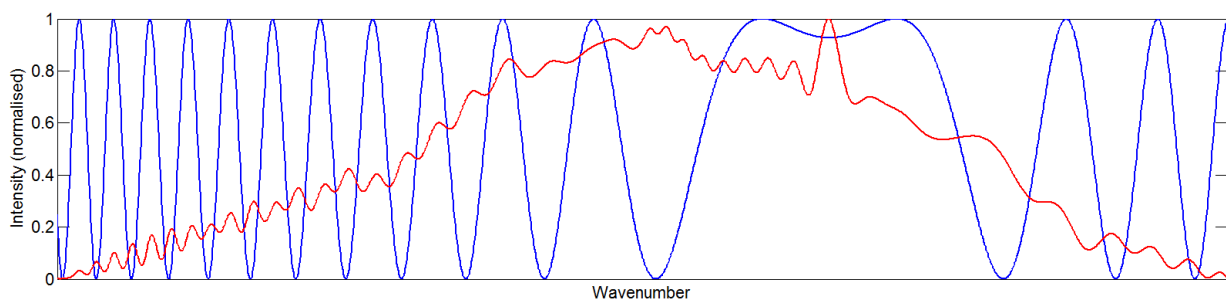
Figure 3.10: A Matlab simulated interferogram (blue) with a grating ruling of 300 l/mm, a perpendicular grating spacing of 330 mm and an offset from z0 of 140 μm. For this offset from the balance point, the peak autoconvolution associated with the interferogram point of symmetry remains the highest part of the autoconvolution result.

61
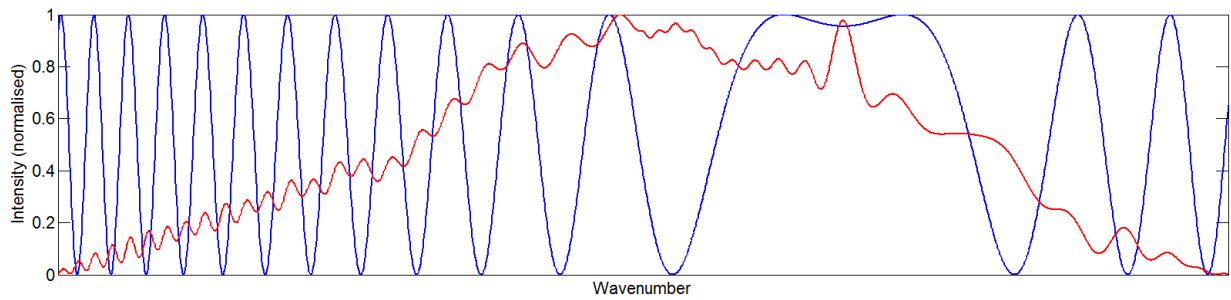
Figure 3.11: Increasing the balance offset to 150 µm moves the symmetry position further to the right and it can be seen that the autoconvolution result begins to deteriorate, with the peak associated with the point of symmetry still a strong peak but no longer the highest point.

Despite this, peak finding algorithms can successfully determine interferogram centre from the autoconvolution peak well past the point where the peak is no longer the highest feature of the autoconvolution result. Figure 3.12, at a 250 µm offset from the balance point, λ_C, demonstrates this. The green line shows the location of the interferogram point of symmetry as well as an autoconvolution peak. Careful selection of peak detection parameters can exclude erroneous peaks as too narrow or having insufficient amplitude but this does become problematic with the introduction of noise with real data. This has the added benefit of providing sub-pixel resolution autoconvolution data.
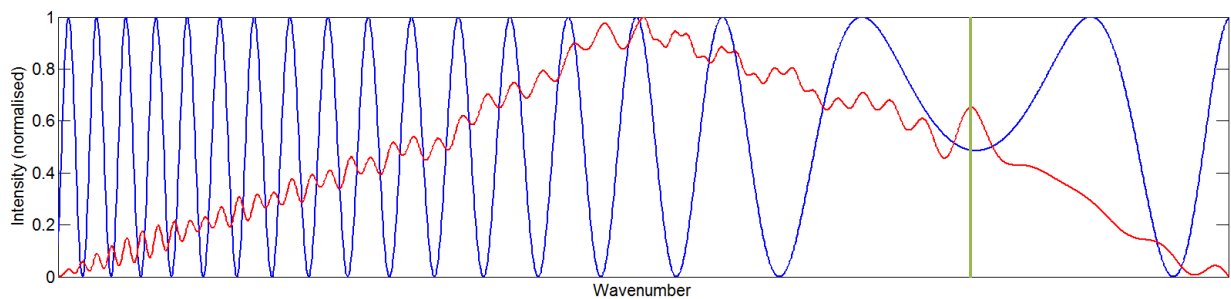
Figure 3.12: When the OPD is 250 µm away from the balance point of the central wavenumber, λ_C, the autoconvolution peak corresponding to the interferogram symmetry is less obvious but remains a strong feature of the autoconvolution data.

An alternative method to peak fitting is subtraction of the DC term from the simulated interferograms. For simulated interferograms this means that the interferogram intensity varies from -0.5 to 0.5 instead of 0 to 1. This has the effect of removing the broad triangular shape from the autoconvolution result and promotes visibility of the autoconvolution peak corresponding to the interferogram centre as seen in figure 3.13.
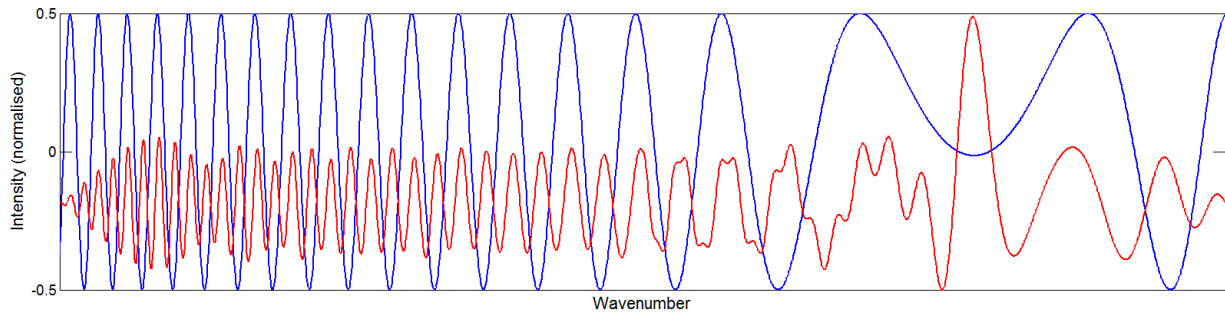
Figure 3.13: Subtraction of the DC offset from the interferogram before autoconvolution substantially improves the range of DRI. This removes the triangular shape from the autoconvolution and improves the visibility of the peak coinciding with the interferogram centre.

In simulation, for a perpendicular grating separation of 330 mm, a grating frequency of 300 lines/mm and a source bandwidth of 21 nm, the range of DRI will be approximately 290 μm using the simple max() method. With the extended range calculation using peak fitting or DC subtraction that are described above this can theoretically be increased to 450-500 μm. In a real interferometer this range extension will be highly dependent on the background illumination, contrast, visibility and low frequency envelopes inherent in the system which will be discussed in the next section.

3.6   Measured results

The interferogram resulting from the bulk optics interferometer described above is processed by a custom Labview virtual instrument (VI). This VI continuously requests data from the FireWire camera, displays a graph of the interferogram and calculated autoconvolution, and then updates a chart with the calculated autoconvolution result.

A screenshot of the front panel for this first Labview VI can be seen in appendix 11.5.1. This VI also provides several other important features. Firstly, it provides a means to record entire interferograms for later analysis with Matlab, important since this allows direct comparison of signal processing methods on an identical real interferogram. Secondly, the VI allows control of attached motorised translation stages.

Figure 3.14 shows a graph of a typical DRI interferogram (red) along with a plot of the normalised and decimated-by-two autoconvolution result. It exhibits excellent signal to noise ratio and contrast. The background intensity and low frequency envelopes from the source are minimal.
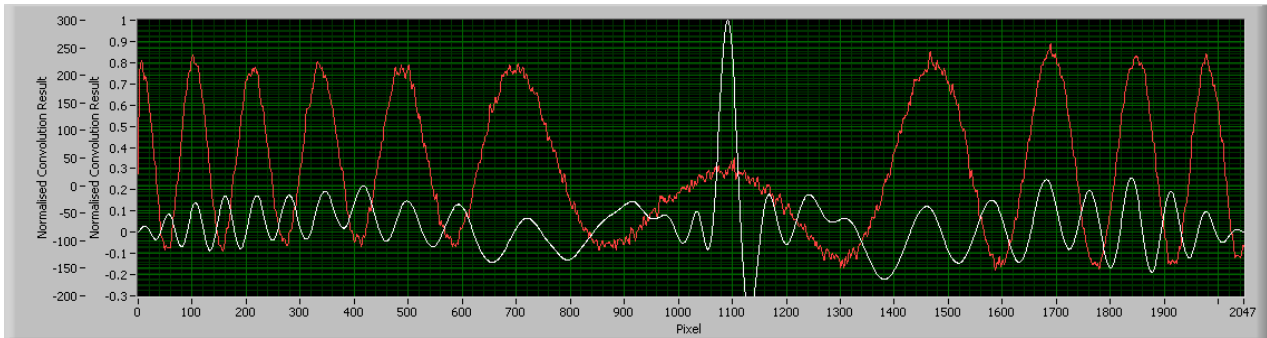
Figure 3.14: Screenshot of one of the first interferograms (red) and resultant autoconvolution results (white) obtained from the bulk optics DRI layout described in section 3.3.

3.6.1 Per pixel axial resolution

Calculation of the resolution of absolute position encoding by wavelength is possible through use of the PZT mounted behind the measurement mirror. The closed-loop precision PZT (Physik Instrumente P-721.CLQ) uses a capacitive displacement sensor to achieve linearity of better than 0.03 % and a bi-directional repeatability of less than 5 nm over a working range of 100 μm. It is desirable to use a PZT since the closed-loop nature allows precision positioning of the measurement mirror along the optical (Z) axis, important to measuring the resolution, range and linearity of the interferometer. While the PZT offers a limited range (100 μm) the stiffness and stability of such a PZT is preferable over the use of a motorised stage where greater errors in flatness, straightness, roll, pitch and yaw will affect the position of the measurement mirror.

While a PZT also exhibits these effects, those of the available PZT are much less than the available motorised stage (Newport MFA-CC). In addition to this, the small physical dimensions and weight of the PZT mean it can be mounted closer to the measurement axis, further reducing the effect of angular stage deviations (roll, pitch, and yaw).

To measure the resolution of the measured scale, the PZT was adjusted to 50 μm: half its total range. The interferometer was then adjusted manually to move the autoconvolution peak to approximately the centre of the detector array (pixel 2048).

Starting from the PZT 0 μm position, 5 μm steps were taken every 0.5 seconds. Interferogram capturing was delayed 0.3 seconds after each translation to allow for mechanical settling of the PZT after which a single frame of the CCD was captured and used to calculate the peak position. This 0 to 100 μm translation and measurement cycle was repeated 10 times and the mean for each position calculated. The mean for each position was then plotted along with a least-squares linear fit of the data (Figure 3.15).
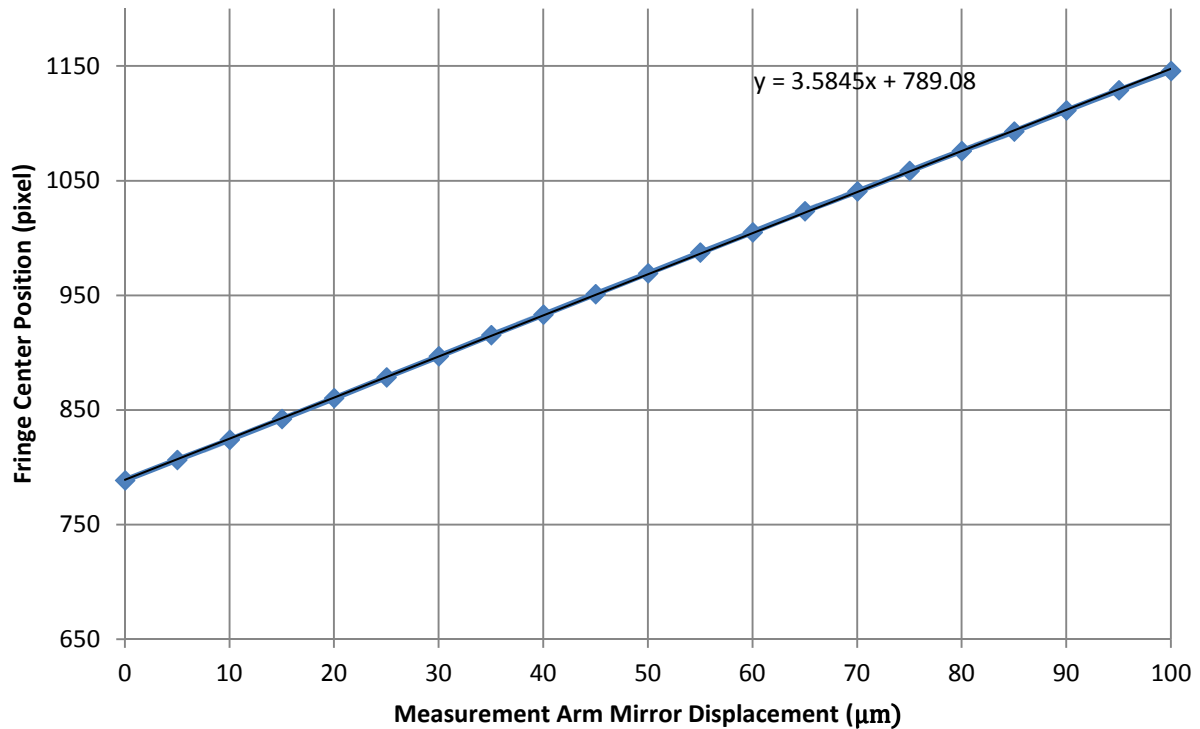
Figure 3.15: Graph showing calculated interferogram symmetry position against measurement arm displacement using the PZT.

The gradient of the line of best fit, 3.584 pixels per µm, then provides the per pixel resolution, $x = 279$ nm as follows:

$$y = \text{gradient} = 3.5845x \implies x = 1/3.5845 = 279.0 \text{ nm} \qquad\qquad 3.21$$

3.6.2 Range

Having calculated the pixel resolution of DRI, the operating range can be calculated if we assume that movement of the interferogram point of symmetry is approximately linear across the entire range. Range cannot be assessed using the PZT, having only a range of 100 µm. Therefore, for range measurement the measurement mirror must be manually translated using a micrometre stage (25 mm travel). By adjusting the measurement mirror position until the autoconvolution result begins to deteriorate at one end of the range, then translating to the other end of the range, the range can be calculated by multiplying the per pixel resolution by the change in pixels from one end of the range to the other.

Use of this method allows estimation of the range for a given source bandwidth, grating separation and grating pitch. The interferograms in figures 3.16 and 3.17 show examples of interferograms near the edges of their range for a bulk optics setup using transmission gratings with 300 lines/mm, separated by 330 mm and with a FWHM source bandwidth of 25 nm. The positions of the autoconvolution peaks in figure 3.16 and 3.17 are pixels 500 and 1520 respectively, with the separation of 1020 pixels multiplied by the per pixel resolution, 279 nm, equating to a range of 285 µm.
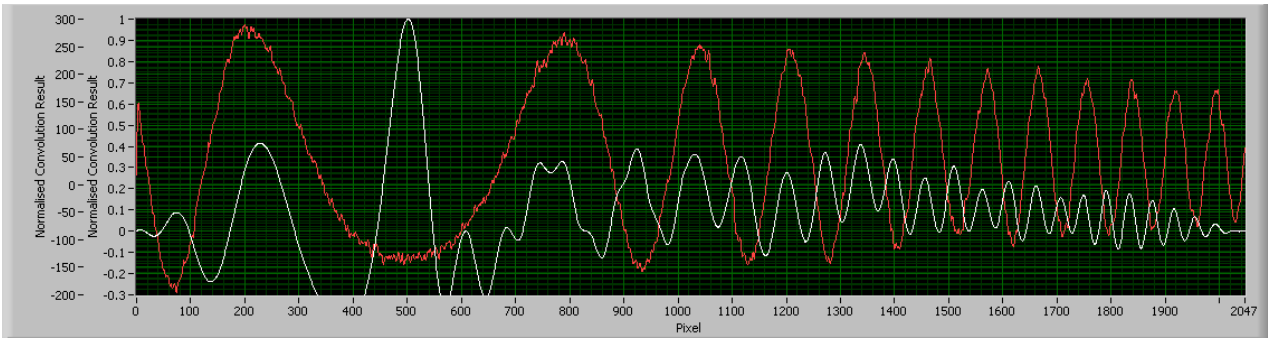
Figure 3.16: Screenshot of a Labview graph of an interferogram showing strong autoconvolution peak with the interferogram centre nearing the left side of the detector.
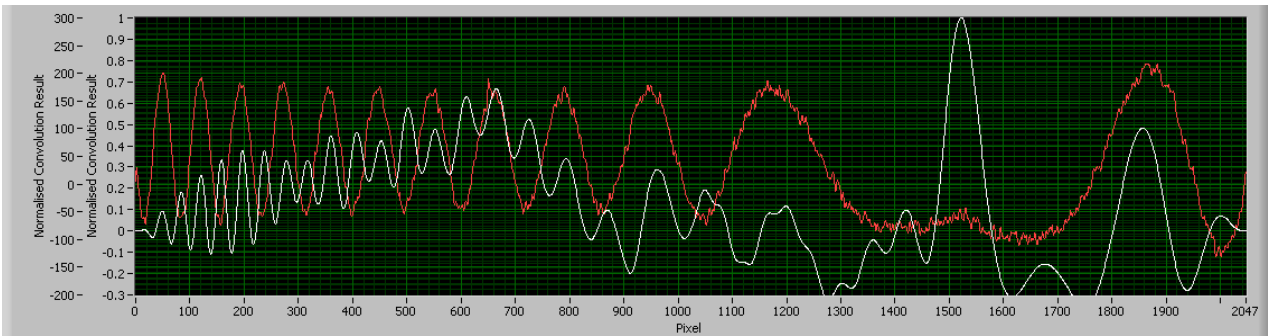
Figure 3.17: Screenshot of a Labview graph showing an interferogram showing strong autoconvolution peak with the interferogram centre nearing the right side of the detector.

3.6.3 Linearity

Due to the limited range of the PZT, linearity of absolute position encoding by wavelength can only be assessed over 100 µm. First, the deviation from the linear fit is calculated for each of the 21 PZT positions measured in figure 3.15; these results are shown in figure 3.18.
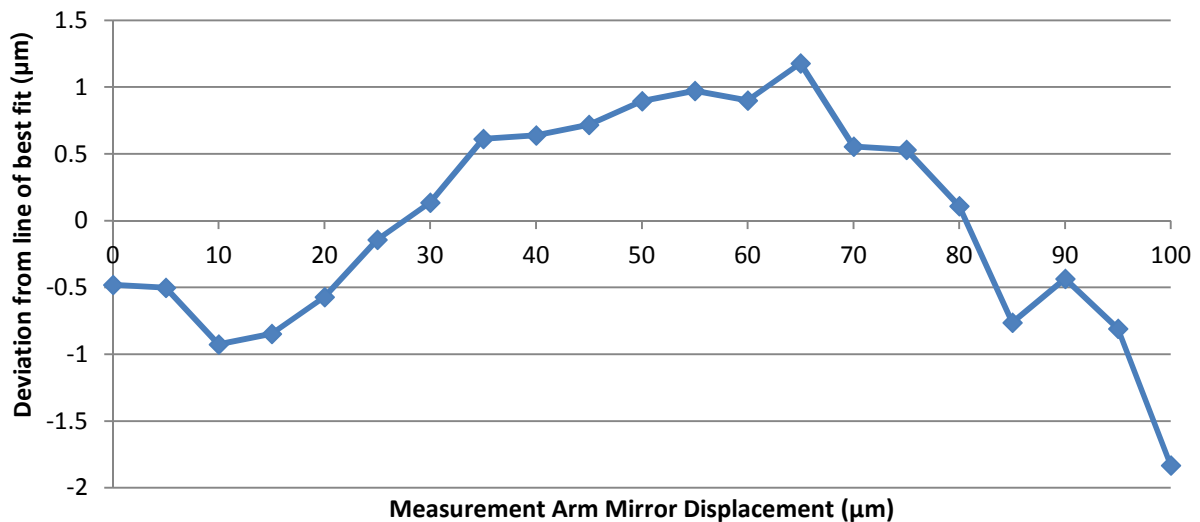
Figure 3.18: Plot of deviation from line of best fit a set of 21 PZT positions separated by 5 µm.

66

Considering this graph, it can be seen that the maximum deviation from the line of best fit was -1.83 pixels (-510.57 nm). This value along with the previously calculated per pixel resolution may be used to calculate a value for linearity of 0.53% across a range of 100 μm.

$$linearity = \left(\frac{resolution \times deviation}{\text{scan range}} \right) \times 100 = \left(\frac{290e^{-9} \times 1.83}{100e^{-6}} \right) \times 100 = 0.53\% \qquad\qquad 3.22$$

3.6.4   Step height measurements

Demonstration of absolute measurement position with DRI is seen as a crucial test of the ability of DRI. Measurement systems able to perform absolute measurement allow surface characterisation of measurands with discontinuous surfaces such as steps, voids or steep features. The absolute nature of such a measurement system means that if some parts of a surface are not measurable, the measurable areas may still be related to each other.

To demonstrate absolute measurement with DRI, a Rubert step height sample is measured by laterally translating it under the measurement beam. This sample (Rubert 513, ISO 5436) has four machined grooves of varying depths, with slopes of minimal width leading from the top surface to the bottom surfaces. These slopes are far steeper than the acceptance angles of all perpendicularly placed optical measurement instruments and as such visibility is lost as DRI measures across these features.
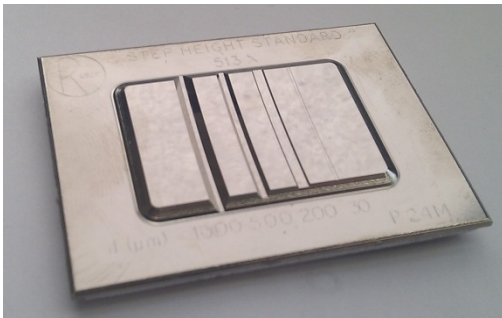
Figure 3.20: Schematic diagram of Rubert sample 513 grooves delineating their labelling scheme.
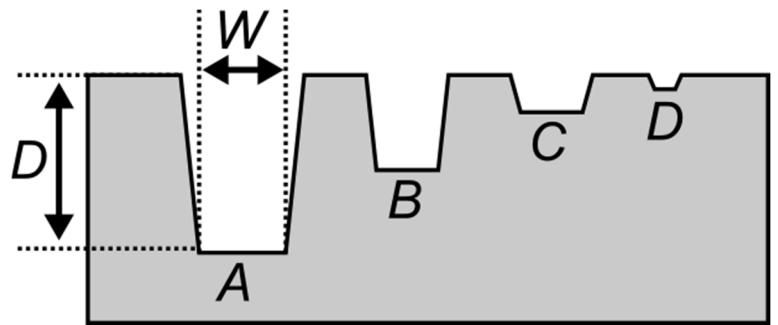
Figure 3.19: Photo of Rubert sample 513 showing the four machined step heights of varying depth and width.

For the purpose of proving the ability of DRI to measure step heights and hence achieve absolute measurement, grooves C and D have been chosen for measurement since these, of depth 200 μm and 30 μm respectively, are within the measurement range of DRI in its current configuration. Table 3.1 shows the specification of the step heights provided by Rubert.

Groove	Depth (μm)	Width (mm)
A	1000	3
B	500	2

| C | 200 | 2 |
| D | 30 | 0.5 |

Table 3.1: Table describing Rubert precision reference sample 513 feature width and depth.

To facilitate step height measurements, several changes in the DRI bulk optics layout are necessary. Firstly, a focusing lens must be included within the measurement arm. Secondly, lateral scanning of the Rubert sample beneath the lens must be implemented to allow scanning of the beam across the sample.
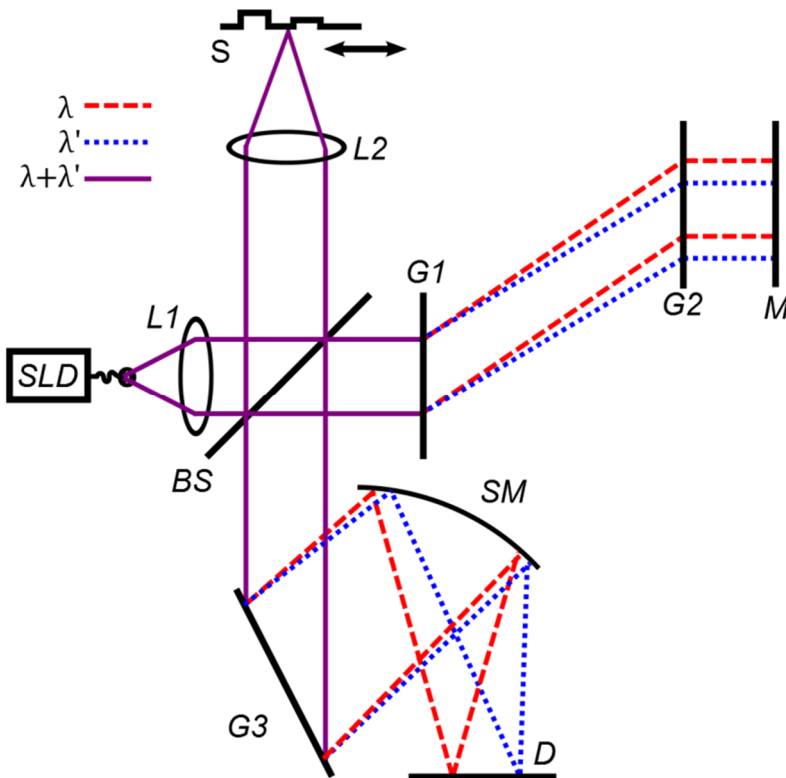
Figure 3.21: Schematic of the modified DRI to include a focusing lens, L1, and a method of translating the Rubert sample.

Figure 3.21 shows the location of the lens within the measurement arm, the focal length of which is chosen to provide a depth of field greater than the depth of the step height. In this instance, a lens with a focal length of 75 mm is chosen (Thor Labs AC127-075-B-ML), with the depth of field for a beam of width 8 mm providing a calculated depth of field of 190 µm (equation 11.14). This value is approximate since the value provided for the beam width of the focal collimator is specified at the beam waist, not at the position along the Z axis at which the lens is placed. The corresponding spot size, ϕ_s, for such a beam width and focal length is 10.10 µm (equation 11.13), increasing to $\sqrt{2}$ times this, 14.28 µm, at the extent of the depth of field.

Despite calculation of the depth of field suggesting that the 200 µm step height is not measurable, the generally accepted depth of field is a commonly imposed arbitrary limit to the acceptable spot size

defining measurement range and not a definitive limit to the operating range of a particular lens. For this reason a lens of 75 mm focal length may still be used so long as a larger spot size is acceptable for a particular measurement. Also of note is that the spot size and depth of field will vary depending on whether the FWHM or $1/e^2$ definition is used.
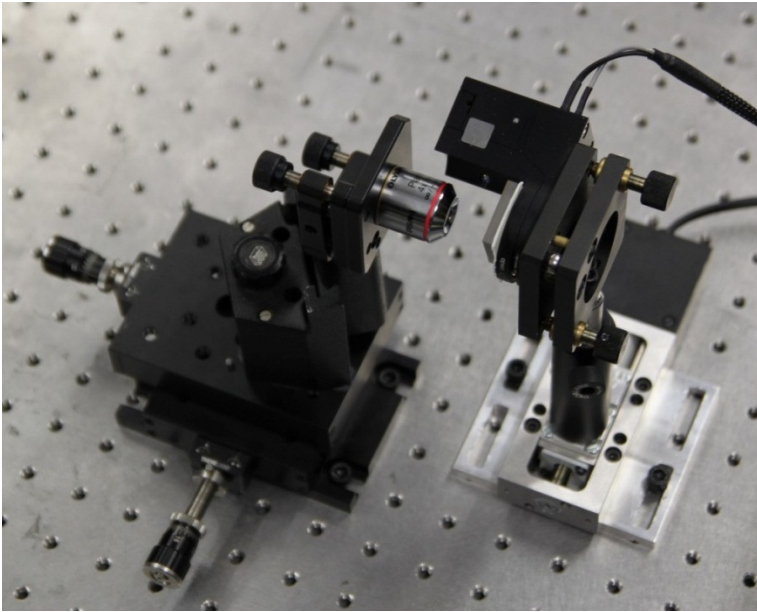
Figure 3.22: Measurement mirror (M1) mounted upon the PZT and motorised translation stage. An objective lens mounted upon a manual XYZ translation stage is also shown.

Lateral scanning of the sample is achieved using a Newport MFA-CC linear stage. This translation stage, marked as S in figure 3.21, has a travel of 25 mm, a per step resolution of 0.1 μm and a bidirectional repeatability of 2 μm [95]. Speed and position commands are provided to the translation stage using Labview with the encoder position matched to the measurement data during translation. The stage is mounted to the table, with the Rubert measurement sample mounted upon a kinematic stage raised to the plane of the Z axis by a ½" optics post. The orientation of the stage perpendicular to the measurement arm Z axis allows scanning of the sample in front of the focused measurement beam. Figure 3.22 shows a photo of a similar setup to that described above with an objective lens with 3 axes of translation as well as the measurement mirror mounted upon the PZT and motorised translation stage.

Raw data (Figure 3.23 (a)) is imported into Surfstand, a software platform providing a surface metrology measurement toolbox. Surfstand provides a variety of functions to manipulate measurement data and extract information about features of interest. In this case, a levelling tool removes the slope caused by the imperfect perpendicularity of the sample to the measurement beam

Errors at the slope interface (also known as "bat wings") can be seen in the image in figure 3.23 (a) with the invalid data between these caused by the high angle and low NA of the lens resulting in less light reflected back into the measurement arm significantly or completely reducing fringe visibility. At this

development stage DRI has no method to automatically calculate the quality factor of an interferogram to signify loss of interferogram visibility. Data with the slope and invalid data removed manually is shown in figure 3.23 (b).
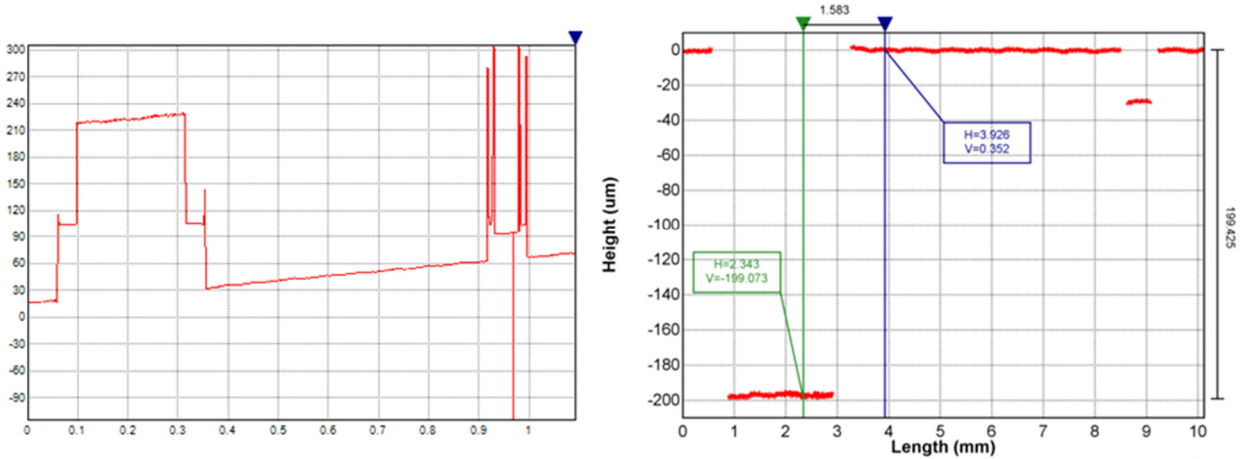
Figure 3.23: (a) Raw measurement data from profile across the 200 μm and 30 μm steps on the Rubert step sample. (left). (b) Measured profile. Slope corrected and repaired step data (right).

Use of a surface topography analysis software suite, Surfstand, is used to evaluate the DRI measured step heights. This results in measurements of 199.425 μm and 29.432 μm for the 200 μm and 30 μm steps respectively. To allow a comparison of the nominal step heights to the DRI measured values, measurement of the Rubert sample was repeated using a Taylor Hobson CCI, a coherence scanning interferometer capable of sub-nanometer resolution measurement when used in a laboratory environment. This resulted in the data shown in figure 3.24 with an areal view on the left and a single X profile shown on the right.
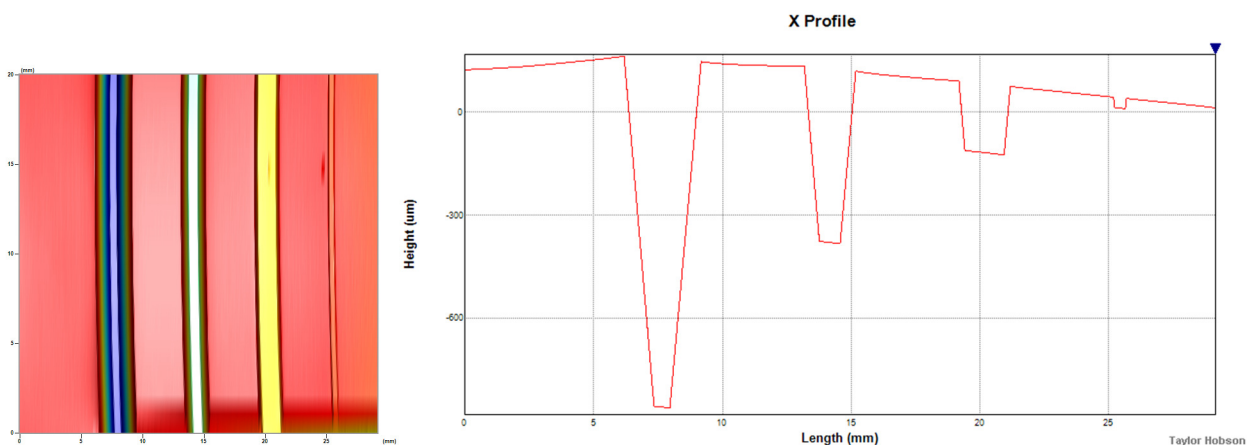
Figure 3.24: Areal measurement of Rubert reference sample performed by Taylor Hobson CCI (left) and a profile view of this data.

The Surfstand subarea form removal tool was used to level the data. Areal cropping of the measurement data resulted in the profile used for measurement which can be seen in Figure 3.25 showing only the 200

70

μm and 30 μm surface steps. The Surfstand spot height cursors were used to determine the height difference between the bottom of each groove and the top surface.
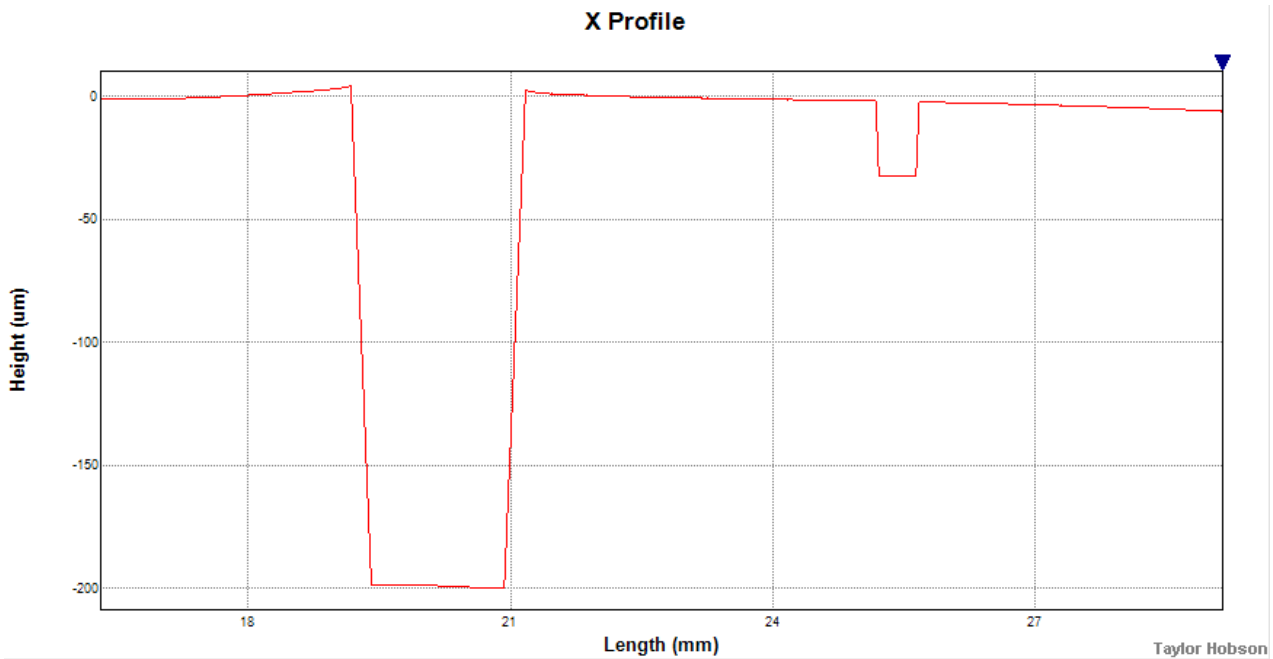
Figure 3.25: Profile measurement of 200 μm (left) and 30 μm step heights on the Rubert sample.

Table 3.2 summarises the step height measurements for grooves C and D with measurement by both CCI and DRI. The measured values agree to within 4% with the differences in measured values attributable to several factors. Unlike the CCI, DRI is a single-point measurement method requiring lateral translation of the sample beneath the lens in order to obtain a measurement. At present the software makes no attempt to calibrate out motorised stage errors such as flatness, straightness, roll, pitch and yaw (see section 11.1.9). Due to the physical setup in this instance, roll contributes most to the measurement error, with roll amplified by the large distance between the stage and the sample leading to Abbe error. Another reason for the mismatch between CCI and DRI is that no attempt was made to filter the DRI measurement data. Low amplitude oscillations are visible from X positions 4 to 8 mm in figure 3.23 (b). This noise, with amplitude of 1-2 microns, will greatly influence the step height as measured by DRI and is investigated further in section 4.6.2.

Groove	Nominal Depth (μm)	DRI (μm)	CCI (μm)
C	200	199.425	199.858
D	30	29.432	30.416

Table 3.2: Table comparing groove depth measurements by DRI and CCI

In summary, this measurement demonstrates the ability of DRI to measure absolute surface position. A comparison to measurement by an established offline method of metrology has been made and the small disagreements between the measurements have been explained. Future work to improve measurement

71

rate and stability and to reduce interferometer footprint will all have positive effects on DRI measurement results. Inclusion of software routines to provide stage calibration will further improve measurement results through removal of stage motion errors.

3.7 Short-term measurement stability study and measurement

Environmental effects have a significant influence on the stability of an interferometer. Changing of beam path lengths, refractive index of the transmission medium (in this case air) and angular misalignments by mechanical disturbances cause the apparent distance to the measurand to fluctuate as well as the visibility/contrast of the interferogram to change. Understanding and minimising these effects results in an improved measurement stability, with the key reasons for instability broken down into three groups below.

Path length change due to refractive index change. In a vacuum, the velocity of light is constant however for light traversing a non-vacuum environment (glass, air, water) the velocity is dependent on the index of refraction of the medium in which it travels. The index of refraction for air can be shown to vary with temperature, pressure, humidity and CO_2 concentration and is described by the Edlén equation. Changes in these variables over hours or days manifest as long term drift in the interferometer path lengths as temperature, atmospheric pressure and humidity change with the weather. Short time changes in temperature and pressure are manifested by air currents through the interferometer beam paths. A +1 part in 10^8 change in refractive index will result with the following changes in environmental conditions [96]:

- -0.01 °C change in air temperature
- +3.73 Pa change in air pressure
- -1 % change in relative humidity
- +67 ppm increase in CO_2 concentration

For absolute position encoding by wavelength used by DRI, these changes are not yet of a concern due to the path length changes caused by these variables being below the resolution of the method.

Path length change due to thermal expansion. A contributing factor to measurement drift over hours or days is the changing angular alignment of optical components and optical path length as a result of thermal expansion of components. As the temperature of the interferometer substrate changes with time, the thermal expansion of the table, optical mounts and kinematic stages may account for large changes in optical path length. During alignment of an experimental bulk optics interferometer, having ample spacing between components improves ease of alignment but a negative point to this approach is the problem of path length change with temperature is exacerbated. However, the time over which this temperature change occurs does not adversely affect DRI operation in its current experimental nature.

For a prototype instrument this will be much more important and the optics separations must remain consistent over days or weeks to maintain calibration and measurement stability. In this case a prototype interferometer would be greatly miniaturised when compared to the experimental bulk optics setup. Additionally, material choices for critical components will allow for low material expansion through use of alloys such as Invar for the base.

Path length change due to vibration. Observation suggests that the effect of vibration on DRI is the current biggest cause of short term instability. A damped optics table as well as active damping table legs reduces coupling of vibration to the table through the floor however this does not eliminate acoustic noise from passage of colleagues through the lab, air currents and external noises. The stiffness of optics kinematics such as posts, magnetic bases and tip/tilt stages is such that environmental perturbations have a large impact on the stability of the interferometer. Future machined prototype bases will lose the flexibility of the magnetic bases for interferometer evaluation but will allow significant reduction of path lengths due to the more compact nature of this configuration. The small size of such a prototype will also be more conducive to enclosure of the interferometer to eliminate such short term environmental effects.

Summary. Having evaluated possible sources of interferogram instability the following changes have been enacted to reduce environmental effects on the DRI bulk optics setup.

- Enclosure of the experimental setup to eliminate air flow through the interferometer paths through manufacture of a custom plastic enclosure. This limits the effect of acoustic vibration and, air pressure and temperature changes
- Minimisation of path lengths to a reasonable extent. The bulkiness of the kinematic stages and magnetic bases restricts complete path length reduction but some care can be taken to minimise separation between components.
- Resolution, range and linearity measurements can be evaluated as fast as possible to reduce the effects of long term drift due to thermal expansion on these measurements.
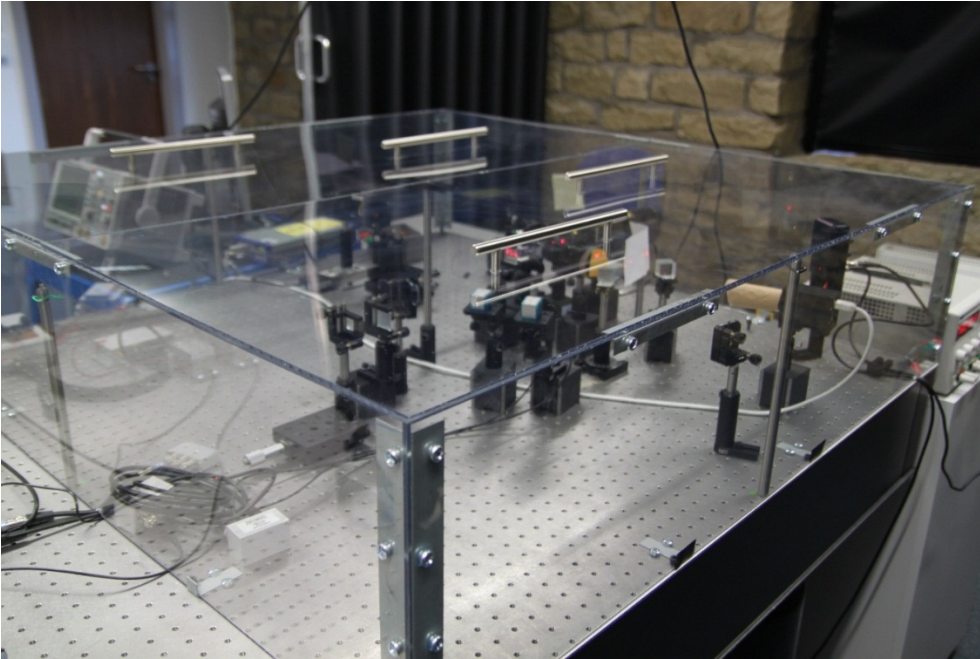
Figure 3.26: Environmental isolation of DRI using a custom enclosure.

With these changes enacted, the stability of absolute DRI position can be evaluated. The position of the measurement mirror is fixed so that the centre of the interferogram is at pixel 1024 after which 50 interferograms are captured over several seconds and the position of the interferogram point of symmetry calculated using autoconvolution. Next the mean of these centre positions as well as the standard deviation from the mean are calculated, with the equations in section 11.1.6 showing calculation of the standard deviation, σ. Repeating calculation of stability across the range of the interferometer is achieved by translating the measurement mirror by 50 and 100 µm.

Having calculated the interferogram stability for an unmodified interferometer the three improvements above are carried out before stability measurements are repeated. The results of such calculations are shown in table 3.3 to allow comparison of the standard deviation before and after alterations for stability. These corroborate the visual inspections of DRI interferogram stability which indicate inclusion of the plastic enclosure and path length minimisation reduces the standard deviation of autoconvolution results by over a factor of ten.

PZT Position (µm)	Before (1 s.d)	After (1 s.d)
0	0.664 pixels	0.039 pixels
50	1.001 pixels	0.032 pixels
100	0.745 pixels	0.085 pixels

Table 3.3: The standard deviation of the interferogram centre was measured at three positions of the PZT, with the 50 µm PZT position corresponding to an autoconvolution peak present on the central pixel of the detector. Improvements were then made to the DRI setup to limit environmental effects and then the standard deviation of the centre position measured again for each PZT location.

3.8 Absolute position by autoconvolution non-monotonicity

Another advantage of both simulation with Matlab and the use of the PZT in the experimental setup is that it is possible to change the OPD by increments smaller than the resolution of the DRI autoconvolution method. While confirming previously published works in sections 3.1 to 3.7 using a bulk optics interferometer it was not immediately apparent that with small increments of OPD the autoconvolution peak does not move linearly across the detector pixels as expected. This means that while the linearity across the entire range is as described in section 3.6.3, the resolution is lower than anticipated. This behaviour was first observed while using the PZT within the experimental interferometer, with figure 3.27 illustrating the oscillatory nature of data, where the blue and red traces show the interferogram centre position by max() function and peak fitting respectively.

The rather significant impact of the observed non-monotonicity is that until it is resolved, resolution of DRI autoconvolution is lower than the previously stated 279 nm. This effect is not observed or explained in existing spectral interferogram literature.
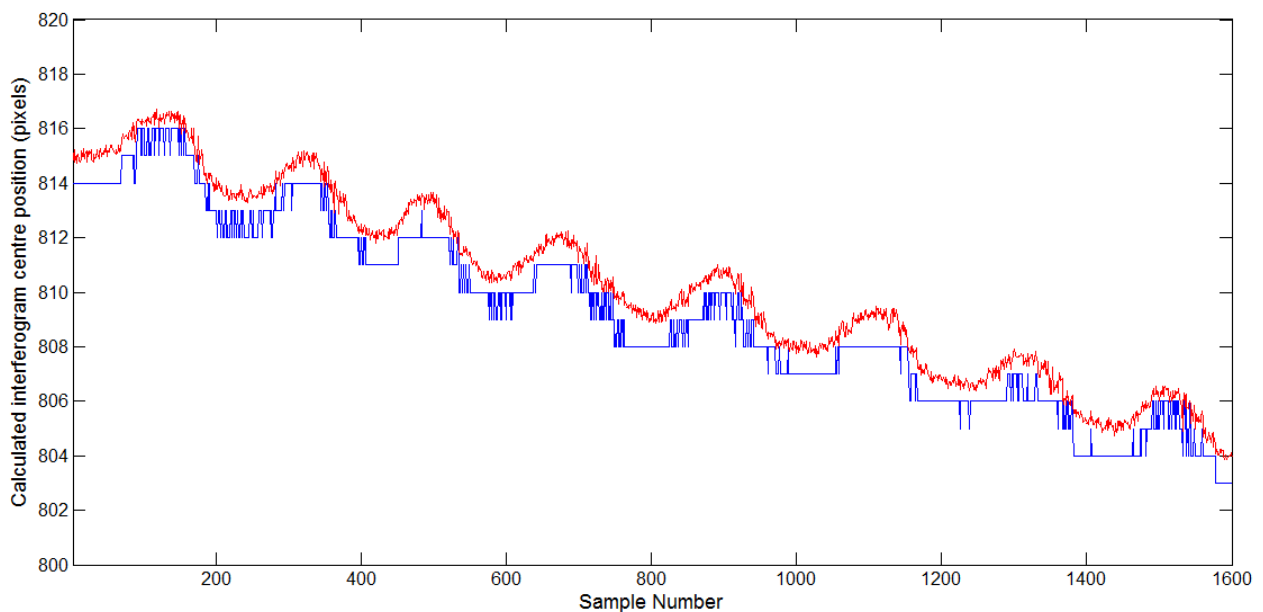
Figure 3.27: Graph showing calculated interferogram centre position change with measurement path length change. Pixel with highest autoconvolution result (blue) and sub-pixel result using peak fitting (red).

This is an excellent example of where having simulation and real measurement data whose results match well is highly advantageous to solving of physical problems. Upon discovery of this effect, it was not known if this was an error with the PZT, errors within the physical setup or a problem inherent with the chosen signal processing methods.

Important to correction of this oscillation is diagnosis of the cause. Through simulation with Matlab it can be determined if this non-monotonicity is a problem inherent with the signal processing methods used or if it is solely present in the real experimental data.

3.8.1 Non-monotonicity diagnosis through simulation

Using the discrete implementation equations described in section 3.5 allows generation of interferograms that closely match interferograms retrieved from the detector of the experimental bulk optics interferometer. Optical path difference is varied by changing the d term in equation 3.18. The simulated OPD is changed in 20 nm steps and the interferogram symmetry position calculated by max() function as well as peak fitting with the results displayed in 3.28 in blue and red respectively. The oscillations shown in the simulated data match the oscillations observed in the real data from figure 3.27. This demonstrates that the oscillations are inherent to the signal processing methods and are not an environmental or physical effect.
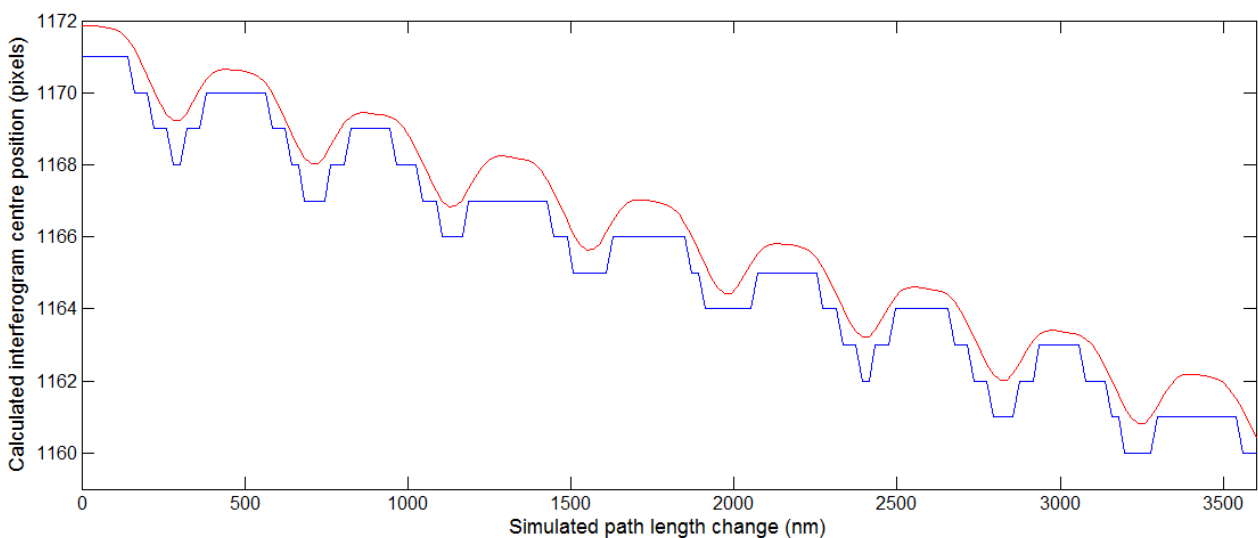
Figure 3.28: Autoconvolution result calculated with max function (blue) and peak fitting (red) for a range of simulated interferograms whose OPD changes in 20 nm increments over 3.5 μm.

3.8.2 Correction of simulated interferograms

With knowledge that the oscillations are inherent to the method, development of appropriate signal processing methods to limit these oscillations and return the absolute position encoding result to monotonicity is possible. Use of simulated interferograms for development of appropriate signal processing methods was chosen due to the lack of environmental effects (noise, DC offset, gain envelopes) on the interferograms as well as the quick turnaround to evaluate new methods.

The cause of the oscillations is hypothesised to be the changing intensities of the interferogram at the edge of the detector. As the instantaneous phase of the spectral interferogram changes while point of symmetry traverses the detector, the intensity at each edge of the detector varies at a different rate due

76

to the increasing frequency of the interference as distance from the stationary phase point increases. This is supported by the fact that while the DRI OPD is zero the interferogram is centred on the detector for which the intensity at the edges of the detector changes at the same rate. For a case such as this the non-monotonicity is not apparent for approximately 2 μm either side of 0 μm OPD.

As a first attempt to eliminate these oscillations for simulated interferograms, a Hanning window is applied to make the intensity near the edges consistent. A Hanning window is chosen since the intensity tends to zero at the edges, unlike a Hamming window which never reaches zero. Equation 3.23 details discrete generation of a Hanning window of length N.

$$\mathbf{w_H} = \left(w_{H1}, \cdots, w_{H\psi}, \cdots, w_{HN} \right)^T$$

$$\text{where } w_{H\psi} = 0.5 \left[1 - \cos \left(2\pi \frac{\psi}{N} \right) \right] \text{ and index, } \psi \in [1, 2, \cdots, N]$$

3.23
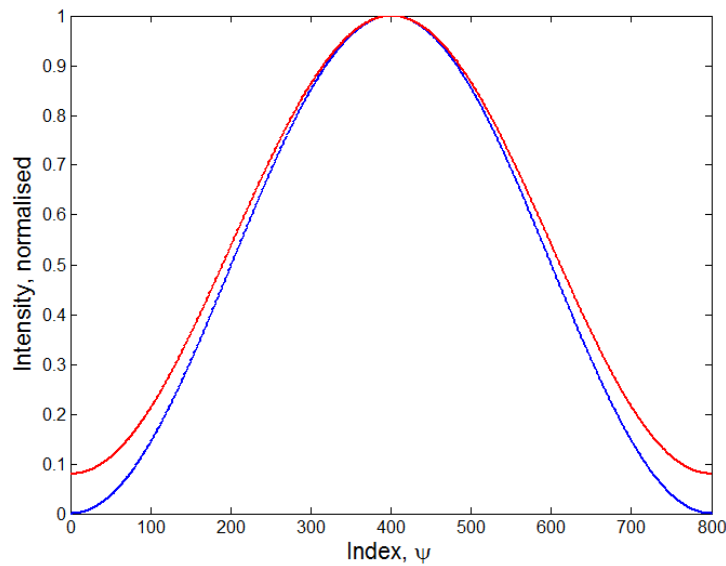
Figure 3.29: Comparison of a Hanning window (blue) with a Hamming window (red)

The Hanning window is next split so that the edges of the detector are attenuated to zero while the centre remains unmodified which allows correction across the entire range of the interferometer. The split Hanning window, $\mathbf{w_S}$, of length m is described as follows, with equation 3.24 re-indexing the Hanning window from equation 3.23 with a graph of the resulting window shown in figure 3.3:

$$\mathbf{w_S} = \left(w_{S1}, \cdots, w_{Si}, \cdots, w_{Sm} \right)^T$$

$$w_{Si} = \begin{cases} w_{Hi} & \text{if } i \leq \left(\dfrac{N}{2} \right) \\[3mm] 1 & \text{if } \left(\dfrac{N}{2} \right) > i < \left(m - \dfrac{N}{2} \right) \\[3mm] w_{H(i-m+N)} & \text{if } i \geq \left(m - \dfrac{N}{2} \right) \end{cases}$$

3.24
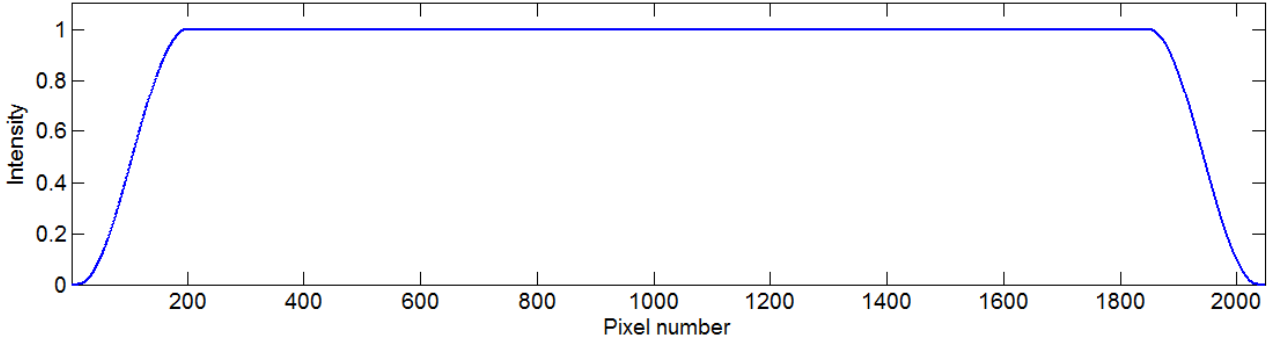
Figure 3.30: Split Hanning window described by equation 3.24.

This window, $\mathbf{w_S}$, and the simulated interferogram, $\mathbf{H}$, are then multiplied element by element as described in equation 3.25. This results in the vector $\mathbf{J}$ containing the windowed interferogram as shown in red in figure 3.31:

$$\mathbf{J} = \left(j_1, \cdots, j_i, \cdots, j_m \right) \text{ where index } i \in \left[1, \cdots, m \right]$$

$$j_i = w_{Hi} \cdot h_i$$

3.25
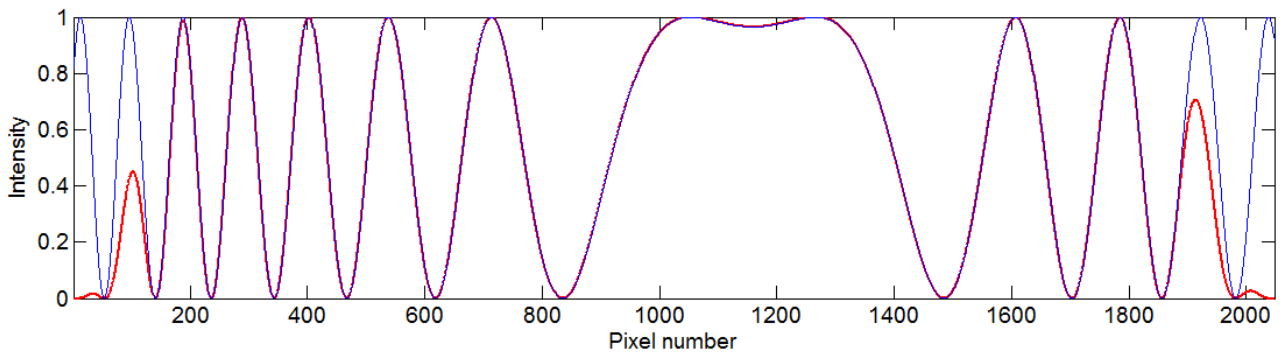
Figure 3.31: Original (blue) and Hanning windowed (red) simulated interferogram.

When this windowing operation is performed on multiple interferograms of increasing OPD, the effectiveness of windowing for centre position oscillation can be demonstrated. The blue trace in figure 3.32 is calculated from interferograms multiplied by the stretched Hanning window before

78

autoconvolution is calculated. It shows much improved monotonicity when compared to the entirely non-monotonic red trace for autoconvolution of non-windowed interferograms. It can be demonstrated that this improvement in autoconvolution result is present across the entire 300 μm range of the simulated interferometer.
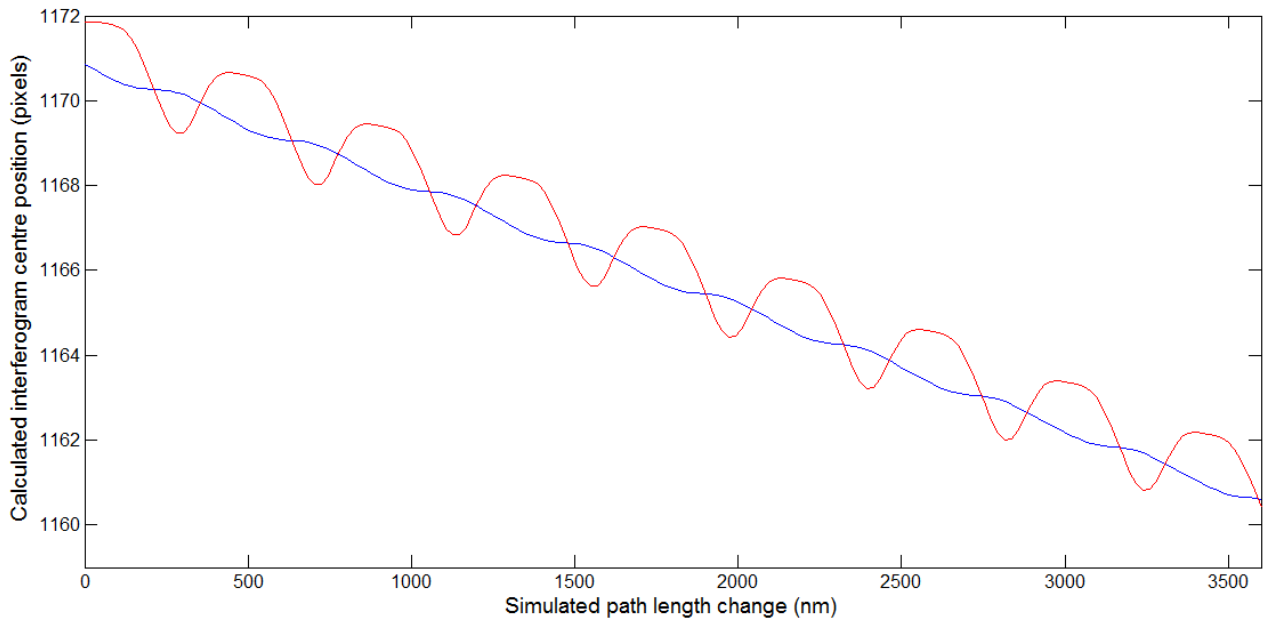
Figure 3.32: Autoconvolution fitted peak position for unmodified (red) and Hanning windowed (blue) series of interferograms.

Difficulties with this method are made apparent when a comparison is made between the simulated interferogram and a measured interferogram. Interferogram features such as DC offset, gain envelopes, noise, skew and distortion all exist in measured but not simulated interferograms. These can be seen on the left in figure 3.33.0.
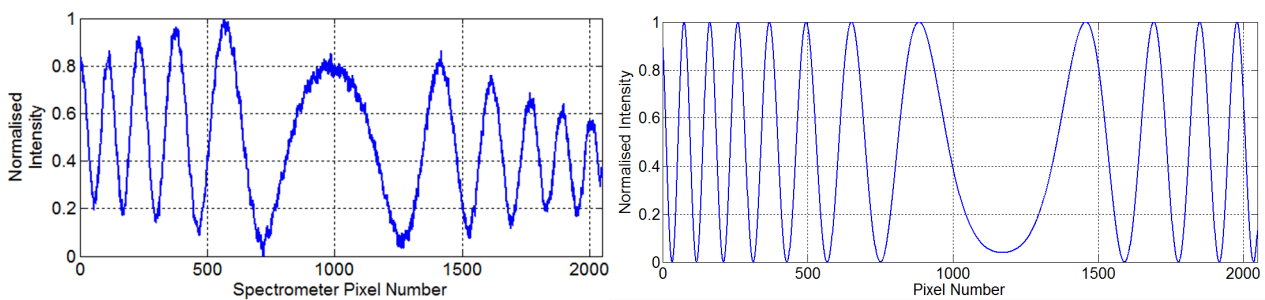
Figure 3.33: A real interferogram (left) and simulated interferogram (right) to aid visualisation of their differences.

Application of the stretched Hanning window to a set of measured interferograms does not result in correction of the non-monotonicity due to the differences between the measured and simulated interferograms. For this reason it is necessary to apply an additional signal processing step to measured interferograms before correction with windowing. This step to correct spectral interferogram shape is well described in the literature [97-101] and named regularisation and normalisation interchangeably.

79

3.8.3 Effect of regularisation on calculated centre position of real interferograms

A regularisation algorithm tailored to use with spectral interferograms is implemented in appendix 11.2. Use of this algorithm before application of the Hanning window has been demonstrated to substantially reduce the non-monotonicity of the measured autoconvolution result. The data presented in figure 3.34 demonstrates this effectiveness, showing the autoconvolution result of autoconvolution of unmodified interferograms (blue) and the autoconvolution of interferograms corrected with regularisation and a stretched Hanning window. To obtain this data, interferograms were captured as 20 nm OPD increments were applied over a 20 µm range. This value was chosen for increments as being far below the current resolution of DRI.
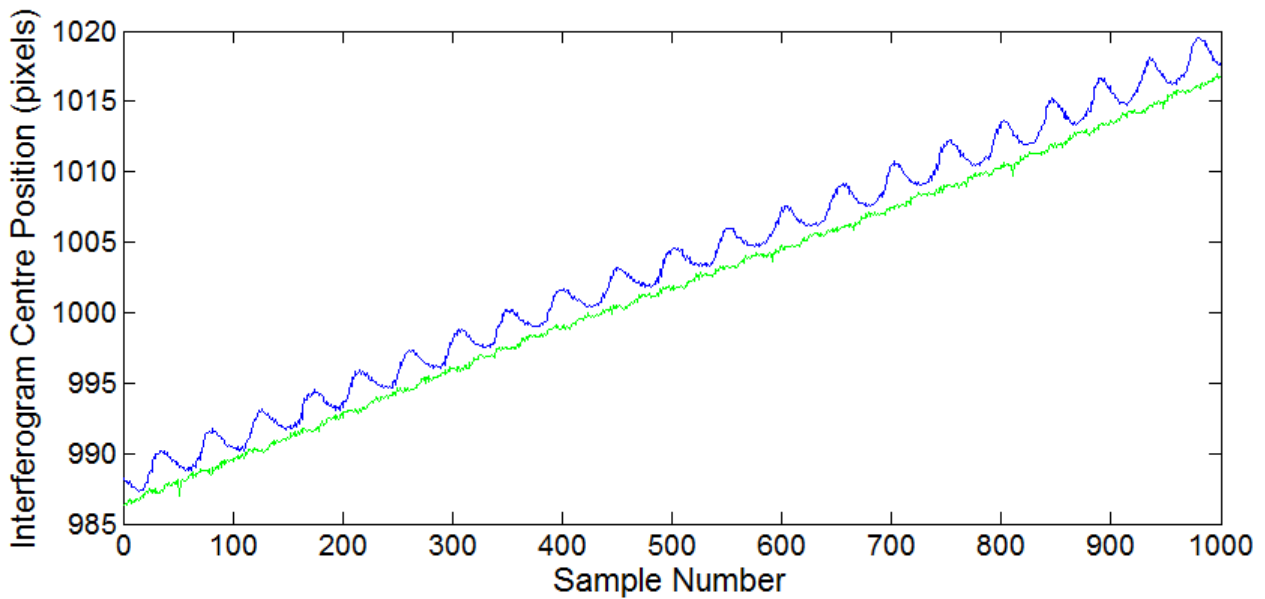
Figure 3.34: Comparison of autoconvolution of unmodified (blue) and windowed and regularised (green) interferograms. Elimination of non-monotonicity is obvious, improving the effective resolution of autoconvolution.

The windowed and regularised green trace shows far reduced oscillations and while there does appear to be small non-linearities it can now be said to be monotonic. This has been confirmed over the range of the interferometer.

3.9 Conclusions

This chapter has confirmed the ability of absolute position encoding by wavelength for DRI to provide single point measurement data over a range of 285 µm while achieving a vertical resolution of 279 nm or better. This results in a dynamic range of 1022 for a method which has been shown to be absolute in nature with capability of measurement for discontinuous surfaces allowing surface profiling of steps and voids.

Linearity has been evaluated to 0.53 % over a 100 µm range of DRI by changing of measurement mirror position with a precision PZT. A tenfold improvement in interferometer stability has been realised through

path length reduction and improved environmental isolation. This is expected to improve in the future based future work to increase measurement rates from 15 Hz and production of a more thermally stable instrument prototype.

Also addressed in this chapter is the discovered non-monotonicity of autoconvolution for small changes in optical path length. This is caused by the differently varying intensity of the interferogram at the detector edges. The oscillations introduced by interferogram imbalances resulted in a lower than expected resolution and so the causes of this have been investigated, with use of regularisation and windowing for correction of measured interferograms appearing novel to improve autoconvolution of spectral interferograms.

This work shows the ability of DRI to perform high range measurements, with changes to the spectrometer, light source and dispersion method expected to yield higher ranges. The current biggest limitation to the method is the low resolution when compared to alternative methods of single-point metrology. The resolution of 279 nm demonstrated by the implementation described by this chapter is not appropriate for many on-machine applications. A method of signal processing to make use of the phase data inherent in the spectral interferograms is necessary but has not been demonstrated in the existing literature on dispersed reference interferometry. Chapter 4 will explore the changing shape of the interferograms as small OPD changes are applied as well as investigate methods of signal processing to leverage this data with an aim to approach nanometre resolution measurement.

4 High resolution DRI – A signal processing scheme for extracting relative position encoding by phase.

4.1 Introduction

Improvement of DRI dynamic range is critical for it to become a meaningful method of embedded metrology. It is an interferometric method whose spectral interferograms inherently contain phase information. The high sensitivity of the interferogram phase to optical path length changes mean that with appropriate algorithms, nanometre axial resolution measurements are achievable without alteration to the DRI apparatus.

The phase difference between the arms of the interferometer varies with wavenumber due to the dispersion introduced in the reference arm. The wavenumber dependent phase results in a quadratic phase function such as that shown in figure 4.1.
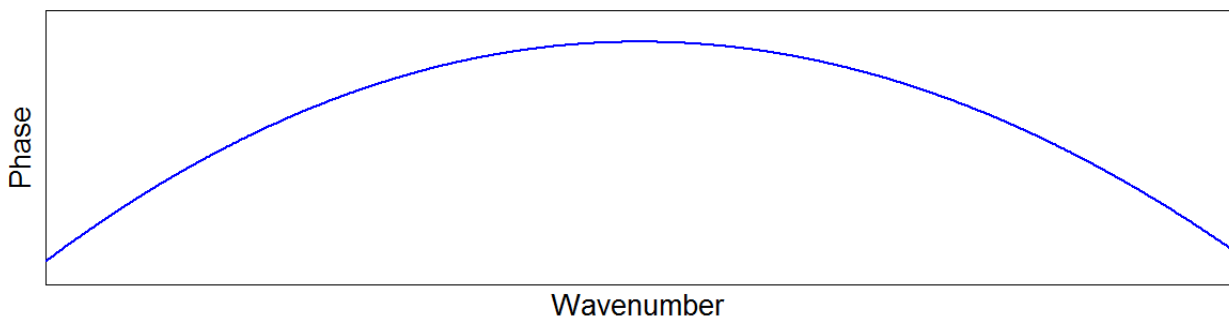
Figure 4.1: Quadratic phase function for DRI when the optical path difference is zero.

The interferometer equation shown below provides a spectral interferogram such as those seen in figure 4.2 when used with the quadratic phase above.

$$I(k) = 0.5\{1 + \cos[\phi(k)]\}$$

4.1

As the OPD changes, the local phase of the interferogram (at each pixel) will then change at a rate proportional to the wavenumber. The challenge therefore is to relate this changing local phase to physical changes in interferometer path length.

The presence of high resolution phase information is demonstrable by observing the shape of the interferogram symmetry position as measurement arm length changes are applied. The interferogram shape changes in a cyclic fashion as the phase difference between the arms of the interferometer changes with increasing OPD. Figure 4.2 illustrates this, with each interferogram shown having a simulated measurement arm length incremented by 40 nm from the last. Observe the increasing intensity of the interferogram point of symmetry (red line) for each increment of the measurement arm length.
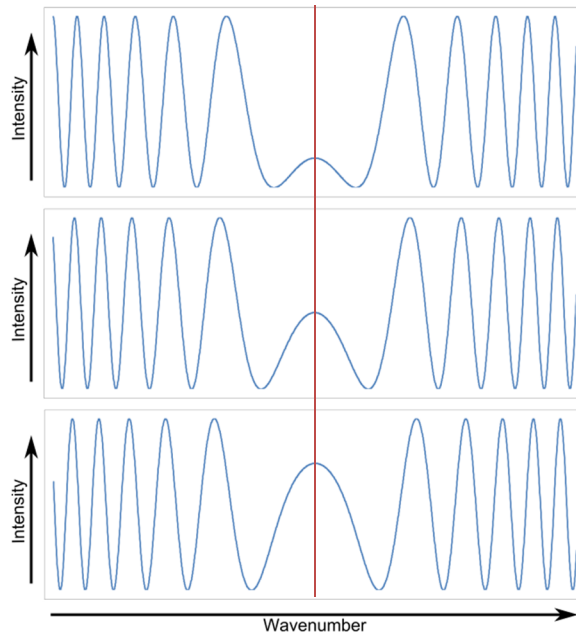
Figure 4.2: Change of SCDRI spectral interferogram with 40 nm changes in OPD

4.2 Template matching

Methods to isolate this phase change with OPD require the calculation of this central shape. The chosen method, template matching, is a technique originating from the fields of image recognition and computer vision [102-104] and provides a method for locating specific shapes/features within an image. Also known as cross-correlation matching, template matching has previously been used in white light interferometry to find the best matching theoretical interferogram to an experimental interferogram [105] achieving 10 nm resolution measurement over 100 µm, albeit very slowly.

In image processing, template matching is a method used to locate image subsets within a larger image. This is achieved by comparing the image subset of interest, also known as a template, with many masks of the parent image by calculating the correlation coefficient of the template and each mask of the original image. This builds up a 2d array of correlation values where values approaching 1 indicate strongest likeness of the template to the image subset. If the size, tilt or rotation of the searched for image is likely to vary, multiple templates each differing in scale, tilt or rotation are used to locate the most likely match in the most likely position within the source image. Alternative methods of feature recognition such as scale-invariant feature transform (SIFT) and rotation-invariant feature transform (RIFT) are often now preferred to template matching due to their reduced computational overheads and intolerance to skew, rotation and scale when compared to template matching.

However, spectral interferograms resulting from DRI benefits from two key features which drastically reduce the computational load of determining the interferogram shape when compared to traditional

image processing applications, making template matching a viable option for high axial resolution measurement with DRI. First, as described in chapter 3, autoconvolution is used to detect the position of the interferogram point of symmetry. This eliminates the necessity of searching for the location of a region of interest – the location of the interferogram centre is known, the problem becomes simply which template is it that best matches the interferogram shape. Second, and most importantly, DRI interferograms are single dimensional, drastically reducing the degrees of freedom over which the matching must occur.

4.3   Template matching implementation

Template matching requires the generation of suitable template data representing interferograms from the DRI at pre-defined OPDs. Once created, the template set is then compared with a spectral interferogram captured from the physical DRI apparatus. The surface height of the DRI can then be determined by calculating the template interferogram whose shape matches that of the measured interferogram most closely. The generation of the template interferogram set is performed through the use of a simulation, representing the physical DRI apparatus, and based upon equations 3.16 to 3.19 in section 3.5.

4.3.1   Generating a template interferogram set

A set of n template interferograms are created using the DRI equations introduced in section 3.5. This implementation differs from that of section 3.5 in that it results in a matrix containing simulated interferograms having an OPD which increments by d for each subsequent interferogram. To reduce the signal processing overhead, template interferograms need not be the full length of the detector, it is sufficient to match shorter template interferograms to a subset of the measured interferogram, centred around the interferogram point of symmetry. This has the added benefit that the same set of template interferograms can be used regardless of the position of the interferogram point of symmetry, simplifying template generation and reducing signal processing time. The signal processing necessary to generate a set of template interferograms is as follows:

First, a column vector, $\mathbf{k}$, of length m is used to represent the discretised angular wavenumbers as follows over the detector length,

$$\mathbf{k} = \left(k_1, \cdots, k_i, \cdots, k_m\right)^T \quad \text{where } k_i = \left(k_L + \frac{\Delta k}{m}\right)$$

and index, $i \in \{1, 2, \cdots, m\}$

4.2

A vector, $\mathbf{r}$ containing the wavenumber dependent optical path, is calculated as follows where L is the perpendicular separation of the gratings and D is the diffraction grating pitch.

$$\mathbf{r} = \left(r_1, \cdots, r_i, \cdots, r_m \right)^T \text{ where } r_i = \frac{L}{\sqrt{1 - \left(\dfrac{2\pi}{k_i D} \right)^2}}$$

4.3

An m by n phase matrix, $\mathbf{P}$, can then be defined containing the phase function for DRI at each OPD used to generate the templates where m is the number of pixels, and n is the number of template interferograms. Each column in the matrix then contains the phase function at a particular OPD where the OPDs of successive columns, j, progress by the template spacing, d, for which an initial value of 1 nm is used.

$$\mathbf{P} = \begin{pmatrix} p_{1,1} & \cdots & p_{1,n} \\ \vdots & \ddots & \vdots \\ p_{m,1} & \cdots & p_{m,n} \end{pmatrix} \text{ where index, } j \in [1, 2, \cdots, n]$$

$$p_{i,j} = 2k_i \left[r_i - \alpha \left(k_i - k_c \right) - l - d_0 - jd \right]$$

4.4

The template interferogram dataset is then calculated column-wise. The resulting m-by-n matrix, $\mathbf{H}$ contains n normalised template interferograms each of length m,

$$\mathbf{H} = \begin{pmatrix} h_{1,1} & \cdots & h_{1,n} \\ \vdots & \ddots & \vdots \\ h_{m,1} & \cdots & h_{m,n} \end{pmatrix} \text{ where } h_{i,j} = 0.5 \left[1 + \cos \left(p_{i,j} \right) \right]$$

4.5

Each individual template interferogram, $\mathbf{H}_j$ represents a simulated interferogram across the entire wavenumber range, Δk. For the template matching procedure to operate it is not necessary to match the entire template interferogram with the captured interferogram. It is sufficient to compare a subset of the interferogram centred about the point of symmetry. This is beneficial since a reduced number of template interferograms, shorter in length, can be generated. This means that the template matching procedure continues to operate effectively as the wavenumber at which the point of symmetry, k_v, occurs changes throughout the measurement range of DRI. This has the added benefit of making the template matching process less computationally intensive.

In order to crop the calculated template interferograms, a rectangular window is applied centrally around the interferogram point of symmetry. First, autoconvolution is used to calculate the point of symmetry of each individual template interferogram, $\mathbf{H}_j$, with the resulting convolution results stored in a $2m-1$ by n matrix, $\mathbf{C}$.

$$\mathbf{C} = \begin{pmatrix} c_{1,1} & \cdots & c_{1,n} \\ \vdots & \ddots & \vdots \\ c_{2m-1,1} & \cdots & c_{2m-1,n} \end{pmatrix} \text{ where index, } q \in [1, \cdots, 2m-1]$$

4.6

$$c_{q,j} = \sum_{i=1}^{2m-1} h_{i,j} \cdot h_{(q-i),j}$$

Next, the index of the maximally valued element of each column vector, $\mathbf{C}_q$, is calculated. Each of these n values is divided by two and rounded down to the nearest integer since the length of the autoconvolution result is twice that of the interferogram. This allows the index of the autoconvolution peak to denote the centre of the interferogram. The index of each template interferogram point of symmetry is stored in a vector, $\mathbf{a}$, of length n. To complete the creation of the set of cropped template interferograms, represented by a W_t by n matrix named $\mathbf{H}'$, a rectangular window of odd length W_t centred on the index value, a_j is applied to each column vector $\mathbf{H}_j$. The operation can be represented as follows,

$$\mathbf{H}' = \begin{pmatrix} h'_{1,1} & \cdots & h'_{1,n} \\ \vdots & \ddots & \vdots \\ h'_{T,1} & \cdots & h'_{T,n} \end{pmatrix} \text{ where index, } z \in [1, \cdots, W_t]$$

$$h'_{z,j} = h_{\beta,j} \text{ where index, } \beta = z + \left(a_j - \frac{W_t}{2} \right)$$

4.7

The four simulated interferograms in figure 4.3 represent OPDs separated by 40 nm with the symmetry position illustrated by the red line. The subsequent square envelopes described by equation 4.7 are shown in pink, with the subsection of the interferograms within this highlighted area becoming the matrix $\mathbf{H}'$.
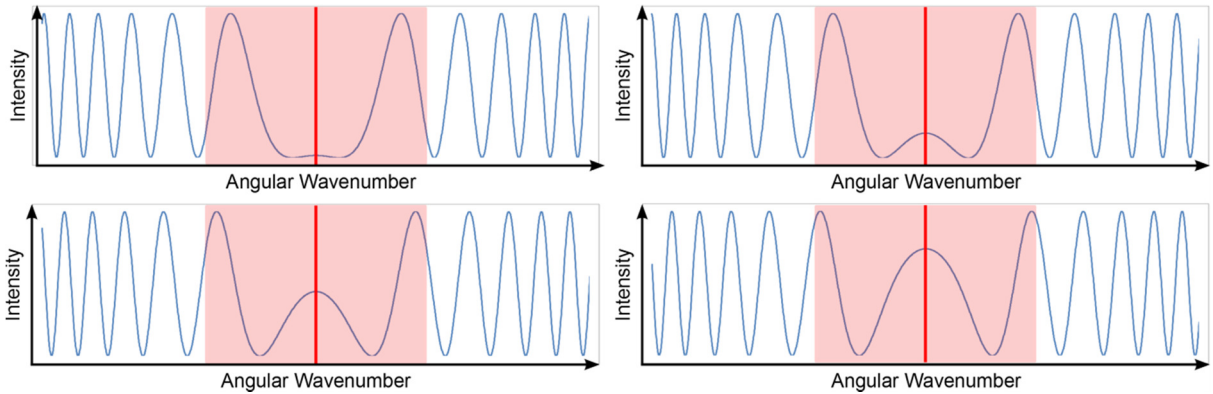
Figure 4.3: Representation of four template interferograms with the cropped portion highlighted.

4.3.2 Surface height calculation with template matching

The template interferograms are created to match the parameters of the acquired interferogram from the DRI apparatus in terms of wavenumber range, Δk and number of samples, m. The interferogram measured by the apparatus can thus be represented by a vector $\mathbf{g}$ of length m having been sampled at angular wavenumbers defined by the vector, $\mathbf{k}$. The acquired interferogram is cropped by applying the

same windowing process as described in equations 4.6 and 4.7 yielding a vector $\mathbf{g}'$ of length W_t. An example of a measured interferogram, $\mathbf{g}$, (blue) the square window (red) and the resulting rectangular windowed interferogram $\mathbf{g}'$ are shown in figure 4.4.
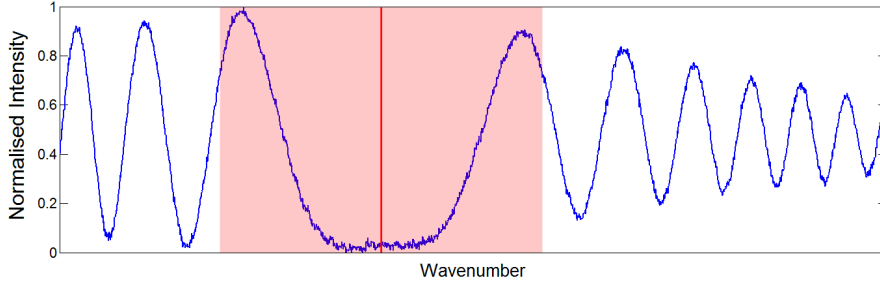
Figure 4.4: Interferogram acquired from the DRI apparatus with windowed portion highlighted.

Template matching is now performed in order to determine the DRI phase represented by the captured interferogram, $\mathbf{g}$. To achieve this, the correlation coefficient is calculated for the acquired cropped interferogram, $\mathbf{g}'$, and each of the n template interferograms, resulting in a vector, $\mathbf{r}$ of length n.

$$\mathbf{r} = \left(r_1, \cdots, r_j, \cdots, \mathbf{r}_n \right) \text{ where } r_j = \frac{\text{cov}\left(\mathbf{H}'_j, \mathbf{g}' \right)}{\sigma_{\mathbf{H}'_j} \sigma_{\mathbf{g}'}} \qquad 4.8$$

The closest matching template interferogram is now simply $\mathbf{H}'_j$ where j is the index of the maximally valued element of the vector, $\mathbf{r}$. The index, j_p, is taken as the position of the interferogram. A typical correlogram resulting from correlation between 800 templates having a 1 nm OPD spacing and a measured interferogram is shown in figure 4.5.
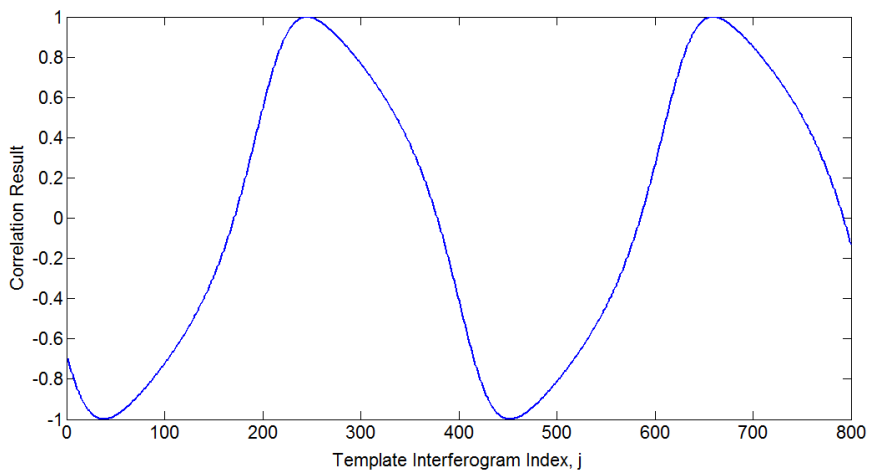
Figure 4.5: Correlogram formed by vector, $\mathbf{r}$, comprised of the correlation coefficient calculated between a measured interferogram and each of n template interferograms.

Template matching tracks the shape of the centre of the interferogram, which changes in a cyclic nature. This leads to a final difficulty before a robust solution to high resolution relative measurement can be realised. The phase difference between the arms of the interferometer progresses as the measurement arm length increases and as this happens a new peak forms at the left of the correlogram. The problem arises when the index of template interferograms at which this peak occurs continues to increase and a choice must be made between which correlogram peak is the correct one. For measured interferograms this is exacerbated by interferogram noise which makes it possible for the two peaks to have minutely different amplitudes.

The solution is to use a peak detection algorithm to calculate the position of both correlogram peaks instead of defining the index of the highest peak as surface position. After peak detection the surface height is calculated by relating the index at which the first peak occurs, j_p, to the template OPD spacing, d, as follows:

$$z = d \cdot j_p \tag{4.9}$$

Figure 4.6 illustrates the elimination of surface height wraparound errors when using peak detection (blue) to calculate the correlogram peak index and the improvement from simply calculating the maximum amplitude (red). Calculating index of maximum correlation with a peak detection algorithm has an added benefit of providing fractional template index data, effectively increasing the resolution of the method.
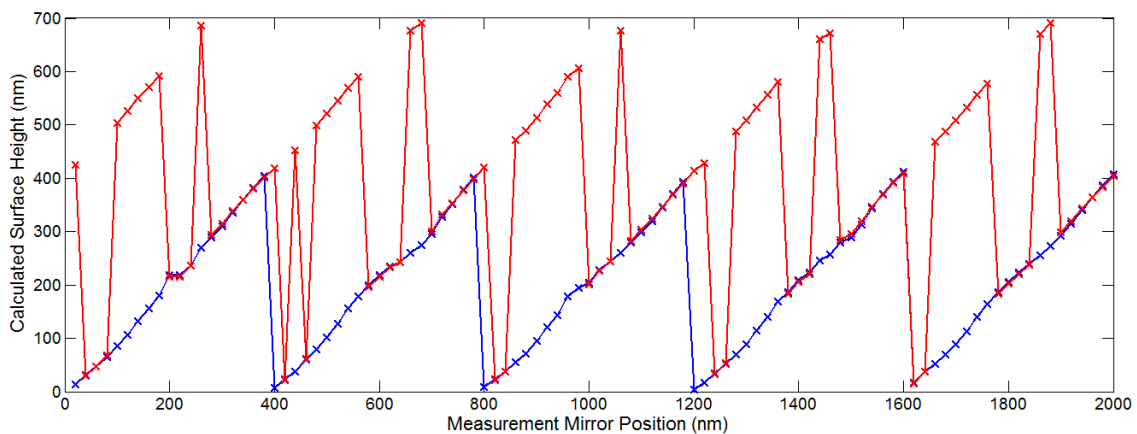
Figure 4.6: DRI apparatus measurement arm length increased in 20 nm increments and surface height calculated with (blue) and without (red) correlogram peak fitting.

The surface height wraparounds shown in figure 4.6 occur for every OPD change of half the wavelength at the phase vertex. These wraparounds can also be seen in the following graph which shows template matching used on a set of simulated interferograms whose OPDs increment by 5 nm.
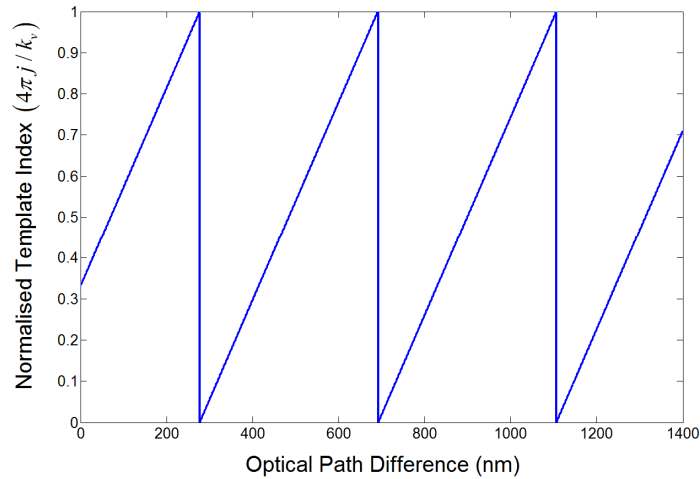
Figure 4.7: Graph of calculated template matching index for 280 simulated interferograms over a 1400 nm OPD change in 5 nm increments.

4.4   Template matching simulated results

This section describes the use of simulated spectral interferograms to evaluate the range, resolution and linearity of the template matching method introduced in section 4.3. The lack of noise, skew, DC offset and Gaussian envelope which are present in the physical DRI apparatus mean that the resolution, range and linearity of template matching may be evaluated for an ideal case.

4.4.1   Wraparound linearity

The linearity of individual surface height wraparounds is examined by generation of a set of interferograms with OPDs which span a single wraparound. It is important to ensure that this linearity is consistent across the entire range of the interferometer and so this is repeated for a set of interferograms with a point of symmetry at the left, centre and right of the detector. To implement this, 80 interferograms are created with 10 nm OPD increments across a range of 800 nm, resulting in at least one full wraparound when the surface height is calculated using template matching. The start and end points of this phase wraparound are then located manually and a line of best fit applied. The linearity of template matching in different ranges of the interferometer is examined by calculating the residuals from the increasing phase and a line of best fit to the same data. Figure 4.8 shows the shape of the interferograms at the start of each of the three interferogram sets, with these having OPDs of +150 μm, 0 μm and -150 μm respectively.
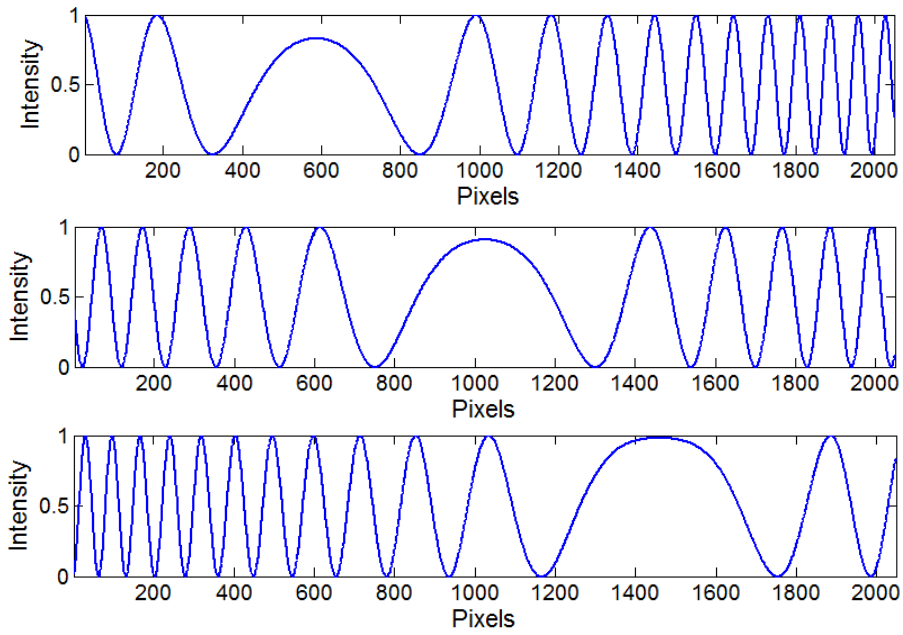
Figure 4.8: Interferogram examples from the data sets used to calculate phase wraparound linearity across the interferometer range. The OPDs of the interferograms from top to bottom are +150 μm, 0 μm and -150 μm respectively.

Figure 4.9 illustrates the template matching result for one set of wraparound data, with the OPD starting at 150 μm and increasing to 150.425 μm in steps of 10 nm. This is shown in blue, with a first order polynomial fit to the data included in red.
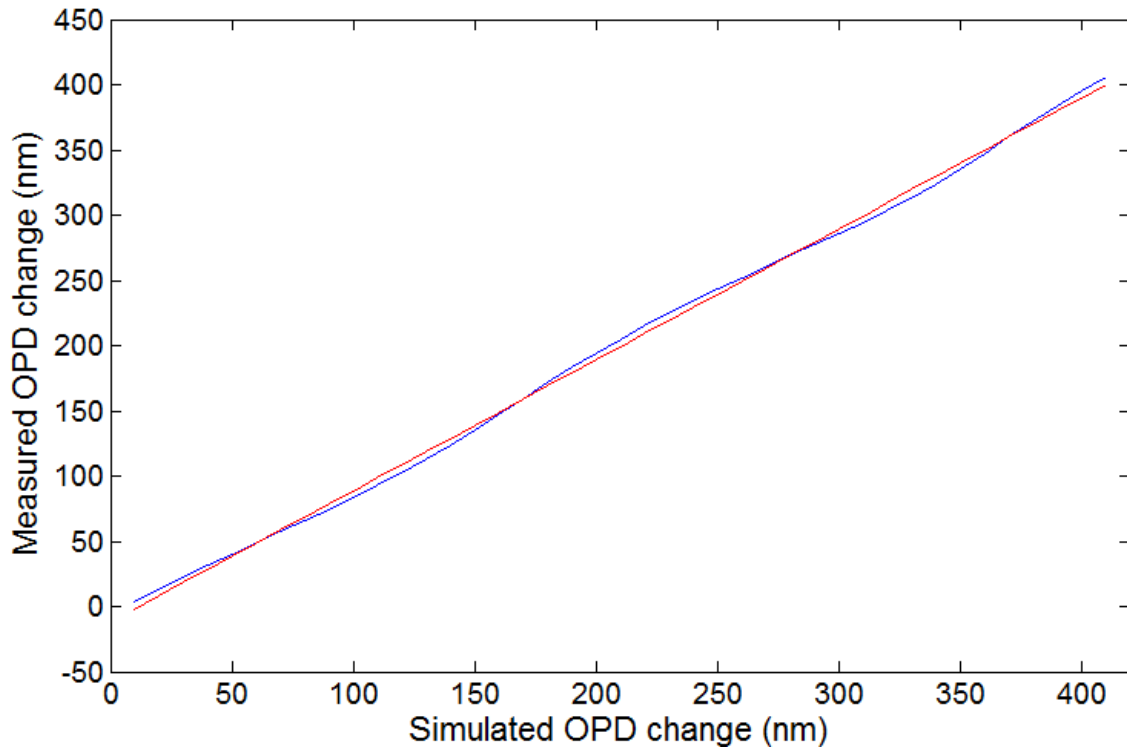
Figure 4.9: Template matching result (blue) calculated with peak fitting for a set of data with an OPD starting at 150 μm and increasing to 150.4 μm in steps of 10 nm. A first order polynomial fit to the phase data is included (red) to show deviation of the template matching method from ideal linearity.

90

Subtraction of the linear fit from the phase data results in the residuals seen in figure 4.10 and are indicative of the non-linearity of the method. From this the standard deviation, maximum and minimum values are calculated to allow comparison of the quality of the method across the range of the interferometer.
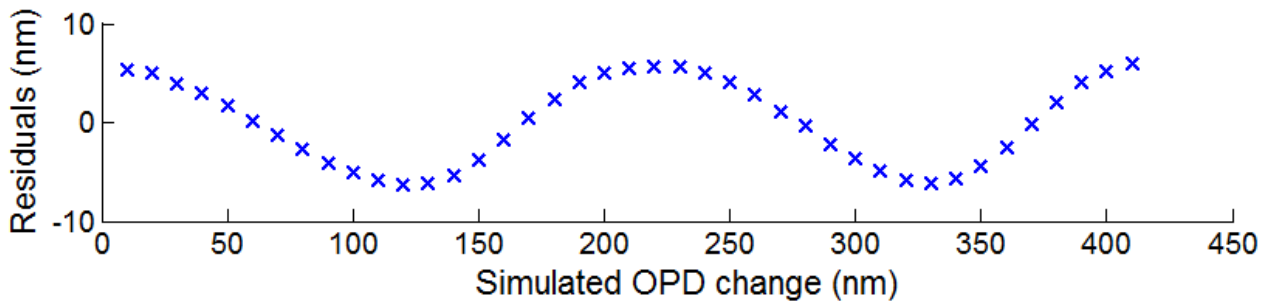
Figure 4.10: Phase residuals obtained from subtraction of phase data from line of best fit, showing phase deviation from ideal linearity for a phase wraparound starting at an OPD of +150 µm.

While performing these calculations it was noticed that peak fitting to the correlogram to attempt to obtain sub-template resolution results in a less linear phase wraparound shape than simply finding the best matching template using a simple max() function. To avoid the wraparound errors illustrated by figure 4.6, the approximate position of the first peak will be calculated using peak fitting after which the maximally valued index within 30 templates of this is then taken as the best matching template. This reduces the non-linearity introduced by using peak fitting to find the best matching template, a comparison of which is provided in table 4.1. The comparison is repeated for wraparounds at OPDs of - 150 µm, 0 µm and +150 µm.

OPD	Peak fitting method std. dev. (nm)	Max() method std. dev. (nm)
+150 µm	4.31 nm	1.57 nm
0 µm	3.61 nm	0.77 nm
-150 µm	4.49 nm	1.74 nm

Table 4.1: Standard deviation of residuals for after line of best fit is subtracted from a single template matching wraparound.

Table 4.1 shows the non-linearity of the peak finding method for determining best matching template. It also highlights the decreased linearity of the template matching method near the edges of the interferometer range. It is probable this is caused by the current method not accounting for the changing wavelength across the interferometer detector. While the max() method of correlogram peak finding does not calculate phase to sub-template resolutions, the improved linearity over the peak finding method is attractive.

4.4.2 Full scale linearity

To calculate the theoretical full scale linearity of template matching, interferograms covering an OPD range from -150 μm to +150 μm were created with 50 nm OPD increments. Template matching was then used to calculate the high resolution position of each of the 6000 interferograms and then a simple unwrapping algorithm (see appendix 11.1.7) was used to resolve the position wraparounds. Unwrapping is necessary due to the relative nature of the method, with the 50 nm step size chosen as a trade-off between steps per wraparound and the computational intensity of such a large number of interferogram calculations. Using the unwrapped position values, a linear fit is calculated and then subtracted from the unwrapped data to provide the residuals shown in 4.11.
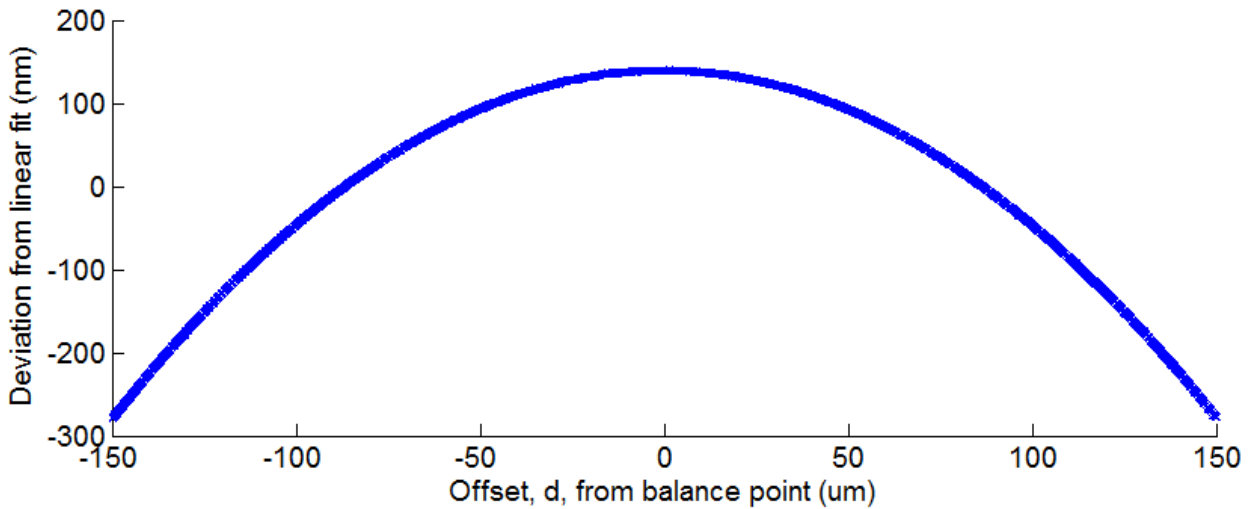
Figure 4.11: Deviation from line of best fit by unwrapped template matching position data. This covers a 300 μm range of simulated interferograms each with a 50 nm increment in OPD.

The key statistics for this data are the maximum deviation from linear fit (279.6 nm), the peak to peak deviation from linear (419.6 nm) and the standard deviation of the residuals (124.8 nm). It is probable that this non-linearity across the range is due to the simplistic phase unwrapping algorithm used. For this simple unwrapping the multiplier used to increase the wraparound order is constant at half the central wavelength, $0.5\lambda_c = 414$ nm.

As a means to improve the full scale linearity, consideration of the wavelength at which the interferogram symmetry occurs will lead to an unwrapping implementation where the wraparound multiplier increases with wavelength. For simulation, this is easily calculated using the discretised wavenumber of the detector and conversion of the balance wavenumber, k_v, to wavelength, λ_v, instead of using the central wavelength, λ_c. A vector containing the discretised wavelength range is created from the wavenumber range used during interferogram creation:

$$\boldsymbol{\lambda} = \left(\lambda_1, \cdots, \lambda_i, \cdots, \lambda_m \right)$$
$$\lambda_i = \frac{2\pi}{k_i}$$

To calculate the wavelength compensated unwrapped measurement position for a set of interferograms, the wraparound order for the position of each interferogram is calculated as per appendix 11.1.7, resulting in a vector $\boldsymbol{\omega}$ of length W_f. The centre of each of the interferograms has previously been calculated during the template matching process, with the resulting indices stored in a vector, $\mathbf{a}$, also of length W_f. These combine to provide an unwrapping multiplier for each of the high resolution surface positions in vector $\mathbf{f}$ as follows:

$$\boldsymbol{\gamma} = \left(\gamma_1, \cdots, \gamma_s, \cdots, \gamma_{W_f} \right)^T \text{ where } \gamma_i = 0.5 \cdot \lambda_{(a_i)} \text{ and index, } s \in \left[1, \cdots, W_f \right]$$

after which unwrapping is achieved by multiplication of the wraparound order of each surface position, $\boldsymbol{\omega}$, by the wavelength dependent unwrapping multiplier, $\boldsymbol{\gamma}$, and addition of the relative position data $\mathbf{f}$:

$$\mathbf{u} = \left(u_1, \cdots, u_s, \cdots, u_{W_f} \right)^T \text{ where } u_s = \left(\gamma_s \cdot \omega_s \right) + f_s$$

While more complicated than the simple unwrapping algorithm, the signal processing overheads are minimal due to previous calculation of the autoconvolution during template matching. Subtraction of the line of best fit from the unwrapped template matching data provides the residuals shown in figure 4.12. The addition of wavelength compensation to the unwrapping algorithm provides improved peak to peak non-linearity of 7.53 nm, with the residuals from the line of best fit having a standard deviation of 0.65 nm, an improvement of a factor of 100 compared to the non-corrected unwrapping. In the case of simulation, the wavelength of each of the pixels is known explicitly due to its use during interferogram calculations. For a real DRI implementation, calibration of the spectrometer will allow similar operation.
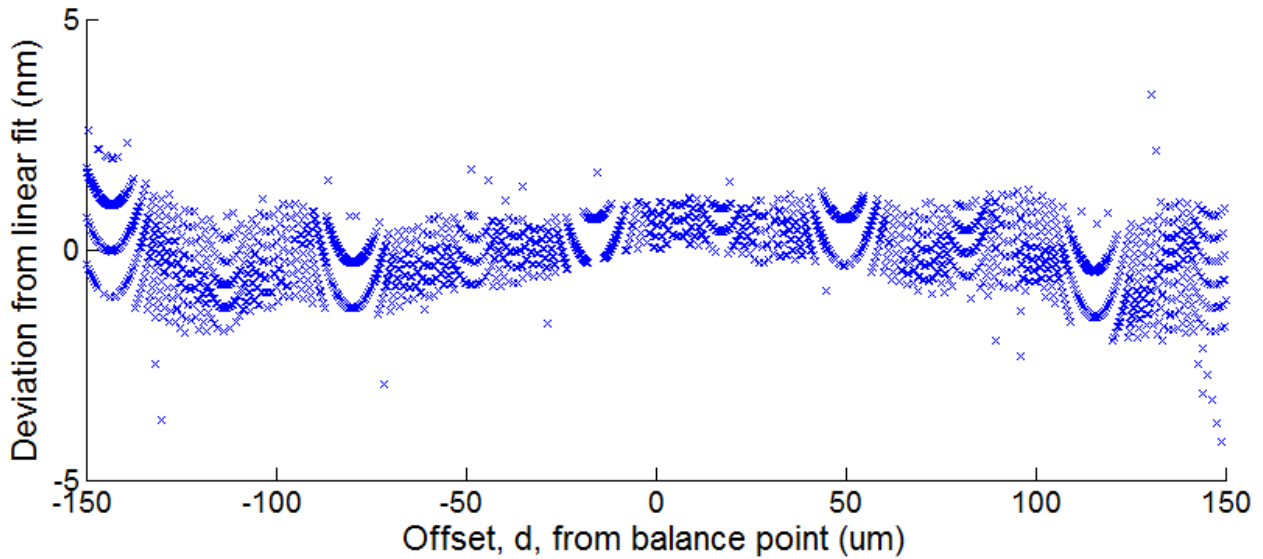
Figure 4.12: Residuals from a line of best fit to unwrapped phase over a range of 300 μm. The wavelength at which the balance point occurs is taken into account when applying phase unwrapping to reduce the non-linearity demonstrated in figure 4.11.

4.4.3 Resolution

The ability of the template matching to resolve small changes in OPD is important to determine the axial resolution of the instrument. In a real interferometric system, optical, electrical and mechanical noise will limit achievable resolution, but for a simulated interferometer lacking these sources of noise, it is possible to determine the effect of template spacing, wavelength and detector pixel count on the template matching method.

Template spacing: Sub-template resolution calculations by peak fitting have been eliminated as a possible resolution improving method due to their non-linearity. The effect of template spacing and count on resolution is discussed below.

To assess the effect of template OPD separation on resolution three sets of template interferograms are generated having counts and separations resulting in a template set whose range covers over 1 phase wraparound, typically 800 nm to be conservative. The characteristics of each of the sets of template data are shown by table 4.2. Each template set was then used to calculate the phase for 1000 simulated interferograms having 0.1 nm OPD separation and covering a range of 100 nm.

Template count,	Template OPD separation,
400	2 nm
800	1 nm
8000	0.1 nm

Table 4.2: Table showing template sets evaluated to study the effect of template spacing on template matching resolution.

94
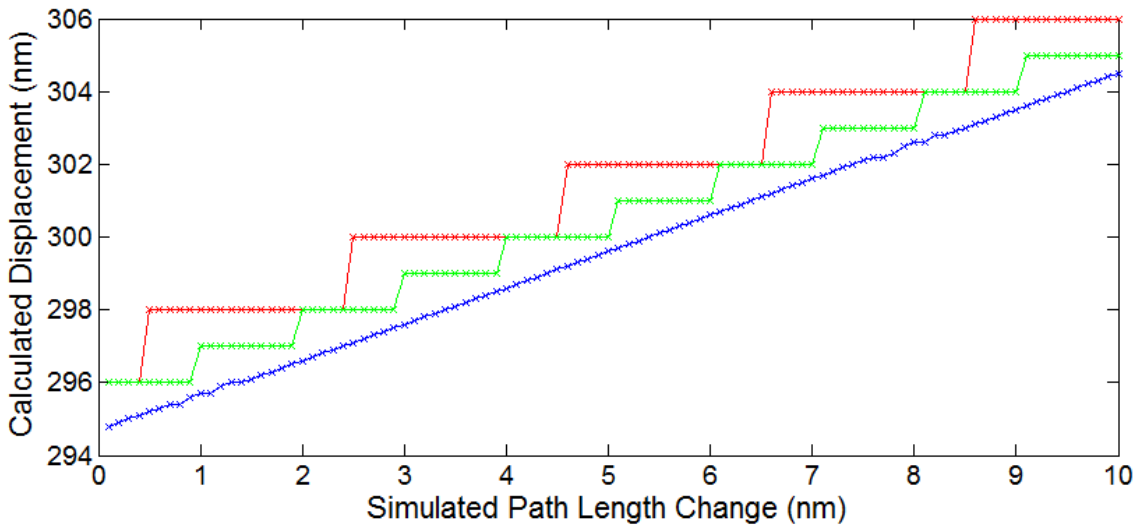
Figure 4.13: Graph showing the effect on resolution of using 8000 templates with 0.1 nm spacing (blue), 800 templates with 1 nm spacing (green) and 400 templates with 2 nm spacing (red).

This graph shows that decreasing the template spacing while increasing the template count will increase the attainable resolution of the template matching method for ideal interferograms. It is probable that environmental noise in the practical apparatus will limit this resolution. A template count of 800 with a spacing of 1 nm will be used since this spacing and template count offers an acceptable initial trade-off between resolution and computational intensity.

4.4.4   Range

The overall range of template matching is expected to be similar to that of absolute position encoding by wavelength due to the reliance of template matching on autoconvolution to locate the interferogram centre. The relative nature of template matching results in the requirement of tracking and unwrapping the surface position during measurement, while any discontinuity in the surface will cause loss of measurement position and thus phase order error.

The range over which phase can be tracked is limited by three factors, two of which are common to absolute position measurement encoding by wavelength.

First, the length of the rectangular window applied to the measured interferogram has a limiting impact on range. This is necessary to allow the interferogram length to match that of the template interferogram. As the interferogram centre approaches the edge of the detector the window width must either reduce or the range be limited to prevent vector index out of bounds errors between the rectangular window and the interferogram.

Second, the ability of the autoconvolution algorithm to detect interferogram centre deteriorates as the centre approaches the detector edges, limiting where the window can be applied due to the reliance of rectangular windowing on interferogram symmetry position.

95

Lastly, the physical attributes of the bulk optics interferometer (wavelength dependent path length, source wavelength and bandwidth) influence the interferogram shape and the rate of change of interferogram centre position with OPD change.

Since the range of template matching is reliant upon absolute position encoding by wavelength, then the theoretical range of template matching for the key attributes outlined in section 3.3 (grating pitch, grating separation and wavelength) is the same as for absolute position by wavelength encoding, 360 µm. This, for a grating pitch of 3.3×10^{-6} m, a grating separation of 330 mm and a 3 dB bandwidth of 25 nm with a centre wavelength of 820 nm. For these parameters, the autoconvolution deteriorates before the halfwidth of the template matching square window reaches the edge of the detector making autoconvolution the limiting factor for the template matching method range.

4.5   Practical implementation for template matching in DRI

To assess the ability of template matching to perform high resolution measurement in the experimental DRI apparatus, a setup identical to that in section 3.3 was used. To briefly summarise, the position of the measurement mirror in the bulk optics Michelson interferometer is translated along the Z axis by a high resolution PZT having a range of 100 µm and a resolution of 0.7 nm. In this case the motion control and template matching algorithm are performed in real time with Labview.
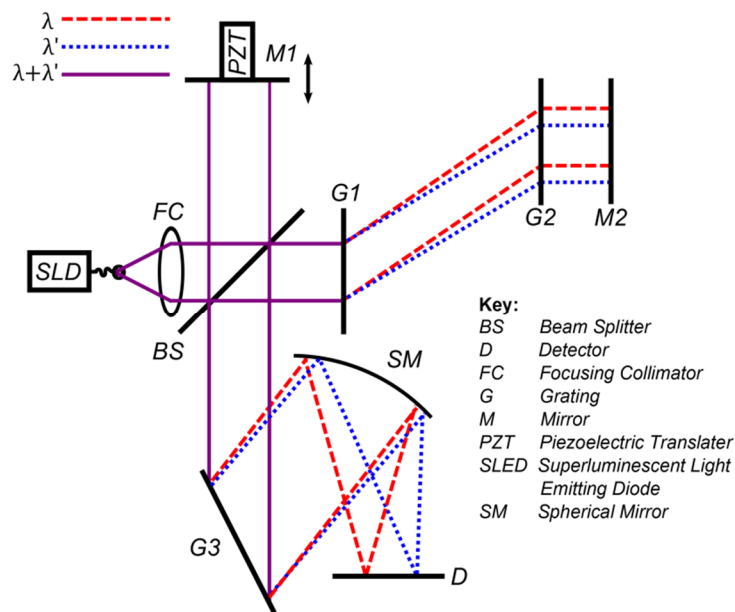
Figure 4.14: Schematic illustrating the physical DRI apparatus used to assess template matching performance.

The template matching method described by 4.2 to 4.8 results in displacement for a single interferogram. In order to assess the resolution and range of this method, these calculations must be repeated for multiple measured interferograms while incremental position changes of the PZT are applied. It is important to repeat at this point, that the PZT is not intrinsic to the measurement method, but a useful

tool to allow analysis of DRI performance for a range of OPDs without introducing problems associated with scanning samples in a single point method.

Figure 4.15 shows an initial result from the bulk optics interferometer. In this graph the axial position of the measurement mirror has been translated in 10 nm increments every 500 ms while the Labview VI calculates the template index at its maximum rate. It is possible to see these steps within the graph as well as some regions of noise, likely from mechanical disturbances within the optics lab. This graph also confirms previous work by simulation which indicated the relative nature of phase calculation by template matching, with a wraparound occurring every nm change in OPD.
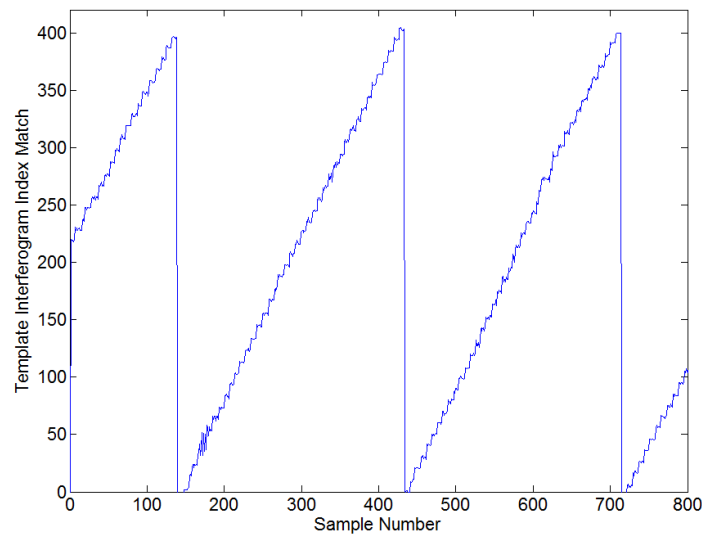
Figure 4.15: Phase calculated for real interferograms as the measurement mirror M1 is advanced by 10 nm steps at 2 Hz.

4.5.1 Range

Due to the reliance of the template matching method on autoconvolution for application of the square window, the range in the current configuration is limited to the 285 µm range measured experimentally in previous work [106] and detailed in section 3.6.2.

This differs from the simulated range of 360 µm (section 4.4.4.) due to the intensity envelopes present for real interferograms.

4.5.2 Axial resolution

The ability of template matching to measure small changes in measurement mirror position is well demonstrated in figure 4.15 in which the PZT is used to translate the measurement mirror position in increments of 10 nm across a range of approximately 1 µm, meanwhile exhibiting two complete phase wraparounds. While the steps in this diagram are clearly visible, it is important to calculate the current axial resolution as well as discuss the current and future limitations.

In section 4.4.3 the theoretical relationship between template spacing and axial resolution was established. The achievable resolution of the DRI apparatus is limited by either the template matching method or environmental, electrical or optical noise. Determining which is the limiting factor for in this particular setup will allow informed decisions for the improvement of DRI. The high frequency noise present in the template matching result appears quantised when using 800 templates spaced by 1 nm. So, while the resolution attainable by template matching is above 1 nm at present, in this section 8000 templates spaced by 0.1 nm will be used to assess the nature of this resolution limiting noise. For this investigation the PZT has been disabled to eliminate the possibility of the closed-loop position control of the PZT from introducing noise.

To achieve the highest measurement rate possible unprocessed interferograms and timing data were saved to a file for processing offline in Matlab. As a method to assess the noise limited axial resolution of template matching, the interferograms were captured over a period of 10 minutes. The non-compact bulk optics nature of the current experimental setup means that temperature change in the DRI base has a large effect on the interferometer path length. This results in surface position drift over a period of minutes or hours.
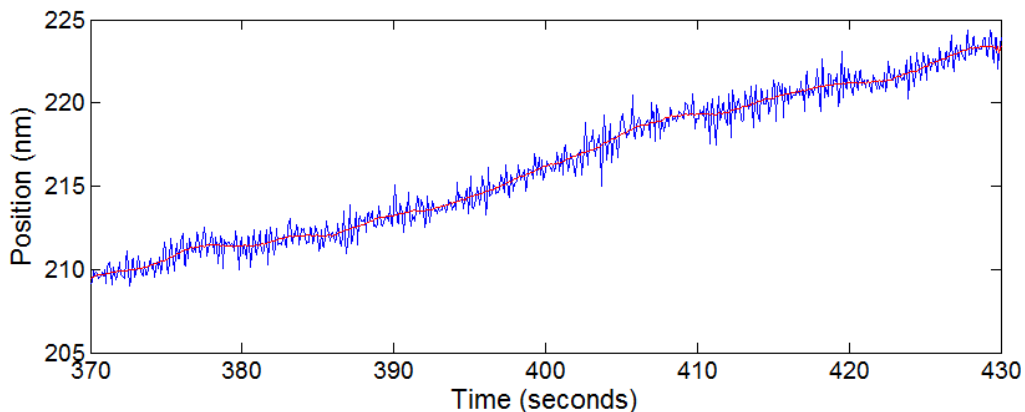
Figure 4.16: A 60 second set of template matching data with no PZT movement.

Future work to improve the thermal stability of the interferometer will attempt to eliminate this drift, but for the purpose of determining the noise floor of the interferometer, it can be removed by high pass filtering. A 60 second section of the data is shown in blue in figure 4.16. Low pass filtering reveals the longer term drift (red).

Subtraction of the low passed data from the original data removes the low frequency drift from the signal, with the remaining high frequency component effectively levelled. This is shown in figure 4.17 where the underlying system noise is easier to study. The standard deviation of this filtered data is 0.6 nm, outlining the noise limited resolution of the bulk optics interferometer in its current configuration.

98
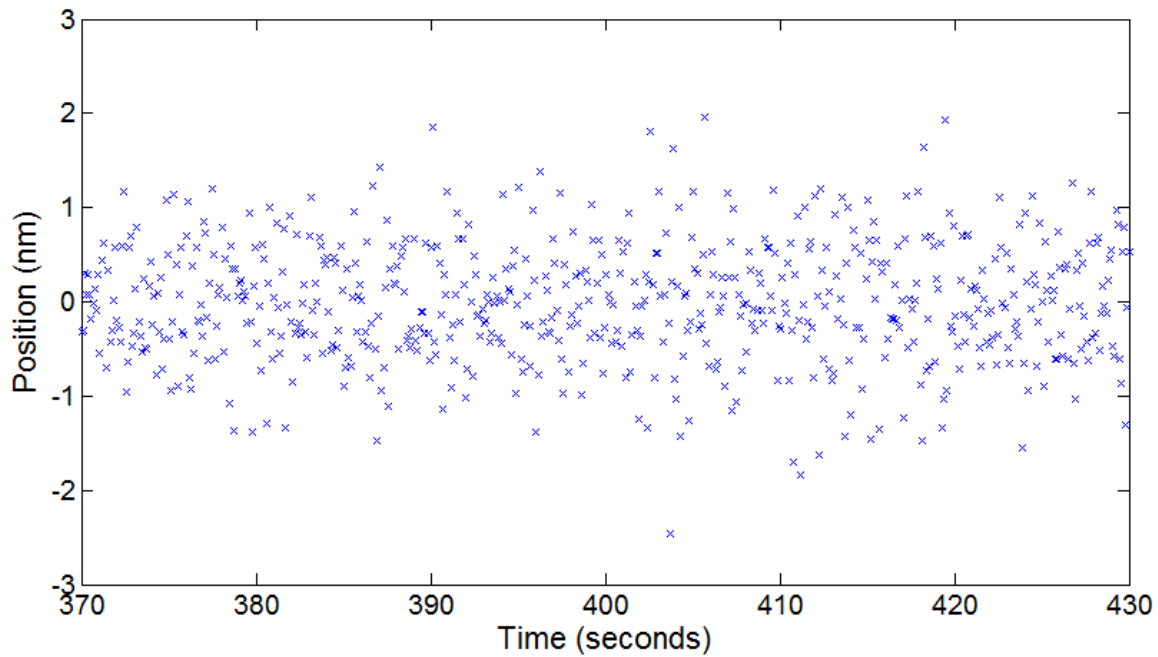
Figure 4.17: Subtraction of the low frequency components from the original phase over 60 seconds results in only the high frequency components, effectively eliminating the effects of phase drive over time due to environmental changes.

Figure 4.18 shows a histogram of the data from figure 4.17 and demonstrates the Gaussian nature of the axial resolution limiting noise. Given the noise in the template matching result, it is currently possible to observe 2 nm steps in the measurement data. One common method of reducing the noise to improve the resolution is averaging of multiple measurement results, though for DRI it is desirable to avoid this if possible due to the measurement rate reduction this enforces.
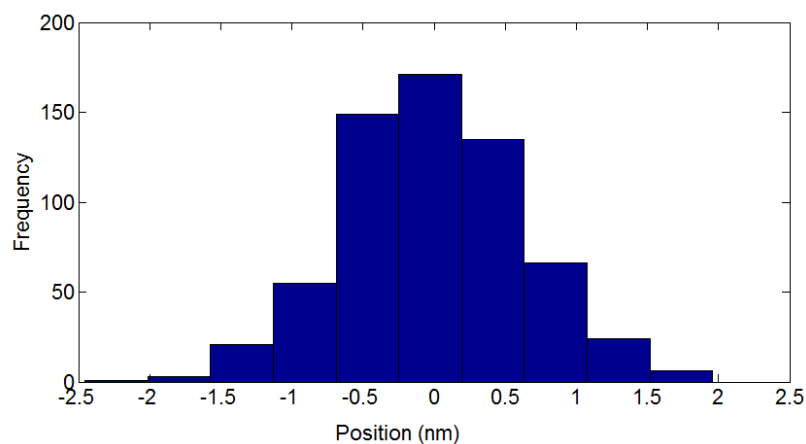
Figure 4.18: A histogram of the filtered data demonstrates the Gaussian nature of the noise.

4.5.3   Linearity

This section considers the linearity of measurements from template matching in two ways. First, the linearity of individual wraparounds will be considered and methods to improve this linearity will be discussed. Second, the linearity of the method across the range of the DRI will be considered, with

99

unwrapping algorithms introduced in section 4.4.1 implemented, evaluated and compared to allow calculation of linearity across 60 μm of the 348 μm range.

Single wraparound linearity: A typical high resolution wraparound of the DRI template matching method, shown in figure 4.19, is examined to assess the linearity of the method for changes in interferometer path length.
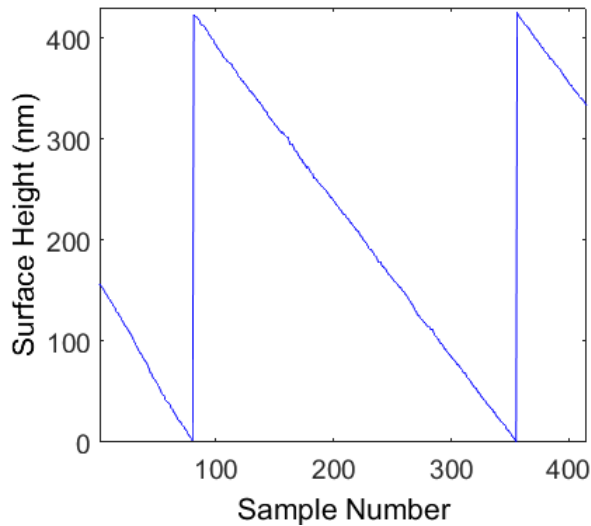
Figure 4.19: Measurement position data obtained by lateral scanning of a tilted mirror across the measurement arm.

A line of best fit was calculated from a section of this which varies from 420 to 0 nm, and the residuals calculated by subtracting the line of best fit from the measurement data. This results in the deviation from ideal linearity which is shown in the graph in figure 4.20.
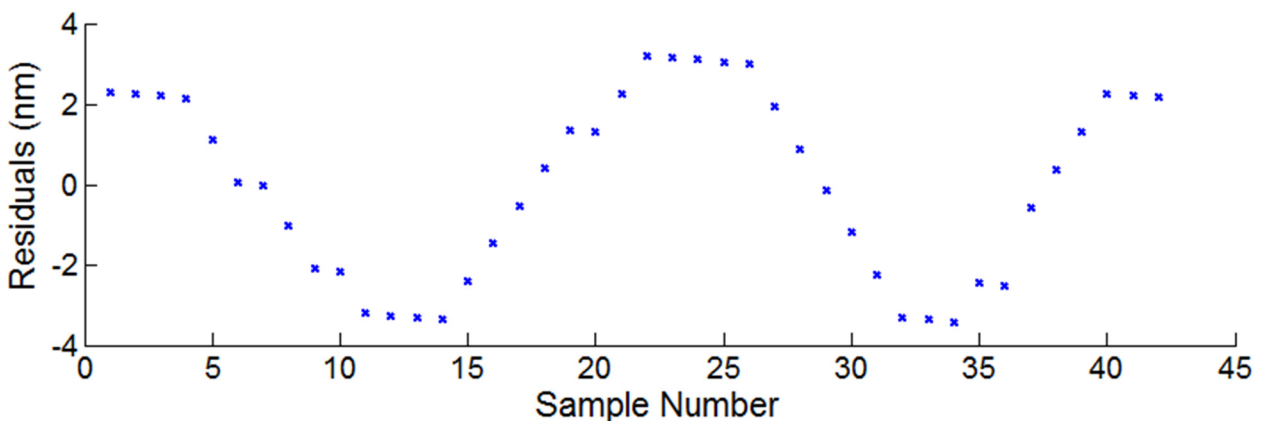
Figure 4.20: Non-linearity of bulk optic phase wraparound obtained by subtraction of line of best fit from phase data. Values agree well with those calculated by simulation.

While this result demonstrates the ability of template matching to produce a measurement result with a better than 7 nm linearity over short distances, the example provided above is an ideal case for which the

measured interferograms exhibit low noise and high visibility. In other instances, the visibility of the raw interferograms used to calculate measurement data is much reduced or contains significant tilt or offset, features which aren't always correctable by regularisation. In these cases it has been demonstrated that similar to the simulated case, linearity of template matching while using peak fitting on the correlogram severely degrades the linearity of the resulting phase. In such a case it is beneficial to sacrifice the sub-template resolution afforded by peak fitting in favour of the increased linearity of the max() method as was described previously.

Full range linearity: To assess the linearity of template matching across the full 348 μm range of the DRI apparatus a replacement PZT was purchased and inserted as shown in the schematic diagram in figure 4.14. The new PZT (PI PiHera 625.1) has a specified range and resolution of 500 μm and 1.4 nm respectively. For the purpose of this investigation, the PZT is stepped in 10 nm increments at a rate of 10 Hz while interferograms are captured and surface position calculated using template matching. The minimal step time attempts to reduce the total capture time while allowing sufficient data for unwrapping, resulting in a set of data captured over a time period of 1000 seconds.

Similar to the simulated data in section 4.4.1, the measurement data is first unwrapped using the simple algorithm (appendix 11.1.7). A first order polynomial is fitted to this unwrapped data, providing a line of best fit, subtraction of which from the unwrapped data results in residuals demonstrating the deviation from ideal linearity across a 400 μm range of the interferometer.

The residuals shown in figure 4.21 demonstrate this non-linearity, the shape of which agrees well with the simulated peak deviation of 209.8 nm and a non-linearity of 0.07 %. The peak-to-peak deviation of the template matching method with measured interferograms is 641.9 nm and the peak deviation is 320.2 nm meaning that the non-linearity over a 400 μm range is 0.096 %.
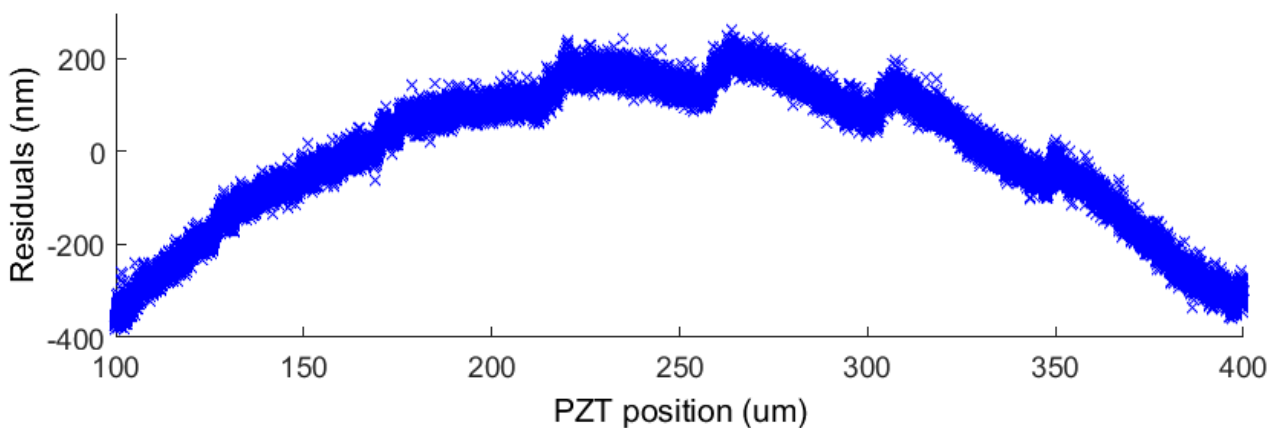
Figure 4.21: Residuals from a line a line of best fit to the unwrapped data after measurement mirror position was translated 400 μm by a PZT.

101

In agreement with the linearity simulation described by section 4.4.1, consideration of the phase vertex position during the unwrapping process improves the linearity of the unwrapped phase residuals, as seen in figure 4.22, though not to the extent that it does in simulation. This additional signal processing step improves the linearity for the bulk optics interferometer to 231.2 nm peak deviation and 0.0289 % linearity.
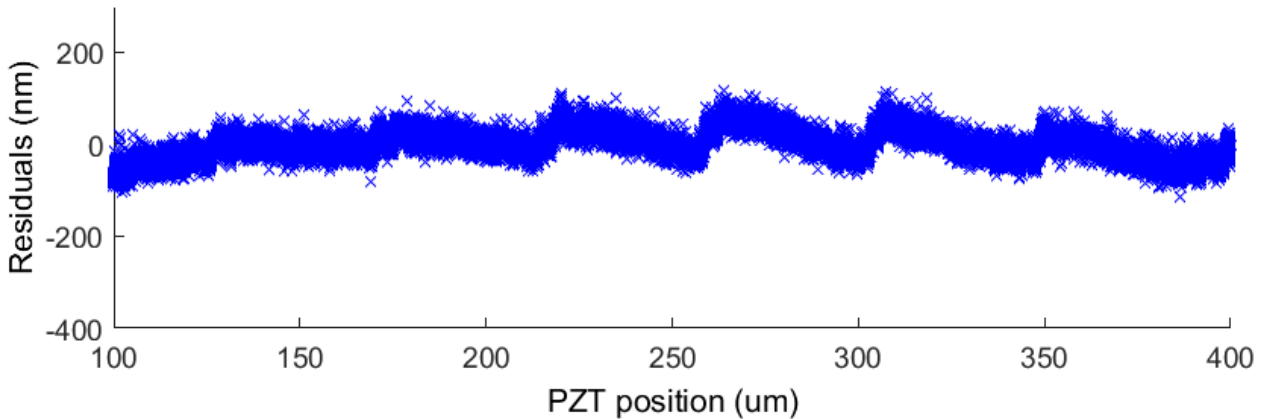
Figure 4.22: Residuals for unwrapped measurement data where the wavelength of the balance wavenumber has been taken into account during the unwrapping process.

The difference in real and simulated full range linearity for wavelength compensated unwrapping is attributable to two main factors. The first is the 100 nm pk-pk high frequency noise observable across the entire set of residuals. The second is the low frequency changes visible at PZT positions 175, 225, 265, 310 and 350 μm in figures 4.21 and 4.22. It is possible the 100 nm pk-pk noise seen across the residuals is attributable to three inseparable processes:

1) Environmental noise. Differential changes in interferometer arm path lengths cause phase fluctuations. In this example they are likely to be caused by mechanical vibration and have been limited to an extent by the plastic enclosure.

2) Wraparound non-linearity as demonstrated in simulation and experimentally in previous sections.

3) Closed loop oscillations of the PZT. At their worst, these were measured with a Renishaw XL-80 laser interferometer to be 20 nm peak to peak, at a frequency of 105 Hz. Due to the reduced stiffness of this PZT stage to achieve an increased range, oscillations may occur. Attempts by the manufacturer to resolve this oscillation were unsuccessful.

Repetition of this measurement multiple times has confirmed that the steep changes in the residuals occurring at 175, 225, 265, 310 and 350 μm are repeatable and so are not due to environmental effects or phase wraparound errors. The only common element between repeated measurements remains the PZT and so it is likely this phase non-linearity is due to the non-linearity of the PZT stage. The full range non-linearity provided by PI for this PZT is 0.03 %. For a range of 500 μm this provides a maximum specified deviation of 15 nm. Low pass filtering of the wavelength corrected unwrapped phase residuals seen in

figure 4.22, results in the graph in figure 4.23, with the smoothing allowing a clearer view of the shape of the non-linearity. The peak-to-peak amplitude of 85 nm is outside the specified linearity of the PZT, however further work with the Renishaw XL-80 to classify the PZT linearity is required.
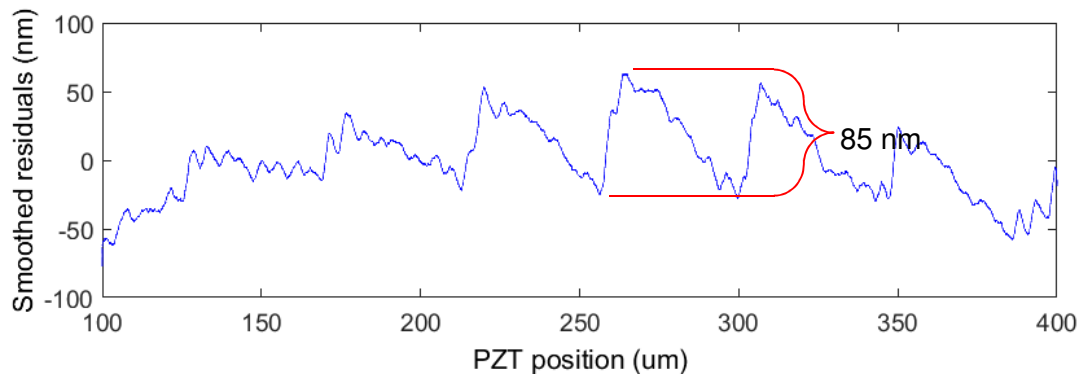
Figure 4.23: Residuals from wavelength corrected unwrapping, smoothed with a 200 wide rectangular smooth to remove the high frequency noise and reveal non-linearity partly attributable to the PZT.

4.6 Step height measurement

The following section demonstrates the ability of DRI to measure small surface step heights through use of an NPL measurement sample. This sample contains four measurement areas where all features are 100 nm deep. Three of these sample areas are composed of waffle patterns, each with a different pitch between the negative wells. The fourth area comprises 100 nm deep trenches spanning the width of the sample area, with the separation between and width of the trenches varying across one dimension of the sample. For this DRI measurement a single set of five trenches were measured, with trench widths of 100 µm each. For measurement on the DRI, the advantage of the trenches over the waffle patterns is the ease of alignment of the sample under the objective for a single point method such as DRI.
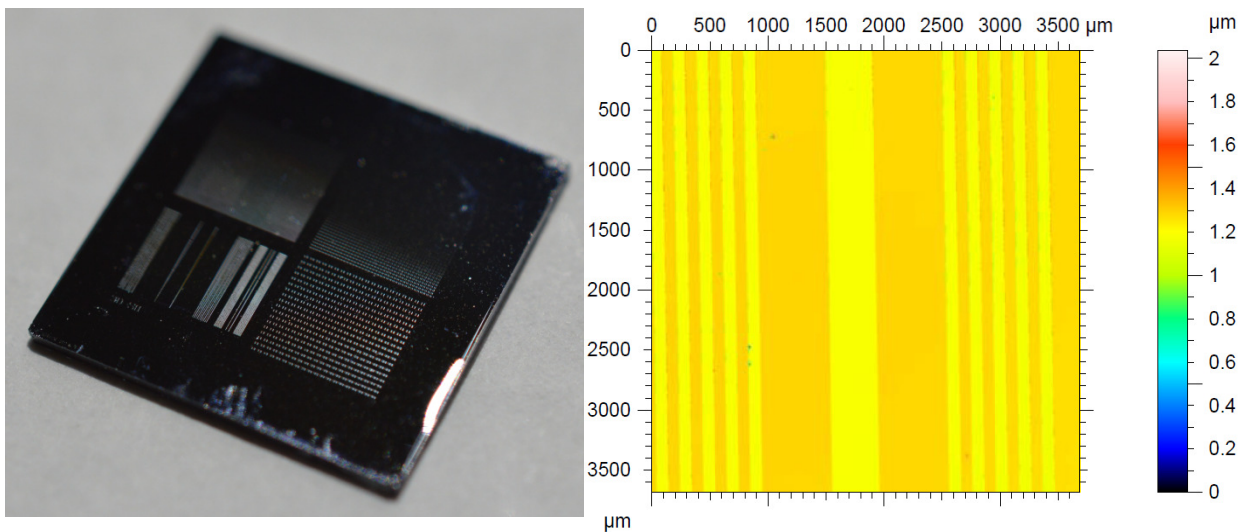
Figure 4.24: Photo (left) and Taylor Hobson CCI measurement data (right) for a nickel replica step height sample provided by NPL. Sample contains three regions of waffle pattern and one region of varying width trench patterns. All features specified as 100 nm deep.

Modification of DRI measurement arm: The schematic provided in figure 4.25 shows the addition of a lens (L2) and a motorised translation stage (S) to the measurement arm of DRI allowing lateral scanning of measurement samples in front of the measurement arm beam. The lens chosen for this application is an achromatic doublet (Thor Labs LA1540-B-ML) with a focal length of 15 mm while a Newport MFA-CC motorised linear stage provides translation of the sample in 0.1 µm increments over a 25 mm translation range.

Mounting of samples for measurement is made easier by the addition of a folding mirror within the measurement arm, redirecting the measurement arm beam downwards towards the optics table. Since mounting of both small but irregular and, heavy samples has been a difficulty previously, with superglue too permanent and double sided tape prone to creep, folding of the beam will allow samples to be set directly onto the translation stage. Mounting in this manner also reduces the effect of stage pitch, roll and yaw by decreasing the distance of the sample from the stage.
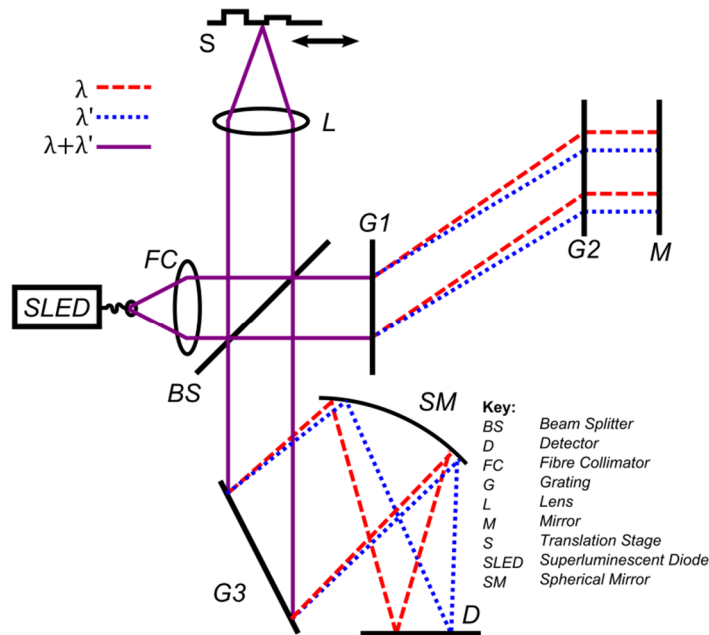
Figure 4.25: DRI schematic showing addition of lens (L2) and Newport motorised stage (S) for lateral scanning of samples.

Figure 4.26: Photo of beam steering in the measurement arm of a bulk optics DRI implementation. A folding mirror turns the measurement arm towards the table after which a lens focuses the beam onto the measurand. The manual X-Z micrometre stages on the left of the photo allow positioning and focusing of the lens.
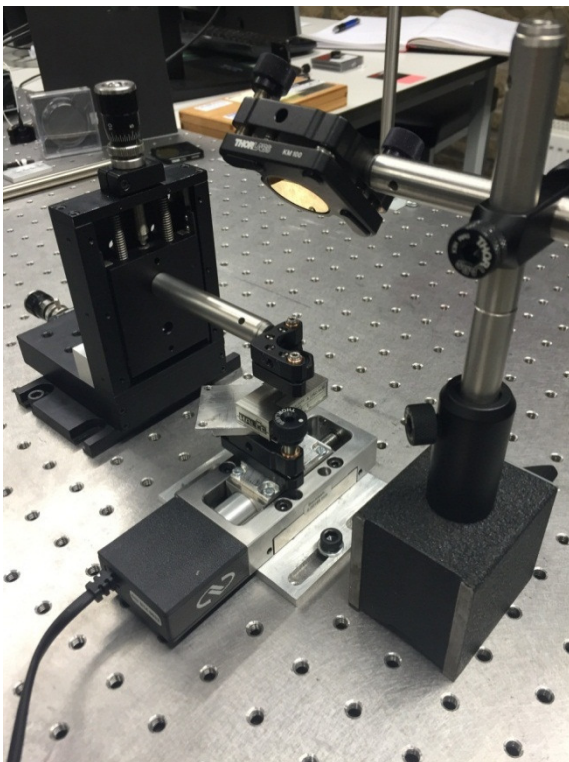
Figure 4.26 shows a photo of this modified setup containing the folding mirror (top right), a 15 mm focal length achromatic doublet lens (centre), Z axis translation stages for the lens (left) and the motorised stage for X translation of the sample (bottom). In this photo a roughness sample is shown, however an identical setup was used for the above NPL artefact.

The axial surface height was calculated using template matching as the motorised stage was translated over a 1 mm sample length at a rate of 0.005×10^{-3} m s^{-1} . This is shown in figure 4.27 where 5 steps can be seen among the measurement wraparounds. Figure 4.28 shows unwrapped measurement data which is then used to calculate a line of best fit (red).

Figure 4.27: A graph showing the calculated template index against translation stage position. The tilt of the sample is apparent from the wraparounds occurring with the steps visible between stage positions 14.85 mm and 15.35 mm.
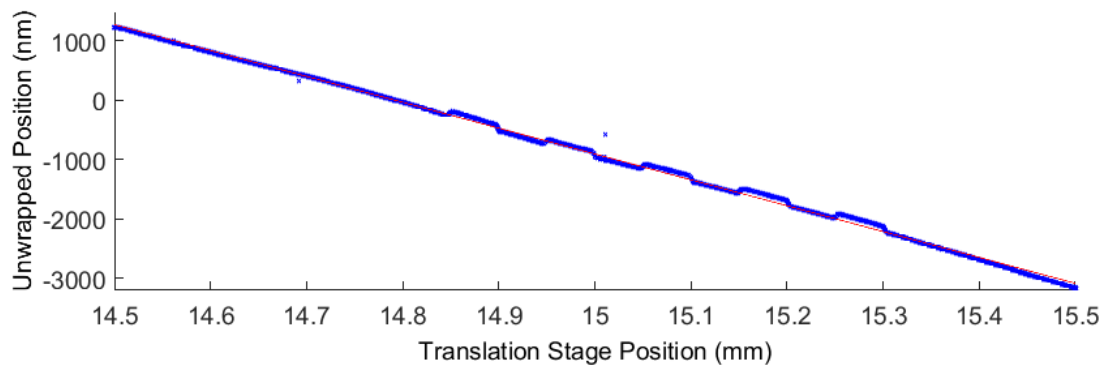
Figure 4.28: Unwrapped position (blue) and a linear least squares fit (red)

Subtraction of the linear fit from the unwrapped surface height results in the residuals (blue) seen in figure 4.29, clearly showing the five 100 nm step heights superimposed upon a lower frequency envelope. Repetition of the step height measurements with identical translation positions of the motorised stage (14.5 to 15.5 mm) demonstrates that this low frequency envelope is repeatable suggesting that it is not environmental drift but likely due to peak to peak stage flatness error in the order of 50 nm. This is evidenced by the red trace shown in figure 4.29 in which measurement of a first surface mirror (Thor Labs PF10-03-M03) was performed from stage positions 14.5 to 15.5 mm at a rate of 0.005×10^{-3} m s^{-1}. Unfortunately the flatness of the MCA-CC stage is not specified by the manufacturer.
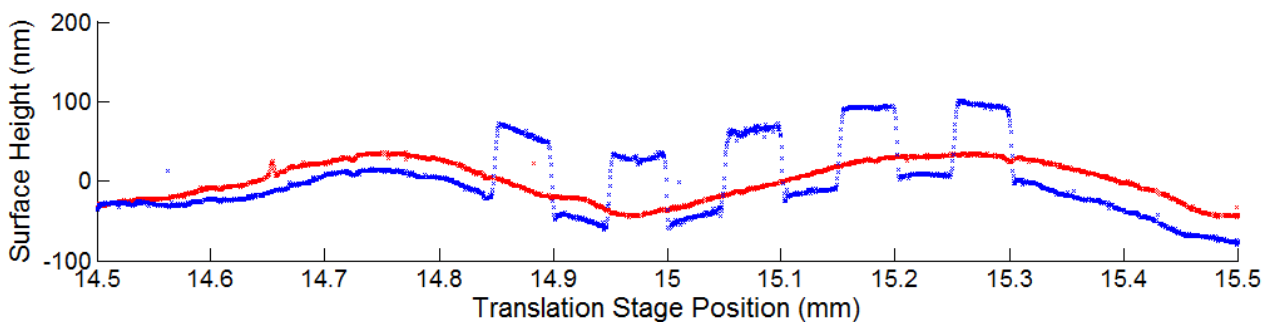
Figure 4.29: Subtraction of the linear least squares fit from the unwrapped phase results in the blue residuals shown in this scatter graph while making the 100 nm steps clear. Overlaying this result (red scatter plot) is the same process described above used to measure a first surface mirror for the same translation of the motorised linear stage.

106

Interpolation between the translation stage X position for the mirror measurement and step height measurement allow subtraction of the mirror measurement from the step height measurement providing a result in which motorised stage flatness error is reduced.
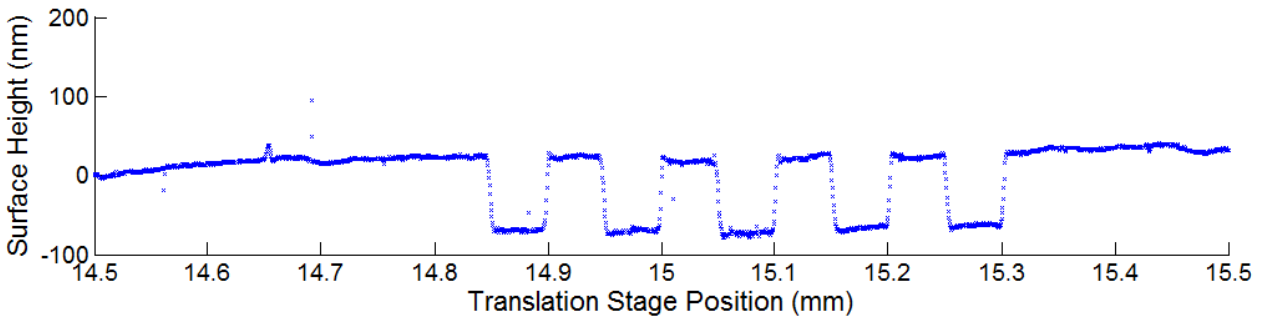
Figure 4.30: Initial attempt at subtraction of stage calibration data to reduce the low frequency envelope.

4.6.1 Step height results

Step height from the top surface to the bottom surface for each channel was measured in accordance to BS EN ISO 5436-1 [107] section A1. Following this method, each step is described as having a width, W. To remove the rounding effect near the top and bottom edges of the step a sample of width $W/3$ at the centre of the step is evaluated, with this region of interest labelled as region C. Two more regions of interest are also evaluated to arrive at a measured step height, with these being the sample areas starting from $W/3$ distance from each top edge of the step and extending to either side as far as to make the total sample width up to $3W$. These two regions to the left and right of the step are labelled A and B respectively. The above described labelling is shown schematically in figure 4.31.
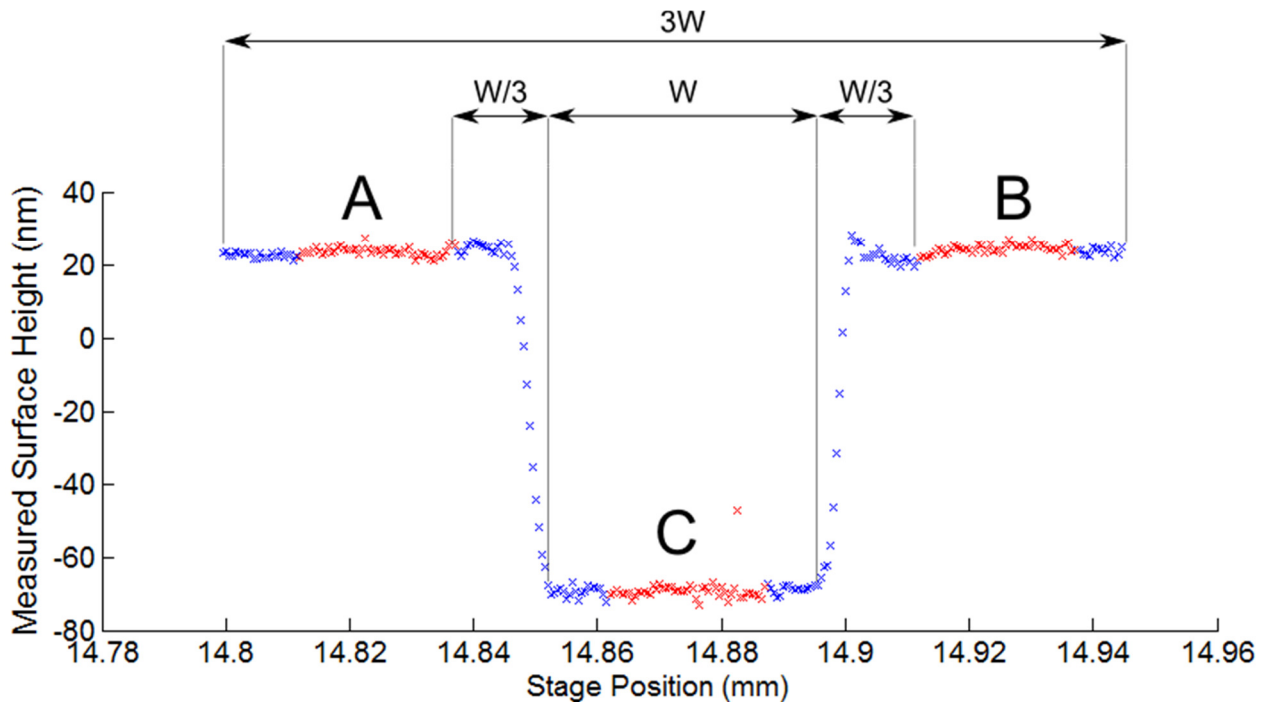
Figure 4.31: Diagram showing measured step height 1. Data of interest for step height calculation is highlighted in red and labelled A, C and B. Step width distances are labelled W.

Next, a least squares fitting of the data to equation 4.13 allows calculation of the value, h, where the step height $d = 2h$ and the variable δ has the value +1 in regions A and B and -1 in the region C.

$$Z = \alpha \times X + \beta + h \times \delta$$

4.13

This is achieved using the Matlab function pinv() to calculate the Moore-Penrose pseudoinverse of a matrix containing the x axis positions of each sample and the region modifier δ. Multiplication of this matrix by a vector containing the surface height values provides a value of half the step height. Calculated step height values for DRI and CCI measurement of the sample are shown in table 4.3. BS EN ISO 5436-1 recommends that a minimum of 5 profile measurements separated in the y direction are undertaken, however the current bulk optics setup limit DRI to a single trace at present.

Step Number	DRI measured step height(nm)	CCI measured step height 5X mag (nm)
1	93.02	105.02
2	90.34	102.82
3	92.96	103.81
4	88.65	103.76
5	89.00	106.79

Table 4.3: Step height results for measurement data obtained by DRI and CCI.

The short-term availability of this waffle sample means that several mistakes made during measurement are not correctable and limit the ability for comparison of these two measurements. The 10-15 nm measured step height discrepancies between CCI and DRI are thought to be attributable to three main components.

Firstly, at the time of measurement the phase was calculated by a template matching implementation making use of peak fitting for correlogram peak detection however it has since been shown by simulation that this increases non-linearity of each phase wraparound, with non-linearities of up to 5 nm for simulated or 10 nm for some measured interferogram sets.

Another unknown is the repeatability of the flatness error. The peak-to-peak flatness error has been measured experimentally to be 50 nm pk-pk, with further study of flatness error showing it likely to be repeatable to no better than 10 nm (see Figure 4.33). It also becomes difficult to differentiate between flatness, straightness, pitch, roll and yaw error, meaning that sample thickness, orientation and distance from the stage will influence this problem. For future studies, Newport's FMS and XMS range of metrology-grade linear stages will be more appropriate than the MFA series stage used in this investigation due to their much improved flatness, pitch and yaw characteristics.

Lastly, the 5X magnification objective used for CCI measurement to allow measurement of all 5 steps within the field of view means that the lateral resolution of the measurement is lower than possible with higher magnification objectives and that the resulting spatial averaging make the slopes of the steps unclear when compared to the higher lateral resolution of the DRI measurement. This results in a CCI step height calculated from only 5 samples per area of interest instead of 50 for DRI leading to a non-ideal step height measurement. Figure 4.32 shows the CCI data (blue) with the areas of interest highlighted in red, in this figure the spatial filtering of the sample is obvious from the rounded nature of the steps.
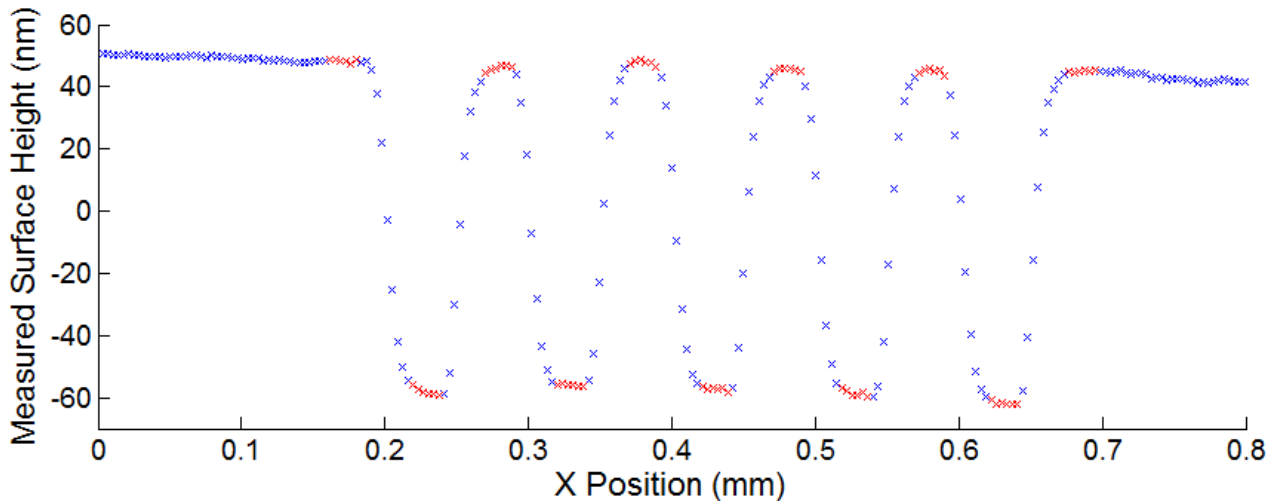
Figure 4.32: Step height measurement of NPL waffle artefact using a Taylor Hobson CCI with a 5x objective.

4.6.2   Improved stage calibration attempt

To further reduce the stage flatness error it was decided to attempt calibration with a precision glass flat (Thor Labs SSM1010B) instead of a first surface gold mirror. The glass flat has a specified flatness and roughness of less than $\lambda/20$ nm and 0.1 nm respectively, although it has a lower reflectivity. The stage position was scanned from 14 to 16 mm while surface height was calculated using template matching. This was repeated four times with the data shown as scatter plots in figure 4.33.
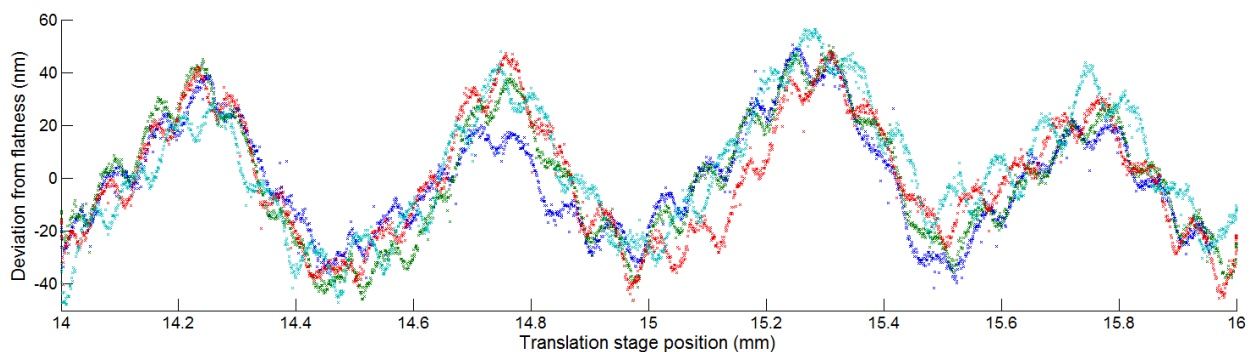
Figure 4.33: Scatter graph showing 4 sets of stage flatness calibration data. The low frequency oscillations (4 across 2 mm) are thought to be stage flatness error. The higher frequency oscillations are thought to be DRI linearity errors due to the low contrast of the interferograms when measuring the glass.

Two features of note can be seen in the four scatter plots in figure 4.33. First is the low frequency oscillations having a peak to peak amplitude and period of approximately 80 nm and 0.6 mm respectively. It is probable these are the stage flatness errors observed previously since their amplitude and frequency match those of figure 4.29. The second feature is the higher frequency oscillations imposed on top of these, having a frequency which matches the wraparound of template matching. Observation suggests that these 20 nm peak to peak oscillations are caused by non-linearity of the template matching process for this specific application, exacerbated by the low visibility of the interferograms when a low reflectivity sample such as the optical flat is measured. During measurement, these oscillations are not visible due to their scale in relation to the position wraparounds. After removal of surface slope caused by imperfect alignment of the measurand to the measurement beam, they become apparent. It was confirmed that these higher frequency oscillations are non-linearity of the phase wraparound by further increasing the tilt of the sample and observing the number of wraparounds across the measured sample change along with the frequency of the oscillations in the slope corrected data.

The low reflectivity of the optical flat resulting in poor visibility mean that further improvements of stage flatness calibration were abandoned. It is expected that a higher reflectivity flat, coating the flat or improved bulk optics efficiency will result in improved visibility interferograms whose calculated surface positions have improved linearity.

4.7   Template matching conclusions

This chapter has introduced template matching as a method to derive DRI measurement mirror displacement with a high axial resolution. Template matching uses signal processing common to the field of image recognition to determine the shape of the interferogram point of symmetry by comparing it to a set of interferograms of known OPD.

Template matching for DRI has been shown to achieve a noise limited axial resolution of 0.6 nm and that this is not a limitation of the method but a result of the mechanical, optical and electrical noise present in this physical setup. It is expected that reductions in path length and alignment errors afforded by development of an interferometer prototype as well as further attention to the optical and electrical error sources will allow improvement of the axial resolution.

The range of template matching, a relative but high resolution DRI signal processing method, has been demonstrated to match that of the lower resolution but absolute variant that makes use of autoconvolution. This range, 285 μm, will be improved upon in subsequent chapters and has been shown to be a function of interferogram shape, influenced by light source bandwidth, grating parameters and spectrometer characteristics. Ability to resolve position wraparounds to perform measurements over a

range greater than the wraparound distance of half the wavelength at the interferogram symmetry point has also been shown, as well as confirming linearity of better than 0.0289 % over the full range.

The ability of DRI template matching to measure sub-micron step heights has been demonstrated. This includes the consideration of compensation for translation stage errors as well as comparison to measurements by an established lab-based measurement method. While less than the 100 nm specified step height and 105 nm step height as measured by an established measurement method, the differences in measured values have been explained and it is expected a closer agreement can be achieved in future work.

A significant technical achievement included within this section is the demonstration of separation of stage movement from surface measurement. An intrinsic problem with single point methods is the necessity of mechanical movement to obtain profile or areal measurements. This significant downside to single-point interferometers is offset by the potential for miniaturisation to allow on-machine integration and so calibration of the translation apparatus has in this example allowed elimination of translation stage flatness errors in excess of 50 nm. In this same measurement investigation, another strength of single point methods has been highlighted, namely the ability to vary lateral resolution without substitution of the measurement objective. The CCI profile shown in figure 4.32 possesses low lateral resolution, resulting in spatial averaging of the waffle steps. Unlike CCI and other areal methods, the lateral resolution and sampling of DRI may be chosen as a choice between measurement rate and lateral resolution and sampling.

Despite this, template matching remains a relative method of measurement, having the ability to measure only minimally varying measurement samples and those without discontinuities leaves it inappropriate for many on-machine measurement applications. Realisation of a nanometre resolution, absolute method of single point measurement is seen as a crucial development to increase eventual uptake and usefulness of DRI in a manufacturing environment. For this reason the next chapter explores methods of combining the absolute measurement regime provided by autoconvolution with the nanometre resolution of template matching to provide an absolute method of measurement with a dynamic range exceeding 500,000.

5 High dynamic range DRI – Combining absolute and relative position encoding

5.1 Introduction

Chapters 3 and 4 describe two different methods to calculate single point measurement data from spectral interferograms obtained through DRI. The key abilities of these two methods are summarised by table 5.1.

Method	Resolution (nm)	Range (µm)	Dynamic Range	Advantages	Disadvantages
Autoconvolution	< 250	285	1,140	Absolute	Low resolution
Template Matching	0.6	285	475,000	High resolution	Relative

Table 5.1: Summary of DRI measurement method capabilities.

From this table it is apparent that a method of combining these two measurement regimes is necessary in order to increase the usefulness of DRI. Using the absolute nature of wavelength encoding and the nanometre axial resolution of template matching, wraparound order determination of template matching should be possible. This will allow unambiguous measurement of high resolution position, not limited by step heights greater than half the wavelength which template matching and other relative methods of metrology suffer from. This section covers the methodologies and signal processing required to use wavelength encoded, absolute, low resolution data to determine the wraparound number of template matching to enable a method exceeding an absolute dynamic range of 500,000, where dynamic range is the ratio of axial range to resolution. This will allow DRI to meet another requirement for on-machine metrology as set out in section 2.4.

Combination of multiple measurement regimes is a notoriously difficult problem [108], one that in the case of coherence scanning interferometry has been successfully solved to allow CCI to provide an absolute method of measurement at nanometre resolution, with a dynamic range to compete with PSI. This chapter introduces a proposed method to solve this problem for DRI to provide a high resolution method of measurement capable of absolute measurement of surface topography over a vertical range of several hundred microns.

After presentation of an improved experimental setup, introduction to the wraparound order determination method is provided and corrective algorithms are discussed to increase robustness. After this an overview of the strengths and weaknesses of this method are outlined and future potential alternative methods outlined.

5.2 Improved autoconvolution range and resolution

Prior to commencing this section of research, three changes were made to the bulk optics interferometer to improve performance. The bandwidth of the SLED and the pixel count of the detector were increased

allowing a large increase in interferometer range to be realised. The SLED was updated to an Exalos EXS210068-01 having a centre wavelength of 850 nm and a bandwidth of 50 nm. A Basler Racer camera with 8192 pixels replaced the previous 2048 pixel camera, allowing a new maximum line rate of 12 kHz.

The last of the three changes was that the perpendicular separation of the reference arm transmission gratings was reduced from 330 mm to 220 mm. This has the effect of reducing the range while simultaneously improving the per-pixel resolution of absolute position detection by wavelength encoding. This change was made with the expectation that an autoconvolution method with a higher axial resolution of 200 nm or better would aid determination of template matching wraparound order.

Figure 5.1 shows an interferogram resulting from this improved physical apparatus. Matlab simulations indicate that for the wavelength encoding method these changes will result in an axial range and resolution improvement to 800 μm and 200 nm respectively. These values will be evaluated experimentally as part of the wraparound order determination investigation that follows.
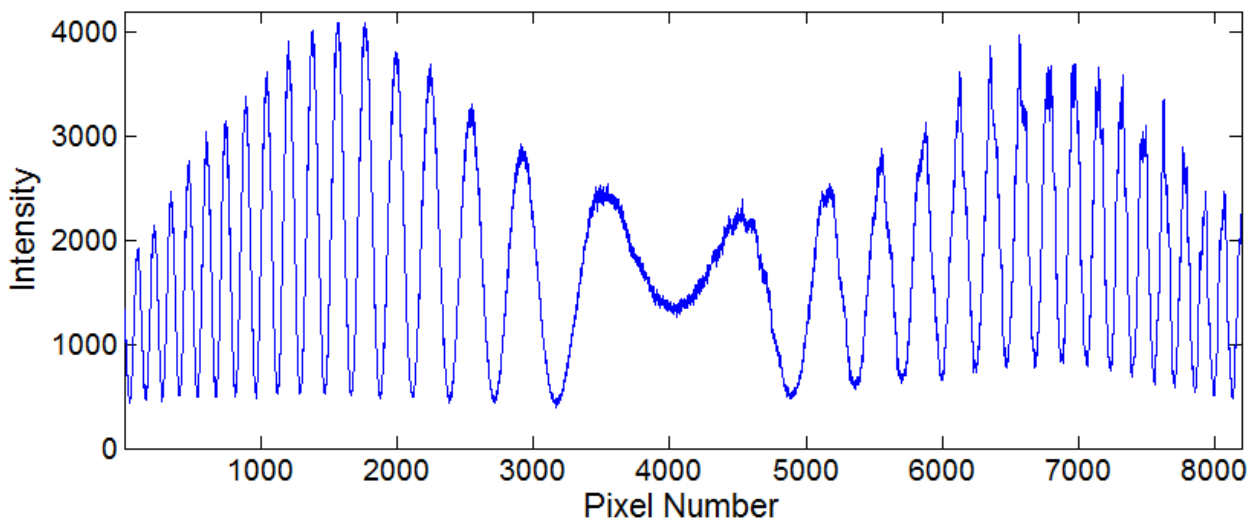
Figure 5.1: Unprocessed interferogram captured from improved DRI implementation with updated SLED bandwidth, camera pixel count and reduced dispersion.

This updated interferogram having more pixels necessitates changes to the signal processing to maintain successful autoconvolution due to the increased number of interference fringes and the change in background intensity shape of the new SLED. Very briefly, these changes include the additions of calculation and smoothing of the first derivative before autoconvolution. For template matching an increased template length of 1401 pixels is used. These changes are covered in more detail in appendix 11.3.

5.3   Template matching wraparound order mapping

For DRI, the approach taken to match the relative template data, t, to the absolute wavelength encoded result, a, is to map the interferogram centre position at which each phase wraparound occurs across the

range of the interferometer. The first step towards achieving wraparound order determination of DRI template matching is creation of a calibration map. This contains the autoconvolution pixel positions at which each template matching wraparound occurs. This map of wrapped high resolution measurement data against interferogram symmetry pixel position will enable later determination of position using a combination of both methods.

Differences in path length and background intensity between the real interferometer and simulated interferometer mean that simulated data cannot be used to create a wraparound order map; this is in direct contrast to template matching. To produce the required map, translation of the measurement mirror is required to obtain a set of experimental interferograms covering the entire range with ten or more interferograms per wraparound. This allows relation of high resolution data to wavelength encoded autoconvolution result and hence pixel position of the interferogram centre. To obtain appropriate interferograms the measurement mirror must be moved across the entire range and so one of two options may be used.

a) Translation along the Z axis of a mirror perpendicular to the axis.

b) Translation of a tilted mirror along the X axis, effectively shortening the Z axis as it scans sideways.

A PI PZT with 500 µm range (P621.1) was initially used to translate the mirror along the Z axis as described by the first option. However, the large range of the chosen PZT resulted in a reduced stiffness that with the closed-loop nature of the control system the mirror position oscillated with an amplitude of up to 20 nm pk-pk, unacceptable for this application. The accepted solution was to mount a tilted mirror on a Newport motorised stage (MFA-CC) and translate it along the X axis of the interferometer, with the tilted nature of the measurement mirror meaning that the measurement arm path length changes as the mirror moves. A 50 mm focal length achromatic doublet was used to ensure that alignment was maintained after reflection of the tilted surface. It should be noted that stage flatness calibration and a precision reference flat are not required since only the relationship between the two measurement methods are of interest, not how they relate to the surface height.

As the measurement arm path length varies, the autoconvolution position, a, and template matching result, t, are calculated and recorded in vectors $\mathbf{a}$ and $\mathbf{t}$ respectively. The stage translation rate is set to ensure more than 10 samples per phase wraparound which prevents unwrapping error and increases wraparound position detection accuracy. However, with current DRI development progress, this means a lengthy calibration process of approximately 20 minutes for the full range.

Figure 5.2 shows a set of data spanning an approximate 3.6 μm range of the DRI total range. This small section is shown to allow visualisation of the relationship between autoconvolution result **a** (green) and template matching result t (blue). In this case it is clear that the autoconvolution is monotonic and so suitable for wraparound order determination.
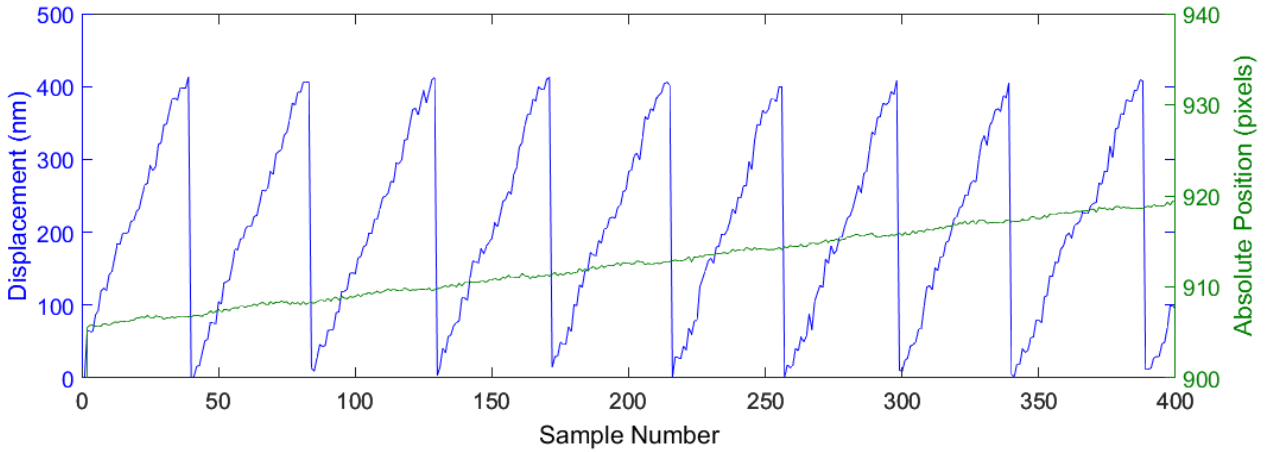
Figure 5.2: Graph showing an approximate 3.6 μm change in measurement arm length and the autoconvolution position (green) and high resolution relative result (blue) of interferograms over this translation.

Next, detection of the wraparound position is necessary. This is achieved by discrete calculation of the first derivative of the wrapped template matching data, with a wraparound detected at any index where the value is less than -200. The first derivative is calculated as follows.

$$\mathbf{t}' = \left(t_1', \cdots, t_i', \cdots, t_{Wt}' \right)^T$$

$$t_1' = \begin{cases} t_2 - t_i & \text{if } i = 1 \\ \dfrac{t_{i+1} - t_{i-1}}{2} & \text{if } 1 > i < W_t \\ t_{W_t} - t_{W_t - 1} & \text{if } i = W_t \end{cases}$$

$\quad$ 5.1

where W_t is the length of the vector containing the data, and $\mathbf{t}$ and $\mathbf{t}'$ are vectors containing the template matching position and derivative position respectively. Figure 5.3 shows the derivative of the template matching position graphically.

Editorial note: Since writing this the author has replaced this centre difference formula (eq. 5.1) with a simple difference operator between neighbouring pixels. Equation 5.1 is inappropriate for phase unwrapping due to the phase wraps occurring between pixels. For simple unwrapping the second value can be discarded, however it is not robust for wraparounds occurring within several samples of each other. This can be observed in figure 5.3 where each negative peak has two X values instead of one.
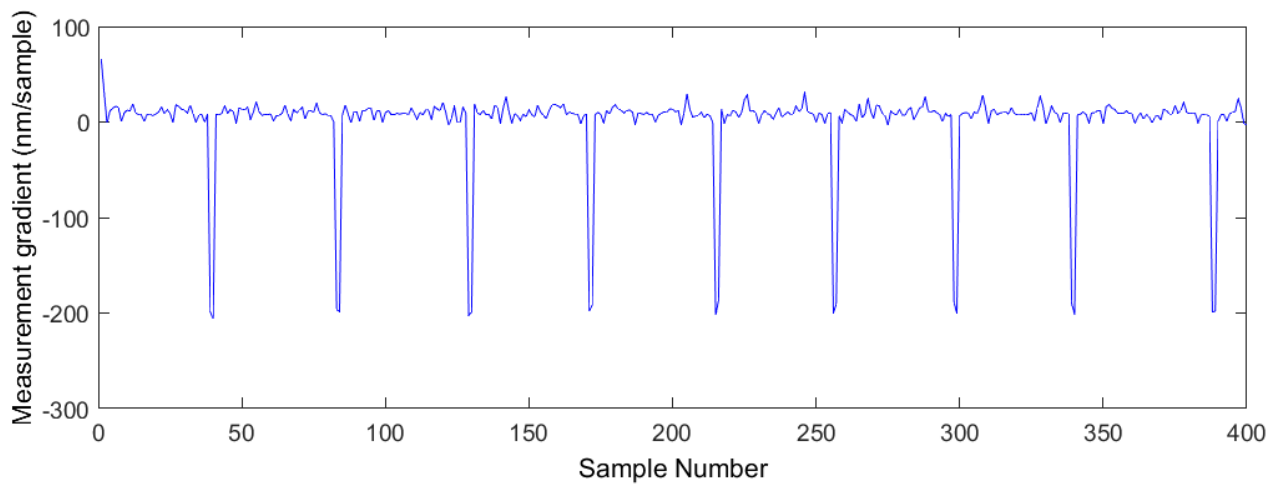
Figure 5.3: First derivative of the high resolution relative measurement reveals the position of the wraparounds.

Finally, to complete wraparound order mapping, the autoconvolution value at each of the detected wraparound boundaries is stored in a vector, $\mathbf{a_w}$, whose length matches the number of detected wraparounds.

5.4 Wraparound order determination

The wraparound order map is next used to determine the absolute position of the high resolution surface position calculated by template matching. It can be used on live data as it is captured by the camera or as a post-processing operation on a batch of data. In this first instance, measurement of the same mirror used for calibration is used as a demonstration of wraparound order determination.

A newly captured interferogram has a low resolution absolute position and a high resolution relative position. Order determination iterates through the wraparound order map and compares the absolute position of the interferogram to the autoconvolution positions stored within the map. Finding the two bounding autoconvolution results within the map provides the order of the interferogram. The high resolution absolute position may then be calculated by multiplying the wraparound order by half the wavelength and adding the high resolution relative position value.

In the following diagram, order determination is used to calculate the high resolution absolute position of 400 measured interferograms as the axial position of the mirror is changed in small increments. The blue trace shows the absolute position at a resolution better than that of autoconvolution, with the calculated wraparound order shown in red. These values are absolute and not simply unwrapped as demonstrated in the previous section.
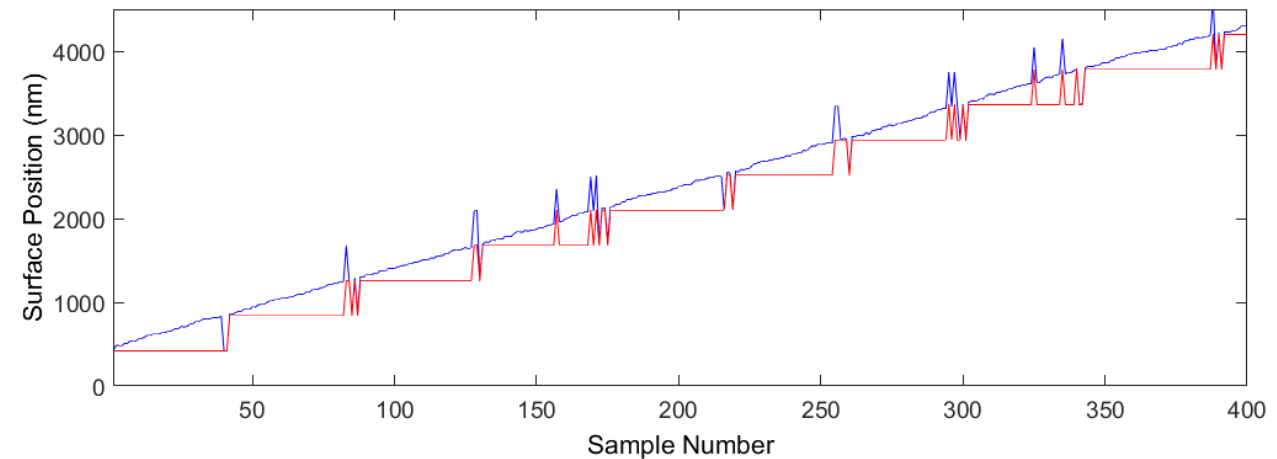
Figure 5.4: Graph of wraparound order (red) and high resolution absolute position (blue).

From the data presented in figure 5.4, the inaccuracy of wraparound order mapping becomes apparent, with order errors appearing in the form of positive spikes appearing near the wraparound order boundaries. This is due to the noise in the autoconvolution or template matching position during calibration or order determination.

These errors manifest due to the imperfect nature of the calibration procedure, with the rate at which the translation stage is moving meaning that only the approximate not exact order wraparound position is recorded. This, in addition to noise between the two methods, means that wraparound order errors exist near the wraparound positions. However, due to the absolute nature of this method, these order errors do not propagate or accrue as they do in phase shifting methods which rely on unwrapping.

5.5 Wraparound order error correction

For wraparound order determination for DRI to be a useful method, an order correction scheme is described below. The diagram in figure 5.5 illustrates the criteria for when wraparound order errors occur and is provided as a way to explain the solution, wraparound order error correction. The diagram shows a representation of the relative position as calculated by template matching as it wraps around (blue) overlaid with the absolute position provided by the autoconvolution result (green). Red dotted lines indicate the detected wraparound positions which are labelled sequentially by the variable, n. The light red areas represent areas of potential ambiguity where imperfect wraparound order calibration could lead to order errors. While the diagram explicitly places the detected wraparound position at the exact wraparound position, in reality this red dotted line could be anywhere within the ambiguous zone due to the positional uncertainty due to the lateral sampling interval during calibration.
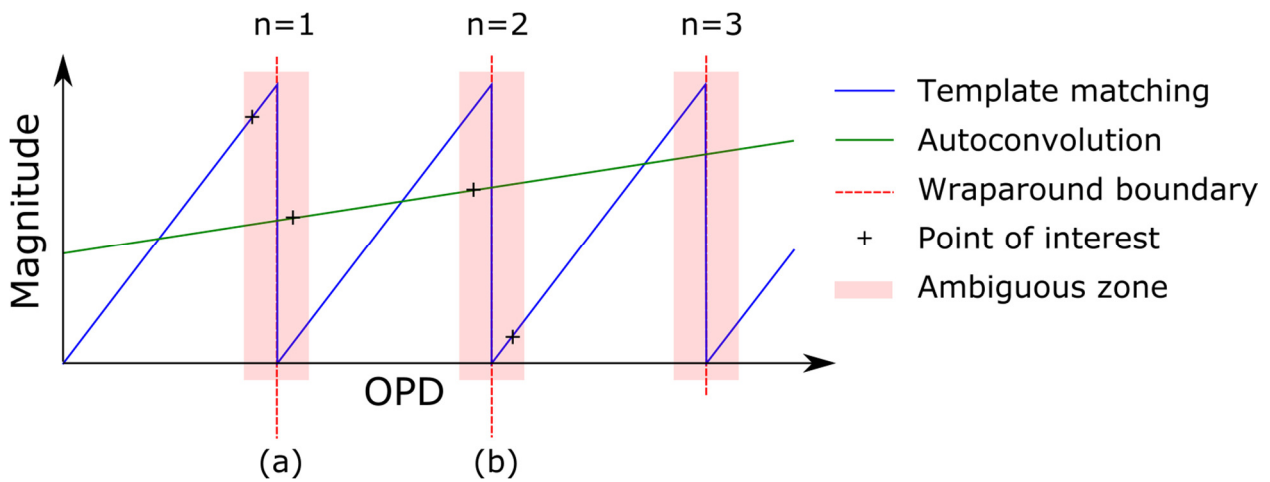
Figure 5.5: Diagram illustrating the regions of interest for use in phase order correction

For the wraparound marked (a), two points have been marked on the template matching and autoconvolution plots. In this example, using the autoconvolution result to determine wraparound order would result in a calculated order where $n=1$, however multiplying the order by the wraparound distance ($\lambda/2$) and adding the template matching result would result in a value of 825 nm when clearly the order should be zero and the result only 400 nm. In this case, to correct for such a positive order error, a comparison of the autoconvolution and relative position results to the order boundary is necessary for correction. If the relative value is high (> 275 nm) but the difference between the autoconvolution value and the lower order boundary is less than 1 pixel then decrementing the wraparound order will correct positive order errors.

Conversely, for the points of interest on the relative position and autoconvolution plots above the ambiguous zone marked (b), a negative order error will result. Correction of this is possible, with errors detectable if the relative position value is low (< 150 nm) but the autoconvolution value is close to the upper wraparound order boundary (< 1 pixel). In this case then incrementing the order will correct negative wraparound order errors.

Figure 5.6 and figure 5.7 demonstrate high resolution absolute position calculated with and without wraparound order correction. In these plots the original high resolution position is shown in green, with the calculated wraparound order in red and the final high resolution but absolute position in blue. The plot without wraparound order error correction (Figure 5.6) shows several negative order errors and many positive order errors. Application of order error correction to the same data results in the graph in figure 5.7 in which all wraparound order errors have been remedied.

This 9 μm axial scan data set demonstrates the method while still allowing visualisation of the template matching wraparounds.

.
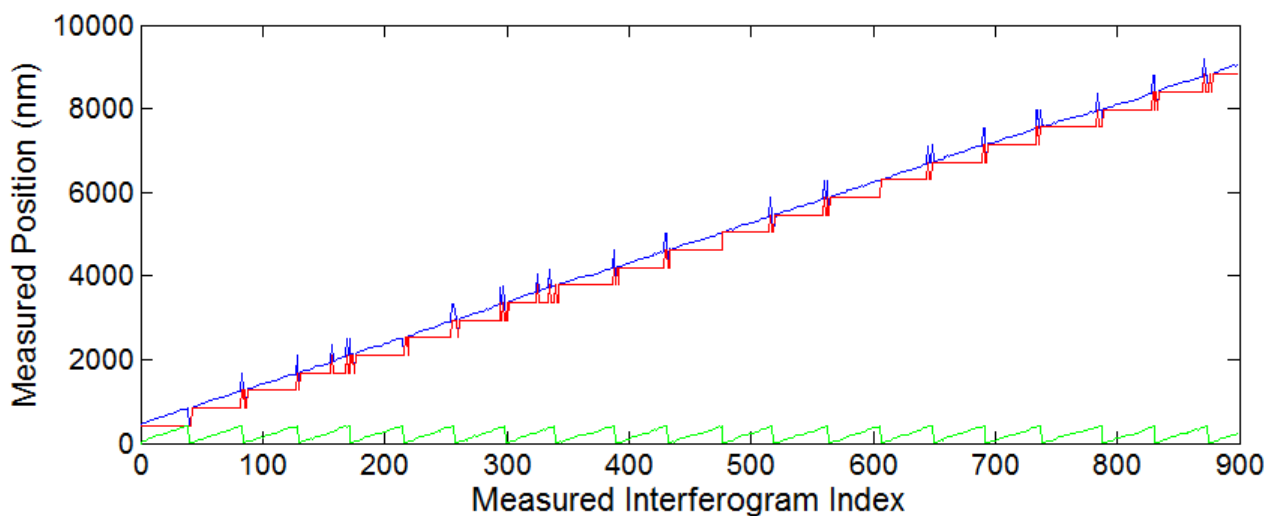
Figure 5.6: Wraparound order determination without order correction. Plots of relative position (green), calculated wraparound order (red) and high resolution absolute position (blue) including wraparound order errors (blue spikes).
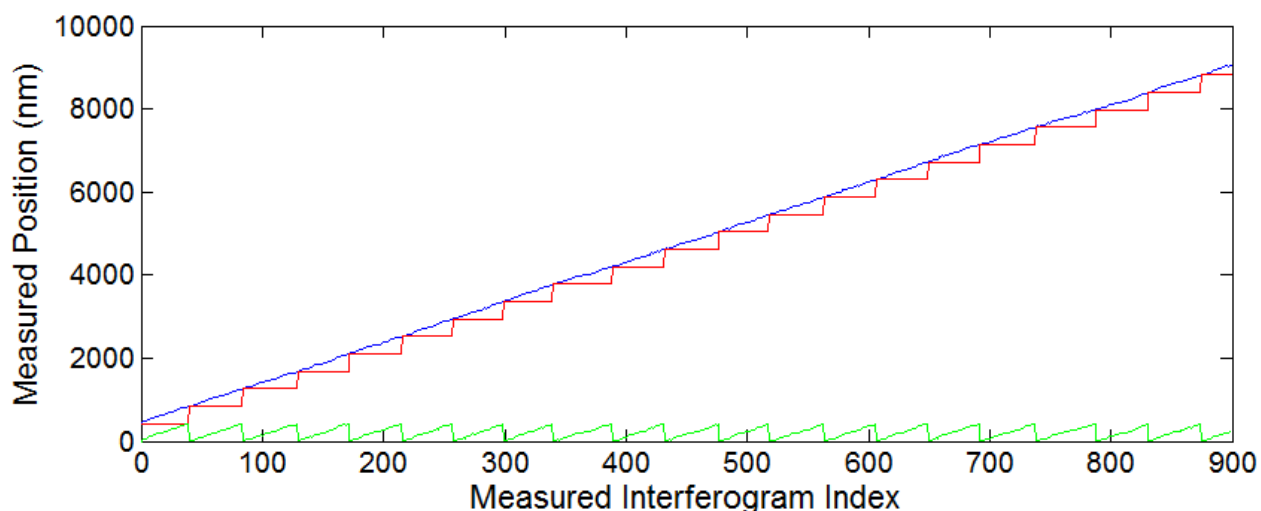
Figure 5.7: Wraparound order determination with order correction using the same data as figure 5.6. Plots of relative position (green), wraparound order (red) and high resolution absolute position (blue) exhibiting no wraparound order errors.

5.6   Range and resolution

Resolution: The resolution of wraparound order determination is defined by the resolution attainable by template matching. Due to the experimental changes (detector width, SLED bandwidth and grating spacing) implemented for this section of work, measurement of the achievable resolution is repeated here using the same method used for template matching in section 4.5.2. For this measurement all relative position values over a 60 second period are recorded before levelling is applied to remove drift. As with previous efforts, the measurement noise is the limiting factor of template matching and hence the resolution of wraparound order determination. The mechanical noise is expected to be nearly

identical to the previous measurement with the optical and electrical noise from the new SLED and detector the only changes.

The standard deviation of a set of data with no axial position changes was calculated to be 0.7 nm, with this being the lower limit of resolution expected. This agrees well with previous simulated calculations, showing that changes to the bulk optics interferometer to increase the range have not degraded the template matching resolution due to the reliance of template matching on the wavelength not grating separation.

Range: The range of template matching order determination is ultimately dictated by the physical characteristics of the interferometer, with light source bandwidth, perpendicular grating separation and grating pitch determining the spectral interferogram shape and hence range.

Due to the increased SLED bandwidth and spectrometer detector pixel count, the wavelength spectrum incident upon the detector is wider and so the number of visible interference fringes is increased. The range of this improved setup has been estimated in simulation as 800 μm and measured experimentally as up to 760 μm. The lower experimental range can be explained by the imperfect nature of the alignment and the background envelope imposed by the SLED spectrum shape resulting in an autoconvolution result whose peak degrades earlier than in simulation. Examples of simulated and real interferograms at one extent of their range are shown in figures 5.8 and Figure 5.9 respectively.
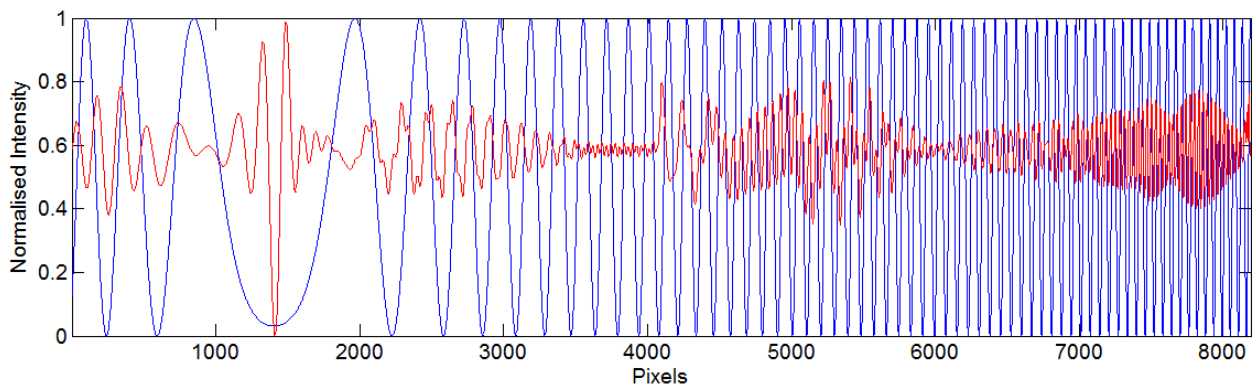
Figure 5.8: Simulated interferogram (blue) at one extent of its autoconvolution (red) range (-400 μm) for a grating separation of 220 mm, source bandwidth of 55 nm and a spectrometer detector having 8192 pixels.
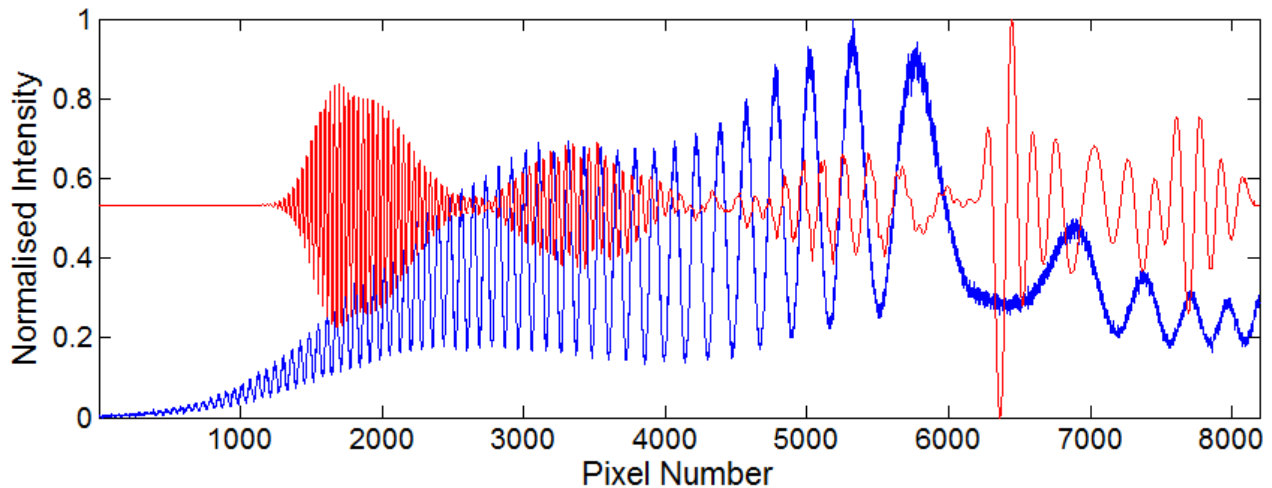
Figure 5.9: Interferogram (blue) and autoconvolution after regularisation, thresholding, derivation and smoothing (red).

To establish the range of wraparound order determination, more important than the range of autoconvolution, is the time that it takes to capture sufficient data to obtain a calibration map. The wraparound map and order determination seen in figure 5.7 is part of a set of calibration data covering a range of 30 μm. The low measurement rate (15 Hz) of current signal processing practices mean that at translation speeds low enough to ensure sufficient lateral sampling, a 30 μm calibration requires 10 minutes. Calibrations of more than ten minutes are problematic due to the low thermal stability of the interferometer in its bench-top configuration. Measurement drift due to temperature changes therefore limits the range over which the interferometer can be calibrated to 30 μm at this time. Section 8.2 of the further work section discusses GPU and FPGA implementations that will realise a 1000-fold increase in measurement rate allowing calibration over a longer range. With the Basler Racer GigE camera capable of 12 kHz line rates and other 8192 pixel line array cameras available capable of 70 kHz , acceleration of signal processing will be necessary to make wraparound order calibration more effective.

5.7   Wraparound order determination conclusions

A method for combination of the two DRI measurement regimes has been demonstrated over a range of 30 μm. The limit to the measurement range, imposed by the low measurement rate and necessity for relating one method to the other, has been described and the increased feasibility of the method with higher signal processing rates outlined.

The current measurement range has made measurement of samples problematic due to their varying sample thicknesses. Replacement of the calibration surface with a sample and levelling of the sample have been found to negate the calibration which is problematic for on-machine use.

Initial attempts to calculate the wraparound order directly from the autoconvolution result without the requirement for experimental mapping of the phase wraparound positions were unsuccessful. It is thought that this is a result of the low autoconvolution resolution (approximately 250 nm) in comparison

to the relative wraparound distance (425 nm). Reduction of the dispersion by shortening of the grating separation and alterations to the spectrometer could achieve an autoconvolution resolution below 100 nm and this would likely allow determination of wraparound order by calculation without the time consuming calibration. This arrangement would however reduce the attainable range by the same factor, providing a range of less than 200 µm. This is considered undesirable considering the focus of this work on achieving high dynamic range to maximise potential measurement applications.

For these reasons future work will include a review of alternative methods of signal processing to develop a more robust method of high resolution, absolute measurement. It should be highlighted that the less than ideal results presented in this section are not a problem inherent with the DRI method but perhaps with a somewhat non-optimal approach to combination of measurement methods.

The development of wraparound order determination confirms the ability of DRI to provide high resolution absolute measurement data, with the range of this method subject to further improvements. A final important aspect of single-point embedded metrology, is the ability for methods of measurement to interrogate remote fibre probes, with miniaturisation of the probe allowing unobtrusive mounting in a machine tool environment. Interrogation optics would therefore consist of the bulk of the interferometer, with light source, bulk optics interferometer components, spectrometer and associated power supplies and computing resources located remotely. A common-path remote fibre probe DRI variant is demonstrated in chapter 6.

6 Prototype DRI – Development of remote fibre-linked probing

6.1 Introduction

Development of a small, light and compact fibre-linked probe is a key feature required to provide DRI the ability to perform on-machine surface topography measurement. This will facilitate separation of bulky and comparatively fragile interrogation optics from a cheaper, smaller and more robust probe. This chapter introduces the changes required to DRI to accommodate remote fibre probing while maintaining the ability to perform high resolution, absolute measurement. Various probe architecture options are introduced before compactness, price and performance of these probe options is discussed. A common-path fibre-linked Fizeau probe layout is then implemented and the core functionality of DRI with this probe is demonstrated.

6.2 DRI configuration with fibre probe

A key feature of any fibre linked probe topology for DRI is the use of common path probes so that both the reference and measurement arms travel identical paths within the fibre. In this way, phase changes in the fibre due to temperature and strain are experienced equally by both arms of the interferometer and thus cancel out. For micron resolution fibre interferometry as demonstrated by Pavlícek and Häusler [78] non-common paths may be acceptable, but for methods approaching nanometre resolution, a common path configuration is an essential feature [37].
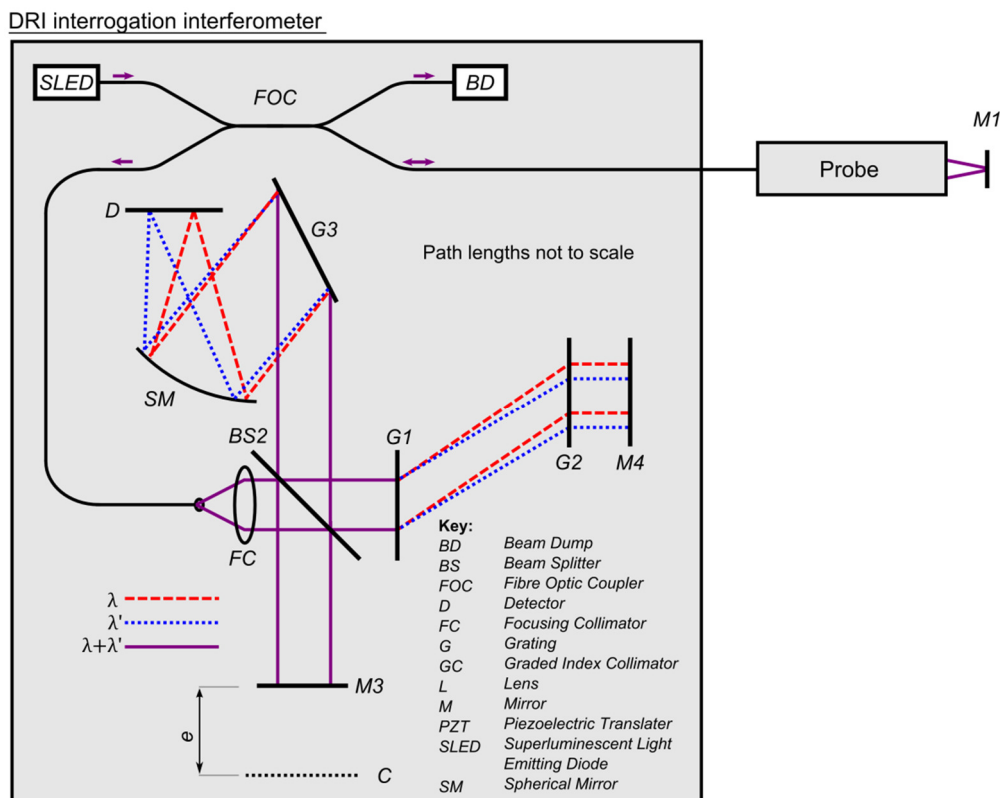
Figure 6.1: DRI interrogation interferometer with a fibre linked probe.

Throughout this chapter, the bulk optics DRI interrogates a remote fibre probe to calculate surface height information. It will be referred to as the 'interrogation interferometer' to separate this fibre linked interferometer version and its operation from previously described variants of DRI.

To implement common path fibre probing for DRI, the measurement system is composed of two parts. The DRI interrogation interferometer contains the light source, detector and bulk optics necessary to perform dispersed reference interferometry. Instead of immediate collimation of the light source into the interferometer however, the SLED is coupled out of the device into a single mode fibre leading to a remotely located probe.

Within this probe the light is collimated and split into two paths, one of which is immediately retroreflected back into the fibre to form the reference beam. The remaining light forms the measurement beam and is focused upon the measurand by a lens before passing back through the lens, collimator and into the fibre. The optical path difference between the reference and measurement beams within the probe is critical to the method, where the additional distance travelled by the measurement beam is the round trip distance, $2e$, travelled by the measurement beam after creation of the reference beam.

The combined reference and measurement beams are next returned to the interrogation interferometer where a fibre coupler directs them into a modified version of the DRI from chapters 3-5. It is not immediately apparent that the measurement and reference beams generated within the probe are separable but after collimation of the light returned from the probe, a beam splitter divides the combined measurement and reference beams into two parts, each containing equal amounts of each beam. Use of these beams with an unmodified DRI would result in a spectral interferogram as normal, but the phase difference between the arms would not change as the measurement surface at the probe moved. In order to make the interferometer sensitive to surface height changes at the probe, the length of the interrogation interferometer arms must be modified to match the path length imbalance between the reference and measurement beams in the fibre probe. This requires increasing the length of the interrogation interferometer reference arm or decreasing the length of the measurement arm by the probe path imbalance length e. To minimise the interferometer size, it is beneficial to choose reduction of the DRI measurement arm length instead of increasing the reference arm length.

Modification of the DRI arm lengths in this way brings the two beams of interest back into coherence. This is possible so long as the coherence length of the light source, in this case approximately 15 μm, is less than the path imbalance, $2e$. While the non-coherent portions of the light will have the effect of adding a

DC offset to the interferogram as well as reducing the visibility, the advantages of a fibre connected probe tolerant of environmental effects far outweigh the reduction in visibility.

6.3 Probe configurations

Consideration of interferometric probe architecture is provided here, with layout of a Michelson and Fizeau variant shown as well as discussion of the advantages and disadvantages of each.

Michelson: In a Michelson configuration DRI probe the collimated light exiting a GRIN collimator, GC, is split by a beam splitter, BS1. The perpendicularly reflected component of the light forms the reference arm and is retroreflected by M2 back through the beam splitter and into the GRIN collimator.
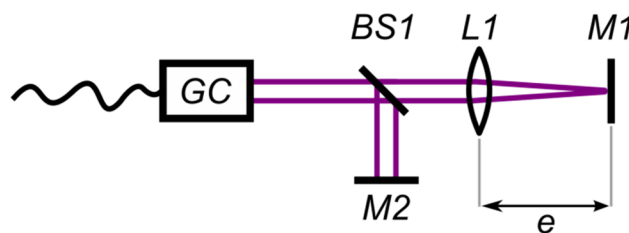
Figure 6.2: Michelson configuration bulk optics probe

The second component of light continuing through the beam splitter comprises the measurement arm of this interferometric probe objective, where it is focused by a lens, L1, and reflected from the measurand surface, M1, before passing back through the lens and beam splitter.

The spatially separated nature of a bulk optics setup make experimental alignment of this method easier than more compact probes and is ideal for an initial attempt at validation of fibre linked probes for DRI. A second advantage of the Michelson configuration is the easy control it allows over the respective reference and measurement arm path lengths. Since the reference arm is not co-axial to the measurement beam then the length of the reference arm can be more easily set independently of the measurement arm length, allowing interchangeability of the probe for differing focal length objectives. The drawbacks of the Michelson probe described above are the limited scope for probe size reduction offered with when compared to alternative configurations as well as the increase in non-common paths experiences by the beams in such an objective. A similar interferometric probe configuration is used by Precitec for use with their CCSI though the low NA of their probe design mean its use is restricted to distance measurement and not surface topography measurement.

Fizeau: A Fizeau configuration DRI probe operates by creation of a reference beam using a co-axially located semi-reflective surface. In the case of a prototype DRI probe this is a plate beam splitter with a dielectric coating, allowing retro-reflectance of a significant component of the light exiting the GRIN collimator. In a commercial probe this will be applied at the fibre-air interface by either a semi-reflective

coating or the reflection from a non-coated fibre termination as in the case of probes designed and supplied by Fionec Gmbh for their LCI instrument [73].
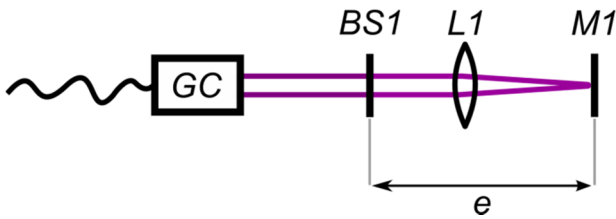
Figure 6.3: Fizeau configuration fibre linked probe

In a prototype Fizeau probe for DRI, light passing through the beam splitter is focused upon the measurement surface by a lens, L1, before passing back through the lens, beam splitter and into the fibre collimator. Distance e again dictates the offset required within the interrogation interferometer but similarly to the Michelson configuration, this distance can be maintained between probes of differing focal lengths by adjusting the distance between the beam splitter and the objective lens accordingly, thus offering interchangeability of probes. Strengths of the Fizeau probe include the co-axial design of the probe, with components arranged along the optical axis in contrast to Michelson probes for which the reference arm protrudes from the side. A disadvantage of this probe for initial validation of fibre probe configurations for DRI is the difficulty in achieving a compact arrangement while providing the adjustability for prototyping.

6.4 Remote probe experimental setup

The schematic in figure 6.4 shows a Fizeau fibre probe coupled to the previously described DRI apparatus. The SLED ($\lambda_c = 850$ nm, $\Delta\lambda = 50$ nm) is coupled into a single mode fibre after which it enters a bi-directional single mode fibre optic coupler, FOC, optimised for use at 830 nm and with a 50:50 split ratio. Light exiting the first output of the coupler is discarded to a beam dump, BD, while the second output is coupled into a gradient-index (GRIN) collimator, GC, which provides an output beam of 0.5 mm at FWHM.
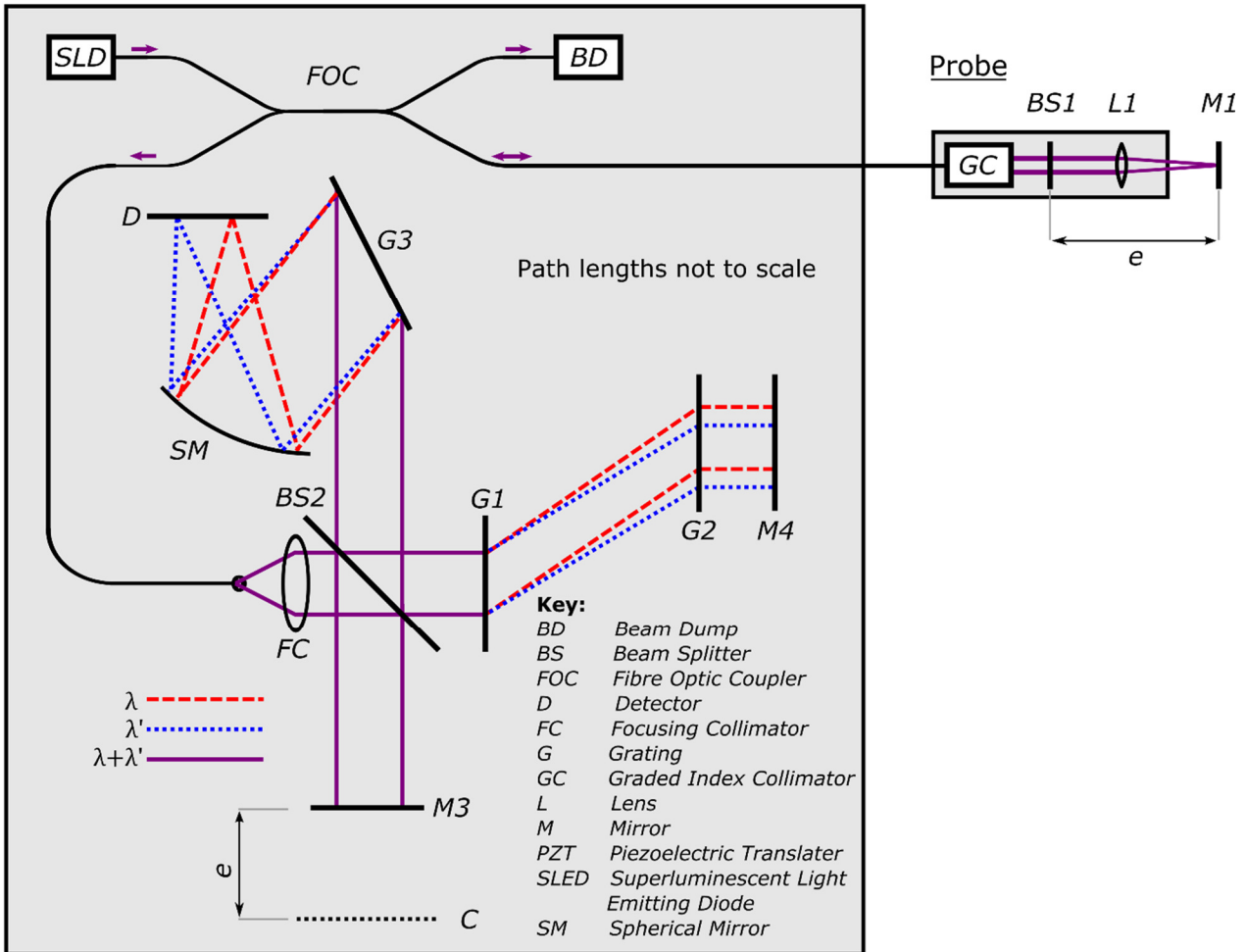
Figure 6.4: Interrogation interferometer (left) with fibre linked probe (right)

Next, a 30:70 R:T plate beam splitter placed perpendicular to the beam axis reflects 30% of the light back into the GRIN collimator, forming the reference arm beam in the process. The remaining 70% is focused onto the measurand by a lens, L1, before being reflected back through the lens and beam splitter. In this initial investigation, a plano-metallic mirror, M1, replaces the measurand. The distance from the partially reflective surface of the beam splitter to the focal point of the lens is henceforth labelled as e, the probe compensation distance.

Once recoupled back into the GRIN collimator, both measurement and reference beams pass back through the fibre coupler where 50% of the light is coupled back towards the SLED and the remaining 50% enters the interrogation interferometer. In future iterations of the interferometer design, if more optical power is required the losses experienced in the fibre coupler can be reduced through use of an optical circulator which would result in as little as 10% loss before the interrogation interferometer instead of more than 75% with the optical coupler. However, the availability and low cost of the fibre coupler make it an attractive alternative to a circulator for an initial investigation into fibre probing for DRI.

Use of the previously outlined interferometer layout with the remote fibre probe configuration described above would result in the measurement and reference beam not interfering coherently due to the $2e$ path length imbalance introduced within the fibre probe head and the low coherence of the SLED light source. In order to compensate for the path difference, the length of the interrogation interferometer measurement arm is decreased by e to eliminate this path imbalance. The interrogation interferometer measurement arm position, C, where the phase vertex of the interferogram would have previously coincided with the spectrometer centre is marked on the diagram in figure 6.4. While both measurement and reference beams generated within the fibre probe are present in both arms of the interrogation interferometer, subtraction of the probe compensation distance from the interrogation interferometer measurement arm means that only the correct beams interfere, albeit with a lower visibility due to the background intensity of the non-interfering beams.

6.5   Prototype Fizeau interferometric probe

For commercial interferometer systems, a compact, cheap fibre probe is desirable, allowing use of optical fibre probes for previously difficult to measure geometries and in manufacturing environments with limited work volume. Small probes allow increased choices of mounting options without obscuring machine-tool attachments thus increasing usefulness of metrology tools. However, miniaturisation of probe technology is expensive for low volume production and so construction of a prototype probe using commercial off the shelf components allows evaluation of proposed probe configurations without the need for expensive prototyping runs of miniaturised fibre probes. As such, this section presents the design and testing of such a prototype probe, drastically reducing the on-machine measurement instrument size when compared to the bulk optics instrument used throughout chapters 3 to 5.

6.5.1   Probe design

Figure 6.5 shows SolidWorks renders of the prototype probe configuration. The beam exits into free-space from a pigtailed GRIN collimator (Thor Labs 50-850-APC). The 0.5 mm FWHM beam is incident upon a 30:70 (R:T) plate beam splitter, the first surface of which reflects 30% of the incident light back into the GRIN collimator. Mounting of the beam splitter within a miniature kinematic mount allows alignment of the beamsplitter to retroreflect 30% of the introduced beam back into the fibre. Light passing through the

plate beam splitter is focused upon the measurand by an aspheric doublet. A custom machined aluminium base holds the kinematic mounts in position allowing easy relocation and alignment of the probe with respect to the work piece where the probe has an assembled size of less than 30 x 40 x 50 mm. Figure 6.5 illustrates the optical components held within the kinematic mounts, with optical components highlighted in blue. Figure 6.6 shows an isometric rendering of the probe in SolidWorks as well as a photo of the finished prototype probe.
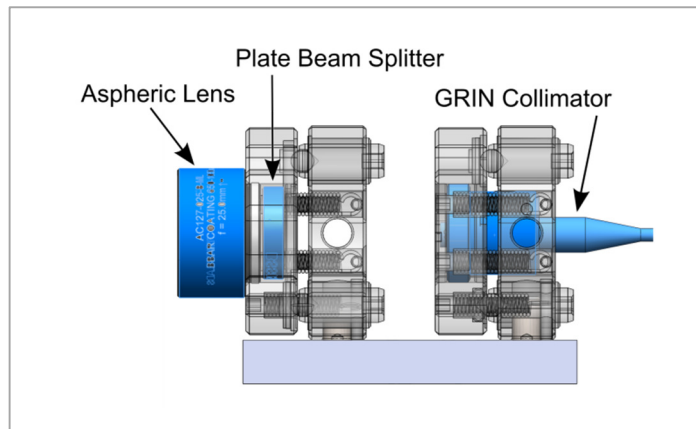
Figure 6.5: Cutaway of kinematic mounts to show location of critical optical components.
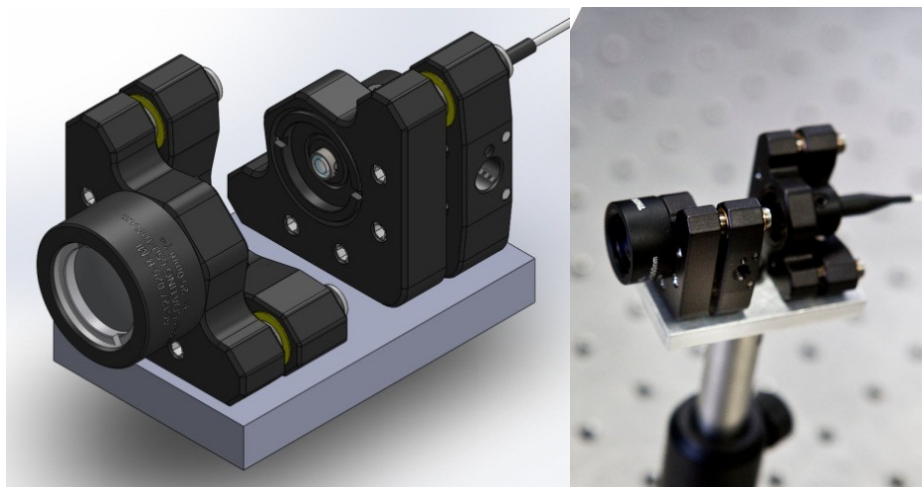
Figure 6.6: SolidWorks render of bulk optics probe miniaturisation (left), and a photo of the manufactured probe prototype (right).

6.5.2   Prototype Fizeau probe initial validation

The greatest strength of such a probe, even in a comparatively bulky prototype configuration such as this one, is the ability to operate in constricted spaces. A key disadvantage of this new configuration when compared to the bulk optics DRI implementation without the probe, is the necessity to compensate for the distance, e, travelled by the beam from the beam splitter to the measurand and back. The effect this has can be seen in figure 6.7 where the interferogram has a DC offset across the entire width of the interferogram as well as significantly lower visibility. This is caused by the component of light in each arm

that does not interfere coherently since the beam splitter in the bulk optics interferometer cannot separate the two arms. The result of this is a limit to the visibility of the interferogram to 50%.

While the interferogram shown in figure 6.7 does exhibit reduced visibility compared to interferograms from non-fibre linked DRI, the visibility remains sufficient to successfully perform autoconvolution as demonstrated by figure 6.8.
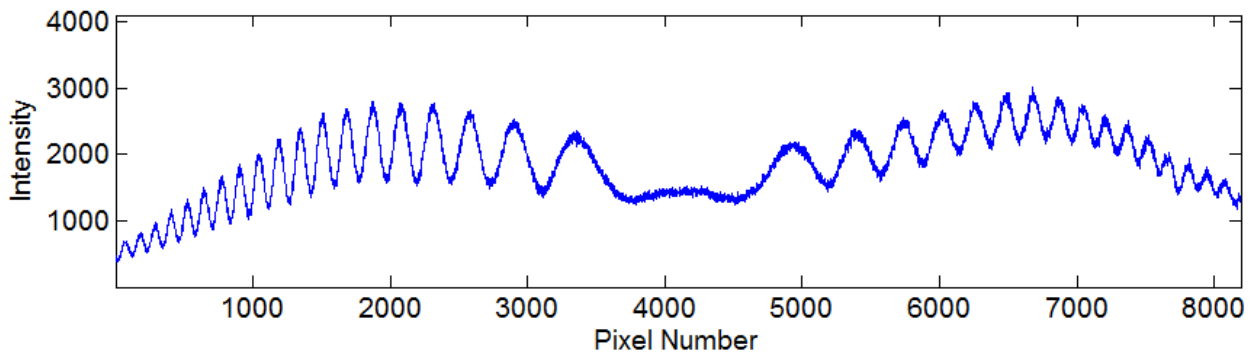
Figure 6.7: Interferogram from fibre linked probe. Demonstrates lower visibility compared to bulk optics interferometer as well as a DC offset caused by the non-coherent portions of the light source present in each arm.
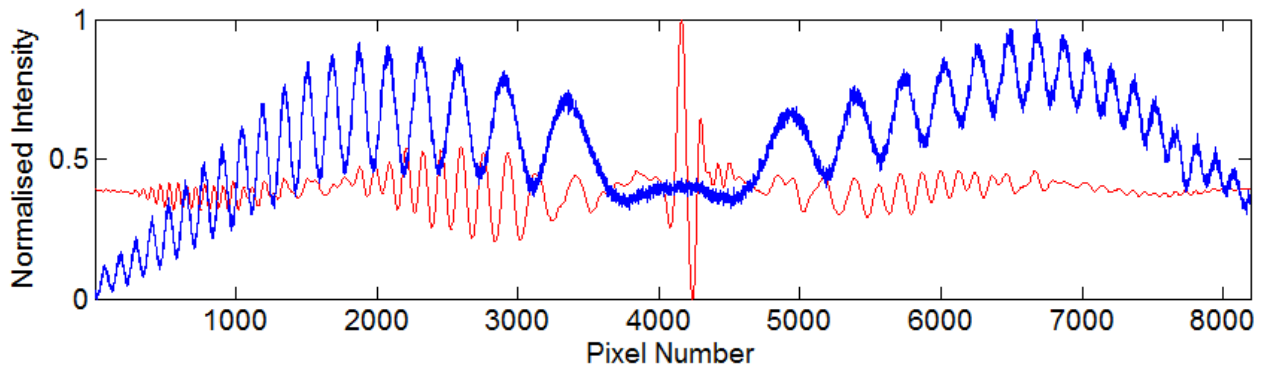
Figure 6.8: Normalised interferogram and autoconvolution result to demonstrate visibility remains sufficient for successful signal processing

6.5.3 Design considerations for remote fibre probes

Having confirmed operation of remote fibre probing experimentally, it is important to consider the effect of fibre probes on the axial range and lateral resolution of dispersed reference interferometry. The following tables outline the attainable beam waist and depth of focus for each available lens and collimator choice. At this development stage, probes are not interchangeable on the interferometer due to the fixed size of the probe base. Changing of the lens focal length requires adjustment of the interrogation interferometer measurement arm length but this will be easily solved in future iterations by manufacture of different probe bases with the lens position in relation to the beam splitter varying depending on the focal length of the lens. In this way the probe offset distance, e, will remain consistent between probes as described in the further work in section 8.4.2.

For a single-point method of measurement such as DRI, the properties of the focused beam dictate both the lateral resolution of the probe and the axial range over which this spot size remains acceptable for measurement. Focused beam characteristics are dependent on the diameter of the input beam and the focal length of the lens. In the work that follows, a selection of 4 fibre collimators and 6 achromatic doublet lenses are used to calculate tables showing the spot size, depth of field and acceptance angle for each collimator and lens combination. These tables of values allow visualisation of the relationships between the collimator/lens pairs and enable informed design of probes for a variety of applications. Comparisons of these component combinations can then be made and applications suggested, though measurement of experimental spot size, depth of field and lateral resolution remain a task for further work.

The collimator and lens characteristics are shown in tables 6.1 and 6.2 respectively, with parameters of particular interest the full width half maximum beam diameter, ϕ_b, as well as the focal length of the lenses, f.

Collimator Model	Design Wavelength (nm)	Beam dia. FWHM (mm)	Working Distance (mm)
50-850-APC	850	0.5	15
CFS11-850-APC	850	1.24	11.1
F280APC-780	780	2.35	18.4
F810APC-842	810	4.59	36.18

Table 6.1: Table of available Thor Labs fibre collimators including their design wavelength and FWHM beam diameter, θ_b.

Lens Model	Focal Length (mm)	Lens Diameter (mm)
A110TM-B	6.24	9.24
A375TM-B	7.5	9.24
LA1540-B-ML	15	12.7
AC127-025-B-ML	25	12.7
AC127-050-B-ML	50	12.7
AC127-075-B-ML	75	12.7

Table 6.2: Table of achromatic doublets (Thor Labs) available for probe configuration and testing.

The spot size (in microns) for a combination of each lens and collimator is calculated using equation 6.1 and results in the values shown in table 6.3. The beam waist radius of a Gaussian beam is the point at which it reaches the minimum beam waist radius, ω_0, and is an important consideration in single point metrology since the beam waist radius of a focused beam determines the minimum spot size and hence the maximum attainable lateral resolution of the system. The beam waist radius, ω_0, for a given wavelength at focal length, F, is given by

$$2\omega_0 = \left(\frac{4\lambda}{\pi}\right)\left(\frac{F}{D}\right) = \phi_s$$

<div align="right">6.1</div>

where λ is wavelength, F is the focal length of the lens and D is the input beam diameter. The beam width may also be determined as the distance from the optical axis at which the intensity drops to 50 % of the original intensity, known as the full width half maximum (FWHM). The beam diameter at the focal point is twice the beam radius and often described as spot size. It is given the symbol ϕ_s.

It is apparent from this table that increased diameter input beams in conjunction with shorter focal length lenses result in the minimum focused spot size.

Beam Dia. (mm)	4.59	2.35	1.24	0.5
Focal Length (mm)				
6.24	1.47	2.87	5.45	13.51
7.5	1.77	3.45	6.55	16.23
15	3.54	6.91	13.09	32.47
25	5.89	11.51	21.82	54.11
50	11.79	23.03	43.64	108.23
75	17.68	34.54	65.46	162.34

Table 6.3: Spot size, ϕ_s, in micrometres for a selection of fibre collimators and achromatic doublet lenses.

In conjunction with spot size, the lens focal length and input beam diameter also dictate the depth of field of the optical probe. The depth of field is defined as twice the Rayleigh length, which describes the distance from the focal point at which the beam remains less than $2\omega_0\sqrt{2}$. The depth of focus and its relation to the Rayleigh length is calculated as follows,

$$DOF = \left(\frac{8\lambda}{\pi}\right)\left(\frac{f}{D}\right)^2 = 2z_R$$

<div align="right">6.2</div>

Where λ is wavelength, f is the lens focal length, D is the input beam diameter and z_R is the Rayleigh length [109].

The depth of field information displayed by table 6.4 illustrates that the depth of field for such small focused spot sizes decreases with the reduction in focal length and with increasing input beam diameter. Conversely, it is apparent that as the depth of field exceeds 100 μm the spot size in turn increases beyond 10 μm. This limit to the spot size to depth of field ratio is a problem inherent with the use of Gaussian optics for single-point metrology. In these instances it is important to choose a lens and collimator combination that provide enough vertical range (DOF) and low enough lateral resolution (spot size) for the measurement application.

Beam Dia. (mm)	4.59	2.35	1.24	0.5
Focal Length (mm)				
6.24	4.00	15.26	54.81	337.12

7.5	5.78	22.05	79.18	487.01
15	23.12	88.19	316.74	1948.06
25	64.21	244.96	879.82	5411.27
50	256.85	979.86	3519.30	21645.07
75	577.90	2204.68	7918.41	48701.41

Table 6.4: Depth of field (DOF) in micrometres for combinations of fibre collimators and achromatic doublets.

While the beam spot size does not equate exactly to the lateral resolution of the probe and must be measured experimentally, it is indicative of the lateral feature sizes which may be measured. Similarly, the depth of field is an arbitrary cut-off for the size of the beam at a distance from the focused beam waist. For some applications a larger beam width may be acceptable beyond that indicated by the spot size or depth of field.

Another important probe parameter which varies with input beam diameter and lens focal length is the acceptance angle of the probe, θ_a. This is the maximum angular deviation from perpendicularity to the optical axis at which the measurand can exist while still returning light to the lens.

$$\theta_a = \tan^{-1}\left(\frac{D}{2f}\right)$$

6.3

The acceptance angle, θ_a, of an optical component (lens, collimator, optical fibre) is half the angular aperture, α, with the acceptance angle being the angle between the beam normal and the path travelled by a ray traced along the outside diameter of the input beam. This is important for measurement purposes as it dictates the maximum measurable surface slope as well correlating strongly with the ability of the lens to collect sufficient scattered light on rougher optical surfaces. Table 6.5 shows the acceptance angle calculated for the same selection of input beam diameters and lens focal lengths.

Beam Dia. (mm)	4.59	2.35	1.24	0.5
Focal Length (mm)				
6.24	20.19°	10.66°	5.67°	2.29°
7.5	17.01°	8.90°	4.73°	1.91°
15	8.70°	4.48°	2.37°	0.95°
25	5.25°	2.69°	1.42°	0.57°
50	2.63°	1.35°	0.71°	0.29°
75	1.75°	0.90°	0.47°	0.19°

Table 6.5: Acceptance angle calculated for available lens and collimator pairs.

While angles above 10° are shown in the top left section of the matrix, these are not desirable for measurements with DRI due to the short measurement ranges (<20 µm) provided by probes with these limited depths of field. For this reason probes for DRI are theoretically limited by Gaussian optics to measurement of surface slopes of less than 9° from perpendicular to the optical axis. It is also important to emphasise that the acceptance angles quoted above are the maximum angle at which a ray can be recollimated after passing back through the lens. Realistically the ability of DRI to measure sloped surfaces will deteriorate at shallower angles as the optical power returned from the measurement surface

decreases. This drop in the measurement arm power will adversely affect the interferogram visibility as the angle of incidence increases and the number of rays collected decreases [110]. It is possible that this limitation of Gaussian optics may be avoided by exploration of non-diffracting beam optics such as Bessel beams.

For demonstration of remote fibre probing, section 6.2 describes design of a probe using a GRIN collimator with a beam diameter of 0.5 mm FWHM and a lens of focal length 15 mm. The spot size, depth of field and acceptance angle for a probe with such components is shown below.

Input beam diameter	Lens focal length	DOF	Spot size	Acceptance angle
0.5 mm	15 mm	1948 µm	32.47 µm	0.95°

Table 6.6: Critical parameters for prototype Fizeau probe

The components for this prototype probe were chosen for maximum ease of alignment, resulting in a probe with parameters which are non-optimal for surface topography measurement. The GRIN lens chosen was found to easily recouple light returned from the reference surface where achromatic doublet collimators resulted in difficult or reduced efficiency coupling of the reference beam back into the fibre. The 1948 µm DOF afforded by this probe is excessive for DRI due to the current 800 µm range, while the low acceptance angle makes alignment of the sample and sensitivity of the probe to tilt problematic.

With successful demonstration of the DRI remote fibre probing configuration using this easily aligned probe, future probe development will focus on probe configurations for specific applications. A DOF of 880 µm, spot size of 22 µm and acceptance angle of 1.42 ° is achievable with a probe consisting of a 1.24 mm input beam and 25 mm focal length lens and would be appropriate for measurement of high aspect ratio features on specular surfaces. It is probable that improved placement of the probe reference surface at the collimated beam waist will allow efficient recoupling of the reference beam back into the fibre where it was found problematic previously.

A probe for measurement of surfaces with higher surface roughness requires a higher acceptance angle to improve the light gathering ability of the probe and so it will be necessary to sacrifice the depth of field to accommodate this. Probe parameters of $D = 2.35 \text{ mm}$ and $f = 15 \text{ mm}$ will result in depth of field, spot size and acceptance angle of 88 µm, 6.91 µm and 4.48 ° respectively and providing a probe for evaluation of the ability of DRI to measure rough surfaces.

6.6 Prototype interrogation interferometer

This section describes the design and manufacture of a prototype DRI interrogation interferometer. Motivations for doing so are introduced, design decisions justified and diagrams and photos of work in progress displayed.

For DRI to be an attractive embedded metrology solution, the interrogation interferometer described above must be reduced in size, with design of a prototype allowing easy relocation of the interferometer for testing on-machine, something not possible with the previous optics table layout.

To achieve these goals it is necessary to use knowledge gained in layout of a bulk optics interferometer to design a prototype instrument that addresses the limitations of the current DRI layout while improving upon the usefulness of DRI in a manufacturing environment. Towards these ends, the following points may be considered design priorities:

- Minimise path lengths to reduce the effect of thermal changes on path lengths and angular misalignments.
- Enclosure to eliminate acoustic vibration and rapid temperature changes of components.
- Reduce cost by elimination of kinematic components where possible.
- Reduce footprint to allow easier relocation of interrogation interferometer to manufacturing environment.
- Improve manufacturability.

Approaching the design of a new instrument objectively, it is also important to predict problems that may arise from transition from a flexible, easy to align table top DRI variant to one that is more optimised for cost, space and performance. To this end the following points may be considered key design concerns:

- Temperature of camera. The camera is the greatest source of heat in the interferometer. It is currently well thermally isolated from the rest of the bulk optics. During integration to achieve miniaturisation the camera will be mounted much closer to other temperature sensitive components and so consideration of thermal isolation is expected to be a future problem.
- Ease of alignment. Further miniaturisation of the system is possible but would require multiple folding mirrors to achieve a substantially smaller prototype. The interferometer seen in figure 6.9 compromises to allow a substantial reduction in area when compared to the current interferometer with use of only 2 folding mirrors.

The initial layout of an interrogation interferometer was provided to a colleague for refinement and mechanical improvements having placed the optical components and kinematics in the correct positions. Ground aluminium plate, 20 mm thick, was chosen as the material for the interferometer base. The lower

cost and improved machinability when compared to steel or invar were the main aspects for this decision. Once classification of interferometer performance has been completed, it can be assessed if the increased cost and difficulty of manufacture from using invar is worth the significantly lower coefficient of thermal expansion.

Another design choice is that external connections to the interrogation interferometer should be minimised. With this in mind the SLED light source and power supplies (PSU) for both the camera and SLED are included within the instrument enclosure. This means that the only external connections are the fibre probe, Gigabit Ethernet for the camera and 240 VAC. Concerns for the inclusion the PSUs and light source are the heat and mechanical noise generated by these components. The high efficiency of modern switched mode power supplies (SMPS) means that little heat will be produced meanwhile the thermal output of the SLED has observed to be minimal when compared to that of the Basler camera. Mechanical noise associated with heat sources within the interferometer enclosure is to be minimised by passive cooling of all components through the base. Firm contact with the interferometer base plate should allow dispersion of the heat throughout the base, with the 20 mm thickness of this base contributing to cooling. However, an important observation required from the construction of this prototype will be the temporal stability of such a design, with heat sources within the interferometer likely contributing to instability.

Figure 6.9 shows a plan view of the CAD design with a manual ray trace of λ_L, λ_C, and λ_U to aid visualisation of the folded beam paths within the interferometer. In this diagram it is easier to visualise the position of the reference and measurement arms, with folding mirrors apparent to enable miniaturisation of the interferometer. Key design considerations for ease of alignment dictated that all optical elements must be adjustable from the top of the interferometer, with minimal wired connections requiring that the electronics are integrated into the prototype base.

The images in figures 6.10 and 6.11 show the manufactured interferometer base populated with kinematics and optics. Classification of resolution, range, linearity, temporal stability and repeatability of this new instrument is yet to be completed but are among the planned future work for DRI development.
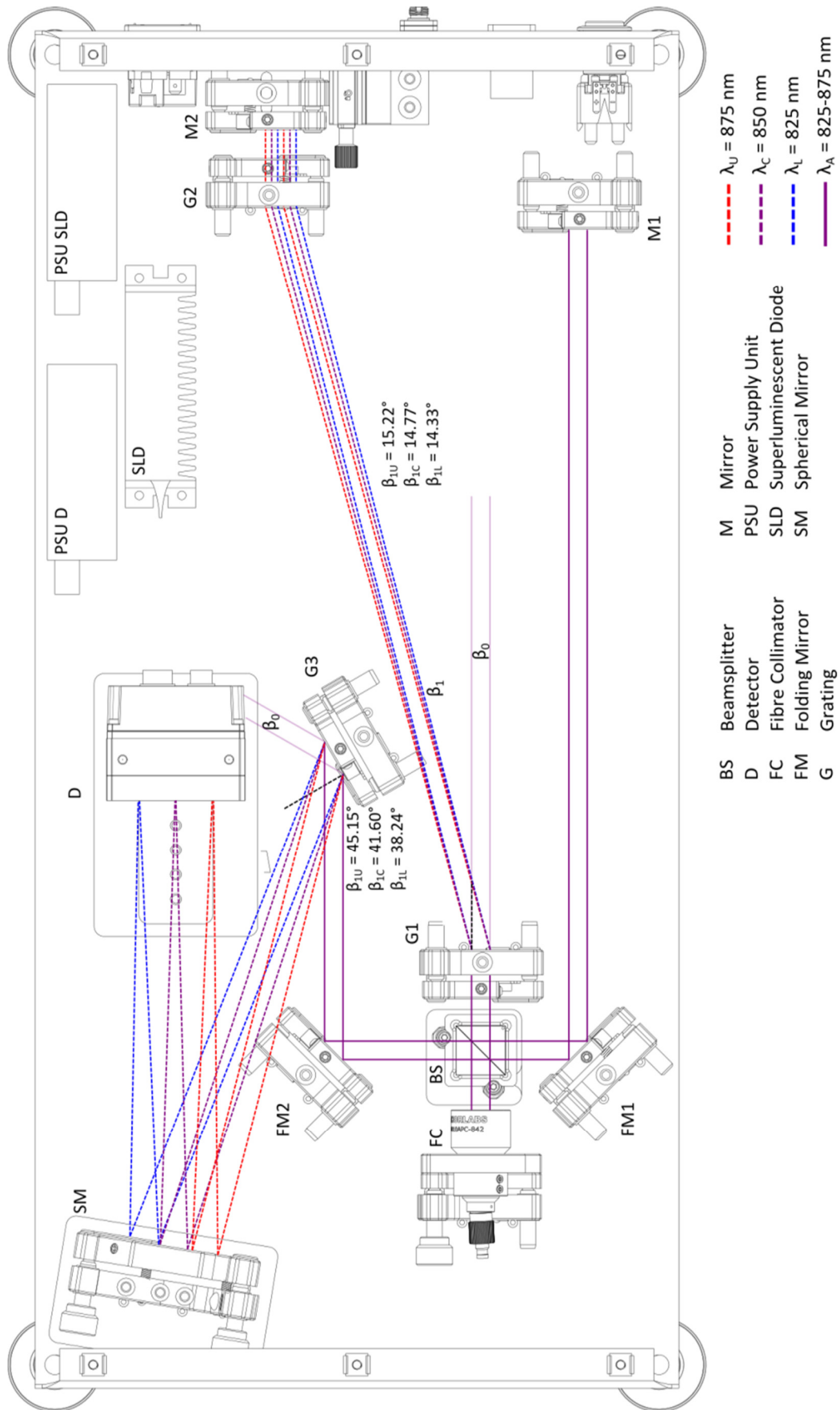
Figure 6.9: Composite Solidworks and Inkscape diagram to show the beam paths through the prototype interrogation interferometer.
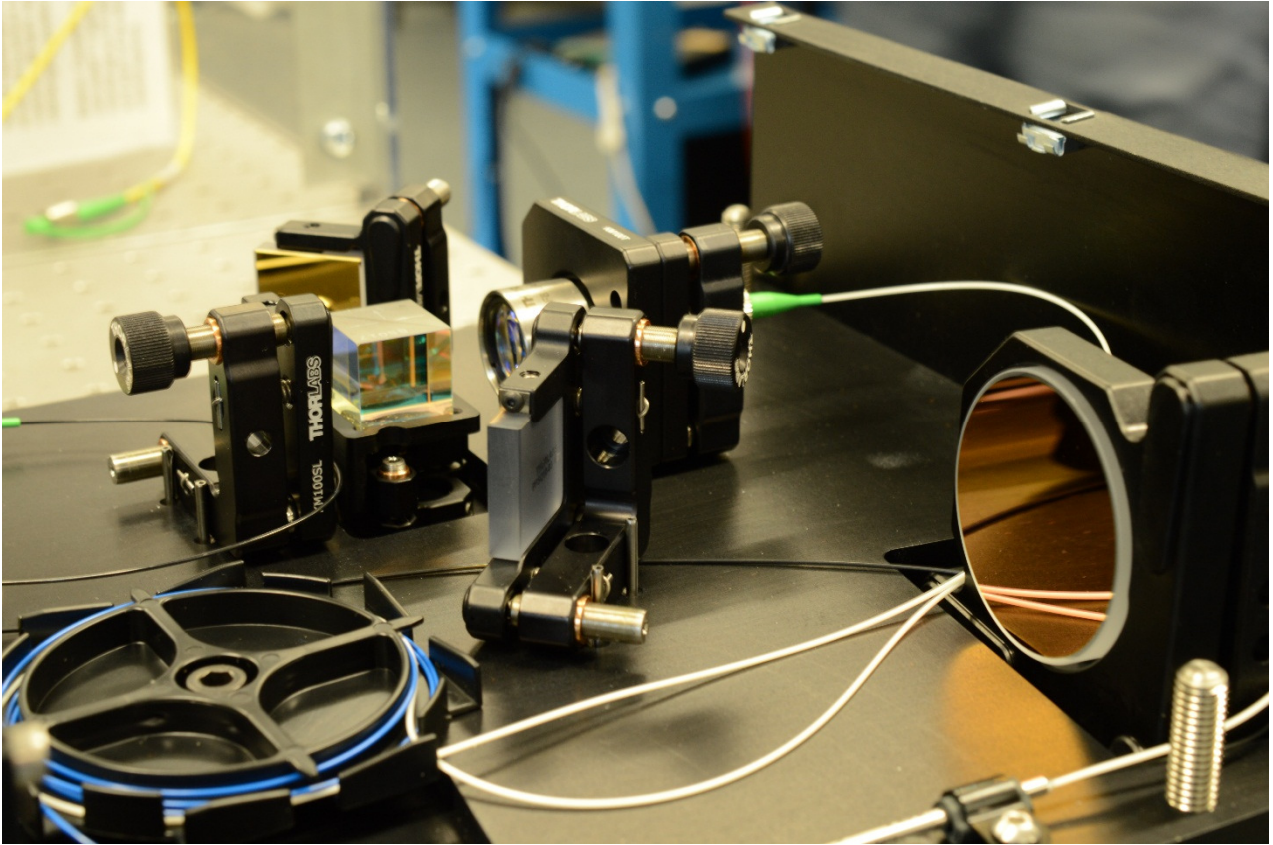
Figure 6.10: Partial view of DRI prototype including the fibre collimator, beam splitter, both folding mirrors and a spherical mirror.
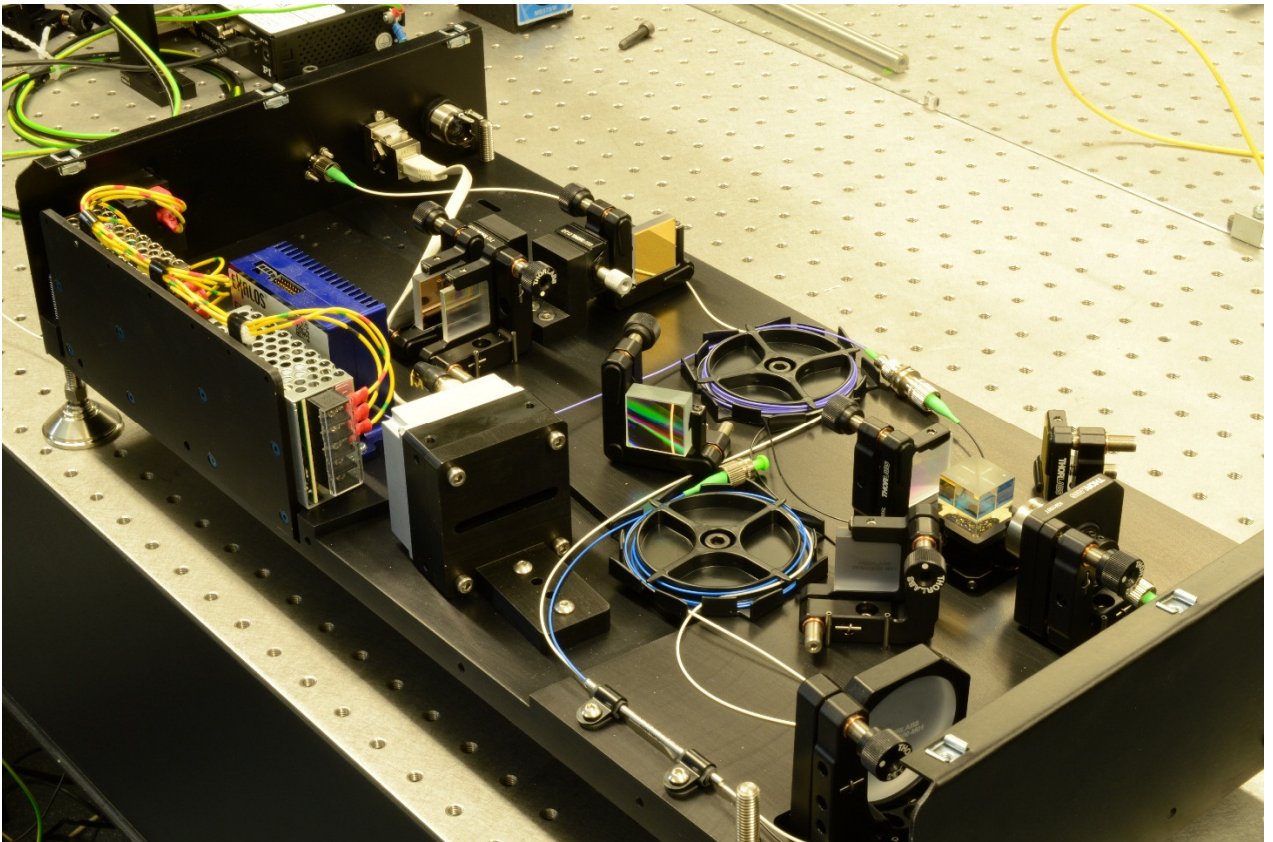
Figure 6.11: Full view of the DRI prototype.

6.7   Remote fibre probing conclusions

Two remote fibre probe configurations for use with a DRI interrogation interferometer have been introduced. The relative merits and disadvantages of each method have been discussed before a Fizeau configuration was chosen due to the increased potential for miniaturisation and reduced component count.

Next, interfacing of fibre probes and separation of the reference and measurement arms of a common-path configuration probe within the interrogation interferometer are explained while extolling the virtues of such a probe in comparison to the inherent drawbacks. The design of a bulk optics prototype probe built from cheap off-the shelf components was presented to allow demonstration of this proof of concept probe. Spectral interferograms from the prototype Fizeau probe are shown as well as the successful use of autoconvolution on these lower than normal visibility interferograms.

Discussion of the diffraction limited spot size and depth of field for remote fibre probes is provided. The parameters of a focused beam are discussed and their relation to range, lateral resolution and ability to measure slopes and rough surfaces is summarised. This will allow informed choices for the design of future probes for a of range measurement applications, be they for steep, rough or smooth surfaces, with the degree of probe miniaturisation affecting the acceptance angle and working distance of these probes.

Development of a prototype interrogation interferometer has been documented, achieving reduction of apparatus size from 700 x 800 x 250 mm to 500 x 250 x 100. This prototype has increased ease of alignment afforded by locating pins and reduced path lengths as well as now offering the possibility to physically relocate the interferometer for future on-machine testing without requiring realignment. This was not previously possible due to construction of the interferometer on an optics table. The range, resolution and linearity of this prototype interferometer are expected to be similar to that of the table-top DRI setup but remain to be confirmed.

The optical efficiency of components used for validation of the fibre-linked DRI method is yet to be considered. Changes to both the probe configuration and interrogation interferometer components will allow improvements to optical efficiency allowing faster measurement of a wider range of surface types. Careful balancing of path intensities and losses will be required for obtaining optimal interferometer performance for a given surface and is discussed further in section 8.4.

7 Conclusions

7.1 Introduction

This chapter reassesses the results from chapters 3 to 6 and places them into context against the objectives for on-machine distance and surface topography measurement presented in chapter 1. It assesses the progress towards achievement of these objectives before outlining of developments required for their full realisation.

7.2 Summary of investigations

The opening chapters of this work introduced the necessity for miniaturisation of optical methods of embedded single-point distance and surface topography measurement for engineering components, surfaces and assemblies in-situ. Faster and cheaper methods of single-point measurement with improved dynamic range and reduced physical size will be beneficial to manufacturers of precision components and machine tools. The availability of methods using remote fibre probes are a necessity to realise this on-machine reduction in size.

7.2.1 DRI implementation and signal processing development

Chapter 3 outlined the operational principles of DRI, a method of single point metrology with potential for on-machine metrology. The dispersed reference interferometer layout presented within this section was then simulated and prototyped to produce spectral interferograms with a high agreement between simulation and experiment. In this chapter tracking of the interferogram symmetry position was achieved using convolution to provide an absolute method of measurement. The absolute nature of this method is essential for an on-machine single-point metrology method allowing for measurement of discontinuous surfaces such as structured surfaces and high aspect ratio features. A vertical resolution of 279 nm was achieved over a range of 285 µm to yield a dynamic range of 1021. Linearity was evaluated to be 0.53 % over the range of the interferometer and measurement of 30 µm and 200 µm step height samples demonstrated. Novel application of regularisation to spectral interferograms was added to reduce oscillations occurring as the optical path distance changed by small amounts. These oscillations, suspected to be caused by the changing intensities at the edge of the detector, were reduced to an acceptable level by the introduction of regularisation and windowing of measured interferograms.

With an aim to improve the dynamic range of DRI, a second measurement regime was introduced in chapter 4 which takes advantage of the interferometric nature of DRI and the resulting spectral interferograms by tracking of the shape of the interferogram point of symmetry using a method called template matching. This provides measurement data that at present reaches an axial resolution of ~0.6 nm as derived from the RMS of the noise floor rather than the signal processing method limit. The axial range of template matching equals that of the absolute measurement regime due to the reliance of the

template matching method on detection of the interferogram symmetry position. The 285 μm range and 0.6 nm resolution of the method yield a dynamic range of 475,000 for template matching. Measurement of 100 nm structures was demonstrated and comparisons to an established offline method of metrology made. The linearity of template matching was established to be 0.0289 % after which the effect of translation stage motion error was assessed and future methods of correction discussed. This is an important aspect of the development of a single point metrology method such as DRI due to the reliance of the method on linear motion stages for translation during measurement.

Improvements to the physical apparatus next allowed extension of the range of DRI to 800 μm without compromising the resolution of template matching. This is achieved by selection of a SLED with an increased bandwidth of 50 nm as well as introduction of a CMOS detector with a four-fold pixel count increase to 8192 pixels. A new dynamic range of 1,333,000 results from this improvement.

7.2.2   High resolution, absolute position measurement

Following examination of these two measurement methods, chapter 5 introduces wraparound order determination as a method to combine the strengths of each method, namely the absolute nature of autoconvolution and the high resolution but relative nature of template matching. Initial investigations indicate use of wraparound order determination is promising, though further work is required to ascertain the robustness of such a method. This method is tested over a 30 μm range using a precision PZT along with an error correction algorithm to improve the robustness to environmental disturbances. At present the method has been demonstrated with a measurement mirror only, with the limited range due to the time consuming calibration processes. It is probable that future DRI measurement rate increases will allow faster calibration and lead to the practicality of a longer range. Alternatively, improved wraparound order determination algorithms and improvement of the accuracy of the numerical model will allow combination of autoconvolution and template matching with much reduced requirement for calibration.

7.2.3   Remote fibre probing for embedded metrology

Chapter 6 introduces the operational principle of a DRI-linked remote fibre probe and the ability to measure a spectral interferogram using DRI interrogating a Fizeau probe has been confirmed. Having demonstrated this, further miniaturisation will ease integration of DRI with machine tools for on-machine metrology, though the current prototype form factor is sufficiently compact for trial investigations of ultra-precision machine tool motion errors and on-machine measurement surface topography in ultra-precision machining environments. The relationships between probe focal length and collimator output beam diameter have been discussed, where the resulting lateral spot size and depth of field are key parameters for probe suitability for measurement applications. With the difficulties of alignment highlighted for such a bulk optics probe, future work will include detailed design of GRIN lens assemblies

and equipment for their alignment with DRI, with an overview of the start of this process given in section 8.4.

7.3 Conclusions

These sub-sections relate the research objectives outlined in section 1.3 to progress demonstrated within this thesis. The objectives are repeated here for convenience:

- Explore the possibility of nanometre **axial resolution** measurement using DRI.
- Investigate improvement of the axial range of DRI to several millimetres.
- Demonstrate **measurement rates** in excess of 10 kHz.
- Development of a **common-path remote fibre probe topology** with considerations for miniaturisation for on-machine operation.
- Design of a **prototype DRI apparatus** for interrogation of remote fibre probes in a manufacturing environment.

7.3.1 Axial resolution

The research objective of nanometre resolution has been met through use of template matching to determine measurand position to a resolution of 0.6 nm. Further work must assess the ability of DRI to maintain this resolution for surfaces with low reflectivity and increasing roughness.

While this nanometre resolution method of measurement remains relative, it is promising that a method of determining the wraparound order has been demonstrated over a short range. It is probable that with increases in measurement rate this high resolution, absolute method will be available across the entire range of DRI.

Future considerations for the resolution of DRI include alternative analytical methods to reduce the computational complexity of achieving nanometre resolution. Initial investigations into frequency domain analysis of DRI spectral interferograms are presented in further work section 8.3.2, though these come with their own set of problems.

7.3.2 Axial range

Demonstration of a range of 800 μm has been achieved through an increase in interferometer source and spectrometer bandwidth as well as modifications to the autoconvolution method to account for background intensity envelopes, as described by appendix 11.3.

While this 800 μm range does not meet the objective of a range of several millimetres, it is probable that minimal changes to the detection of the autoconvolution peak will result in a measurement range increase to 1 mm. The simple method of detecting the interferogram symmetry used at present relies on the autoconvolution result having a maximal value coinciding with the interferogram centre. It has been

shown experimentally (Figure 3.12) that as the autoconvolution peak deteriorates, it is still possible to observe a strong peak even if it is no longer the maximally valued element.

Having demonstrated a resolution of 0.6 nm over a range of 800 μm, DRI currently boasts a dynamic range of 1,333,000 which will allow use of DRI for a wide range of applications. For measurements demanding an increase in range, there is also scope for further improvement through use of wider bandwidth sources and spectrometer detectors with increased pixel counts. Increased dispersion either by use of more dispersive elements or increase of grating separation is also a possibility to increase the range of DRI beyond 1 mm and is attractive for future DRI implementations.

7.3.3   Measurement rate

The current measurement rate of approximately 20 Hz has been measured for DRI using a single core of an i7 CPU for real-time signal processing. It is encouraging that the limiting factor is presently software and not optics, with capture of unprocessed interferograms of sufficient visibility currently achievable at more than 4000 Hz if real-time signal processing is forgone.

As yet, the effect of signal processing improvement on DRI measurement rate has not been quantified, where exploration of parallelisation with GPGPUs and concurrent processing with FPGA implementations is part of the further work in section 8.2. It is probable that measurement rate increase from 20 Hz to more than 1000 Hz using GPUPUs/FPGAs is possible for the algorithms detailed within this thesis as they exist now.

Following software changes to improve algorithmic efficiency and parallelisation of algorithms, it will be necessary to optimise the optical efficiency of the apparatus. Reduction in fibre to fibre coupling losses, substitution of a circulator instead of a fibre coupler as well as increased source power will allow reduction in detector integration time to increase measurement rate.

Further studies must observe the effect of measurand roughness and reflectivity on the interferogram visibility and hence attainable detector integration time, though this is an issue experienced by all the described single-point measurement alternatives methods, whose measurement rates are described to be dependent on surface finish and slope.

It is possible that through careful design of the optics, software and hardware for DRI that measurement rates in excess of 10 kHz will remain achievable for specular measurands.

7.3.4   Common-path fibre-probe topology and prototype DRI

A DRI probe volume of 30 x 40 x 50 mm has been achieved, a form factor that is smaller than some commercially available chromatic confocal probes. It is probable that probes less than half this size will be achieved with commercially available bulk optic components through careful design and alignment of

probes with lens tubes to reduce probe diameter. Further miniaturisation of probes is planned to eliminate kinematic components within the probe, with GRIN assemblies available for low NA measurement with diameters of several hundred microns. Despite these promising further miniaturisations, the existing probe is sufficiently miniaturised to begin trials of DRI in manufacturing environments, with further size reduction expected to progress incrementally.

The newly developed interrogation interferometer prototype is sufficiently compact to allow easy relocation to machine tools. The 250 x 500 x 100 mm volume is of similar size to a typical desktop computer, with the current size of the instrument making it possible to fit it within a three unit 19 inch server rack, something which may be attractive for industrial applications. Further reduction in size of the interrogation interferometer is possible through a change to reflective gratings or dispersive fibre as well as continuing spectrometer improvements and refined mechanical design.

Component costs for the DRI interrogation prototype were £6,300 including optics, power supplies, detector, light source, kinematics and machined aluminium parts. It is probable this can be reduced to less than £5000 by: a) elimination of further kinematic components, b) a switch to 12.7 mm optical components instead of 25.4 mm where appropriate and c) careful reconsideration of the interferometer base plate for ease of manufacture. This price does not yet account for economies of scale which may see a further reduction in cost of up to 50 %. The cost of components for the prototype probe were £276, with savings of up to 50 % possible with new probe topologies and economies of scale.

With the expected increase of measurement rate, new interesting fibre probe topologies become possible. As measurement rates increase it will be possible to switch between multiple remote fibre probes with a single interrogation interferometer, sharing the cost of metrology between machine tools without requiring physical movement of the apparatus.

7.4   Closing statement

This research has led to the development of an interferometric method of single-point measurement and associated prototype apparatus which is ready for on-machine integration and evaluation. Completion of characterisation of the prototype instrument range, resolution and linearity will allow evaluation of the method in a manufacturing environment and allow testing of the temporal stability as well as the robustness to noise.

Measurement and correction of linear stage motion errors for ultra-precision manufacturing will be followed by on-machine post-process measurement of component surface finish and form, allowing correction by re-machining of non-conformant components. The possibility of micro-scanning mirrors for beam profile scanning is also highly attractive to decouple single-point surface measurement from machine tool translation stage motion errors.

8 Further work

8.1 Introduction

The preceding chapters have introduced methods of on-machine metrology, identified shortcomings in existing single-point measurement topologies and set forth a proposed solution to improve the capability of single-point on-machine metrology instrumentation after which demonstration of this technology in a laboratory setting has followed. This chapter introduces on-going research and ideas, completion of which will provide improvements beneficial to use of DRI as an on-machine measurement tool in a manufacturing environment.

8.2 Signal processing acceleration

At present the measurement rate of the bulk optics interferometer is not hardware but software limited. The available light power is sufficient for the camera running at higher rates than is currently possible due to the slow nature of the signal processing. This results in loss of frames while the signal processing is carried out at between 15 and 25 Hz.

The absolute upper limit to the measurement rate is that of the available cameras, with GigE connectivity of a 8192 pixel camera limiting the measurement rate to 12 kHz. The added cost of CameraLink connectivity for the same camera will allow measurement rates of up to 70 kHz, though for this to be realised the optical power and efficiency as well as the signal processing capability must match this.

The following subsections detail potentially useful software methods for increasing measurement rates which will need to be explored further to allow on-machine integration of DRI at useful measurement rates of more than 1 kHz.

8.2.1 Data reduction

While the resolution attainable using template matching is attractive, the large number of calculations required to obtain high resolution measurement data is a major impediment to the measurement rate of the method. Instead of calculating 800 templates at 1 nm resolution, the use of pyramid methods [111] to obtain the same resolution faster is a possibly beneficial method.

Pyramid methods first calculate a low resolution solution to the problem, and then search for a high resolution answer within a targeted area. In the case of template matching this would involve 40 instead of 800 templates, at a resolution of 20 nm. Once the approximate position of the matching template is discovered then a full resolution of 40 templates at 1 nm spacing can be calculated near to the approximate position to give full resolution template position. This has the potential to be up to ten times faster than normal template matching.

The graph in figure 8.1 demonstrates how this would apply to template matching, with the blue scatter showing 40 calculated correlation coefficients spaced by 20 nm and the red scatter showing 40 correlation coefficients spaced by 1 nm.
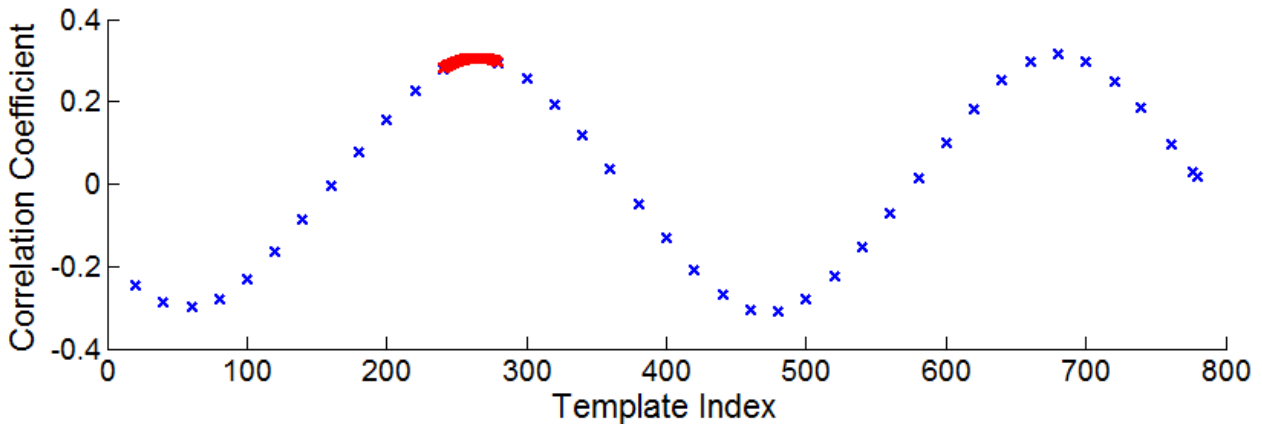
Figure 8.1: Example of pyramid methods of calculation relating to template matching correlation coefficient. Blue scatter shows 40 templates spaced by 20 nm. The red scatter shows 40 templates spaced by 1 nm.

8.2.2 General purpose graphics processing units

The 15-25 Hz measurement rate attainable using an i7 processor makes use of a single core of the 4 core CPU. The computing overhead involved with management of multiple CPU cores and threads means that use of multiple cores for increase of measurement rate is not realistic. However, the availability of cheap, high performance general purpose graphics processing units (GPGPUs) means that graphics cards with over 2000 cores are available for less than £500 (Nvidia GTX 980). With hundreds or thousands of cores, parallelisation of algorithms then becomes attractive. Taking template matching as an example, correlation coefficient calculations for all 800 templates can be performed at once. An alternative approach would be to compute each of the template correlation coefficient values for a measured interferogram sequentially, as with a CPU, but to do so for one measured interferogram on each core the GPGPU. In this way a set of thousands of measured interferograms could be cached from the camera with their timestamps and the axial height for each interferogram be calculated at once. It seems obvious that this would be a more parallelisable approach to measurement rate increase so long as the measurement application is tolerant of increased measurement latency while achieving high measurement rate. This should be a solution that is easily expandable as GPGPU computing power increases over time.

8.2.3 Field programmable gate arrays

Field programmable gate arrays (FPGAs) allow hardware instead of software implementation of algorithms through use of arrays of programmable logic gates. In many cases they offer a small, low power and fast solution to signal processing problems, with embedded use of FPGAs common within cameras for handling of signal conditioning, communication and data transfer. The programmable nature of the gates mean that both series and parallel algorithms are possible, limited only by the number of

146

available gates. A particular advantage over GPGPUs and CPUs is the nature with which data is processed, whereby the sequential steps in an algorithm can be carried out on multiple data sets concurrently with one result clocked out as new raw data is clocked in. The advantage of this approach is the low latency, offset by the disadvantages of notoriously long development cycles and inflexibility of FPGAs to algorithm changes.

8.3   Signal processing improvements

This section discusses the possible alternative methods of signal processing to achieve improved range, resolution, measurement rate and simulation accuracy. The signal processing methods shown here have had initial investigations performed with simulated interferograms but the effects of real interferograms on these approaches have not yet been explored fully.

8.3.1   Virtual reference interferometry

The range of DRI spectral interferograms for absolute position measurement is limited by the ability of autoconvolution to resolve the position of the interferogram point of symmetry as previously illustrated in figure 3.12. As the d value changes and the interferogram point of symmetry approaches the edge of the detector, the autoconvolution result distorts until a clear peak is no longer present.

In the case of virtual reference interferometry (VRI), the author describes spectral interferograms having a visible point of symmetry as balanced spectral interferograms (BSI) and interferograms having an increasing frequency with wavenumber but no point of symmetry are described as unbalanced spectral interferograms (USI) [79, 80]. In the case of VRI, range is extended by point-wise multiplication of a unbalanced spectral interferogram (USI) with a simulated USI of opposing imbalance has been shown to result in amplitude modulation of the interferograms from which a balanced spectral interferogram (BSI) may be obtained after low pass filtering of the amplitude modulated signal.
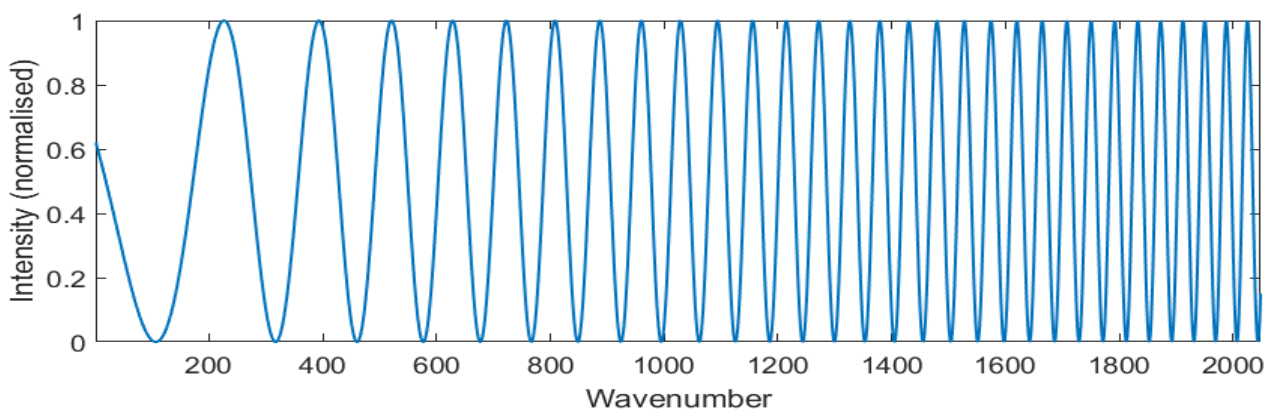
Figure 8.2: Simulated spectral interferogram for an OPD offset of +500 µm

Initial Matlab simulations using VRI for DRI suggest that this method is applicable if a simulated USI of known d is used. The resulting BSI offset allows calculation of the total distance from the balance point.

Take the example interferogram shown in figure 8.2 for which convolution with itself does not yield an autoconvolution vector with a resolvable peak. However, point-wise multiplication of the interferogram for $d=500$ μm by an interferogram with a value of $d=-500$ μm results in a valid autoconvolution result. This is shown in blue in figure 8.3. Also seen in figure 8.3 are autoconvolution results for pointwise multiplication of $d=520$ and $d=-500$ (green) as well as $d=540$ and $d=-500$ (red). This shows that it may be possible to extend DRI range further than previously expected by multiplication of unbalanced spectral interferograms by a spectral interferogram with an opposite sign to the OPD, a method previously described as virtual reference interferometry. Further work to verify this method with measured interferograms remains to be performed.
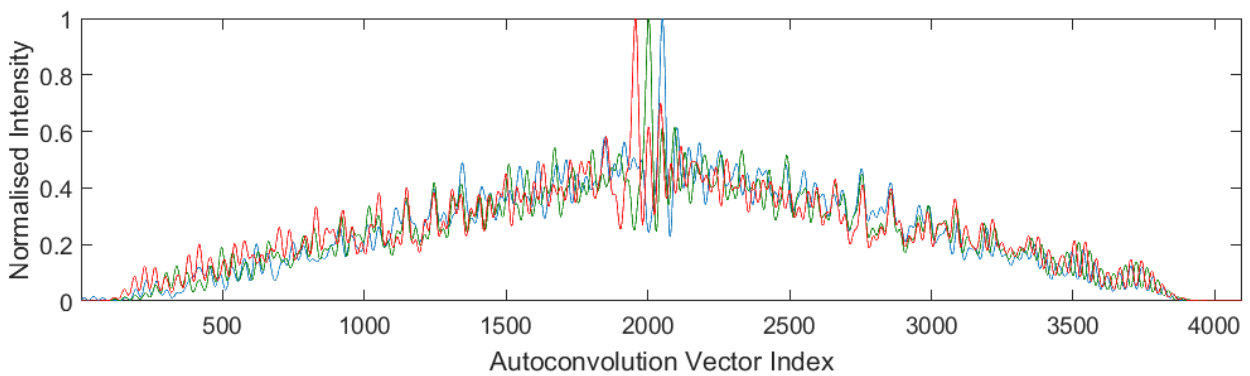
Figure 8.3: Simulated interferograms having OPDs of 500 (blue), 520 (green) and 540 (red) μm are point-wise multiplied by an interferogram with an OPD of -500 μm. This allows determination of absolute position for an interferogram whose autoconvolution normally does not result in a useful peak.

8.3.2 Fast Fourier transform methods of phase extraction

FFT based methods of phase extraction have been demonstrated previously for interferometry in the case of FFT profilometry as well as determination of phase in spectral interferometry [112].

This section details observations from initial investigations into FFT based phase extraction for DRI, with a proposed method outlined, initial results displayed and possible advantages and disadvantages discussed. The following flow diagram shows the proposed signal processing flow for FFT calculation of DRI phase:
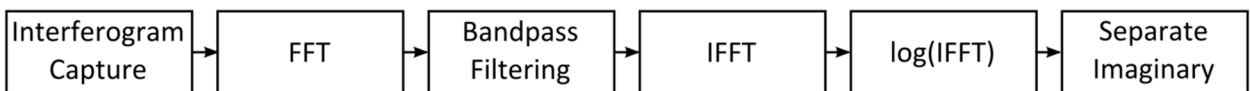
Figure 8.4: Flow diagram showing initial signal processing steps to retrieve phase information from DRI interferograms using FFT.

Starting with an interferogram, $\mathbf{H}$, of length m, whose pixels are indexed by the variable i, the FFT of the interferogram is calculated.

Band-pass filtering is achieved by setting lower and upper ranges of the FFT values to zero. The upper and lower frequency cut-offs are f_U and f_L respectively and can be values between 1 and m depending on

the desired bandwidth to pass. For the purpose of this initial simulated attempt, f_U and f_L are set to 10 and 6000 where m is 8192. The IFFT of this data is a vector, $\mathbf{H}'$, containing real and imaginary components.

The complex logarithm of $\mathbf{H}'$ is taken before finally the imaginary component of the signal is separated from the real component. This results in the instantaneous phase for each pixel of the original interferogram, varying from $-\pi$ to π. This result is shown in Figure 8.5 where the frequency of the phase wraparounds can be seen to reduce towards the middle after which they increase again.
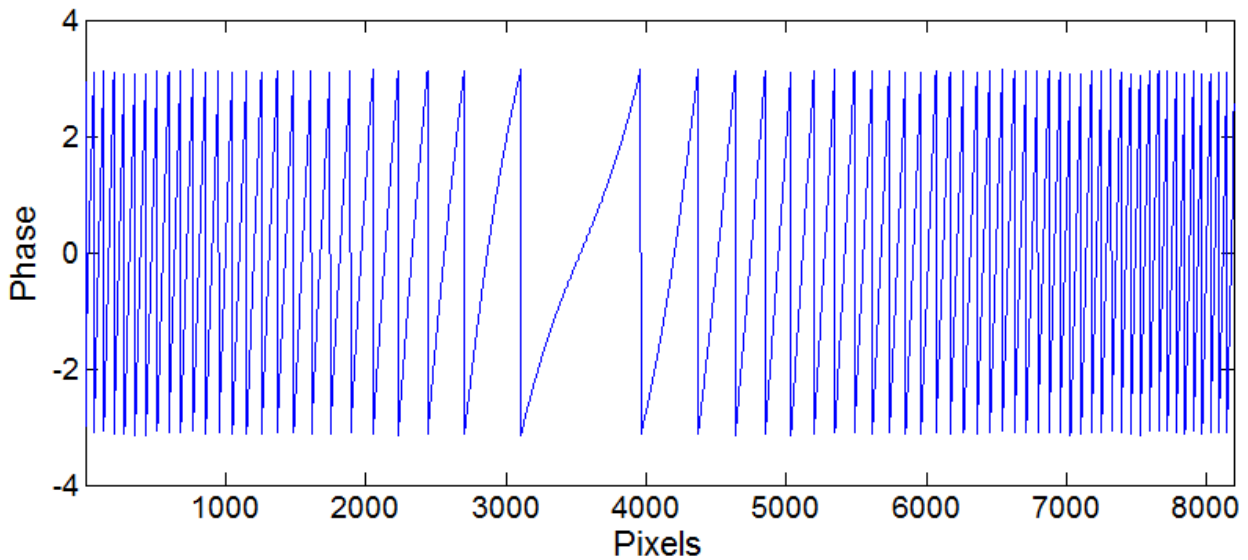
Figure 8.5: Instantaneous phase across the 8192 pixels of a simulated interferogram calculated by FFT methods.

Figure 8.6 demonstrates how the phase of a single pixel of the interferogram changes, with this graph showing the phase at pixel 6500 (blue), 6600 (red) and 6700 (green) as the simulated interferogram OPD is incremented by 1 nm steps over a 1000 nm range. It is expected that if necessary, phase shifting algorithms can be implemented with this data to account for the changing frequency of the wraparounds with wavelength and measurement mirror translation.

149
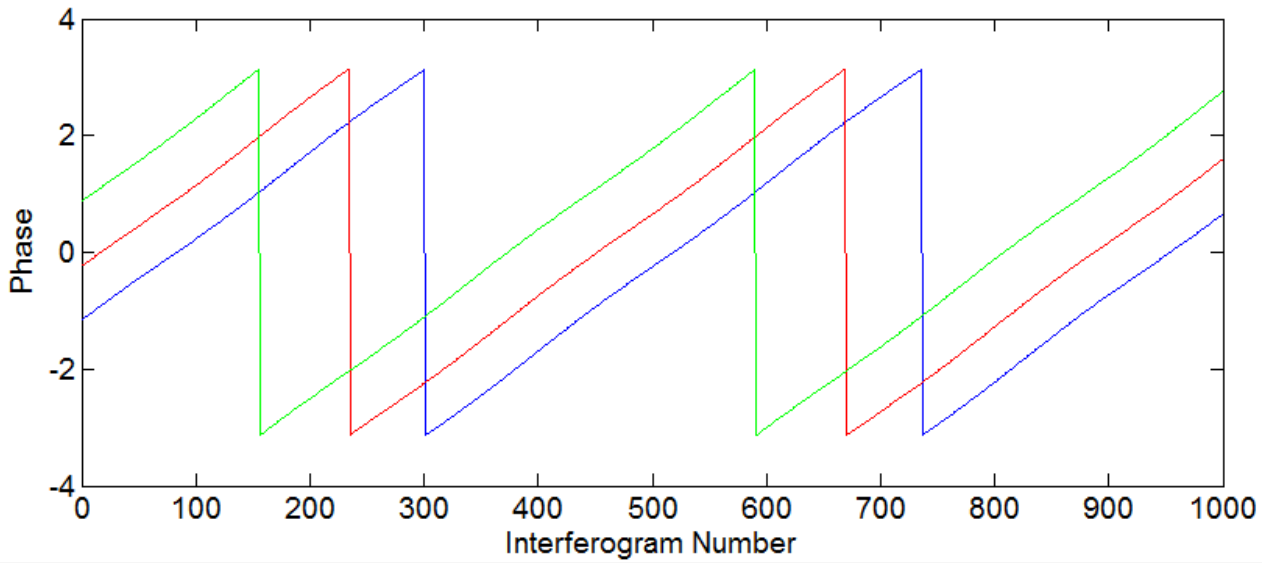
Figure 8.6: Instantaneous phase for a single pixel over 1000 nm for three different pixels (6500 (blue), 6600 (green) and 6700 (red)) separated by 100 pixels.

Also potentially useful is the unwrapped phase of the interferogram, as shown in Figure 8.7. It is likely that this will suffer from edge effects as mentioned by Hlubina et al. in their 2001 paper on FFT analysis of spectral interferograms [112]. Also warranting further investigation is the unwrapped instantaneous interferogram phase (Figure 8.7) and use of FFT for real phase, an initial example of which is shown in 8.8. Of particular interest is the much reduced computational overhead of FFT-based phase extraction when compared to template matching, with an i7 CPU able to calculate phase by FFT at 220 Hz compared to 15-25 Hz for template matching.
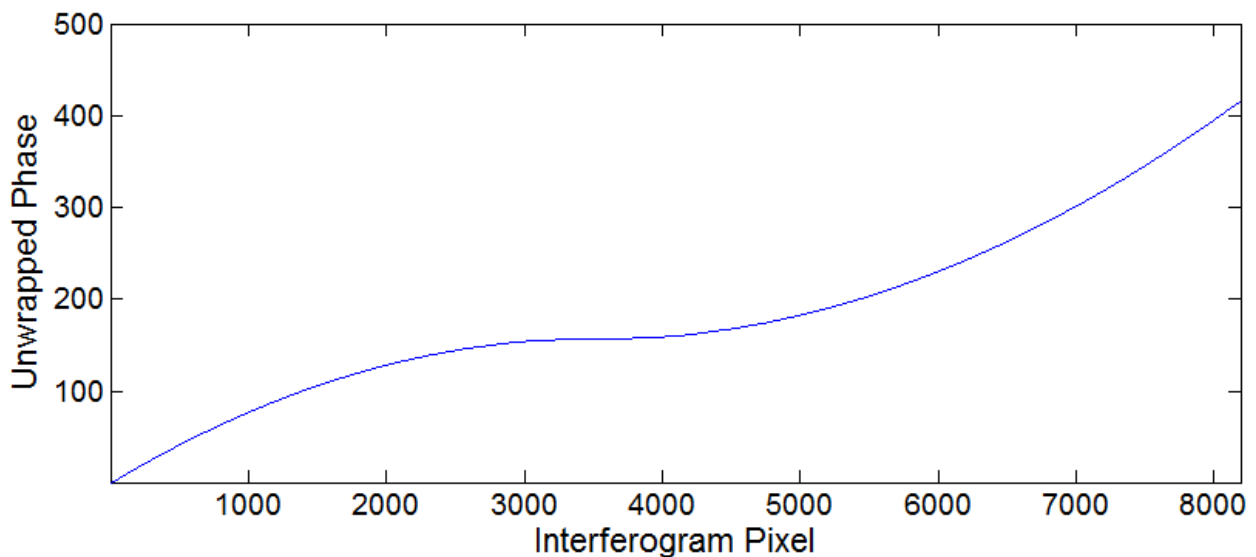
Figure 8.7: Unwrapped instantaneous phase
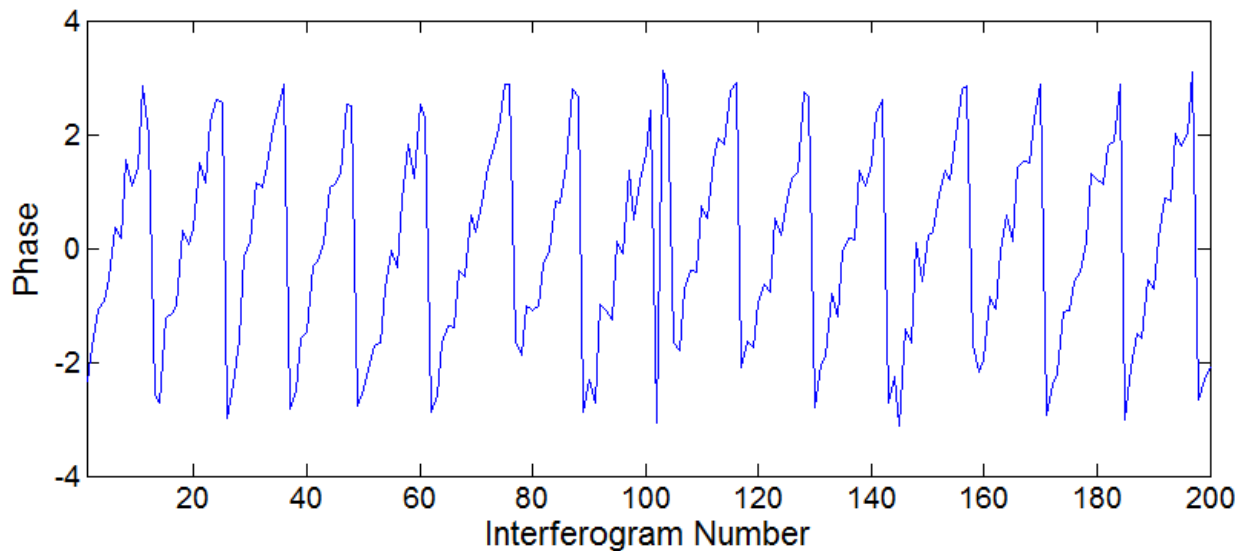
Figure 8.8: Phase of real interferograms as 40 nm OPD changes were introduced using a PZT upon which the measurement mirror was mounted.

An inherent problem with this method which must yet be explored is the changing frequency of the instantaneous phase wraparounds across the width of the detector. For this reason it may be necessary to calculate instantaneous phase as described above and then apply a phase shifting algorithm such as the 7-point phase shifting algorithm described for spectral interferograms by Cohen-Sabban [50].

8.3.3   Noise immunity of DRI signal processing methods

The range and resolution of autoconvolution and template matching for ideal simulated interferograms are considered in sections 3.5 and 4.4 respectively. This is followed in sections 3.6 and 4.5 with use of these signal processing methods for non-ideal, measured interferograms containing features such as noise, imperfect visibility and low frequency envelopes. Future application of the DRI measurement method to measurands having higher surface slopes and optically rougher surfaces will lead to cases where the range and resolution begin to deteriorate due to poor interferogram visibility caused by reduction in measurement arm intensity. It is important to understand the extent of the immunity DRI has to these changes. Addition of Gaussian white noise and changes to interferogram visibility are difficult to control in a repeatable manner experimentally and so simulation of these factors is an attractive method to study their effect on DRI range and resolution more completely.

Figure 8.9 shows such a simulated interferogram with the addition of white noise, DC offset, reduced visibility and low frequency envelopes. The impact of the signal-to-noise ratio resulting from the noise and visibility are of particular interest due to their strong link to lower visibility samples and fibre polarisation and the effect this will have on their measurement.
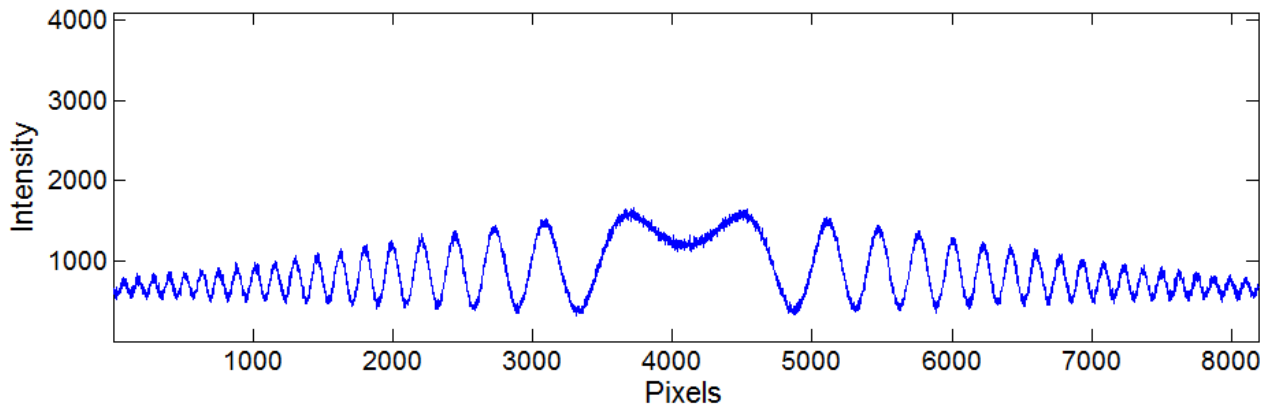
Figure 8.9: Simulating interferogram with addition of white noise, DC offset, reduced visibility and low frequency envelopes.

8.4 Miniaturised Probe Design

The bulk optics probe discussed previously, while compact compared to an interferometer, makes use of large diameter lenses and requires the use of bulky and expensive kinematics to align optical elements. While advantageous for measurement of steeper slopes and rougher surfaces, the physical size of such a probe makes measurement prohibitive for certain applications and so it is obvious that further size reduction will enact a greater market for on machine metrology.

The introduction to DRI of fibre probing using gradient index (GRIN) lenses allows a reduction in size of the probe assembly by ensuring that all alignment is intrinsic to the construction, thus eliminating the bulky kinematic stages required for the alignment of the previous design as well as reducing the lens diameter. An additional benefit of GRIN lenses is that the focusing effect of the lens is distributed across the entire body of the lens as opposed to just surface refraction with conventional lenses enacting further miniaturisation. In a GRIN lens, the index of refraction, n, of the lens decreases with increasing radial distance, r. The index of refraction often forms a parabolic profile where the index at a distance, r, from the optical axis can be described as,

$$n(r) = n_0\left(1 - \frac{ar^2}{2}\right)$$

8.1

Where n_0 is the maximum index at $r=0$ and a is a constant. This changing index profile causes propagation of light through GRIN structures to be periodic, realizing a cosinusoidal ray trace through the material, with the gradient of index change with radius determining the distance over which an entire period of ray propagation occurs. For this reason, GRIN lenses with a pitch of 1 result in an output beam identical to the input beam and those with a pitch of 0.5 resulting in an output beam the inverse of the input beam. Similarly a 0.25 pitch collimates a beam exiting a fibre at the GRIN lens first surface or focuses a collimated beam upon the second surface. The length for a single pitch of a lens with index gradient profile, g, can be calculated as follows,

152

$$P = \frac{2\pi}{g}$$

<div align="right">8.2</div>

meaning the length, z_i, of a lens of pitch, P, goes as,

$$z_i = \frac{2\pi P}{g}$$

<div align="right">8.3</div>

Through appropriate choice of pitch, the focal length of lenses can be adjusted to modify the working distance and output beam properties. For example, a 0.23 pitch GRIN lens will collimate a point source located at the working distance, s, or focus a collimated beam at distance s. For a given gradient profile, focal length, f, and working distance, s, can both be modified by lens length z_i as follows,

$$f = \frac{1}{n_0 g \sin(gz_i)}$$

<div align="right">8.4</div>

$$s = \frac{1}{n_0 g \tan(gz_i)}$$

<div align="right">8.5</div>

With the optical theory of GRIN lenses covered we can begin to investigate their use in our application.

8.4.1 Simple GRIN DRI probe

At their simplest, GRIN lens assemblies are comprised of three components. A fibre ferrule which terminates the fibre with a polished face (at 0° or 8°), the GRIN lens spaced from the fibre by the working distance, s, and lastly, the alignment sleeve, manufactured from UV transparent glass to allow permanent fixing of the assembly using optical adhesive once the components are aligned. Additionally, a precision ground glass spacer may be included by some manufacturers to facilitate easier alignment at the expense of complexity. Placed between the fibre ferrule and the GRIN lens, it allows the positioning of the GRIN lens at the exact working distance from the fibre without the use of expensive translation stages during assembly.

For DRI, a COTS GRIN lens will not suffice since a reference surface must be provided to return a percentage of the incident light back into the fibre, forming the reference arm of the interferometer. Unlike the bulk optics probe however, this can be achieved without alignment by depositing a beam splitter coating upon a surface within the GRIN probe assembly. If a fibre ferrule with a 0° face is chosen, placing the coating on the ferrule face or the face of the glass spacer abutting it, the expensive and bulky kinematic stages can be eliminated. For both commercial and prototype quantities of this probe configuration, coating of the spacer is preferable since as both a cheaper and smaller component than the fibre ferrule, batch coating becomes cheaper per unit due to the greater quantity which can be coated at once as well as the lower capital cost of spacer purchase.
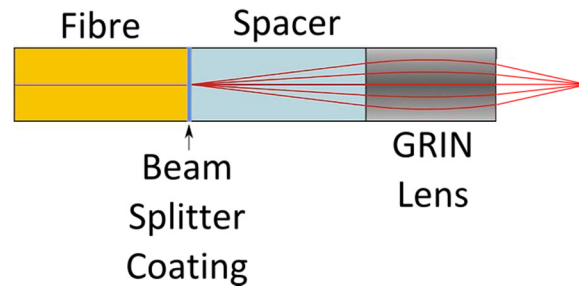
Figure 8.10: Example configuration (not to scale) of a GRIN probe with beam splitter coating applied for DRI reference generation.

A considerable disadvantage of the probe assembly method described above is the available tolerances on the spacer and GRIN lens lengths leading to non-interchangeability of individual probes. Manufacturing tolerances on GRIN lens lengths and glass spacer thicknesses are listed as ± 5% by Grintech and ± 0.14 mm by Thor Labs. This means that for a nominal lens length of 2.0 mm, lenses lengths within that tolerance could range from 1.9 to 2.1, a range of 200 μm, increasing the 2e distance that must be compensated within measurement arm of the bulk optics interferometer to 400 μm. This distance is almost half the expected interferometer range highlighting difficulties experienced from interchangeable use of probes of identical focal lengths. This difficulty is exaggerated further when considering probes of different focal lengths meaning adjustment within the bulk optics interferometer will be necessary when switching between probes. This may be done manually with a micrometre stage or with a motorised stage to allow for automated interchangeability of probes. In many applications, the additional expense, complexity and bulkiness of such a stage is unacceptable and interchangeability of probes is a major consideration.

8.4.2 Interchangeability

To maintain true interchangeability of probes without operator input or automatic path length adjustment of the bulk optics interferometer, the $2e$ distance must remain consistent between probes to within 10 μm. This arbitrary value has been chosen as a reasonably achievable tolerance for probe construction length while minimising the effect of probe change on the interferometer setup.

To achieve this small path length difference across a range of probe focal lengths, a dual GRIN lens probe configuration is proposed. Dual GRIN lens designs have been used previously for lateral beam scanning [113] while GRIN lens doublet configurations have been used for OCT endoscopy [114]. For DRI, similar to the simple GRIN probe design in section 8.4.1, at the fibre/probe interface a portion of the light is retro-reflected back into the fibre by a partially reflective coating upon the first surface of the glass spacer. The remaining portion of light is incident upon the first GRIN lens, L1, which, unlike the previous design, collimates the beam. An air gap between L1 and L2 allows adjustment of L2 position along the Z axis during assembly. L2 has the effect of focusing the collimated beam upon the measurement surface. By introducing an air gap between the pair of lenses, focusing lenses with a longer focal length can be placed

closer to L1, maintaining the important $2e$ distance. This is demonstrated in figure 8.12 where a pair of dual GRIN probes are shown having different focal lengths while maintaining an identical e value. Previously, the difference in focal length of these two probe examples would have made interchangeability impossible. With this new proposed design, when assembled carefully these two designs will be interchangeable and not dependent upon the tolerances of the components.
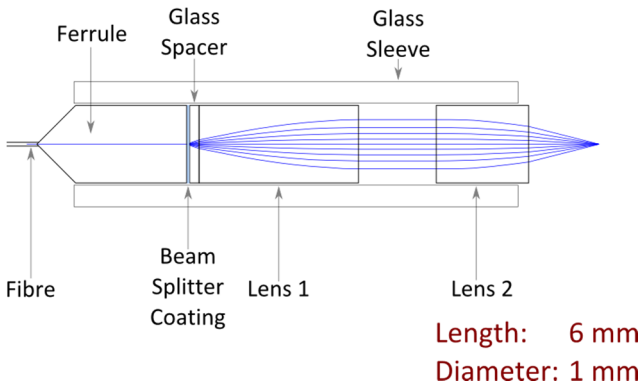
Figure 8.11: Example of compound GRIN lens design to maintain distance e. Diagram is a composite Zemax and Inkscape illustration.

Use equation 22 to justify the lens choice. Show how we can change the length of the collimating lens using different values of n_0 and g with pitch 0.23 to collimate the exiting beam.
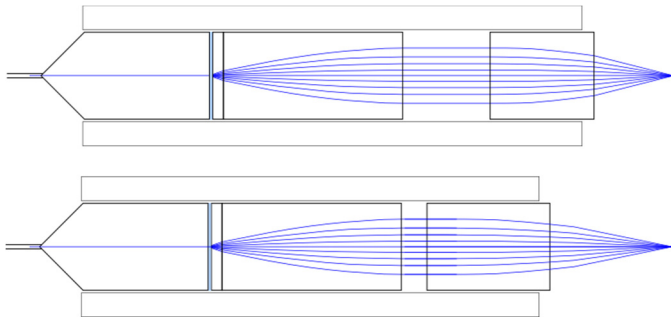
Figure 8.12: GRIN lens separation to maintain distance e and ensure interoperability of probes despite differences in GRIN lens focal length and thickness tolerance of lenses and spacers.

9 Publications and Awards

Journal Papers:

J. Williamson, H. Martin and X. Jiang, *High resolution position measurement from dispersed reference interferometry using template matching*. Optics Express (publication pending)

Conference Presentations:

J. Williamson, H. Martin and X. Jiang, *Phase Calculation of Spectral Interferograms using Template Matching*. Manufacturing the Future Conference 2014, University of Strathclyde.

J. Williamson, H. Martin and X. Jiang, *Dispersed Reference Interferometry*. Manufacturing the Future Conference 2013, Cranfield University.

Awards:

Worshipful Company of Scientific Instrument Makers Postgraduate Award, 2015

10 References

1.   Jiang, X.J. and D.J. Whitehouse, *Technological shifts in surface metrology.* CIRP Annals - Manufacturing Technology, 2012. **61**: p. 815-836.
2.   Jiang, X., *Precision surface measurement.* Phil. Trans. R. Soc. A, 2012. **370**(1973): p. 4089–4114.
3.   Kimbrough, B. and E. Novak, *In-line roll-to-roll metrology for flexible electronics.* Proc. of SPIE, 2015. **9576**.
4.   Elrawemi, M., et al. *Comparative study between online and offline defect assessment methods for roll to roll flexible PV modules.* in *4th International Conference on Nanomanufacturing.* 2014. Germany.
5.   Ametek Precitech Inc., *Surface finish and form accuracy results on a steep slope Al asphere.* 2015: www.precitech.com.
6.   Jiang, X., et al., *Paradigm shifts in surface metrology, part 2.* Proceedings of the Royal Society, 2009. **463**: p. 2071-2099.
7.   Botsaris, P.N. and J.A. Tsanakas, *State-of-the-art in methods applied to tool condition monitoring (TCM) in unmanned machining operations: a review*, in *Proceedings of The International Conference of COMADEM*. 2008: Prague. p. 73-87.
8.   Danzl, R., F. Helmli, and S. Scherer, *Focus Variation – a Robust Technology for High Resolution Optical 3D Surface Metrology.* Strojniški vestnik - Journal of Mechanical Engineering, 2010. **57**(3): p. 245-256.
9.   Danzl, R., F. Helmli, and S. Scherer, *Comparison of roughness measurements between a contact stylus instrument and an optical measurement device based on a colour focus sensor.* NSTI-Nanotech, 2006. **3**: p. 284 - 287.
10.   Hemli, F., *Focus Variation Instruments*, in *Optical Measurement of Surface Topography*, R. Leach, Editor. 2011, Springer.
11.   Danzl, R., F. Helmli, and S. Scherer, *Focus Variation - A new technology for high resolution optical 3d surface metrology*, in *The 10th International Conference of the Slovenian Society for Non-Destructive Testing* 2009: Ljubljana, Slovenia. p. 8417.
12.   Hiersemenzel, F., et al., *Areal Texture and Angle Measurements of Tilted Surfaces using Focus Variation Methods*, in *3rd International Conference on Surface Metrology*. 2012, Universite de Savoie: Annecy (France)
13.   Alicona Imaging GmbH, *Alicona IF-SensorR25 Datasheet*. 2015.
14.   Faber, C., et al., *Deflectometry challenges interferometry the competition gets tougher.* 2012. **8493**.
15.   Lehmann, P.H., et al., *Deflectometry vs. interferometry.* Proc. of SPIE, 2013. **8788**: p. 87881C.
16.   Olesch, E., et al., *Quantitative Deflectometry Challenges Interferometry.* 7th International Workshop on Advanced Optical Imaging and Metrology, 2014: p. 907-910.
17.   Röttinger, C., et al., *Deflectometry for Ultra-Precision Machining - Measuring without Rechucking.* Preceedings of the German Society of Applied Optics, 2011. **8493**.
18.   Gorthi, S.S. and P. Rastogi, *Fringe Projection Techniques: Wither are we.* Optics and Lasers in Engineering, 2010. **48**(2): p. 133-140.
19.   Li, D., C. Liu, and J. Tian, *Telecentric 3D profilometry base on phase-shifting fringe projection.* Optics Express, 2014. **22**(26): p. 31826-31835.
20.   Leonhardt, K., U. Droste, and H.J. Tiziani, *Microshape and rough-surface analysis by fringe projection.* Applied Optics, 1994. **33**(31): p. 7477-7488.
21.   Kimbrough, B., et al., *Low Coherence Vibration Insensitive Fizeau Interferometer.* Proc. of SPIE, 2006. **6292**: p. 62920F
22.   Leach, R., *Optical Measurement of Surface Topography*. 2011.
23.   Creath, K., *Phase-measurement Interferometry Techniques*. 1988: Elsevier.
24.   Izatt, J.A. and M.A. Choma, *Theory of Optical Coherence Tomography*, in *Optical Coherence Tomography*, W. Drexler and J.G. Fujimoto, Editors. 2008, Springer. p. 47-72.

25. Groot, P.d., *101-frame algorithm for phase shifting interfermetry.* Proceedings of SPIE, 1997. **3098**.

26. Groot, P.d., *Phase Shifting Interferometry*, in *Optical Measurement of Surface Topography*, R. Leach, Editor. 2011.

27. Graham Optical Systems. *How Phase interferometers work*. 2011 2015-09-16]; Available from: http://www.grahamoptical.com/phase.html.

28. Wizinowich, P.L., *Phase shifting interferometry in the presence of vibration: a new algorithm and system.* Applied Optics, 1990. **29**(22): p. 3271-3279.

29. Deck, L.L., *Model-based phase shifting interferometry.* Applied Optics, 2014. **53**(21): p. 4628-4636.

30. Gronle, M., et al., *Laterally chromatically dispersed, spectrally encoded interferometer.* Applied Optics, 2011. **50**(23): p. 4574-4580.

31. Hassan, M.A., H. Martin, and X. Jiang, *Surface profile measurement using spatially dispersed short coherence interferometry.* Surf. Topogr.: Metrol. Prop. 2, 2014. **2**(2).

32. Martin, H., P. Kumar, and X. Jiang, *A hybrid photonics based sensor for surface measurement.* CIRP Annals Manufacturing Technology, 2014. **63**(1): p. 549-552.

33. Sykora, D.M. and P.d. Groot, *Instantaneous Interferometry: Another View*, in *International Optical Design Conference and Optical Fabrication and Testing*. 2010, Optical Society of America: Jackson Hole, Wyoming United States.

34. Koliopoulos, C.L., *Simultaneous phase shift interferometer.* Proc. of SPIE, 1992. **1531**.

35. Millerd, J.E., et al., *Pixelated Phase-Mask Dynamic Interferometers.* Proc. of SPIE, 2004. **5531**(304).

36. 4d Technology. *4d Technology :: Dynamic Interferometry*. 2015 [cited 2015 2015-09-21]; Available from: http://www.4dtechnology.com/products/dynamictechnology.php.

37. Wyant, J.C., *Dynamic Interferometry.* Optics & Photonics News, 2003. **14**(4): p. 36-41.

38. Morris, M.N., *Dynamic Interferometry for On-Machine Metrology Summary.* Frontiers in Optics 2010/Laser Science XXVI, OSA Technical Digest, 2010.

39. Zeeko Ltd. *On-Machine Stitching Interferometer (OMSI) _ Zeeko Ltd*. 2015 [cited 2015 2015-09-19]; Available from: http://www.zeeko.co.uk/site/tiki-read_article.php?articleId=54.

40. Zhao, C., D. Kang, and J.H. Burge, *Effects of birefringence on Fizeau interfermetry that uses polarization phase shifting technique.* Applied Optics, 2005. **44**(35): p. 7548-7553.

41. Takeda, M., H. Ina, and S. Kobayashi, *Fourier-transform method of fringe-pattern analysis for computer-based topography and interferometry.* Journal of the Optical Society of America, 1982. **72**(1): p. 156-160.

42. Sykora, D.M. and M.L. Holmes, *Dynamic measurements using a Fizeau interferometer.* Proc. of SPIE, 2011. **8082**.

43. Zygo Corporation, *Dynafiz Specifications*. 2015.

44. Kitagawa, K., *Single-shot interferometry without carrier fringe introduction.* Journal of Electronic Imaging, 2012. **21**.

45. Sykora, D.M. and P.d. Groot, *Instantaneous measurement Fizeau interferometer with high spatial resolution.* Proc. of SPIE, 2011. **8126**.

46. Hassan, M., H. Martin, and X. Jiang, *A single-shot line-scanning spatially dispersed short coherence interferometer using Fourier transform profilometry*, in *LAMDAMAP 2015*. 2015: Huddersfield.

47. Groot, P.d., *Coherence Scanning Interferometry*, in *Optical Measurement of Surface Topography*, R. Leach, Editor. 2011.

48. Wyant, J.C., *White Light Interferometry.* Proc. of SPIE, 2002. **4737**.

49. Deck, L.L., *Method and apparatus for optical interferometric measurements with reduced sensitivity to vibration*. 1996.

50. J.Cohen-Sabban and D. Reolon, *Vibration insensitive 3D-profilometry: A new type of white light interferometric microscopy.* Proc. of SPIE, 2008. **7064**.

51. Suematsu, M. and M. Takeda, *Wavelength-shift interferometry for distance measurements using the Fourier transform technique for fringe analysis.* Applied Optics, 1991. **30**(28): p. 4046-55.

52. Yamamoto, A., et al., *Surface Shape Measurement by Wavelength Scanning Interferometry Using an Electronically Tuned Ti:Sapphire Laser.* Optical Review, 2001. **8**(1): p. 59–63.

53.   Jiang, X., et al., *Fast surface measurement using wavelength scanning interferometry with compensation of environmental noise.* Applied Optics, 2010. **49**(15): p. 2903-2909.

54.   Muhamedsalih, H., X. Jiang, and F.Gao, *Acceleration computing process in wavelength scanning interferometry*, in *10th International Symposium on Measurement Technology and Intelligent Instruments*. 2011, Unpublished: Daejeon, South Korea.

55.   Huntley, J.M., T. Widjanarko, and P.D. Ruiz, *Hyperspectral interferometry for single-shot absolute measurement of two-dimensional optical path distributions.* Measurement Science and Technology, 2010. **21**(7).

56.   Zhu, P. and K. Wang, *Single-shot two-dimensional surface measurement based on spectrally resolved white-light interferometry.* Applied Optics, 2012. **51**(21): p. 4971-4975.

57.   Widjanarko, T., J.M. Huntley, and P.D. Ruiz, *Single-shot profilometry of rough surfaces using Hyperspectral Interferometry.* Optics Letters, 2012. **37**(3): p. 350-352.

58.   Widjanarko, T., *Hyperspectral interferometry for single-shot profilometry and depth-resolved displacement field measurement*. 2011, Loughborough University.

59.   Blateyron, F., *Chromatic Confocal Microscopy*, in *Optical Measurement of Surface Topography*, R. Leach, Editor. 2011, Springer.

60.   Precitec, *CHRocodile Optical Probes Overview*. 2015.

61.   WLyda, et al., *Advantages of chromatic-confocal spectral interferometry in comparison to chromatic confocal microscopy.* Meas. Sci. Technol., 2011. **23**(5).

62.   Precitec, *CHRocodile SE Datasheet*. 2015.

63.   Kim, T., et al., *Chromatic confical microscopy with a novel wavelength detection method using transmittance.* Optics Express, 2013. **21**(5): p. 6286.

64.   Papastathopoulos, E., K. Körner, and W. Osten, *Chromatically dispersed interferometry with wavelet analysis.* Optics Letters, 2006. **31**(5): p. 589-591.

65.   Depiereux, F., et al., *Fiber-optical sensor with miniaturized probe head and nanometer accuracy based on spatially modulated low-coherence interferogram analysis.* Applied Optics, 2007. **46**(17): p. 3425-3431.

66.   Yaqoob, Z., J. Wu, and C. Yang, *Spectral domain optical coherence tomography: a better OCT imaging strategy.* BioTechniques, 2005. **39**(6).

67.   Yun, S.H., et al., *Motion artifacts in optical coherence tomography with frequency-domain ranging.* Optics Express, 2004. **12**(13): p. 2977-2998.

68.   Shelton, R.L., et al., *Optical coherence tomography for advanced screening in the primary care office.* Journal of Biophotonics, 2013. **1**(9).

69.   Davidson, B.R. and J.K. Barton, *Application of optical coherence tomography to automated contact lens metrology.* Journal of Biomedical Optics, 2010. **15**(1).

70.   Alarousu, E., A. AlSaggaf, and G.E. Jabbour, *Online monitoring of printed electronics by Spectral-Domain Optical Coherence Tomography.* Scientific Reports, 2013. **3**(1562).

71.   Joo, C., et al., *Spectral-domain optical coherence phase microscopy for quantitative phase-contrast imaging.* Optics Letters, 2005. **30**(16): p. 2131-2133.

72.   Yan, Y., et al., *High-sensitive and broad-dynamic-range quantitative phase imaging with spectral domain phase microscopy.* Optics Express, 2013. **21**(22): p. 25734-25743.

73.   Schmitt, R., N. Konig, and F. Depiereux, *Miniaturization and evaluation of fiber-optic probes for low-coherence interferometry.* Proceedings of SPIE, 2008. **7003**.

74.   Berger, G. and J. Petter, *Non-contact metrology of aspheric surfaces based on MWLI technology.* Proceedings of SPIE, 2013. **8884**.

75.   Berger, G. and J. Petter, *Novel technology for high precision, fast non-contact asphere metrology.* Technisches Messen, 2014. **81**(1): p. 2-7.

76.   Petter, J. and G. Berger, *Non-contact profiling for high precision fast asphere topology measurement.* Proceedings of SPIE, 2013. **8788**.

77.   Hlubina, P., *Dispersive white-light spectral interferometry to measure distances and displacements.* Optical Communications, 2002. **212**(1-3): p. 65-70.

78. Pavlícek, P. and G. Häusler, *White-light interferometer with dispersion: an accurate fiber-optic sensor for the measurement of distance.* Applied Optics, 2005. **44**(15): p. 2978-2983.

79. Galle, M.A., et al., *Characterizing short dispersion-length fiber via dispersive virtual reference interferometry.* Optics Express, 2014. **22**(12): p. 14275-14284.

80. Galle, M.A. and L. Qian, *Low-Coherence Virtual Reference Interferometry for Dispersion Analysis.* IEEE PHOTONICS TECHNOLOGY LETTERS, 2014. **26**(20): p. 2020-2022.

81. Galle, M.A., et al., *Virtual reference interferometry: theory and experiment.* J. Opt. Soc. Am. B, 2012. **29**(11): p. 3201-3210.

82. Hlubina, P. and I. Gurov, *Spectral interferograms including the equalization wavelengths processed by autoconvolution method.* SPIE Proceedings, 2002. **5064**: p. 198-205.

83. Schnell, U. and R. Dandliker, *Dispersive white-light interferometry for absolute distance measurement with dielectric multilayer systems on the target.* Optics Letters, 1996. **21**(7): p. 528-530.

84. Deng, Y., et al., *Wavelet-transform analysis for group delay extraction of white light spectral interferograms.* Optics Express, 2009. **17**(8): p. 6038-6043.

85. Reolon, D., et al., *High resolution group refractive index measurement by broadband supercontinuum interferometry and wavelet-transform analysis.* Optics Express, 2006. **14**(26): p. 12744-12750.

86. Luphos GmbH, *LUPHOSpin - Ultra-precise roundness measurement based on MWLI technology.*, in *Luphos GmbH*. 2011.

87. Physik Instrumente, *PIFOC® Microscope Objective NanoFocussing Positioners & Scanners with Capacitive Sensors*, in *Physik Instrumente*. 2013.

88. P. Hlubina *, J.L.a.c.e., D. Ciprian, R. Chlebus, *Windowed Fourier transform applied in the wavelength domain to process the spectral interference signals.* Optics Communications, 2008. **281**: p. 2349–2354.

89. Gurov, I.P. and O.B. Rufanova, *Verifying measuring accuracy of the fractional part of interference fringe order by interferometric signal autoconvolution method* SPIE Proceedings, 1996. **2969**(381).

90. Pavel, K. and S. David, *Chapter 8: Algorithms for Efficient Computation of Convolution*, in *Design and Architectures for Digital Signal Processing*, G. Ruiz and J.A. Michell, Editors. 2013, InTech.

91. Galle, M., *Virtual Reference Interferometry: Theory and Experiment*, in *Electrical & Computer Engineering*. 2014, University of Toronto.

92. Yi, J.H., S.H. Kim, and Y.K. Kwak, *Peak movement detection method of an equally spaced fringe for precise position measurement.* Optical Engineering, 2002. **42**(2): p. 428-434.

93. Zhong, J. and H. Zeng, *Multiscale windowed Fourier transform for phase extraction of fringe patterns.* Applied Optics, 2007. **46**(14): p. 2670-2675.

94. Liebling, M., et al., *Continuous Wavelet Transform Ridge Extraction for Spectral Interferometry Imaging.* Proc. of SPIE, 2005. **5690**.

95. Newport Corporation, *MFA Series Miniature Linear Stages*. 2012.

96. Estler, W.T., *High-accuracy displacement interferometry in air.* Applied Optics, 1985. **24**(6): p. 808-815.

97. Penalver, D.H., D.L. Romero-Antequera, and F.-S. Granados-Agustin, *Interferogram smoothing and skelotonizing using Bessel functions of the first kind.* Optical Engineering, 2012. **51**(4).

98. Quiroga, J.A., J.A. Gomez-Pedrero, and A. Garcia-Botella, *Algorithm for fringe pattern normalization.* Optics Communications, 2001. **197**: p. 43-51.

99. Restrepo, R., N. Uribe-Patarroyo, and T. Belenguer, *Improvement of the signal-to-noise ratio in interferometry using multi-frame high-dynamic-range and normalization algorithms.* Optics Communications, 2012. **285**(5): p. 546-552.

100. Romero-Antequera, D.L., et al., *Background illumination regularization on interferograms.* Optical Engineering, 2012. **51**(9): p. 095601.

101. Tien, C.-L., S.-S. Jyu, and H.-M. Yang, *A method for fringe normalization by Zernike polynomial.* Optical Review, 2009. **16**(2): p. 173-175.

102. Bourke, P.D., *Cross correlation and autocorrelation for 2d pattern identification*. 1996.

103. Lewis, J.P., *Fast Template Matching.* Canadian Image Processing and Pattern Recognition Society, 1995: p. 120-123.
104. Brunelli, R., *Template Matching Techniques in Computer Vision: Theory and Practice*. 2009: Wiley.
105. Smith, L.M. and C.C. Dobson, *Absolute displacement measurements using modulation of the spectrum of white light in a Michelson interferometer.* Applied Optics, 1989. **28**(15): p. 3339.
106. Martin, H. and X. Jiang, *Dispersed reference interferometry.* CIRP Annals Manufacturing Technology, 2013.
107. ISO, *BS EN ISO 5436*, in *Geometrical Product Specifications (GPS) — Surface texture: Profile method; Measurement standards —*. 2001, ISO.
108. Groot, P.d., et al., *Determination of fringe order in white-light interference microscopy.* Applied Optics, 2002. **41**(22): p. 4571-8.
109. Hecht, E., *Optics*. 2002.
110. Petzing, J., J. Coupland, and R. Leach, *Good Practice Guide No. 116, The Measurement of Rough Surface Topography using Coherence Scanning Interferometry*. 2010, National Physical Laboratory.
111. Adelson, E.H., et al., *Pyramid methods in image processing.* RCA Engineer, 1984. **29**(6): p. 33-41.
112. Hlubina, P. and I. Gurov, *Analysis of the spectral interferograms using Fourier-transform and recurrence non-linear data processing methods.* Proceedings of SPIE, 2001. **4356**.
113. Fujimoto, J.G., et al., *Endoscopic optical coherence tomography of the retina at 1310 nm using paired-angle rotating scanning.* Proceedings of SPIE, 2007. **6429**: p. 642911-642911-11.
114. Jung, W., et al., *Numerical analysis of gradient index lens-based optical coherence tomography imaging probes.* J Biomed Opt, 2010. **15**(6): p. 066027.
115. Wyant, J.C. and E.P. Goodwin, *Field Guide to Interferometric Optical Testing*. 2006: SPIE.
116. Smith, W.J., *Modern Optical Engineering*. 2000: SPIE Press.
117. Edlén, B., *The Refractive Index of Air.* Metrologia, 1966. **2**(2): p. 71-80.
118. Polyanskiy, M.N. *Refractive index database*. Available from: http://refractiveindex.info.
119. Thor Labs. *Equilateral Dispersive Prisms*. 2015; Available from: https://www.thorlabs.com/newgrouppage9.cfm?objectgroup_id=148.
120. Palmer, C. and E. Loewen, *Diffraction Grating Handbook*. 6th ed. 2005.
121. Hobbs, P.C.D., *Building Electro-Optical Systems*. 2000.
122. Hill, D. *How to convert FWHM measurments to 1/e^2 halfwidths*. 2007; Available from: http://www.zemax.com/support/knowledgebase/how-to-convert-fwhm-measurements-to-1-e-squared-ha.
123. Stroud, K.A., *Engineering Mathematics*, in *Engineering Mathematics*. 2001.
124. Pramod Rastogi, E.H., *Phase estimation in optical interferometry*. 2014: CRC Press.
125. O'Haver, P.T. *Intro. to Signal Processing: Smoothing*. 2014 [cited 2014 05/03/2014]; Available from: http://terpconnect.umd.edu/~toh/spectrum/Smoothing.html.
126. Newport Corporation. *Motion Basics and Standards*. Available from: http://www.newport.com/Motion-Basics-and-Standards/140230/1033/content.aspx.
127. Leech, R., *Abbe Error/Offset*, in *CIRP Encyclopedia of Production Engineering*. 2014, Springer Berlin Heidelberg: http://link.springer.com/book/10.1007/978-3-642-35950-7. p. 1-4.
128. O'Haver, P.T. *Peak Finding and Measurement*. 2008 [cited 2013 15/12/2013]; Available from: http://terpconnect.umd.edu/~toh/spectrum/PeakFindingandMeasurement.htm.

11 Appendices

11.1 Theory and nomenclature

Included within this section is the fundamental knowledge required to explain the operation of DRI and competing technologies as well as information to justify experimental, theoretical and design choices. It is hoped that by separating commonly available knowledge from discussion of DRI this section can be referred to for strengthening explanations without interrupting the flow of thesis chapters. The following sub-sections attempt to explain and clarify their content in the context of on-machine metrology.

11.1.1 Coherence

The temporal coherence of a light source is the delay one beam may experience in relation to another beam and still produce interference with a visibility of 50%. The coherence is measured by the distance the light can travel in a vacuum in this amount of time [115]. Coherence length, L_c, therefore goes as

$$L_c = \frac{\lambda_c}{n} \frac{\lambda_c}{\Delta \lambda} \qquad\qquad 11.1$$

Where λ_c is the central wavelength and $\Delta\lambda$ is the bandwidth of the source. And so L_c is inversely proportional to the spectral bandwidth of the source. By example, a He-Ne laser ($\lambda_c = 632.8\ nm$) having a narrow bandwidth (0.001 nm) has a long coherence length (0.4 m), compared to a SLED ($\lambda_c = 820\ nm$) with a comparatively wide bandwidth (25 nm) having a short coherence (26 μm).

11.1.2 Interference

For calculation of the interference between two beams, the intensity goes as,

$$I(k) = \frac{I_0(k)}{2}\left(1 + V\cos\left[\phi(k)\right]\right) \qquad\qquad 11.2$$

Where of the interference $\lambda_c = 820\ nm$

11.1.3 Refraction

The speed of light in a vacuum is given as approximately $3 \times 10^8\ ms^{-1}$. The ratio of the velocity of light in a vacuum to the velocity in a medium is important for the calculation of the propagation of light in optical systems [116]. This is known as the refractive index of the material.

Index of refraction, $n = \dfrac{\text{velocity in vacuum}}{\text{velocity in medium}}$ 11.3

The wavelength of electromagnetic radiation is affected by the refractive index of the medium through which it travels [117] with the wavelength in a vacuum related to the wavelength .

$$n\lambda_{air} = \lambda_{vac}$$ 11.4

Light passing from a material of one index, n_1, into a material of a second index, n_2, is said to be refracted with the angle of refraction determined by Snell's law where the angle of refraction, θ_2, is governed by the angle of incidence, θ_1, and the refractive indices of each material, n_1 and n_2 (equation 11.5).

$$\frac{n_1}{n_2} = \frac{\sin\theta_2}{\sin\theta_1}$$ 11.5

11.1.4 Dispersion

Dispersion is the phenomenon where the index of refraction of a material is dependent on the frequency of the electromagnetic wave passing through it [109]. In the context of dispersed reference interferometry it is necessary to introduce dispersion to separate the wavelengths of the light source angularly so that the path length travelled in the reference arm varies with the wavelength of light.

The refractive index for a material at a given wavelength is determined by the Sellmeier equations, where each material is assigned a set of coefficients which can be used to describe the index of refraction with wavelength over a described wavelength range.

$$n^2(\lambda) = 1 + \frac{B_1\lambda^2}{\lambda^2 - C_1} + \frac{B_2\lambda^2}{\lambda^2 - C_2} + \frac{B_3\lambda^2}{\lambda^2 - C3}$$ 11.6

Table 11.1 shows the Sellmeier coefficients for the Schott glass Flint F2 resulting in the graph of index change with wavelength shown in Figure 11.1. Of particular interest to DRI operation is the linear region where $\lambda > 800$.

	B	C
1	1.34533359	0.00997743871
2	0.209073176	0.0470450767
3	0.937357162	111.886764

Table 11.1: Sellmeier coefficients for Schott glass Flint F2[118].
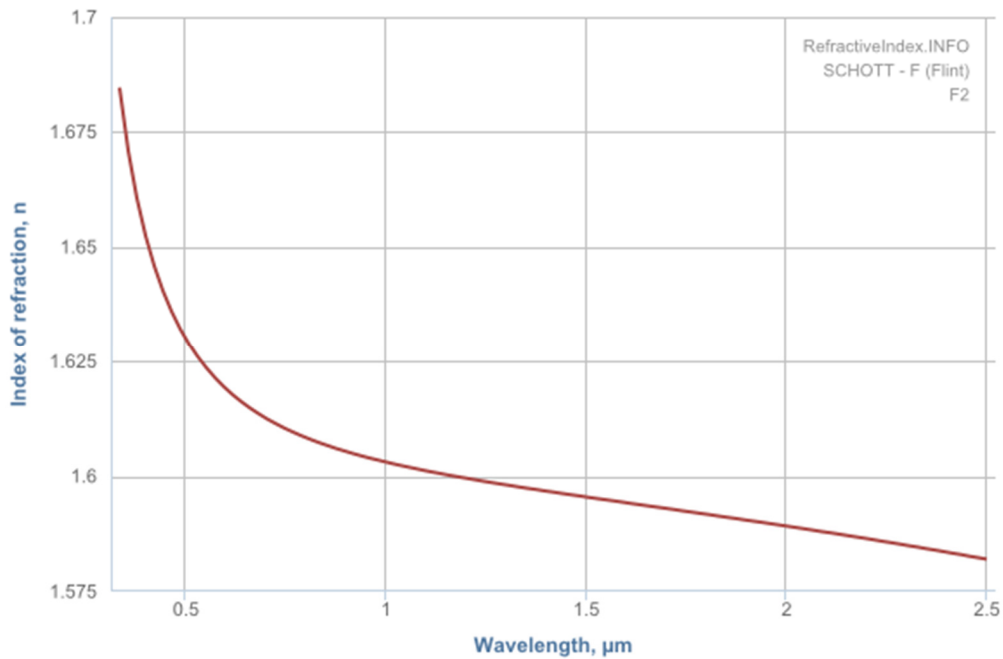
Figure 11.1: Refractive index change with wavelength for Schott glass Flint F2 [118].

In the following subsections common methods of introducing angular dispersion are described and examples of their relevance to use with DRI explained. Equations for deriving dispersion for these methods are presented and an analysis of their advantages and disadvantages for this application described. Their performance over the near infra-red (NIR) wavelength range is calculated in order to further explain their usefulness. Finally, some exotic methods of dispersion are described and their relevance discussed.

11.1.4.1 Prisms

Rays entering a prism are deflected at each surface where index change occurs. For an equilateral prism, this is once upon entering the prism and once upon leaving. The angular deviation, δ, and the angle of refraction, $_v$ exiting ray are dependent upon the angle of incidence, θ_i, the apex angle of the prism, α, and the index of the prism material, n, which is known to change with wavelength, λ, as described above.
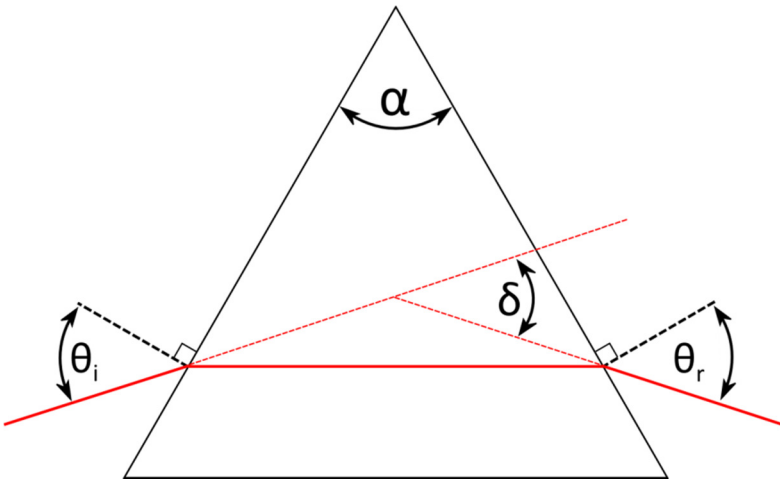
Figure 11.2: Refraction of light in an equilateral prism.

The angle of refraction, θ_r, can be calculated as follows and makes use of geometric rules and Snell's law [109]:

$$\theta_r = \frac{1}{\left(\sin\alpha\right)\left(n^2 - \sin^2\theta_i\right)^{0.5} - \sin\theta_i\cos\alpha} \qquad\qquad 11.7$$

The Sellmeier equation in equation 11.7 describes the change of refractive index with wavelength and as such a broadband light source entering a prism will disperse chromatically as it traverses the prism. For use in DRI an identical inverted prism may therefore be used as in figure 11.3 to recollimate the beam before reflection back through the same path by a mirror.
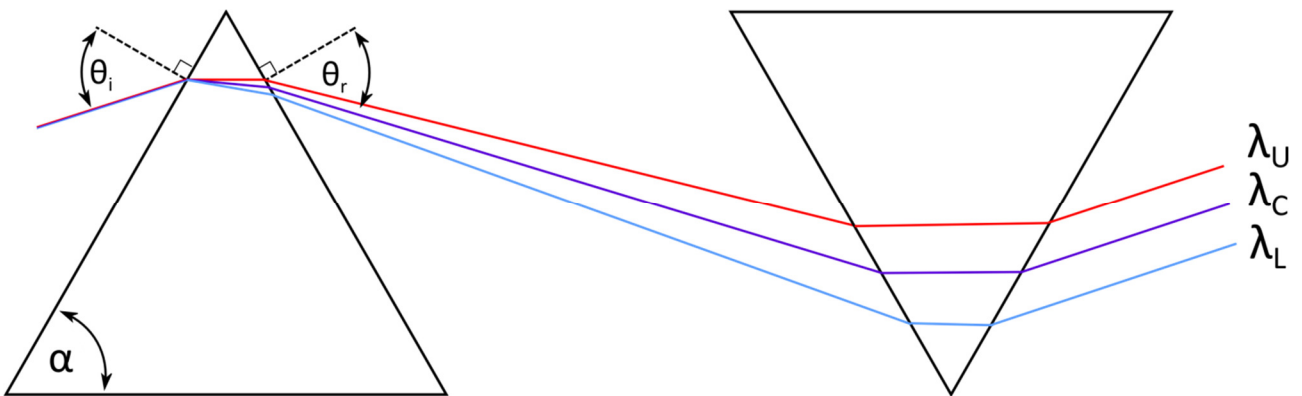
Figure 11.3: Collimated light, dispersed by prism 1 and recollimated by prism 2.

Table 11.2 tabulates the refractive indices of three prisms of different glass types which are available from Thor Labs. Wavelength dependent glass index values [118] are used with a Matlab script (appendix11.4.1) to calculate the angle of refraction, θ_r, for each for an α value of 45°. This allows a direct comparison of the quantity of angular dispersion compared to other dispersion methods.

Prism	Glass	Refractive index, n		Refraction angle, θ_r		$\Delta\theta_r$
		at $\lambda=825$ nm	at $\lambda=875$ nm	at $\lambda=825$ nm	at $\lambda=875$ nm	
PS852[119]	F2	1.6075	1.6061	39.4791°	39.5854°	0.1063°
PS853[119]	N-SF11	1.7632	1.7607	30.0639°	30.1848°	0.1209°
PS863[119]	CaF$_2$	1.4303	1.4299	58.1617°	58.2202°	0.0585°

Table 11.2: Table of Thor Labs dispersive equilateral prisms and their angle of refraction for wavelengths $\lambda=825$ and $\lambda=875$ for an angle of incidence of $\theta_i=40$.

Advantages of prisms include their low cost compared to alternative methods of dispersion as well as their robustness to handling and dust in comparison to diffraction gratings. The most desirable aspect of prisms is the linearity of angular dispersion over the NIR wavelength spectrum of interest for DRI.

Additionally, prisms are highly efficient with no light lost to unwanted diffraction orders unlike gratings. With the use of NIR anti-reflective (AR) coatings the light lost to undesirable reflections can be limited to <0.5 %.

11.1.4.2 Diffraction Gratings

The primary purpose of a diffraction grating is to disperse light spatially by wavelength [120]. This is achieved by a set of closely spaced parallel lines ruled on a glass substrate which have the effect of diffracting incident light. Due to the high cost of producing ruled gratings, nearly all gratings sold are replicas [121], made by casting of a polymer with a precision ruled master grating.

Transmission and reflective gratings produce one or more diffracted orders with the labelling and numbering convention for each shown in figure 11.4.
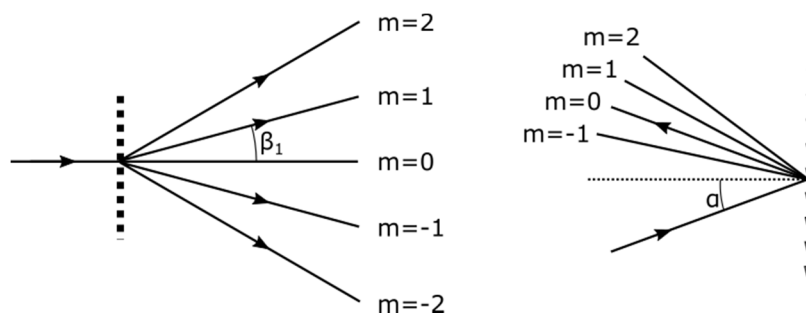
Figure 11.4: Diffraction grating order naming conventions for transmission (left) and reflective (right) diffraction gratings.

The incident beam at angle α to the grating normal is diffracted into multiple orders where the diffracted beam of order m departs the grating at an angle β_m to the grating normal. The zeroth order beam, β_0, leaves the grating at the inverse of the angle of incidence, making $\beta=-\alpha$. The grating equation describes the angle from the normal at which a diffracted order leaves the grating. It goes as

$$\beta_m = \arcsin\left(\frac{m\lambda}{d} - \sin\alpha\right) \qquad\qquad 11.8$$

Where d is the grating pitch, the reciprocal of which is the groove density, G, having the relationship $G = d^{-1}$. Commonly available groove densities for transmission gratings in the NIR spectrum are 300 and 600 lines per millimetre (l/mm) with reflective gratings available at 1200, 1800 l/mm.

This increased angular dispersion over the wavelength when compared to prisms makes gratings highly attractive for use in DRI since a greater angular dispersion allows reduction in grating separation for the same optical path difference range. This in turn provides a more compact bulk optics interferometer setup, a major consideration for commercial interferometry but more importantly less prone to angular misalignments.

However, downsides to use of gratings include the decreased linearity of angular dispersion compared to prisms as well as the lower optical efficiency offered by gratings due to power lost to unused diffraction orders. Lastly, when compared to prisms, gratings are expensive and fragile with the impossibility of cleaning them making their lack of robustness a consideration for use in a factory environment.

11.1.4.3 Dispersive fibre

Dispersed reference interferometry has previously been demonstrated with the use of single mode fibres for the reference and measurement arms where the dispersion factor of the reference arm fibre is higher than that of the measurement arm [78]. By calculation of the length of fibre required to provide sufficient dispersion a Michelson fibre interferometer can be realised where by the resulting spectral interferogram can provide a range of several hundred microns.

The quantity of chromatic dispersion experienced by light traversing a single mode fibre is dependent upon the dispersion parameter of the fibre. The differing refractive index of the fibre for a range of wavelengths mean that some wavelengths travel faster than others within the fibre, leading to chromatic dispersion.

Advantages of fibre for dispersion over other methods include the compactness of such a dispersive element as limited only by the minimum bend radius of the fibre, the reference arm can be coiled up into a tight space. It is also cheap (~£5 /m) and robust to dust and handling when compared to diffraction gratings.

Disadvantages include the expense and time required for connectorising as well as the difficult adjustability of fibre lengths when compared to the separation of bulk optics elements such as gratings and prisms.

11.1.5 Gaussian beam properties

This section details the equations used in Gaussian optics to describe the parameters critical to characterising Gaussian beams during their propagation through an optical system. The intensity of a Gaussian beam at a distance, r, from the optical axis goes as,

$$I = I_0 e^{=2r^2/w^2}$$

11.9

Where I_0 is the intensity at the beam axis. The beam width at any distance, z, from the beam waist can be described as,

$$w(z) = w_0 \left[1 + \left(\frac{\lambda z}{\pi w_0^2} \right)^2 \right]^{1/2} = \frac{\lambda z}{\pi w_0}$$

11.10

Beam diameter can be measured experimentally using the Foucault knife-edge test in which occlusion of the beam occurs gradually as the power at a photodiode is measured [116].

11.1.5.1 Definitions of beam power and diameter

The Gaussian distribution defined by equation 11.9 is often used to describe the power of a beam with distance from an optical axis as well as power of a light source with wavelength. This equation describes the power from 0 to infinity and so for beam width and spectrum width of a Gaussian beam, an arbitrary level must be applied to define beam features such as beam waist or bandwidth.

One commonly used value is the full width half maximum (FWHM), or the beam/spectrum width at which the power decreases to half its original value. A second description of beam or spectrum width is the $1/e^2$ point, the width of the beam at which the power decreases to $1/e^2$ of the maximum or 13.5 % of the full power. These values can be used interchangeably by manufacturers or users of optical components, sometimes without defining how a beam or spectrum width is described and so it is important to be wary of how beam spot sizes, lateral resolutions or light source bandwidths are presented. For example, a lateral resolution described by the FWHM beam spot size is going to be favourable compared to the $1/e^2$ definition for the same spot if lateral resolution is being promoted. Equally, the manufacturer of a wide bandwidth light source may use the $1/e^2$ spectrum width to maximise the apparent usefulness of a light source.
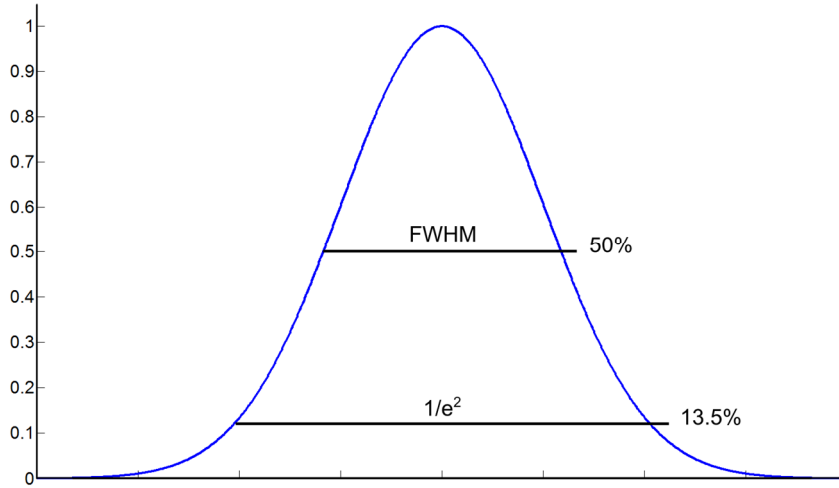
Figure 11.5: Diagram of Gaussian beam shape with the FWHM and $1/e^2$ points described. Axes explained in description.

With this in mind, the beam/spectrum parameters can be easily switched between to maintain calculation consistencies. To convert from a beam diameter calculated as FWHM to the $1/e^2$ definition [122]:

$$I_e = 1.699 \times I_{FWHM} \tag{11.11}$$

The inverse of which can be calculated as follows:

$$I_{FWHM} = \frac{I_e}{1.699} \tag{11.12}$$

11.1.5.2 Beam waist radius

The beam waist radius of a Gaussian beam is the point at which it reaches the minimum beam waist radius, ω_0, is an important consideration in single point metrology since the beam waist radius of a focused beam determines the minimum spot size and hence the attainable lateral resolution of the system. The beam waist radius, ω_0, for a given wavelength at focal length, F, is given by

$$2\omega_0 = \left(\frac{4\lambda}{\pi} \right) \left(\frac{F}{D} \right) = \theta_s \tag{11.13}$$

Where λ is wavelength, F is the focal length of the lens and D is the input beam diameter. The beam width may also be determined as the distance from the optical axis at which the intensity drops to a factor of 0.5 of the original intensity, known as the full width half maximum (FWHM). The beam diameter at the focal point is twice the beam radius and often described as spot size. It is given the symbol θ_s.

11.1.5.3 Depth of field

The depth of field (DOF) of a beam is the distance over which the beam diameter remains within an arbitrarily defined acceptable width. This value gives a consistent method of calculating DOF to allow comparison of the range over which a lens will work for a given input beam diameter. Depth of field

is defined in relation to another important beam parameter, namely it is twice the Rayleigh length which describes the distances from the focal point at which the beam remains less than $2\omega_0\sqrt{2}$. The depth of focus and its relation to the Rayleigh length can be calculated as follows,

$$DOF = \left(\frac{8\lambda}{\pi}\right)\left(\frac{F}{D}\right)^2 = 2z_R \qquad\qquad 11.14$$

Where λ is wavelength, F is the beam focal length, D is the input beam diameter and z_R is the Rayleigh length [109].

11.1.5.4 F-number

The F-number or F# is a term commonly used to denote the ratio of the focal length of an optical system to the aperture. In the case of interferometry it is useful in calculating the numerical aperture. The $F\#$ is calculated using the focal length, f, and input beam diameter, D, as follows:

$$F\# = \frac{f}{D} \qquad\qquad 11.15$$

11.1.5.5 Numerical Aperture

The numerical aperture (NA) of a lens is a term commonly used to describe the ability of an optical system to gather light. It is calculated as twice the reciprocal of the $F\#$ as follows:

$$11.16$$
$$NA = \frac{1}{2\cdot F\#}$$

11.1.5.6 Angular Aperture and acceptance angle

The angular aperture of a lens is the angle at which rays traced along the outside diameter of an input beam will meet after focusing by the lens. The acceptance angle, θ_a, is half this value.

$$\alpha = 2\tan^{-1}\left(\frac{D}{2f}\right) \qquad\qquad 11.17$$

$$\theta_a = \frac{\alpha}{2} \qquad\qquad 11.18$$

11.1.5.7 Acceptance Angle

The acceptance angle, θ_a, of an optical component (lens, collimator, optical fibre) is half the angular aperture, α, with the acceptance angle being the angle between the beam normal and the path travelled by a ray traced along the outside diameter of the input beam.

$$\theta_a = \alpha/2 \qquad\qquad 11.19$$

The acceptance angle is a useful description of the maximum incident angle at which sufficient light is still returned in an optical system and provides a good indication of how well the lens will gather light from diffuse sources such as rough surfaces.

11.1.6 Standard deviation

The standard deviation describes the distribution of values around the mean of a sample. It is defined as:

$$\sigma = \sqrt{\frac{\Sigma (x - \bar{x})^2}{n}}$$

11.20

Where x is a value within the sample, $\bar{x}$ is the sample mean and n is the sample size [123].

11.1.7 Simple phase unwrapping

Throughout this thesis, simple single-dimensional phase unwrapping is implemented for unwrapping of relative measurement data calculated by template matching. This algorithm makes no allowance for common sources of error such as noise, discontinuities, invalid data or under sampling [124] however its simplicity makes it attractive for an initial attempt at unwrapping where noise is low and interferogram contrast is high. Figure 11.6 illustrates how the surface height position calculated by template matching is relative and requires unwrapping for a 60 μm translation over a Rubert roughness sample which has a specified Ra of 100 nm.
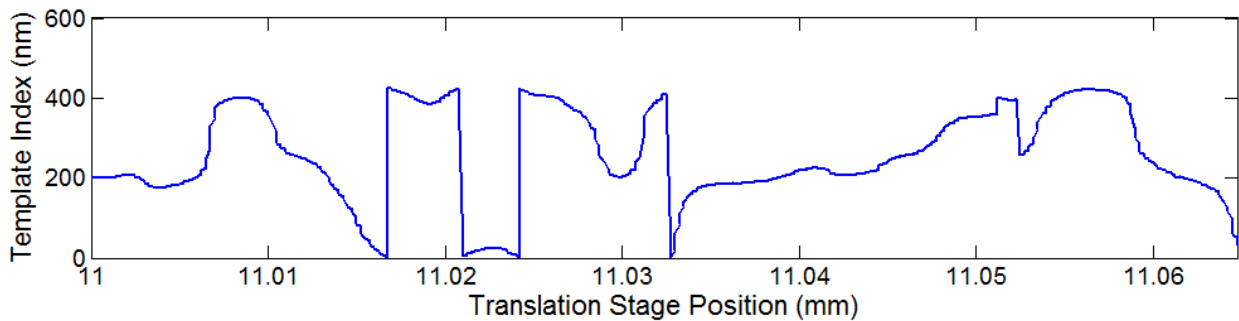

Figure 11.6: The template matching calculated phase across a 0.18 mm section of a Rubert roughness sample. Wraparounds are frequent and bi-directional.

By comparison of this phase with the first derivative it is possible to observe the position of the phase wraparounds. Equation 11.21 describes the discrete calculation of $\mathbf{f}'$, the first derivative of the phase signal, adapted from code by O'Haver [125].

$$\mathbf{f}' = \left(f_1', \cdots, f_i', \cdots, f_{W_f}' \right)^T$$

$$f_i' = \begin{cases} f_2 - f_1 & \text{if } i = 1 \\ \dfrac{f_{i+1} - f_{i-1}}{2} & \text{if } 1 > i < W_f \\ f_{W_f} - f_{W_f - 1} & \text{if } i = W_f \end{cases} \qquad\qquad 11.21$$

Where $\mathbf{f}$ is a vector of length W_f containing the template matching position of the interferograms as the measurement beam is translated across the sample. With comparison of the original measurement data to the first derivative the wraparound positions and their direction become clear.

Figure 11.7: The first derivative of the phase, calculated by two-point central difference. Wraparounds can be observed where a large peak or valley occurs.

Next the first derivative is used to calculate a vector providing a map of the locations of the wraparounds. Where the value of the first derivative exceeds 150 the wraparound counter, ω, is decremented. Where the first derivative is less than -150, ω is incremented.

$$\boldsymbol{\omega} = \left(\omega_1, \cdots, \omega_i, \cdots, \omega_{W_f} \right)^T$$

$$\omega_i = \begin{cases} 1 & \text{if } i = 1 \\ \omega_i + 1 & \text{if } f_i < 150 \\ \omega_i - 1 & \text{if } f_i > 150 \\ \omega_{i-1} & \text{if } f_i = 0 \end{cases} \qquad\qquad 11.22$$

With a vector containing wraparound order across the measurement, the unwrapping can occur by multiplying the wraparound order by half the central wavelength and summing with the template matching result for each position along the scan, with figure 11.80 showing the resulting unwrapped data.

$$\mathbf{u} = \left(u_1, \cdots, u_i, \cdots, u_{W_f} \right)^T$$

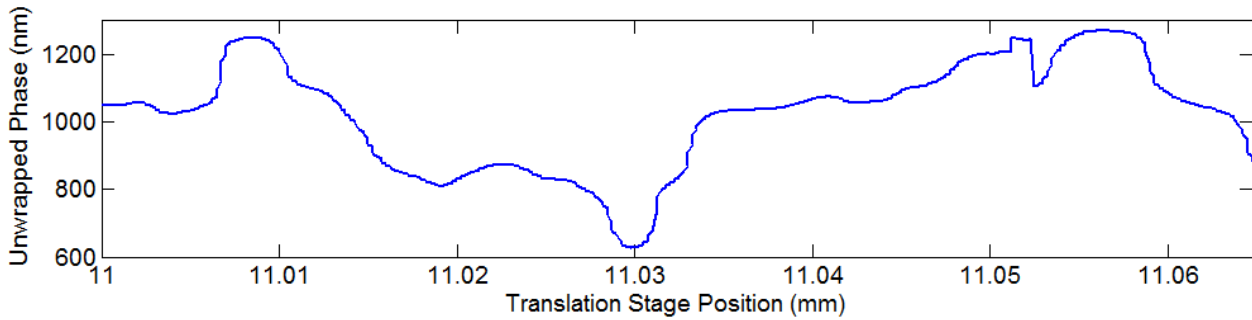$$u_i = 0.5 k_c \omega_i + f_i \qquad\qquad 11.23$$

Figure 11.8: Unwrapped measurement data calculated by thresholding of first derivative of the measurement position values.

11.1.8 DRI bulk optics layout component list

Section 3.3 describes the physical apparatus used to demonstrate a bulk optics layout of the dispersed reference interferometer. The following table describes the suppliers, part numbers and nominal values of the components chosen for initial validation of DRI.

Label	Supplier	Part Number	Description
SLED	Exalos	EXS210036-01	Superluminescent diode
FC	Thor Labs	F810APC-842	Fibre collimator
BS	Thor Labs	BS017	50:50 non-polarising beamsplitter cube
M1	Thor Labs	ME1S-M01	Planar gold coated protected mirror
G1	Thor Labs	GTI25-03	25 mm 300 l/mm transmission grating
G2	Thor Labs	GTI25-03	25 mm 300 l/mm transmission grating
M2	Thor Labs	ME1S-M01	Planar gold coated protected mirror
G3	Thor Labs	GR25-1208	25 mm 1200 l/mm reflective grating
SM	Edmund Optics	32-819	2" spherical mirror, f=12"
D	ISG	LW-SLIS-2048A-1394	2048x1 CMOS FireWire camera

Table 11.3: Table of optical components used for initial layout of a bulk optics DRI interferometer.

11.1.9 Translation stage motion errors

The reliance of single-point measurement methods on the motion of a precision stage for translation of a probe or sample mean that understanding the relevant terminology is important for correction and compensation of such errors. Presented here are the stage motion errors for linear translation stages. Flatness is defined as the displacement of the stage along the Z axis of a stage moving in the direction of travel along the X axis. Straightness is defined as deviation along the Y axis as the stage travels in the X direction.
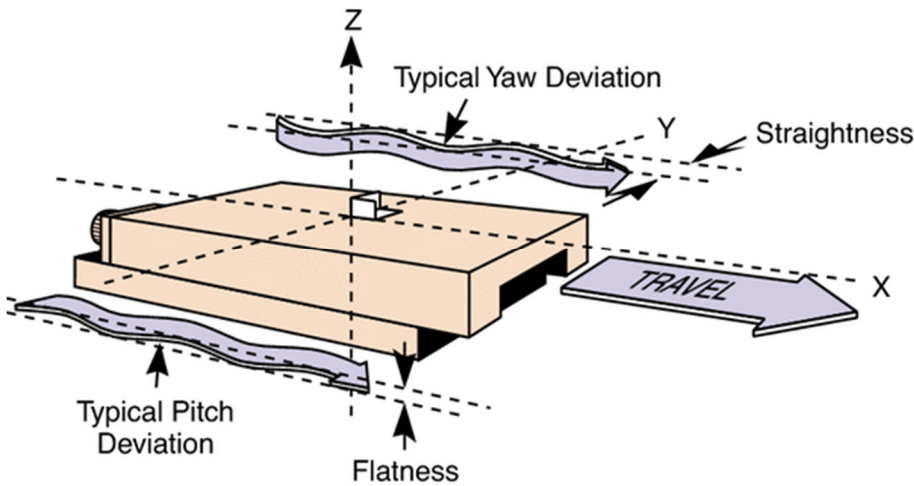
Figure 11.9: Flatness and straightness runout labelling convention for a linear stage [126].

Rotation of the stage around the axes as it travels is undesirable with the terms roll (X axis), pitch (Y axis) and yaw (Z axis) used to differentiate angular translation around the respective axes.
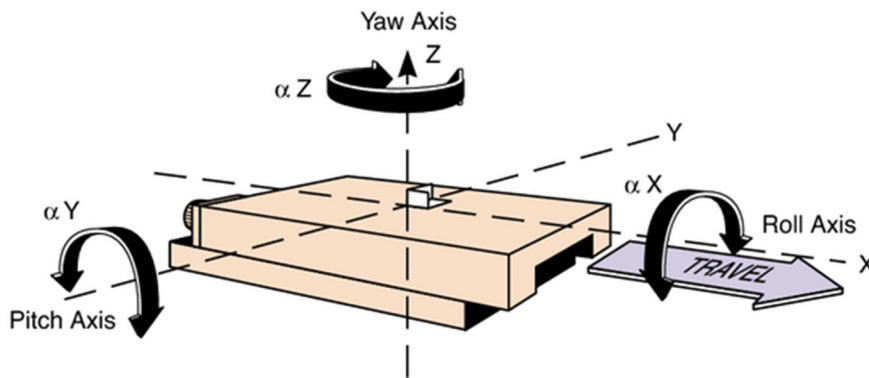

Figure 11.10: Angular runout labelled as roll, pitch and yaw [126].

These are important in motion as they lead to angular misalignments as well as Abbe error. This is an effect where the position of the stage load is affected by a combination of the angular misalignment as well as the distance of the load from the stage axis of rotation. Abbe error can be defined as follows:

$$\varepsilon = d \tan(\theta)$$ 11.24

Where ε is the Abbe error, d is the offset and θ is the angular error of the positioning system [127].

11.2 Interferogram regularisation

Interferogram shape correction is a well-studied topic, with a number of authors detailing methods to correct distortions in interferogram shape [97-101] for extraction of information in a single phase or for removal of background illumination. Regularisation is the process of detecting the maxima and minima of the interferogram and locally changing the amplitude to remove gain envelopes and visibility

inconsistencies. This results in an interferogram whose intensity ideally varies between 0 and 1 across the entire interferogram, with regularisation different from normalisation in that it is not simply a scaling operation. Section 3.8.2 outlines reasons that interferogram regularisation would be advantageous for DRI; a summary of the regularisation process is as follows, based on a method outlined by Romero-Antequera et al [100]. In the first instance of this work, Matlab has been used to process offline interferograms saved from the apparatus. This will allow for optimisation of the many parameters to achieve an acceptable regularisation result.

Figure 11.11: Flow diagram for the regularisation of single dimensional interferograms.

The following equations and descriptions detail the analysis and corrections of the unmodified interferogram taken from the bulk optics interferometer seen in figure 22.37. The DC offset and low frequency envelopes present in this figure may not be obviously apparent, but as the regularisation progresses the overlaid graphics will make this clear.
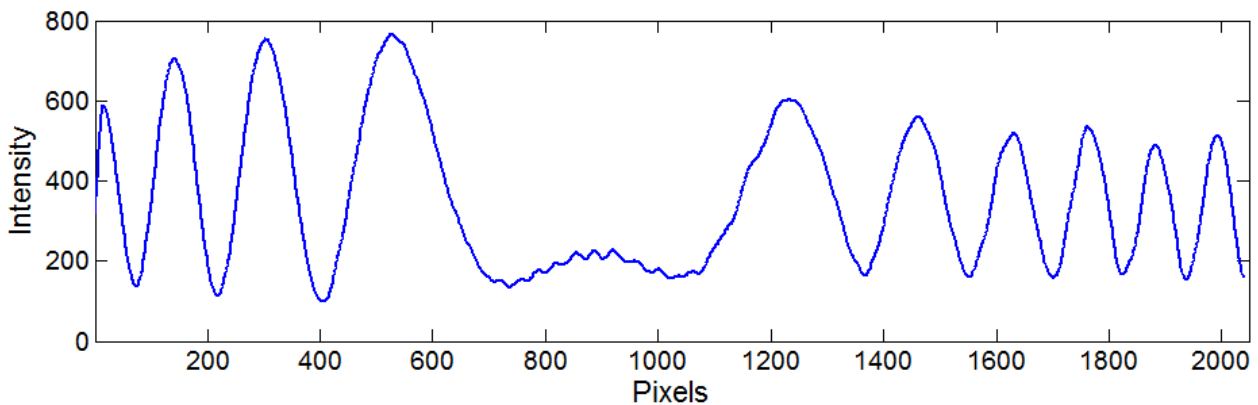

Figure 11.12: Interferogram from the bulk optics interferometer. Shows a DC offset and an upper and lower low frequency envelope.

11.2.1 Maxima/minima detection

$$\mathbf{D} = \left(d_1, \cdots, d_i, \cdots, d_m \right)^T$$

11.25

$$d_i = \begin{cases} h_{i+1} - h_k & \text{if } i = 1 \\ \left(h_{i+1} - h_{k-1} \right)/2 & \text{if } 1 < i > m \\ h_i - h_{i-1} & \text{if } i = m \end{cases}$$

Peak fitting is achieved using a pair of Matlab functions by Prof. Tom O'Haver [128] which provide peak and valley detection respectively. The first step of these functions is to calculate the first derivative of the signal, providing the slope. The theory of peak finding is that at a peak or a valley the gradient of the

175

signal reduces to zero as the signal changes direction when forming the peak or valley. Derivation of the signal provides the gradient, and where the gradient crosses the X axis denotes the location of the peak or valley. To this end, the first step to finding the peak positions is derivation of the signal, as shown by equation 11.25 and illustrated by the blue trace in 11.13. The red trace is a plot of $y = 0$ to allow visualisation of the zero crossing points.
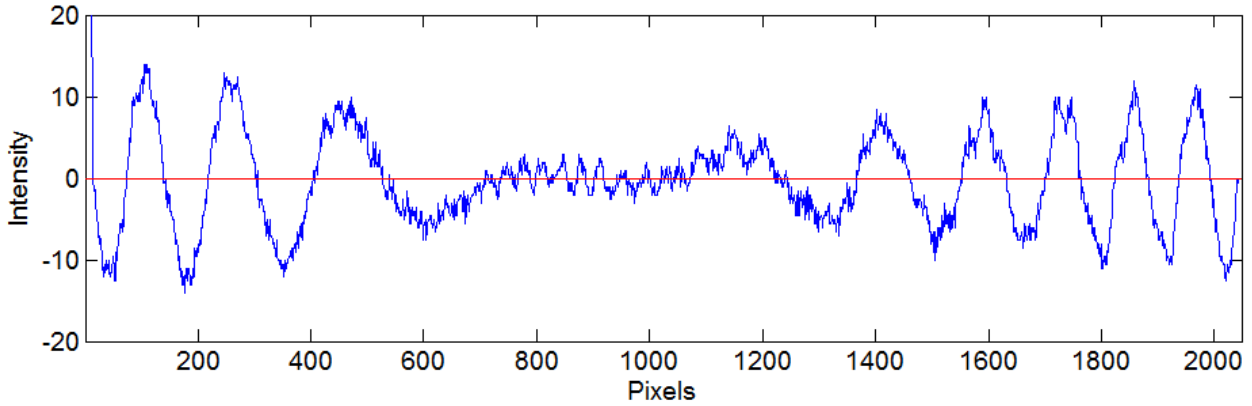

Figure 11.13: A graph showing the first derivative of the interferogram signal (blue) with a line at y=0 to aid in visualisation of the zero crossing points.

Having calculated the first derivative as above, the signal is next smoothed using an unweighted centred sliding average smooth, replacing each point in the interferogram derivative with the average of w_U adjacent points:

$$\mathbf{S} = \left(s_1, \cdots, s_i, \cdots, s_m\right)^T$$

$$s_i = \begin{cases} \dfrac{d_i + d_{i+1}}{2} & \text{if} \quad i = 1 \\[2ex] \dfrac{\sum\limits_{n=1}^{2i-1} d_n}{2i - 1} & \text{if} \quad 1 < i \leq 0.5\left(w_U + 1\right) \\[2ex] \dfrac{\sum\limits_{n=i-f}^{i+f} d_n}{w_U} & \text{if} \quad w_U < i < \left(m - w_U\right) \\[2ex] \dfrac{\sum\limits_{n=2i-m}^{m} d_n}{2(m-i)+1} & \text{if} \quad \left(m - w_U\right) \leq i < m \\[2ex] \dfrac{d_i + d_{i-1}}{2} & \text{if} \quad i = m \end{cases}$$
11.26

where window width, w_U, is an odd integer, $f = 0.5\left(w_U - 1\right)$ and the components 1, 2, 4 and 5 of the equation deal with the edge conditions where the width of the sliding window must be decreased as it approaches the edge of the detector. Figure 11.14 shows the smoothed first derivative of the

interferogram using a smooth width of 51 pixels, larger values of smooth width will result in the smoothing of smaller peaks.
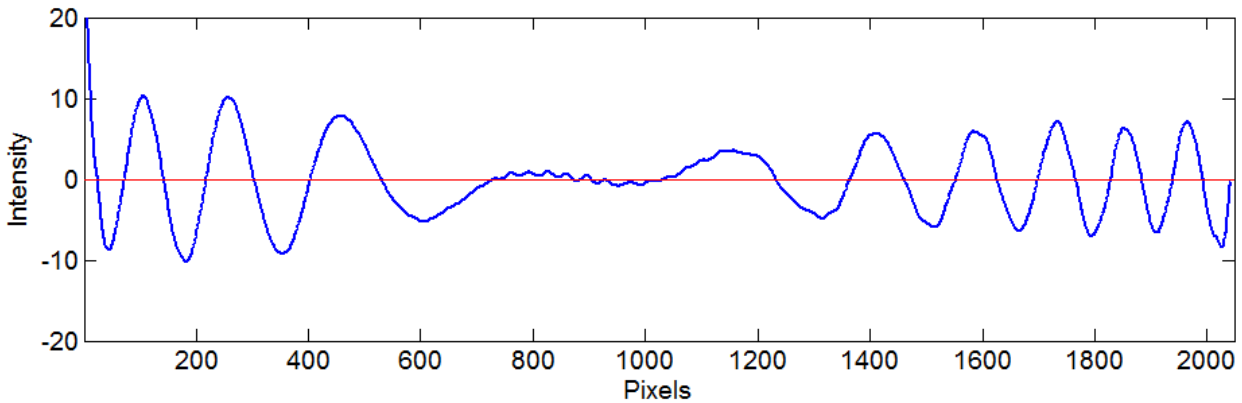

Figure 11.14: First derivative of the interferogram smoothed with a centred sliding average smooth of width 51.

The next step is detection of the pixels where the smoothed derivative crosses the X axis, with these points indicative of peaks or valleys when the zero crossing points have a negative or positive sloping gradient respectively. Iterating through the vector, the Matlab function compares the intensity of the smoothed first derivative for each pixel to that of the next. When the sign of the intensity changes, 'findpeaks.m' and 'findvalleys.m' use k values to exclude peaks that are not of interest. These are:

Slope Threshold: The gradient of the derivative is indicative of the width of the peak. The slope threshold parameter allows exclusion of peaks which are too wide.

Amplitude Threshold: This threshold is used to exclude peaks which are too short by comparing the intensity of the detected peak on the original interferogram with the provided amplitude threshold.

Having excluded peaks that may be too low or too wide, the result is a pair of vectors containing (a) the index of each detected peak or valley and (b) the amplitudes of the original unsmoothed interferogram at these indexes. The locations and amplitudes of these peaks may currently not be accurate due to the distorting effects of applying smoothing. The final step in detecting the extrema positions is to use least squares fitting of a parabola to the original data around each detected peak to calculate peak position and intensity to a higher accuracy than possible with smoothed data. The resulting peak and valley positions, and the amplitudes and widths of each are stored in the peak and valley matrices $\mathbf{P}$ and $\mathbf{V}$ respectively. An example of the detected peaks and valleys are shown as red crosses in figure 11.15.
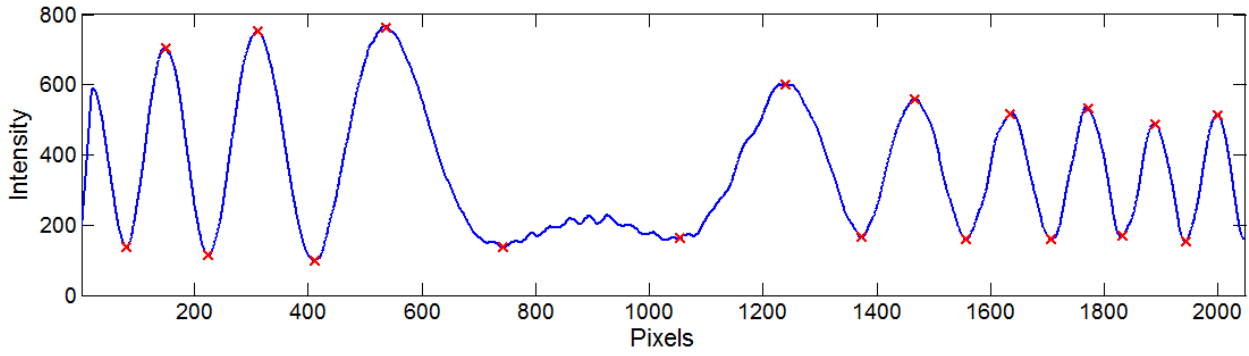
Figure 11.15: Plot of interferogram (blue) with scatter showing the detected peak and valley positions (red crosses).

11.2.2 Envelope calculation

With successful detection of the peaks and valleys it is now necessary to calculate the upper and lower envelopes formed by the peaks and valleys of the interferogram respectively. To achieve this a polynomial fit is calculated for the set of peaks and valleys using matrices $\mathbf{P}$ and $\mathbf{V}$ as inputs. This results in two vectors of length m containing the upper envelope, $\mathbf{e_U}$ and lower envelope, $\mathbf{e_L}$, where the central envelope, $\mathbf{e}_C$, is simply the average of the upper and lower envelopes and is calculated element-wise as follows.

$$\mathbf{e_C} = \left(e_{C1}, \cdots, e_{Ci}, \cdots, e_{Cm} \right)^T$$
$$e_{Ci} = 0.5 \left(e_{Ui} + e_{Li} \right)$$

11.27

The graph in figure 11.16 shows an interferogram (blue) from the bulk optics interferometer along with the calculated upper and lower envelopes (red) and the central envelope (green).
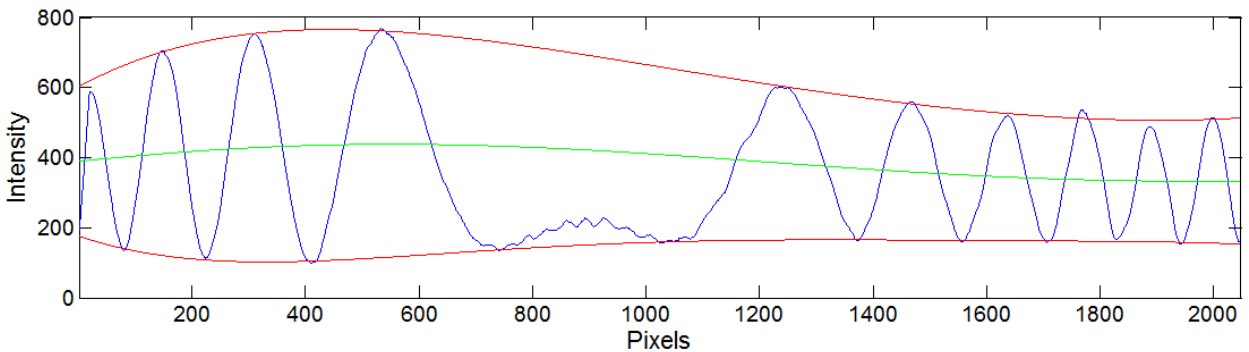

Figure 11.16: Interferogram (blue) with calculated upper and lower envelopes (red) and central envelope (green).

11.2.3 Background intensity and envelope removal

The aim of this step is to transform the upper envelope, centre envelope and lower envelope so every value of each is 1, 0.5 and 0 respectively while applying the same transform to the intensity of the interferogram. This will result in a regularised interferogram.

To do this, the local fringe visibility is first calculated for each pixel.

178

$$\mathbf{f} = \left(f_1, \cdots, f_i, \cdots, f_m \right)^T$$

$$f_i = \frac{e_{Ui} - e_{Li}}{e_{Ui} + e_{Li}}$$

<div align="right">11.28</div>

Finally, the local fringe visibility, $\mathbf{f}$, is used with the average intensity envelope, $\mathbf{e}_C$, and the interferogram, $\mathbf{H}$, to calculate the regularised interferogram $\mathbf{R}$.

$$\mathbf{R} = \left(r_1, \cdots, r_i, \cdots, r_m \right)^T$$

$$r_i = 0.5 \left(1 + \frac{1}{f_i} \left[\frac{h_i}{e_{Ci}} - 1 \right] \right)$$

<div align="right">11.29</div>

The resulting interferogram (figure 11.17), while not perfect, is much improved over the previous unregularised interferogram (figure 22.37);
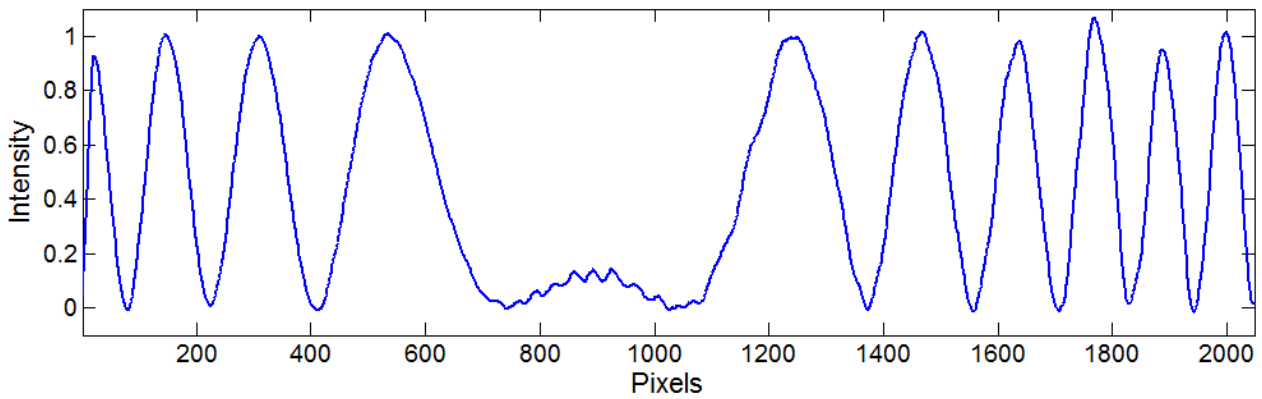

Figure 11.17: Graph of a regularised interferogram showing much improved low frequency envelopes.

11.2.4 Correction for all interferogram cases

Due to the nature of an interferogram with a stationary phase, as the phase evolves, peaks and valleys will be detected near the centre and cause problems with removal of the low frequency envelopes. Figure 11.18 shows an example of an interferogram where the centre has incorrectly been identified as part of the upper envelope. Included in this diagram is the original interferogram (blue), the upper and lower envelopes (red), the central envelope (green) and the positions of the peaks used to calculate the polynomial fits for the envelopes (black crosses). It can be seen that the peak detected at pixel 900 alters the polynomial fit for the upper envelope, forcing it to an incorrect fit to the remaining points for the polynomial order used here.
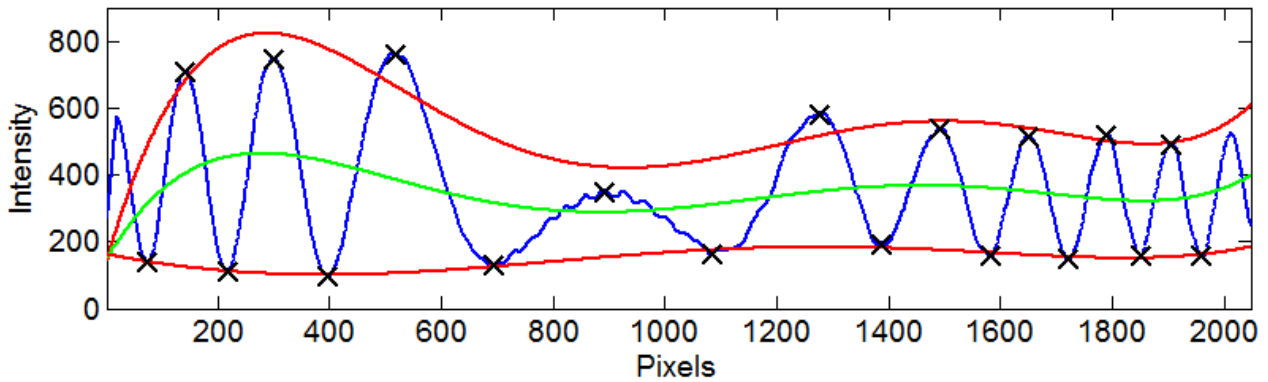
Figure 11.18: Interferogram with an incorrectly calculated upper envelope due to a peak detected at the centre of the interferogram.

It is not immediately clear that matching to the peak at pixel 900 is incorrect. For clarification of this issue, figure 11.19 shows a simulated interferogram of similar shape, having ideal upper and lower envelopes but still with a central peak well below the envelopes. It is difficult to exclude this peak from the peak fitting algorithm using amplitude and slope thresholds alone, and so with knowledge of the approximate location of the interferogram point of symmetry from autoconvolution, this erroneous peak can be excluded.
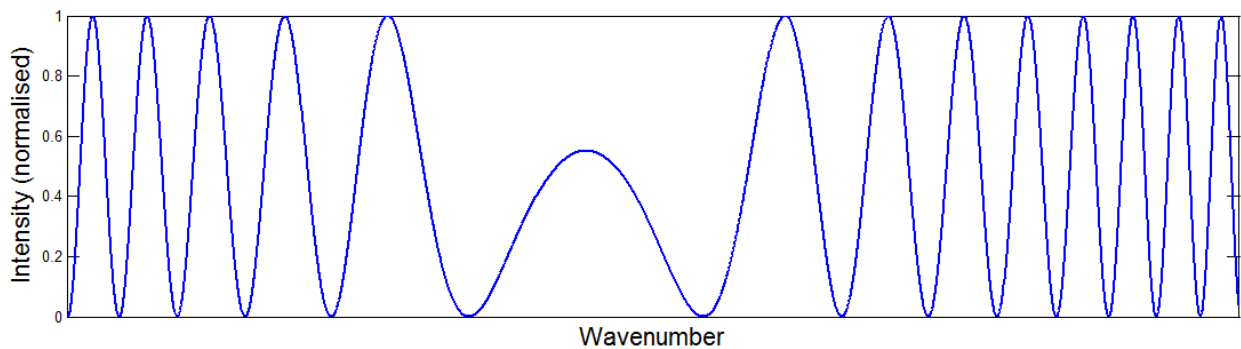

Figure 11.19: Simulated interferogram having ideal visibility and no envelopes. This demonstrates how the peak detected at the centre of the interferogram cannot always be considered part of the detected envelopes and how it is necessary to exclude peaks and valleys detected near the centre of the interferogram to eliminate errors.

It is because of this erroneous central peak that a peak exclusion zone is implemented around the point of interferogram symmetry. All peaks and valleys which are detected within 100 pixels of the centre position are removed from the vectors $\mathbf{P}$ and $\mathbf{V}$ containing peak and valley positions respectively. Figure 11.20 shows the same pre-regularisation interferogram shown in figure 11.18, the shape of the upper envelope however is a far better fit to the shape of the interferogram due to the polynomial fit not attempting to include a much lower amplitude peak near the symmetry position. This results in a much improved interferogram regularisation.

It should be noted at this point that although in the case of figure 11.18 it would appear that simple amplitude thresholding would successfully exclude this erroneous peak, it is difficult to do this in reality

since the visibility and offset from 0 intensity change as surface measurement slope and reflectivity as well as other environmental effects vary during measurement.
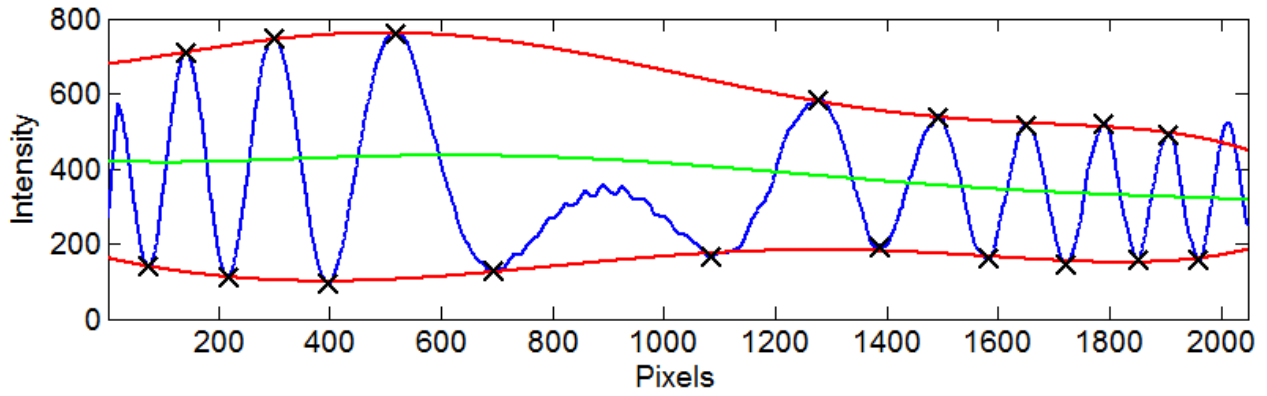

Figure 11.20: Real interferogram corrected using the regularise.m Matlab function. Centre peaks and valleys are excluded, while peaks at either end of the interferogram can be seen to be not detected due to their proximity to the detector edges.

11.3 Signal processing updates for longer interferograms

Changes made to the bulk optics interferometer layout are described at the start of section 5 and include introduction of a wider bandwidth light source and use of a detector with an increased number of pixels to improve the spectrometer bandwidth and hence the interferometer range. The perpendicular separation of the reference arm diffraction gratings was also reduced to 220 mm to improve the resolution of absolute position measurement by autoconvolution. These changes to ease combination of autoconvolution and template matching require an additional set of signal processing steps to allow determination of spectral interferogram symmetry position by autoconvolution and are described below.

Figure 11.21 shows an interferogram from the new bulk optics setup whose distance from the 0 OPD position is 400 μm. If symmetry position calculation with autoconvolution can be made possible for this interferogram then the range of the improved interferometer will be 800 μm. The autoconvolution of such an interferogram does not exhibit a strong peak in the location of the interferogram point of symmetry, near pixel 6400 and for this reason the following corrective steps are required to obtain measurement data for these extended range interferograms.
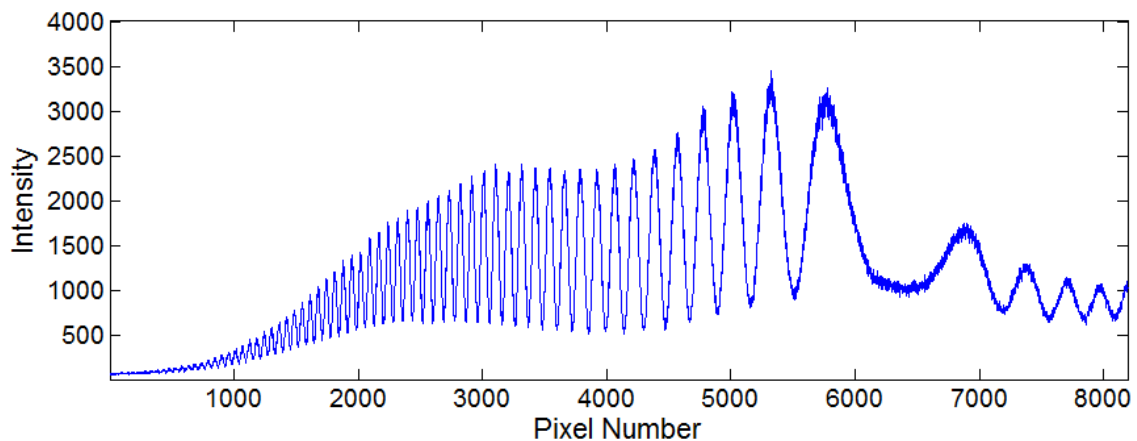

Figure 11.21: Typical spectral interferogram produced by new bulk optics layout.
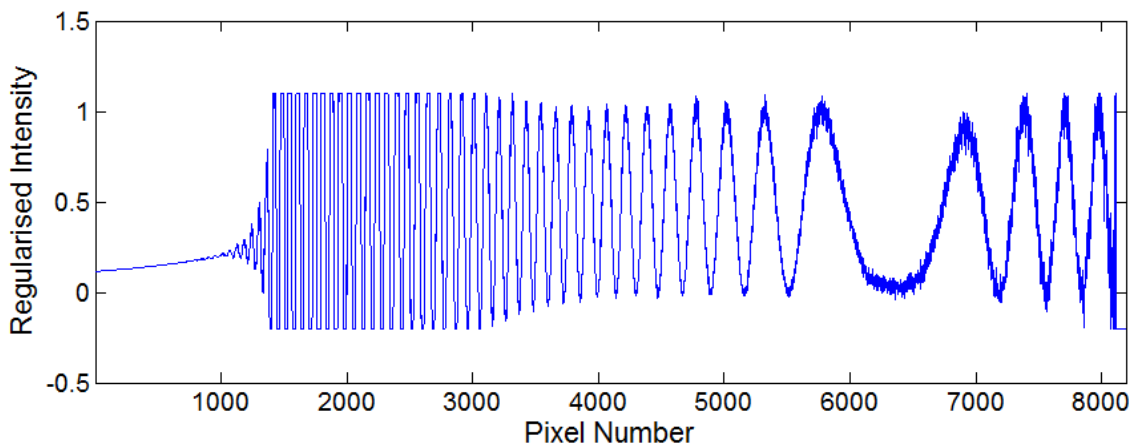

Figure 11.22: Regularised interferogram with values limited to between 1.2 and -0.2.

Regularisation, as described by section 11.2, corrects the low frequency envelope of the interferogram. The values of this regularisation are limited to 1.2 and -0.2 to reduce errors which can be seen on the left half of the regularised interferogram in figure 11.22.

Calculation of the first derivative yields the gradient of each pixel. Application of a smoothing algorithm to this data results in the graph shown in figure 11.23. Finally the autoconvolution is calculated with the result shown in red in figure 11.23. Unlike previous implementations of autoconvolution, calculating the gradient and smoothing results in an autoconvolution result whose negative, not positive, peak indicates the stationary phase point of the interferogram.
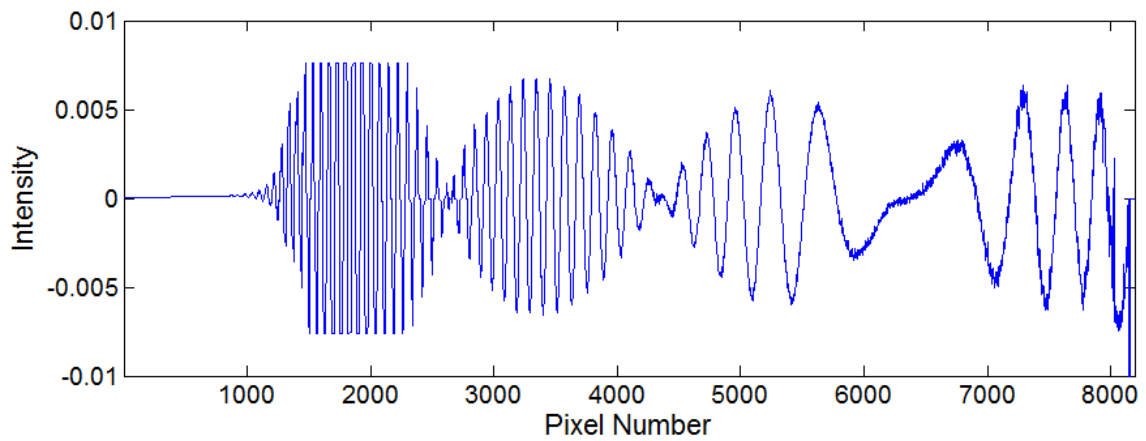

Figure 11.23: Graph of the smoothed first derivative of an interferogram from the extended range DRI setup.
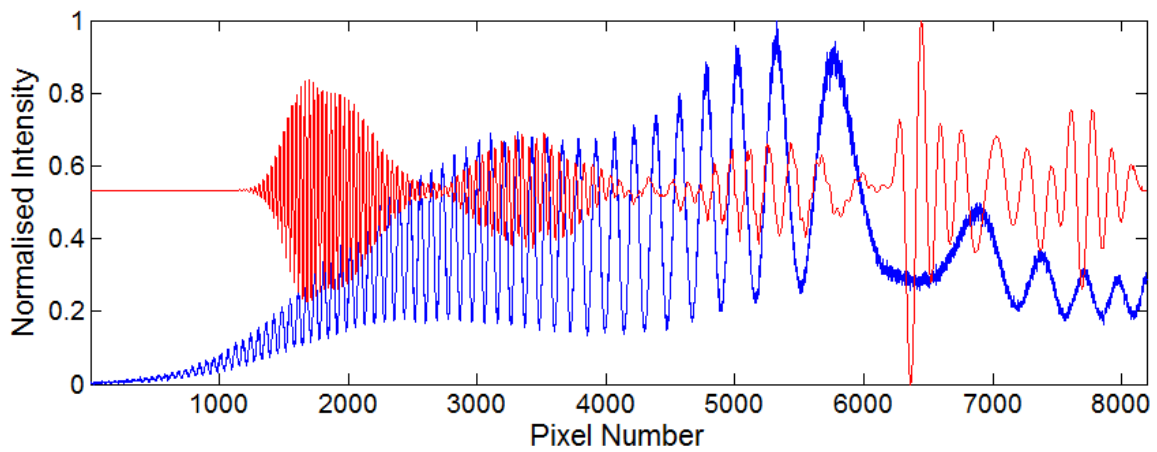

Figure 11.24: Interferogram from improved range bulk optics DRI (blue trace) and the autoconvolution result whose negative peak is indicative of the interferogram point of symmetry.

11.4 Matlab Code

11.4.1 Matlab: prism_refraction_angle.m

```
% Authors:    James Williamson
% Date:       2015-02-16
function [theta_o]=prism_refraction_angle(alpha, theta_i, n)
    theta_i = theta_i*(pi/180);      %Angle of Incidence. Converted to radians
    alpha = alpha*(pi/180);          %Apex Angle. Converted to radians
    theta_t=1/((sin(alpha)*((n^2)-(sin(theta_i)^2)))-(sin(theta_i)*cos(alpha)));
    theta_o=theta_t*(180/pi);        %To convert back to degrees
end
```

11.4.2 Matlab: dri_interferogram_simulation.m

```
% Authors:    James Williamson, Haydn Martin
% Date:       2015-02-16
% Creates a spectral interferogram to match the physical properties of the bulk optics interferometer.
%% Set up all of the necessary constants
lambda1 = 818.7e-9    % Lower end of source wavelength
lambda2 = 839.7e-9    % Upper end of source wavelength
pixels = 2047;        % Detector width -1
L = 330e-3;           % Length of orthogonal seperation of gratings
D = 1/330e3;          % Grating period
d = 0e-6;             % Distance away from balance point to start generating the interferograms

%% Calculate wavenumber array
Wc = ((lambda2-lambda1)./2)+lambda1;            % Calculate centre wavelength
Kc = (2*pi)/Wc                                  % Convert wavelength to wavenumber
lambdaArray = lambda1:(lambda2-lambda1)/pixels:lambda2;
kArray = 2*pi*(1./lambdaArray);
rc = L/sqrt(1 -(((2*pi)/(D*Kc))^2));            % Dispersion path for central wavenumber
alpha = (-4*(pi^2)*L)/(((D^2)*(Kc^3))*((1-(((2*pi)/(D*Kc))^2))^(3/2)));
d0 = (alpha .* Kc) - L + rc;                    % Balancing term to shift Kv to the centre

%% Calculate wavenumber dependent path for each discretised wavenumber
WNDispersion = zeros(1, length(kArray));
for k = 1:length(kArray),
        r(k) = L./sqrt(1-(((2.*pi)./(D.*kArray(k))).^2 ));
end

phase = 2.*kArray .* (r -d0 - d - L);
interferogram=0.5.*(1+cos(phase));
```

11.4.3 Matlab: normalise.m

```
% Authors:    James Williamson
% Date:       2014-12-11
function [normalised_array]  = normalise(array)
minimum = min(array);
maximum = max(array);
```

```matlab
normalised_array = (array - minimum)/(maximum - minimum);
end
```

11.4.4 Matlab: deriv.m

```matlab
function d=deriv(a)
% First derivative of vector using 2-point central difference.
%  T. C. O'Haver, 1988.
n=length(a);
d(1)=a(2)-a(1);
d(n)=a(n)-a(n-1);
for j = 2:n-1;
  d(j)=(a(j+1)-a(j-1)) ./ 2;
end
```

11.4.5   Matlab: simple_unwrap.m

```matlab
% Author:    James Williamson
% Date:      2015-02-16
position_deriv = deriv(positions);
wraparound_counter = 2;

for j=1:e        %where e is the number of samples
    unwrapped_position(j) = (wraparound_counter*425)+positions(j);
    if position_deriv(j) > 150
        wraparound_counter = wraparound_counter - 1;
    elseif position_deriv(j) < -150
        wraparound_counter = wraparound_counter + 1;
    end

end
```

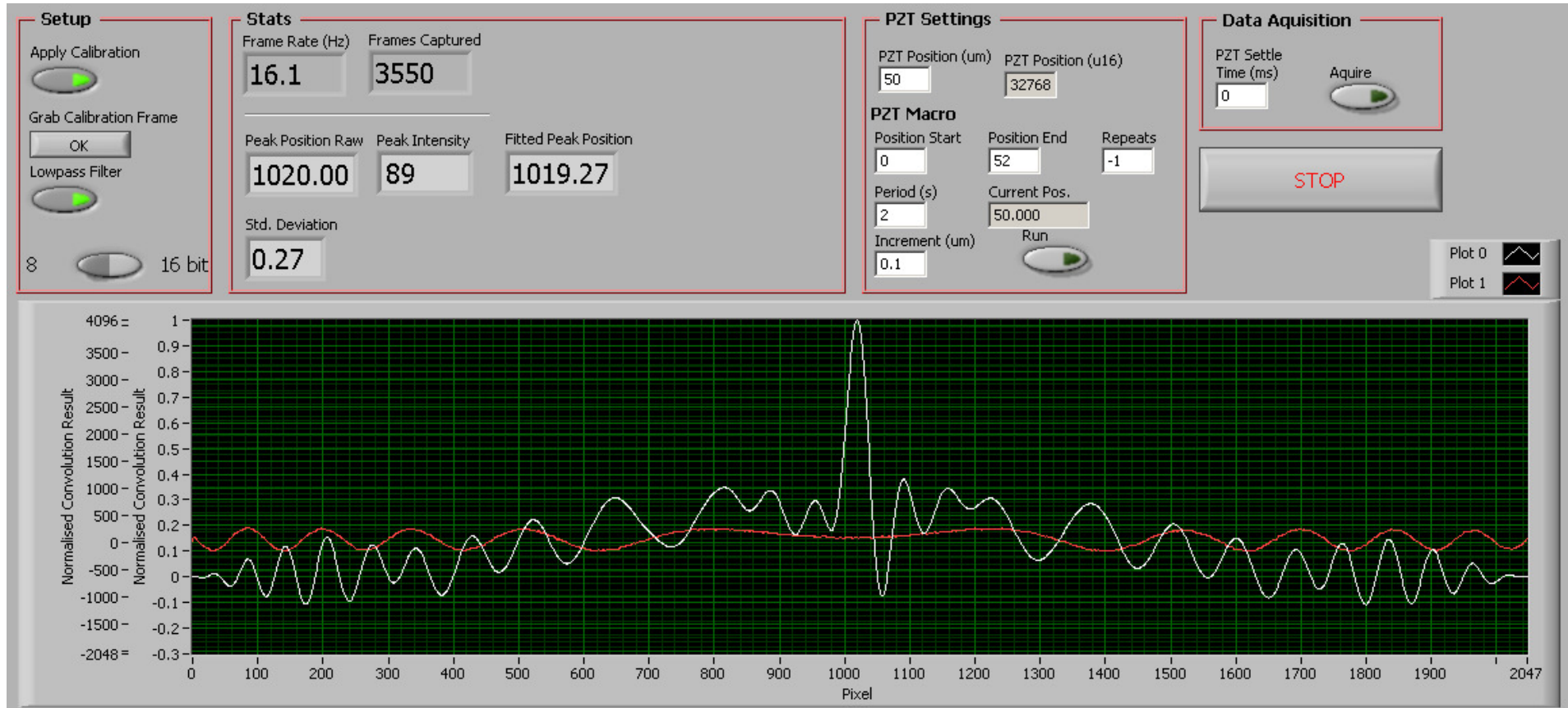## 11.5 Labview Code

11.5.1 Screenshot of 'DRI_Control_Panel.VI' front panel

Figure 11.25: Screenshot of DRI Labview control panel.